Evaluating enzymatic reactions, microbial growth and small molecule detection with a new thermal principle: the Heat-Transfer Method (HTM)

Kai Betlem

PhD

2019

Evaluating enzymatic reactions, microbial growth and small molecule detection with a new thermal principle: the Heat-Transfer Method (HTM)

Kai Betlem

A thesis submitted in partial fulfilment of the requirements of Manchester Metropolitan University for the degree of Doctor of Philosophy

Department of Natural Sciences

Manchester Metropolitan University

2019

I. Acknowledgements

Years ago I decided to go to Belgium for my master's degree and to participate in the Bioelectronics and Nanotechnology program. Where I was introduced to. Bart. van Grinsven (who was doing his PhD at that time) by Prof. Dr. P. Wagner, who suggested that carpooling would be a good option since we both lived in the same town. This was a great opportunity for the both of us to not always have to drive home after a busy day at university. The carpool group did get bigger over the years and became a nice environment for discussion and entertainment. After obtaining my degree I started looking for a PhD position and somewhere near the end of 2015 I received an unexpected call from Dr. B. van Grinsven. Who asked me if were interested in taking a PhD position with Dr. M. Peeters, whom we both knew from our period in Hasselt, the only surprise was that it would not be somewhere nearby. I needed to go Manchester, in the United Kingdom. Now, three years later am finalizing my PhD at Manchester Metropolitan University.

Dr. M. Peeters, Marloes, I would like to thank you for the opportunity to perform my research, and the countless suggestions and opportunities to improve not only research but my skills as well. I had a wonderful time as your single full time student for the better part of 2 years. Thank you very much.

Dr. M. Zubko, I am grateful for the time you took to reintroduce me to the world of microbiology. The countless suggestions on alternatives and extensions for experiments that I did not even think of myself. My sincere thanks to you, your comment were always much appreciated.

Dr. D. Sawtell, The introduction you did give me on SolidWorks and helped to make the first 3D model of the flow cell which will be of use for many years to come. I thank you for the support on the mechanical parts of this process

Prof, Dr. P. Kelly, my gratefulness for the supervision, guidance and suggestions on the manuscripts.

II.   Table of contents

III. Abstract

The Heat Transfer Method (HTM), invented in 2012 by van Grinsven *et al.* [1], is a thermal analysis technique that can monitor DNA denaturation using only two thermocouples and a heat source. The advantage of this thermal sensing is its simplicity, low-cost and use as a portable set up that does not require a lab environment. This work will explore novel applications of the HTM including studying of enzyme catalysis, monitoring of microbial growth, and detection of biomolecules using novel Molecularly Imprinted Polymer-based sensor platforms.

The first objective of this work was to determine whether HTM could be used to for the study of enzyme activity, this is yet unexplored in the HTM. Currently applied techniques for the study of enzyme activities are labour intensive or require expensive equipment whilst not all reactions can be studied. The HTM is not limited by these factors and with the ability to sense changes in DNA length a proof of concept is designed using the EcoR1 restriction enzyme, for which an microbial sample is available as next step. Therefore, it was necessary to functionalise DNA on gold electrodes. To this end, self-assembled monolayer (SAM) on gold electrodes was formed followed by conventional 1-Ethyl-3-(3-dimethylaminopropyl) carbodiimide (EDC) coupling to DNA strands bearing an amine end. This protocol is adapted from previous work by van Grinsven *et al.* [1], but fluorescence microscopy revealed limited attachment of the DNA to the surface. The short comings in the protocol are discussed and alternatives are suggested to promote DNA binding.

Due to difficulties in studying of DNA with HTM, the focus switched towards real-time monitoring of microbial growth, which is important an important factor in many fields, such as study of quality control in food industry, antimicrobial resistance and waste water management, whilst is also an unexplored area for the HTM. Adaptations were made to the existing flow-cell design in order to facilitate longitudinal measurements. First measurements were performed with baking yeast, *Saccharomyces cerevisiae*, and suspensions of the microorganisms were applied to a flow cell containing a plain gold electrode. After it was confirmed that it was possible to study the kinetics of yeast growth, including factors (pH, presence of toxic compounds, temperature) that impact on microbial growth, *Staphylococcus*

aureus was studied. Measurements conducted in buffered solutions showed that the growth of *Staphylococcus* is temperature dependent, and the optimum growth temperature is in accordance with literature. Following on, the growth of *S. aureus* in a complex digestate sample is studied that is composed of several colonies of microorganisms. It is shown that the developed thermal sensor platform is capable of determining the overall microbial load, corresponding to both the amount of *S. aureus* in the system and microorganisms present in the digestate sample. While this could have useful applications in the wastewater and food industry, gold electrodes used as recognition elements are not selective towards particular bacterial strains. Therefore, Molecularly Imprinted Polymers were developed and integrated onto electrode materials.

MIPs are synthetic mimics of antibodies that possess high affinity for their target molecule but are low-cost, can be produced in large quantities, and possess superior thermal and chemical stability compared to their natural counterparts. A novel functionalisation procedure is proposed that directly incorporates the polymer particles into screen-printing ink. The main advantage of using MIP-modified Screen-Printed Electrodes (SPEs) is the simplicity of this sensor platform, low-cost, and high reproducibility due to the use of SPEs. Furthermore, the electrodes can be printed onto paper which provides a sustainable alternative compared to polyester as traditional support material.

Measurements with MIP-modified SPEs were conducted with a range of neurotransmitters and caffeine. Caffeine serves as an anthropogenic marker of water quality and therefore it was of high relevance to study its presence in digestate samples. It is proven that the detection of caffeine with HTM is temperature dependent, and the measurement temperature can be used to fine tune the detection limit of the sensor platform. Sensitivity of the MIP-based platform can be improved by the use of nanoMIPs, nanoparticles that are produced via a solid-phase approach. These particles possess superior affinity (into the sub nano molar range) and are water-soluble due to their small size, which enables the simple functionalisation of thermocouples using dip-coating. These functionalised thermocouples are positioned into flow cells of the HTM set up and it is proven that the temperature recorded by the thermocouple is dependent on the biomolecule

concentration. These measurements are conducted for a range of compounds, highlighting the versatility of this system and the possibility to measure from small molecules (vancomycin) to larger macromolecules (protein EGFR). The limit of detection compared to the use of traditional MIP bulk micro particles improved with an order of three, indicating the superior affinity of the nanoMIPs.

Therefore, it is shown that the HTM is a highly versatile diagnostic tool that can has the potential to offer a quick and easy analysis for a variety of analyses, ranging from high precise medical diagnostics to quality control in for industry and monitoring of environmental changes. While the monitoring of enzyme catalysis was not successful, it is possible to monitor microbial loads in complex samples using simple gold electrodes. Furthermore, by the use of MIPs, it is possible to determine trace amounts of organic molecules and micro-pollutants in water samples.

IV. List of abbreviations

11-MUA	Mercaptoundecanoic acid
A	Adenine
AA	Acrylic acid
AC	Room air conditioning
Al	Aluminium
AM	Acrylamide
ANOVA	Analysis of variance
Au	Gold
bp	Base pair
C	Guanine
CA	Contact angle
C_b	Bound concentration
C_f	Free concentration
CFU	Colony-forming unit
C_i	Initial concentration
CO_2	Carbon dioxide
C_V	Coefficient of variation
DBD	Dielectric-barrier discharge
DMSO	Dimethylsulfoxide
DNA	Deoxyribonucleic acid
dsDNA	Double-stranded DNA
EDC	1-Ethyl-3- (3-dimethylaminopropyl) carbodiimide
EDTA	Ethylenediaminetetraacetic acid
EGDMA	Ethylene glycol dimethacrylate
EGFR	Epidermal growth factor receptor
ex-YEPD	Nutrient-deficient medium
FISH	Fluorescent in-situ hybridization technique
FTIR	Fourier-transform infrared spectroscopy
G	Cytosine
GO	Graphene Oxide
HEMA	Hydroxyethyl)methacrylate
HTM	Heat transfer method
IA	Itaconic acid
IF	Imprint factor
ITP	Indium tin oxide
LOD	Limit of detection
LSD	Least Significance Difference
MAA	Methacrylic acid
MED	YEPD medium
MES	2-(N-morpholino) ethanesulfonic acid
Mg^{2+}	Magnesium 2+

MIP	Molecular Imprinted Polymer
MRSA	Methicillin-resistant *S. aureus*
mut.	Temperature sensitive mutant
NA	Nutrient agar
NB	Nutrient broth
NCD	Nanocrystalline diamond
NHS	N-hydroxysuccinimide
NIP	Non Imprinted Polymer
nmr	Nuclear magnetic resonance
OD	Optical density
PBS	Phosphate buffered saline
PCR	Polymerase chain reaction
Pd	Palladium
PDI	Polydispersity
pH	Potential hydrogen
PID	Proportional integral derivative controller
PLLA	Polylactic acid
PVC	Polyvinylchloride
R_{th}	Heat transfer resistance
S. aureus	*Staphylococcus aureus*
S. cerevisiae	*Saccharomyces cerevisiae*
SAM	Self-assembled monolayer
SEM	Scanning Electron Microscopy
SF	Selectivity factors
Si	Silicon
SIP	Surface-Imprinted Polymer
SNP	Single-nucleotide polymorphisms
SPE	Screen Printed Electrode
SSC	Saline-sodium citrate
ssDNA	Single-stranded DNA
T	Thymine
TEA	Triethanolamine
TGA	ThermoGravimetric Analysis
T_m	Midpoint of denaturation
TRIM	Trimethylolpropane trimethacrylate
tris	Tris(hydroxymethyl) aminomethane
TWTA	Thermal Wave Transport Analysis
UV-vis	Ultraviolet-visible spectrophotometry
wild type	Wild type
YEPD	Yeast extract peptone dextrose
σ	Standard deviation

1. General introduction

1.1. Biosensors

A biosensor is self-contained integrated device that incorporates a biological (derived) material or a biomimetic material on a transducer for the (semi-) quantitative detection of a (group of) analyte(s) [2, 3]. The transducer converts the bio-recognition event into a measurable signal (Figure 1-1). These measurements are conducted for various applications such as environmental monitoring, food safety, healthcare, defence and drug discovery; the sensors can be operated by trained professionals in a lab environment or in a point-of-care application on the spot by a lay person [4, 5].
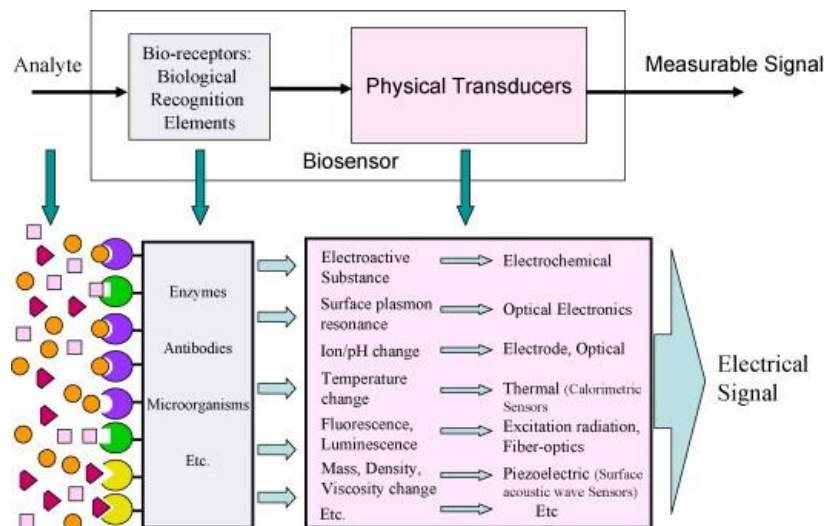
Figure 1-1. Schematic representation of a biosensor adapted from Maki K. Habib (2007) [6].

With the increasing use of biosensors towards point of care applications, there is a continuous effort to overcome the drawbacks on current biosensors, including sensitivity, stability, usability by improving the efficiency of the different parts of a biosensor [7-10]. The ultimate goal is to develop an 'ideal' biosensor, which would have superior properties in areas of accuracy, assay time, sensitivity, selectivity, specificity, stability, sample processing, reproducibility, cost effectiveness, validation and portability while being user-friendly. A more detailed description of each of these parameters is given by de Dieu Habimana *et al.* in Table 1-1 [11].

Table 1-1. characteristics of and ideal biosensor modified from de Dieu Habimana *el al.* (2018)[11].

Criteria	Parameter	Biosensor description	References
1	Accuracy	Should provide the results close to the agreement between a test result and the true value, or if not known, the accepted reference value can be considered	Ellison (2014) [12]
2	Assay time	Should produce a 'real-time' response, especially when perishable foods are being tested.	Cosio *et al.* (2015) [13]
3	Sensitivity	Excellent sensitivity is required	Bhardwaj *et al.* (2017) [14]
4	Selectivity	Should easily discriminate between the bacteria strains and other strains.	Bhunia (2014) [15]
5	Specificity	Should relate to the number of false positive and false negative results that are found with the validated method.	BarbauPiednoir *et al.* (2015) [16]
6	Stability	Should be stable in various environmental parameters and conditions during execution. Should have a good shelf life.	Andrews (1996) [17]
7	Sample processing	Should be able to process minimal sample provided.	Bhardwaj *et al.* (2017) [14]
8	Reproducibility	Should provide same response when the same concentrations are measured at various times.	Eggins (2013) [18]
9	User friendly	Should be fully automated and require minimal operator skills.	McMeekin (2003) [19]
10	Validation	Should be evaluated against current standard techniques in terms of accuracy, limit of detection, recoveries, simplicity.	Leonard *et al.* (2003) [20]
11	Portability	Most important features that helps to eliminate the need for sample transport to the on-site analysis, minimizes the risk of sample contamination and degradation, and the need for sample transportation for analysis.	Almeida *et al.* (2018) [21]
12	Cost	Using cost-effective methods could substantially reduce many needless deaths	Jamieson *et al.* (2006) [22]
13	Compatibility	Biocompatibility of biosensors remains a critical issue in limiting device longevity and functionality	Onuki *et al.* (2008) [23]

Improving the overall performance of a biosensor is a challenging task since each of these factors are to be optimized. The choice of the transducer will play an important role and most biosensors make use of either electrochemical, optical, gravimetric, or thermal detection [5]. Most optical techniques have a high accuracy and selectivity, but require expensive equipment (several thousands of US dollars) and trained personnel. Electrochemical detection allows for fast measurements and data analysis is straightforward; the most common example of a biosensor used in a clinical setting is the glucose biosensor that determines the glucose concentration in a single drop of blood in only a few seconds [24, 25]. This sensor dominates the electrochemical biosensor market with approximately 85% of the total sales in 2004 [26]. However, the accuracy of these assays is >5% which is above the American diabetes association recommendations for a blood glucose test, and is less accurate than the methods used in central laboratories [27]. The application of thermal detection methods is limited due to the requirement of complex and expensive instrumentation, poor sensitivity and the interference of non-specific heating effects.

In 2012, the Heat-Transfer Method (HTM) was patented as a novel thermal measurement technique, which is based on the analysis of heat-transfer through a functionalized chip [1]. The first application of the HTM was to determine single-nucleotide polymorphisms (SNPs) in DNA. Figure 1-2 is modified from this application by van Grinsven *et al.* [1] and shows the transition from double-stranded DNA (ds-DNA) at low temperature to coiled single-stranded DNA (ss-DNA) which is present at high temperatures. This coiled structure of ss-DNA has a 150 % surface coverage compared to the ds-DNA, causing additional resistance for the heat flow through this electrode. The HTM determines this heat transfer resistance (R_{th}) using a heatsink and two thermocouples , one of which is used to control the temperature of the heat sink (T_1), while the other records the temperature opposite of the electrode in the flow chamber (T_2). The temperature difference between these two points is divided by the power input needed keep the heat sink at a constant temperature, resulting in the R_{th}. A more detailed description of the setup and its operation principle can be found in section 2.2.1. Depending on the position of the SNP in the DNA strand the melting temperature of the DNA difference as is observed as is shown in Figure 1-2.

For further studies with the HTM a home-made device was developed for less than £1000 making it low-cost (***criteria 12***), portable (***criteria 11***), can be made into a user friendly device (***criteria 9***), requiring minimum sample preparation (**criteria 7**) and it is biocompatible (***criteria 13***). Drawbacks of this developing technology include the long assay time (15 min/sample) (***criteria 2***), stability (***criteria 6***) and low sensitivity (***criteria 3***). The sensitivity (***criteria 3)*** is closely related the selectivity (**criteria 4**) and specificity (***criteria 5***) and depends on the bio-interface used to recognize the target. By adapting the recognition layer of the system the efficiency can be increased, as will be discussed in Chapters 6 and 7. The long assay time (***criteria 2***) has been addressed by the implementation of Thermal Wave Transport Analysis (TWTA) [28, 29], a novel thermal technology similar to HTM that reduces measurement time significantly to < 5 min. The remaining criteria (***1, 8 and 10***) are target specific and depend on the recognition elements in combination with the read-out technique used. These criteria need to be evaluated for each application of HTM independently and will be discussed in the corresponding chapters. An overview of

applications and the improvements since the invention of the HTM can be found in Table 1-2 to Table 1-4. Table 1-2 shows all applications aimed at the detection of DNA, starting with the original discovery by van Grinsven *et al.* in 2012 [1]. Improvements on this work where made using different substrates and detection of denaturation of longer DNA fragments.

Table 1-2. DNA based applications for HTM.

DNA			
Detection	**Electrode surface**	**Year**	**Comments**
SNPs in DNA	ssDNA bound on NCD	2012 [1]	Discovery of HTM, using short sequences (36 bp)
SNPs in DNA	ssDNA bound on NCD	2013 [30]	Improved sensitivity of HTM towards SNP
DNA	ssDNA bound on NCD	2014 [31]	Concentration dependent measurements on DNA
DNA	ssDNA bound on Gold	2014 [32]	First use of microfluidics to detect DNA denaturation
SNP's in the PAH gene	ssDNA bound on NCD	2014 [33]	DNA denaturation using exon length fragments up to 150 bp
DNA	Sapphire	2016 [34]	DNA measurements on sapphire reduce the noise level on the signal

After the thermal detection of dsDNA denaturation, extensions of the technique to other applications were investigated, including the detection of small molecules using Molecularly Imprinted Polymers (MIP). Table 1-3 provides an overview of this particular application ranging from its first published appearance in 2013 to future developments over the following layers. Originally the MIPs were functionalized on an aluminium substrate using an adhesive layer, which later was replaced by incorporating the MIPs directly into the graphite ink of screen-printed electrodes (SPE). Simultaneously with the use of SPEs, the measurement time was reduced to less than five min due to a new protocol, the Thermal Wave Transport Analysis (TWTA). Finally, the use of nanoMIPs on a thermocouple led to a significant increase in the detection limit. These nanoMIPs were fabricated using a solid-phase support for a range of templates with different sizes, including small molecules,

peptides and a protein. The results from this study will be further discussed in Chapter 7.

Table 1-3. HTM applications using MIPs as recognition elements

Detection	Electrode surface	Year	Comments
L-nicotine, histamine and serotonin	MIPs	2013 [35]	First use of HTM with MIPs for small organic molecules
L-nicotine	MIP	2013 [36]	Parameter optimization to increase detection limit
Histamine	MIP in Graphene Oxide (GO) on a Silicon wafer	2014 [37]	Using Reversible addition-fragmentation transfer (RAFT) polymerization to bind MIP's to GO
L-nicotine, histamine and serotonin	MIP	2014 [38]	Four chamber flow cell, first attempt of assay format
Dopamine	MIP on SPE	2016 [28]	New technique: Thermal Wave Transport Analysis (TWTA)
Noradrenaline	MIP modified on SPEs	2017 [39]	Integrating MIPs into Screen-Printed Electrode (SPE)
Dopamine	MIP on a thermocouple	2017 [40]	First use of MIP functionalized thermocouple
Serotonin	MIP	2017 [40]	Single shot flow cell for whole blood
Aspirin	MIP	2017 [41]	TWTA study of drug delivery kinetics
Biotin, trypsin, vancomycin and an EGFR epitope	NanoMIP	2018 [42]	NanoMIP functionalized thermocouple
Vitamin K	MIP	2018 [43]	TWTA on hexane extracted blood serum
Caffeine	MIP-modified SPE	2019 [44]	High temperatures measurements increase the limit of detection

After using MIPs to detect a variety of smaller components, an adaptation was made to use a Surface-Imprinted Polymer (SIP) for the detection of whole cells and bacteria (Table 1-3). Contrary to MIPs for small organic molecules where in general

binding sites are distributed over the bulk of the material, in the case of SIPs binding sites are solely located on the surface of the material. This has advantages for the use of large macromolecules since it increases the imprint efficacy and reduces costs since less of the template is required to prepare the polymer layers. To increase the sensitivity of the setup, the flow cell was redesigned and this significantly reduced the noise on the signal. To facilitate longitudinal measurements on the viability of microorganism an adaptation of the original flow cell was made by moving the outlet to the top.

Table 1-4. Detection of whole cells using the HTM.

Cells and large molecules			
Detection	Electrode surface	Year	Comments
Macrophages and cancer cells	Surface-Imprinted Polymer (SIP)	2013 [45]	First use of HTM with SIPs for detection of cells
Protein expression on cell membrane	SIP	2014 [46]	Cell recognition based on membrane protein expression and glycosylation
Cancer cells	SIP	2015 [47]	Discrimination between cell lines and monitoring the quality in time
Cancer cells	SIP on Polished Aluminium	2015 [48]	Electrode optimization to increase sensitivity
Escherichia coli	SIP on Al chips	2016 [49]	Quantitative and qualitative detection of *E. coli*
Escherichia coli	SIP on Al	2017 [50]	Redesign of flow cell improving the effect size and detection limit
Various bacteria	SIP on Al	2017 [51]	Selective detection of bacteria using TWTA
Saccharomyces cerevisiae	SIP on Al	2018 [51]	Detection and study of SIP interactions with yeasts
Saccharomyces cerevisiae	Au	2018 [52]	First reported viability study of microorganisms
Escherichia coli	SIP on Al	2018 [53]	Detection of bacteria from a contaminated surface
Escherichia coli	SIP on Al	2019 [54]	Detection of bacteria in Urine samples

Lastly, there are two additional applications that show the versatility of the system; an aptamer-based bio-interface to determine the concentrations of peanut allergens Ara h1 [55], and a study of the phase transitions in lipid vesicles [56]. The aptamer-based sensor was the first application of the HTM toward the detection of proteins, closing the gap between the detection of small molecules and whole cells. The phase transition study was the first to show the fingerprint of the main phase transition of a lipid layer to vesicles, as a sudden increase in thermal resistance was recorded upon changing in the structural composition of the lipids. This study can be taken as a starting point for further investigations on more complex lipid mixtures.

From this overview it is clear that the HTM is a versatile and evolving technology, that has made significant improvements toward becoming an ideal biosensor (Table 1-3). Among these improvements are: the reduction of noise on the signal by optimizing the settings of the temperature control feedback loop [36]; the detection of small molecules was simplified by directly incorporating the MIPs into an disposable electrode [28]; or the functionalizing of the temperature sensor with MIPs [57]; a decrease of the measurement time by imposing a sinusoidal modulation of a linear temperature ramp on the signal (Thermal Wave Transport Analysis (TWTA))[28] and an over whole of the flow cell design, creating a new adiabatic flow cell that has a lower heat loss to the environment [58]. The majority of these improvements will be utilized in this study, except for the adiabatic flow cell, since there was no access to this particular design, to increase the knowledge and understanding of the HTM and find new applications for this devolving technology. One of such applications is the study of enzyme activity, which to date has not been reported for the HTM

1.2. The potential of the HTM to evaluate enzymatic reactions using restriction enzymes

The study of enzyme activity, is a sensitive process and depends on a variety of factors such as pH, temperature, concentration of enzymes, cofactors and substrates [59]. These studies of enzyme activity are collectively called enzyme assays and most are based on optical techniques, requiring for one of the reaction components to be detectable by UV-vis or fluorescence. These techniques are either labour intensive or require expensive equipment, thereby limiting their

application. The HTM will provide the flexibility to adjust the parameters required for the enzyme to be active, while obtaining experimental data on the activity itself. As a first proof-of-application DNA containing a restrictions sight for the EcoR1 enzyme will be investigated. This enzyme will cut the dsDNA according to the pattern shown in Figure 1-3.

EcoR I

```
5´...G AATTC...3´
3´...CTTAA G...5´
```

Figure 1-3. The recognition site for the restriction enzyme EcoR1

EcoR1 is part of a restriction-modification system in *Escherichia coli* that was first isolated from strain RY13 [60]. The restriction-modification system consists of a restriction enzyme and a modification methyltransferase [61], which together defend against foreign DNA such as that from viruses [62, 63]. The cognate modification enzyme methylates and protects the host DNA whilst the restriction enzyme cleaves non-methylated foreign ds-DNA within or near its specific recognition sequence [61]. EcoR1 recognizes a palindromic DNA sequence of six base pairs (bp) (GAATTC). The EcoR1 enzyme cleaved between G and A residues in the presence of Mg^{2+} as a cofactor [60], forming a 4 bp overhang at the 5'-end [64].

For initial experiments DNA oligonucleotide will have to be functionalized onto the gold surface of an electrode. To obtain a more accurate representation of previous work by van Grinsven *et al.* [1], a self-assembled monolayer (SAM) is formed on the gold electrode to which the DNA is attached. They interface of the setup will thereafter be adapted to longer sequences, such as the CDC13 gene of *Saccharomyces cerevisiae* (*S. cerevisiae*), a microorganism that is relatively harmless and easy to manipulate. Of particular interest for this study will be the DLY1108 mutated strain. The *cdc13-1* mutation that is present in this strain generates one restriction sight for the EroR1 enzyme in the CDC13 gene.

1.3. Yeast cells as a model system

Microorganisms are ubiquitous in nature and are involved in many clinical, industrial, and environmental phenomena. Over the last decades there has been an increase in overall outbreak of infectious diseases (such as: cholera, ebola or meningitis) and food poisoning that are caused by microorganisms, but the cases *per capita* appear to be declining over time [65-68]. The source of the infection differs but does not exclude food, drugs and cosmetic products and the prevention of contamination remains for industries operating in these markets [69]. All of these applications need fast and accurate analyses in order to assess the danger for the compromised materials. The identification of the microbes present in the sample is qualitative and largely relegated to the laboratory. The main alternatives included direct microscopic examination of the cells, DNA identification by means of PCR amplification, ELISA assays, enzyme-based assays and fluorescence based measurements[70-72]. Each of these techniques has its own benefits, however the majority are not cost effective (high start-up and operations cost), have a long assay time, labour intensive or suffer from low sensitivity (~10^6 colony forming units per mL (CFU/mL)) and low specificity, especially in mixed samples [69]. The HTM is able to overcome most of these limitations and can detect and differentiate cells using a SIP layer down to approximately 10^4 CFU/mL [46, 49, 73, 74]. However, no information is obtained about viability of the cells (defined here as the capacity to form progeny) [75]. Conventional methods to detect cell viability are culture based and time consuming [76], alternatives are faster and more expensive include: the use of dyes and stains, viability PCR [75], metabolic assays, RNA based, protein based or microwave-based resonator [77]. Drawbacks depend on the applied method and among others include: cost efficiency, need for trained personal, selectivity issues, labour intensive [76]. In this work, the ability of the HTM to evaluate the viability of microorganism is evaluated using *S. cerevisiae* as a model organism.

S. cerevisiae is an ideal organism as it is low-cost, does not require special handling, easy to manipulate and it bears a good similarity to higher eukaryotic cells[78, 79]. Furthermore, *S. cerevisiae* is the microorganism behind the most common type of fermentation and divides by the process known as budding (hence, budding yeasts) [80-82]. Providing sufficient nutrients are present, *S. cerevisiae* doubles in number

approximately every 100 min [83]. The carbohydrates are reduced to alcohols and carbon dioxide (CO_2), this provides the energy needed for budding process (Figure 1-4) [84-88].
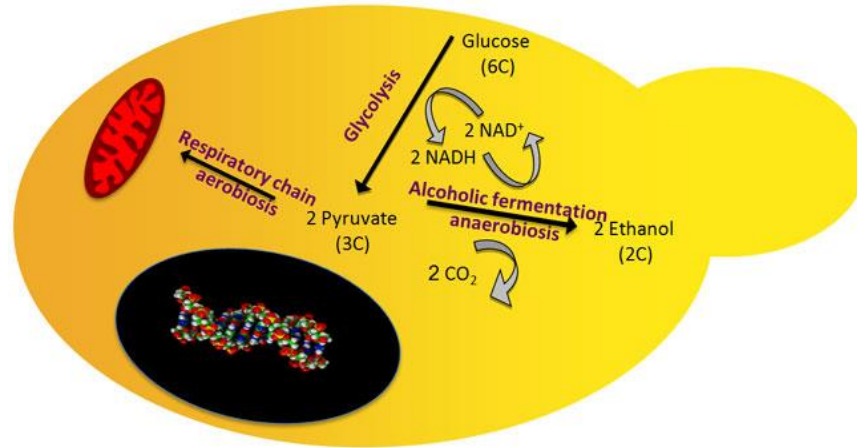
Figure 1-4. Schematic representation of the fermentation process in yeasts (adapted from ref [85]).

In contrast to bacteria, *S. cerevisiae* has no motility in suspension and will sink to the electrode and replicate there. This will cause a significant impact on the thermal resistance at the interface [89]. However, the current design of the flow cell will become unsuitable due to the build-up of CO_2, that has a distinctly higher thermal resistance than buffered solutions in the HTM [90]. Attempts to remove the build-up of gas by inducing different flow conditions either interfered significantly with the thermal signal or removed the budding yeast cells from the surface. To enable the gas removal, the flow cells where redesigned and manufactured using 3D-printing techniques [91].

In this work, laboratory strain DLY640 (optimum growth temperature of ~35 °C [92]) will be used a standard wild type strain (WT) and DLY1108 as a mutant strain (*cdc13-1* mutation), with both strains originating from the Rothstein lab [93]. The *CDC13* gene plays an essential role in the formation of the telomere-capping complex. Budding yeasts that have a *CDC13* gene deletion (*cdc13Δ*) will rapidly form excessive single-stranded DNA (ssDNA) at telomeres, leading to arrest and ultimately cell death[94-97]. The *cdc13-1* mutant strain will grow normally up to a temperature of 30 °C and has an optimum growth temperature between 22-24 °C. When grown at a temperature above 30 °C faulty ssDNA is formed where normally dsDNA is formed, ultimately resulting in cell death [94, 95].

The growth kinetics of yeast cells was studied for a WT strain and a temperature sensitive strain. After optimization of the electrode surface the growth temperature was investigated. To this end the temperature was increased by 1 ± 0.02 °C every 5 h and the temperature that resulted in the highest growth rate was selected for all further experiments. Lastly the growth of yeast was inhibited by either the addition of copper [98], a nutrient deficient medium or by thermal elimination.

1.4. Determining microbial load in digestate samples

The ability of the HTM to measure the viability of *S. cerevisiae* in real-time, provides it with great potential use in waste water management, where it can monitor in real time the viability of the microorganisms involved in the process. The use of molecular techniques in wastewater microbiology made it possible to determine the species composition of microbial communities in these complicated and dynamic systems [99]. Knowledge of the structure of microbial communities is crucial for the understanding of biodegradation pathways of organic pollutants within organic waste treatment facilities [100]. Organic pollutants can be resistant to degradation by microorganisms and therefore persist in wastewater, which compromises water quality [13]. Bio-augmentation (the addition of microorganisms to wastewater) is a low-cost and environmentally friendly biodegradation method relative to physiochemical approaches for removal of organic pollutants [13]. While this approach has been used for decades, there are numerous reports on bio-augmentation failure due to difficulty in monitoring interactions between the inoculated organisms and the host ecosystem [101]. In addition, membrane bioreactors that are used for filtration are prone to biofouling, and this can hamper their efficacy in degrading organic pollutants [102].

Besides issues related to biodegradation processes, there are concerns about the incidence of antimicrobial resistance in organic waste treatment facilities [103, 104]. These microorganisms are potential launch pads for the proliferation of antibiotic resistance as antibiotic residues and other substances with potential selective pressure are present in high quantities within sewage water [105]. Conditions during the wastewater treatment process, such as the presence of chemicals and changes in temperature, can favour horizontal gene transfer [106]. Therefore, it is of a great

interest to monitor bacteria in effluent streams in *real-time* to gain insight in to changes in the composition and the total amount of bacteria present.

The harsh conditions in wastewater, including pH levels, contaminants, and solid fractions complicate the development of biosensors for measuring in this media. The fluorescent *in-situ* hybridization technique (FISH) allows characterisation of bacterial populations in complex ecosystems [107]. Culturing assays, such as the Total and Fecal Coliform Assay, rely on the use of indicator organisms to estimate the number of pathogens in wastewater samples [108]. The cultivation and analysis of these indicator microorganisms is a labour-intensive and time-consuming process [109], which can be overcome by the use of nucleic acid-based methods. Real-time PCR is a fast method and can be combined with pre-treatment steps that involve the addition of intercalating dyes, that enable exclusive detection of DNA from viable microorganisms, but also enable the discrimination between deceased and living bacteria [110, 111]. However, this method would not allow evaluation of the dynamics in bacterial communities and influence of stochastic factors [112].

The redesigned flow cell that is able to measure the viability of *S. cerevisiae* will be employed to monitor growth of *Staphylococcus aureus (S. aureus)* in solution, for the first time bacterial growth will be monitored using a thermal analysis technique. In contrast to yeast cells that readily adhere to surfaces, most bacteria can be motile in liquid media, therefore choice of electrode material as well as nutrients are key experimental factors [113]. *S. aureus* is non-motile in liquids and, although it is a common member of the microbiota in the body, it is an opportunistic pathogen that is the frequent cause for skin infections, respiratory infections, and food poisoning [114]. It is one of the most common causes for hospital-acquired infections and recognized as a worldwide problem in clinical medicine due to the emergence of antibiotic-resistant strains including methicillin-resistant *S. aureus* (MRSA) [115]. Therefore, it is of great interest to develop a sensor platform that can monitor the impact of external factors (the presence of other bacteria, temperature, pH, etc.) on the growth of *S. aureus*. In this study, we demonstrate the influence of temperature and presence of other microorganisms on the growth rate of *S. aureus.* Complex digestive samples contain sediments, which required modifications in sample handling and pre-treatment, are studied to demonstrate proof-of-application of our

developed sensor platform. In the future, it is envisaged that the set-up is used for determining water quality and studying the influence of contaminants, such as micro-pollutants, on growth and structural properties of bacteria, whilst obtaining qualitative and quantitative information on the bacterial composition of complex matrices, such as in digestate samples. To obtain the qualitative information the surface interface needs to be optimized for the species of interest, this can be done using a synthetic interface such as SIPs or MIPs when investigating metabolic components from these microbes.

1.5. Molecularly Imprinted Polymers (MIPs)

Synthetic components can be used as a biomimetic interface for a biosensor with the advantage of superior chemical and thermal stability compared to their biological alternatives such as proteins, enzymes and DNA. For example, synthetic DNA that has a polyamide backbone instead of a sugar phosphate backbone, shows improved chemical and enzymatic stability [116, 117].

MIPs mimic the specificity and selectivity of antibodies and have therefore been labelled "plastic" antibodies. They possess high affinity for their template molecules but have superior thermal and chemical stability, are low-cost, have a scalable synthesis and do not require animals for their production process [118-124]. Furthermore, as these plastic antibodies are not proteins, they are not susceptible to degradation by proteolysis [125]. This is beneficial for the *in situ* monitoring of biomolecules, making them re-usable and a viable alternative for the use in geographical more remote areas with restricted healthcare infrastructure [126].

The imprint is formed by co-polymerizing functional and cross-linking monomers in the presence of a (molecular) template [127, 128]. By removing the template, a porous material that contains high-affinity nano cavities remains, as is schematically represented in Figure 1-5 [119, 123, 129-131]. The traditional approach to synthesize these MIPs is by bulk imprinting. After formation of the polymer the solid material is ground down using a ball mill to form micron-sized particles, for which commercial applications, such as column filtration, are available. Alternative ways to form MIPs are also available and have recently led to the incorporation of a MIP as an active ingredient in a cosmetic product [132]. MIP particles are extremely suitable for the

extraction and quantification of target molecules in complex matrixes such as the extraction of catecholamine from human plasma samples, using a chromatographic approach [133-135]; or the chiral separation of (-)-noradrenaline (a catecholamine) from buffer solutions using a monolithic MIP [136].
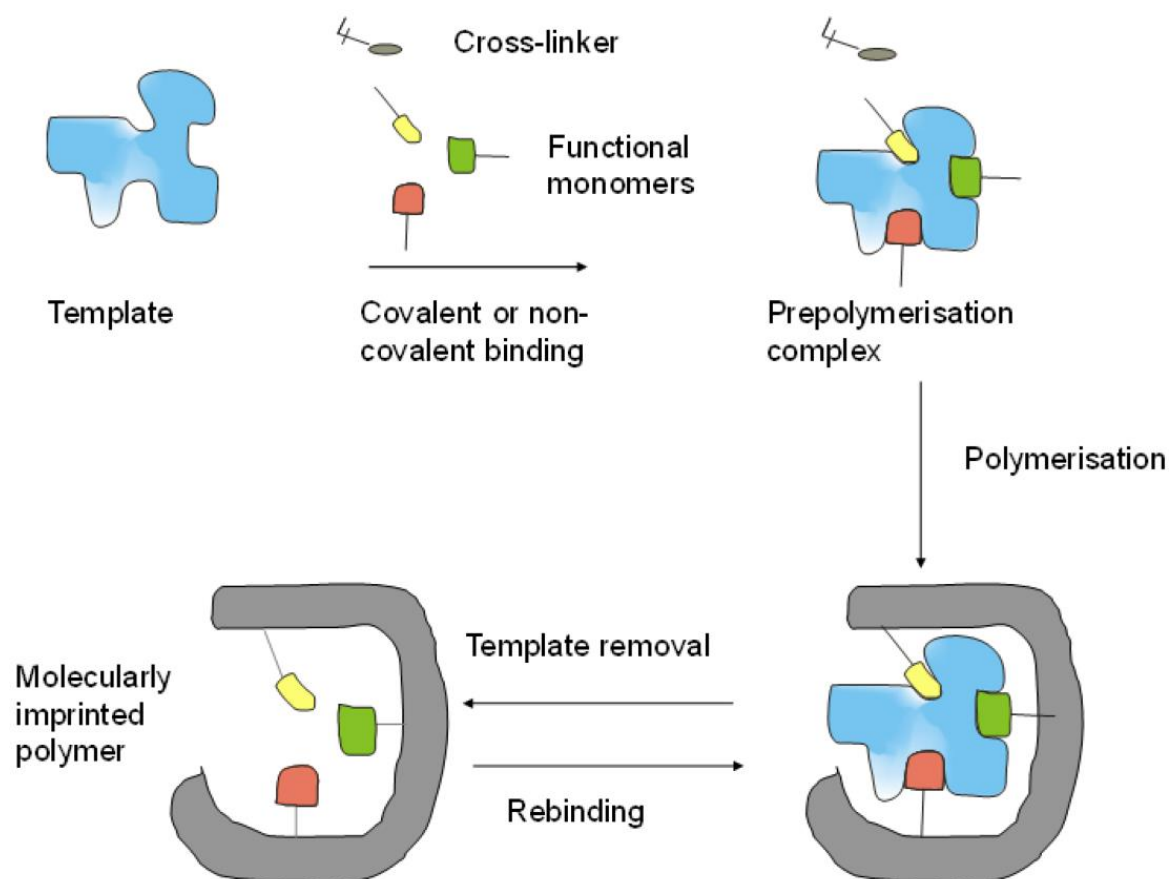
Figure 1-5. schematic representation of the formation of a molecular imprinted polymer (MIP), adapted from Menger *et al.* [131]

The use of MIPs as the bio-interface layer in a sensor is limited and mainly based on electrochemical detection [137-142] or gravimetric methods [143-145]. The explanation for this is twofold; first, difficulties related to incorporating MIPs into sensor platforms and, second, a lack of detection methods that allows for straightforward interpretation suitable for integration into portable devices [119, 146, 147]. While the electrochemical techniques offer fast and low-cost readout, they are not compatible with every target molecule.

In this work MIPs will be used as a recognition element in the HTM, the binding of target species to the specific cavities will obstruct the heat flow and increase the thermal and electrical resistance [35]. To integrate the MIPs into the bio-interface two approaches will be discussed:

1) The micron-sized particles are mixed with a graphite-based ink and screen printed onto different substrates.
2) Functionalization of the thermocouple with high affinity nanoparticles, referred to as nanoMIPs.

1.5.1. MIP-based SPEs

Recently, Peeters *et al.* reported a method that enables fabrication of low-cost and mass producible of MIP based electrodes [28]. Micron-sized MIP particles were mixed with a graphite based ink, which was used to produce SPEs. This resulted in a disposable electrode with low batch-to-batch inconsistencies, that offers additional material advantages such as flexibility and low-cost [148]. As a first proof of concept for these MIP-modified SPEs the binding of a neurotransmitter (dopamine) was evaluated, using a standard polyester substrate as base of the electrode [148]. This work investigated the application of an additional array of substrates that have not been used in combination with MIPs before namely, polyvinylchloride (PVC) household printing-paper and tracing paper. The effect of the SPE substrate on the thermal detection is investigated using a highly specific MIP for noradrenaline that was developed by evaluating the composition of various charged monomers. This MIP incorporated into the graphite ink and printed on the different substrates, which are then exposed to an aqueous solution containing noradrenaline.

The analysis of biological components such as proteins, enzymes and neurotransmitters with HTM is limited up to a maximum of 50.0 °C [149], due to the thermal stability of these components. Measurements at higher temperatures would minimize the noise on the signal, thereby significantly increasing the limit of detection. To demonstrate this, a MIP-modified SPE was made that has high sensitivity and selectivity towards caffeine. A thermally stability of up to ~180 °C [150] makes caffeine the ideal candidate to evaluate the influence of temperature on detection with HTM. To verify that the system remains selective at higher

temperatures, the response of caffeine was compared to chemically similar compounds theophylline, theobromine and another stimulant of the central nervous system (dopamine) (Figure 1-6), for which MIP based sensors have been reported [151, 152].
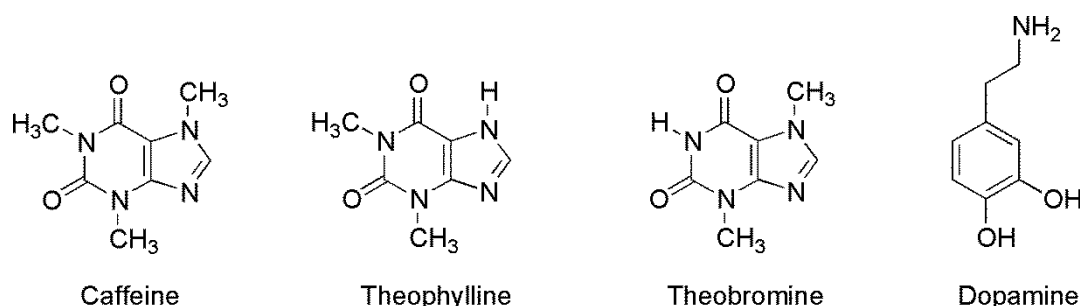
Figure 1-6: Chemical structures of theobromine, caffeine, theophylline and dopamine.

Whilst several MIPs for caffeine have been developed for the extraction and purification of samples [153, 154], this will be the first study utilising caffeine based MIPs for the thermal analysis of complex food samples and water control management. For the latter, the presence of caffeine is used as an anthropogenic marker for waste water contamination and can be correlated to the abundance of various microbial contaminants [155].

1.5.2. NanoMIP functionalized thermocouple

The micron-sized MIPs can be used to mass fabricate MIP-modified SPEs and subsequently obtain quantitative information based on the changes in thermal resistance at the solid-liquid interface [1, 39]. The limit of detection can be improved by increasing the measurement temperature [156], however this is not suitable for thermally unstable targets, such as most biological components. To determine the heat-transfer resistance, additional algorithms are required resulting in an indirect route to determination of the concentration of the biomolecule in question. By depositing the MIP particles directly on the thermocouple the functionalization procedure is simplified [57]. However, the attachment of the micron sized particles requires the use of additional layers on the thermocouples. These particles obstruct the heat-flow through the thermocouple, thereby decreasing the efficiency of detection and increasing the noise on the signal. This can be overcome by directly functionalizing the thermocouples with nanoparticles from a solid-phase support

(nanoMIPs). These nanoMIPs show good biocompatibility and show great potential in the diagnostic and therapeutic sectors [157, 158], where they are already used in optical and electrochemical sensors and assays [159, 160]. The solid-phase support allows for the formation of a variety of targets that differ in size, ranging from a small molecule (biotin), to peptides (vancomycin and an epitope of the epidermal growth factor receptor) to a large protein (trypsin). All of the later forms are high affinity nanoMIPs that even can be considered as replacements for antibodies, where they have been used in ELISA-type assays [42, 125, 161-164].

1.6. Aim of the study

The HTM is a novel and developing technology with wide variety of applications as was discussed in Section 1.1. Over the years several improvements have been made and the versatility of the system was demonstrated (Table 1-2, Table 1-3and Table 1-4). This work will utilize these improvements and provide a more detailed description of their implementation in the sections following section 2.2.1.bringing it one step closer to an ideal bio-sensor.

The main aim of the project was to further expand the scope of the HTM to other applications. To achieve this aim the following objectives were set:

1. Functionalisation of DNA on electrodes to study enzyme catalysis
2. Monitor growth of microorganism *in-real* time with bare electrodes
3. Use of Molecularly Imprinted Polymers as recognition elements in order to improve upon the specificity and selectivity of the sensors

This thesis will provide a summary of all the work that was performed towards this aim. The general introduction (Chapter 1) provides an introduction to the different topic in this thesis, and is further supplemented with an chapter specific introductions. The implementation of objective 1, its fall backs and suggestions for improvements will be discussed in chapter 3. The second objective will be discussed in chapters 4 and 5, were chapter 4 provides the proof of concept using *S. cerevisiae* and has been published by Betlem *et al.* (2018) [52]. Chapter 5 utilizes *S. aureus* for a proof of application to monitor microbial load in digestates, and is based on a manuscript in preparation by Betlem *et al.*(2019). Objective 3 is demonstrated with chapter 6 showing that the electrode can be made to a specific target using MIPs

(published work by Casadio *et al.* 2017 [39]), whilst it is shown that the selectivity of the system is temperature dependent (published work by Betlem *et al.* 2017 [156]). Chapter 7 provides a short discussion using highly specific nanoMIPs (as published in: Canfarotta *et al.* 2018 [42]) as a future improvement on the HTM. The work is concluded in chapter 8, whilst offering suggestions towards an ideal biosensor and the continuation of this project. First, a general materials and methods section in chapter 2 will provide a detailed description of all the methods used.

2. General materials and methods

2.1. Chemicals

An overview of all used chemicals arranged according to the source can be found in Table 2-1. All aqueous solutions were prepared with deionized water of restively 18.2 Ω cm.

Table 2-1 Chemical used in this study

Obtained from Acros (Loughborough, UK)			
Chemical	**Abbreviation**	**Chemical**	**Abbreviation**
Acrylic acid	AA	Serotonin hydrochloride salt (98%)	
Dopamine hydrochloride salt (99%)		Itaconic acid	IA
Ethylene glycol dimethacrylate	EGDMA	(Hydroxyethyl) methacrylate	HEMA
Methacrylic acid	MAA	Trimethylolpropane trimethacrylate	TRIM
Obtained from Alfa Aesar (Heysham, UK)			
Adenine sulfate			
Obtained from Fisher Scientific (Basingstoke, UK)			
Chemical	**Abbreviation**	**Chemical**	**Abbreviation**
Agar bacteriological (Agar NO.1)		Nutrient agar	NA
Copper (II) sulfate		Nutrient broth	NB
D(+)-glucose		Peptone bacteriological	
Glycerol		Yeast extract	

Table 2-1 Continued

Obtained from Sigma Aldrich (Gillingham, UK)				
Chemical	**Abbreviation**	**Chemical**	**Abbreviation**	
(±)-Adrenaline hydrochloride		Hydroxylamine		
(±)-Noradrenaline hydrochloride		2-(N-morpholino) ethanesulfonic acid	MES	
Mercaptoundecanoic acid	11-MUA	NaCl		
1-Ethyl-3-(3-dimethylaminopropyl)carbodiimide hydrochloride	EDC	N-hydroxysuccinimide	NHS	
3,4- Dihydroxy-L-phenylalanine (98%)	L-Dopa	Phosphate buffered saline tablets	PBS	
4,4'-Azobis(4-cyanovaleric acid)		Saline-sodium citrate	SSC	
Acrylamide	AM	Tris(hydroxymethyl) aminomethane	Tris	TE-Buffer
Ascorbic acid		Ethylene diaminetetraacetic acid	EDTA	
Biotin		Theobromine		
Caffeine		Theophylline		
Dimethyl sulfoxide-d6		Triethanolamine	TEA	
Dimethylsulfoxide	DMSO	Tyramine		

2.2. Methods

2.2.1. Heat Transfer Method

2.2.1.1. Flow cell design

The flow cells used for HTM measurements are designed in-house using Solid Works (2016, 3D CAD SP4) and 3D printed with a FORM2 stereolithography printer from Formlabs (USA). FORM2 Clear Resin (GPCL04; a mixture of methacrylic acid esters and photo initiator) was used as resin and deposited with a layer height of 25 µm. The holes were tapped (M3) to allow secure attachment of the copper lid [91].

The flow cells are based on the design described by van Grinsven *et al.*, (2012) [1], and consist of a flow chamber of 110 µL, a fluorocarbon elastomer O-ring with an 6.07 mm inside diameter (RS Components Ltd., UK) that seals a 28 mm^2 area of

the electrode, a copper heat sink, a 22 Ω thick film 20 W power resistor (Conrad Electronic, Germany), and two type K miniature thermocouples (RS Components Ltd., UK). The thermocouple positioned at T_1 measures the temperature of the copper heat sink. A second thermocouple is placed 1.7 mm above the electrode surface and measures the temperature T_2 in the liquid (Figure 2-1). For a full working drawing see Appendix 1.
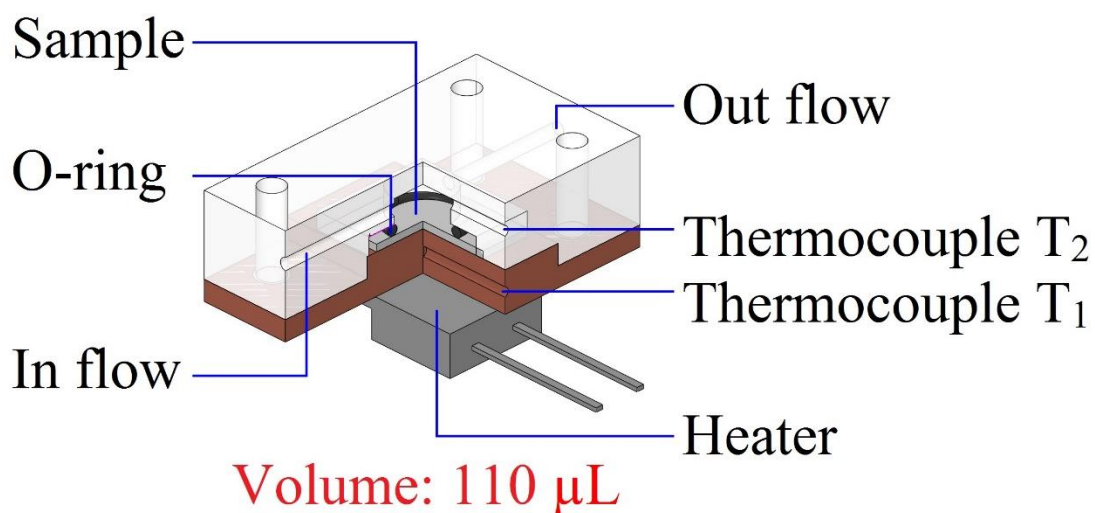
Figure 2-1. Schematic representation of the flow cell.

2.2.1.2.　　Operations principle

The HTM device has the ability to collect temperature information on eight channels and is able to regulate the power output on four independent channels. This allows running up to four measurements simultaneously. A schematic representation of the device is given in Figure 2-2.
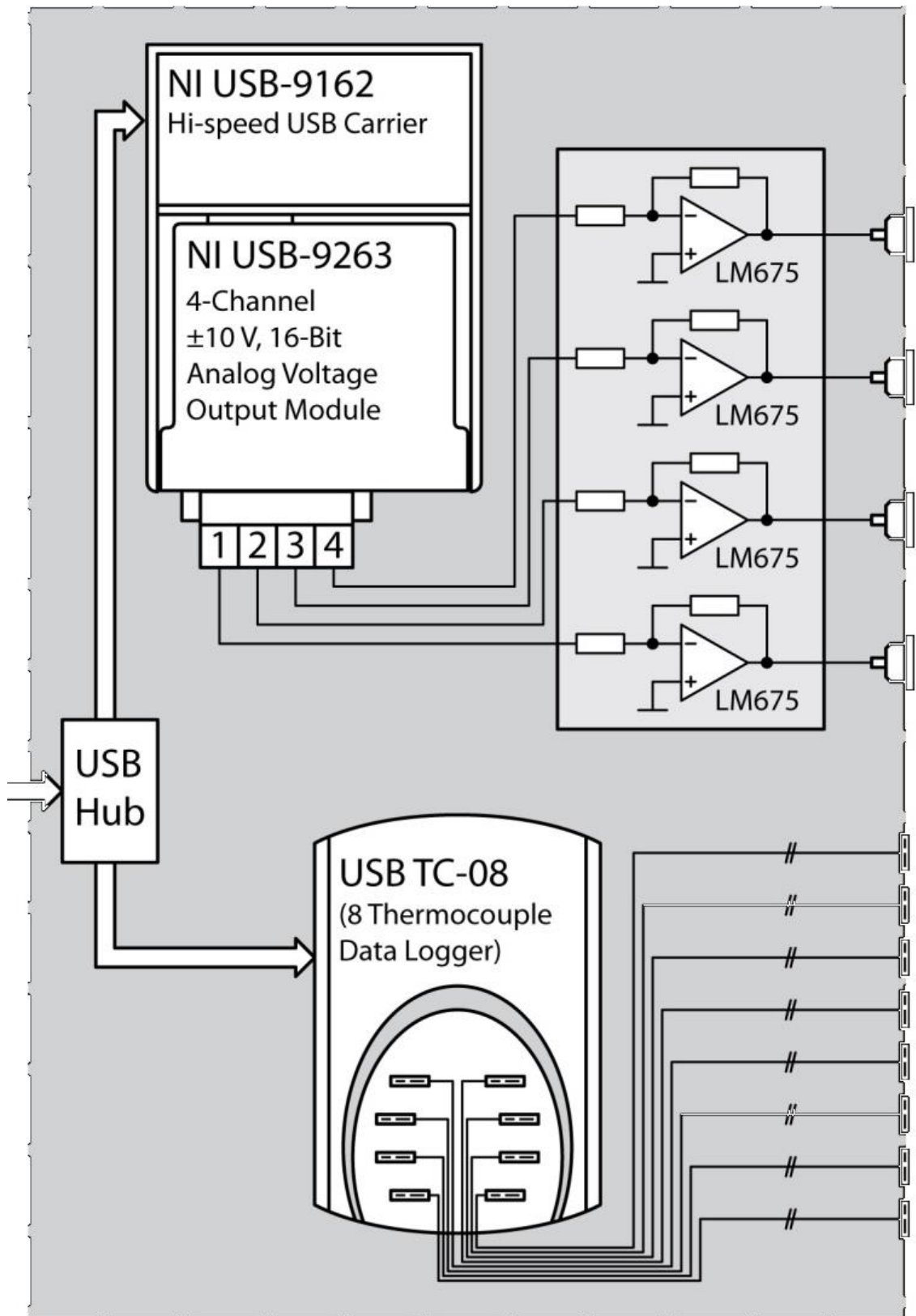
Figure 2-2. Schematic representation of the inner components of the HTM device. Image modified from B. van Grinsven [165]

The TC-08 dataloger (Picolog TC08, Picotech, Cambridgeshire, UK) collect the temperature from the thermocouples and feeds this to the custom designed HTM software (running in Labview). Inside the software the measurement profile is created, by setting the temperature, run time, and the injection parameters when required to control the syringe pump (see Section 2.2.1.4). The set temperature is controlled over PID (Proportional, Integral, Derivative) setting in the software. These settings need to be optimized for each electrode (see Section 2.2.1.3). The calculated output voltage was sent via a second controller (NI USB 9263, National Instruments, USA) (connected by a hi-speed USB carrier [NI USB-9162, National Instruments, USA]) to a power operational amplifier (LM675, Farnell, Belgium) and fed back into the power resistor on the flow cell.

Heat flows from the heat sink through the attached electrode into the flow chamber where it is registered at T_2, creating a temperature gradient over the electrode. The heat transfer resistance (R_{th}) (°C/W) is obtained by dividing this temperature (°C) gradient by the power input (P) (W) to the heat source (Equation 2-1) [1, 42, 45].

$$R_{th} = \frac{T_1 - T_2}{P}$$
<div align="right">**Equation 2-1**</div>

The flow cell used loses heat to the environment due the materials used to construct the flow cell. Stilman *et al.* [58] have developed an adiabatic flow cell in which the heat loss is significantly reduced, however during this study there was no access to this design.

2.2.1.3. Temperature control

2.2.1.3.1. Optimization of the PID feedback loop

The thermal resistance depends on the thermal conductance of the electrode and on the surface functionalization that is applied. Table 2-2 describes the various electrodes used throughout this work. In addition to their source, and respective thermal conductance values, the PID settings, used to obtain the lowest % of noise (as measured by the coefficient of variation (C_V)) on the signal for each electrode, at 37.00 ± 0.02 °C are also included in this table. An Au/Pd target (Emitech,UK) was used in a Polaron SC7400 sputter coater at 800 V for two minutes to create the Au/Pd electrode.

Table 2-2. Electrode specifications. In the Au row [a] indicates the uses of the default PBS as medium, while at [b] YEPD was used as medium.

Electrode type	Source / type	Thermal conductance (W/mK) [166]	PID settings	C_v (%)
Al (ANALAR grade)	BDH chemicals, UK	237	1-3-0.9	1.18
Si (P-type, boron doped <100>)	Sigma Aldrich, China	149	1-9-0.1	0.75
Au/Pd on Si	In-house	(for Pd) 71.8	1-9-0.2	0.96
Au (80 nm adhered on Si, with 20 nm of chromium)	Hasselt University [55]	318	1-8-0 [a]	0.83 [a]
			1-11-0 [b]	0.85 [b]
Printing paper	A4 text and graphic paper 160 g/m^2	130	1-10-0	1.05
Tracing paper	A4 tracing paper 73 gm^2	--	1-10-0	0.90
Polyvinylchloride (PVC)	MacDermid Autotype Ltd., UK	0.13-0.17	1-10-0	0.95
Polyester	Autostat, the Netherlands	0.15	1-10-0	0.85
Glass	Academy Science , Kent, UK	0.96	1-13-0.3	0.95

An electrode with higher thermal conductivity is beneficial for the HTM, as the heat is transported faster trough such an electrode, functionalization of the electrode will result in a decreased conductivity and increased R_{th}. Other parameters that need to be considered include the thickness of the electrodes and whether the substrates are compatible with the media that is used in the measurements. To compensate for the difference in the thermal conductivity between each of the electrode surfaces, the PID feedback loop needs to be optimized [36]. A high P value results in a high response rate. To decrease the fluctuation around the set point a low D value is required; however, more energy will be used to keep it to the set point (higher I value). For each tested setting, the system was allowed to stabilize for 15 min to 37.00 ± 0.02 °C, the 600 data points hereafter were averaged and the S/N ratio

determined according to Equation 2-2. The lowest values found are displayed in Table 2-2 and were used for all further measurements with this specific type of electrode.

$$C_v = \frac{\sigma}{\mu} \times 100\%$$

Where: C_v is the coefficient of variation, σ is the standard error and μ is the average signal over 600 data points.

Optimization of the PID settings additionally decrease the smallest concentration of analyte that can be detected without imprecision of the technique as can be deducted from Equation 2-3, this is also known as the limit of detection (LOD)[167].

$$LOD = \frac{3 \times \sigma}{m}$$

Where: LOD is the limit of detection, σ the standard deviation of the signal and m the slope of the regression line in the calibration curve.

2.2.1.3.2. Environment temperature control

To increase control over the environmental temperature, the flow cell was placed inside either a INCU-Line IL10 incubator (VWR, China) that was set at 27.5 ± 0.1 °C, or an INCU-Line IL 23R cooled incubator (VWR, China) that was set at a temperature of 17.5 ± 0.1 °C. The environmental temperature and the temperature inside the incubators was monitored during the measurements, serving as an additional control for the temperature

2.2.1.4.   Injection control

2.2.1.4.1. Discontinuous injections

A NE-500 Syringe pump (ProSense, the Netherlands), with a minimum flow rate of 0.73 μL/h and a maximum of 1699 mL/h, was controlled by the HTM software written in Labview (2013 V. 13.0) and used for all measurements that required multiple injections[58]. At the start of a measurement, the electrode is stabilized in plain medium for at least 45 min. For each addition, a volume of 3 mL was injected at a

flow rate of 250 µL/min (unless otherwise stated), and left to stabilize for a minimum of 30 min.

2.2.1.4.2. Continuous flow

The flow rate was kept constant at 800 µL/h for all viability studies on yeast cells and at 1 mL/h for the waste water studies.

2.2.1.5. Electrode preparation

2.2.1.5.1. Si based electrodes

Doped Si substrate with (100) crystalline orientation and a thickness of 450 µm were acquired from Sigma (China) and cleaved into 1x1 cm^2 electrodes. For a Si electrode surface, no further modifications were made.

Gold-coated electrodes (hereafter referred to as gold electrodes) were prepared by physical vapor deposition at 5✕10-5 Pa. A chromium layer of 20 nm was deposited onto the silicon substrates, serving as an adhesive layer between the Si and the 80 nm gold layer that was deposited on top as is described by Peeters *et al.* (2015) [55].

The Au/Pd electrode surfaces were formed using a SC7640 sputter device from Polaron (Hertfordshire, United Kingdom) and a Au/Pd target (Emitech, UK). The Si electrode were placed in the sputter chamber and coated at 600 V for 2 min.

All Si based electrodes were cleaned using the standard RCA cleaning protocol [168], except for the gold electrodes; these were cleaned using 70 °C ammonia and hydrogen peroxide in water (1:1:6) for 5 min.

2.2.1.5.2. Screen Printed Electrodes (SPE)

A detailed procedure for preparation of Screen-Printed Electrodes modified with Molecularly Imprinted Polymers (MIP-modified SPEs) is given by van Grinsven *et al.* (2016)[28]. To maintain a conductive and printable ink, a maximum of 30 mass-% of MIPs was incorporated into a carbon-graphite ink formulation (Gwent Electronic Materials Ltd, UK). This ink was printed onto tracing paper (WHSmith, UK), printing paper (Tesco UK), polyvinylchloride (PVC) film (MacDermid Autotype Ltd., UK), or polyester film (Autostat, the Netherlands), before a final curing at a temperature of 60 °C for 30 min [39, 169]. The presence of MIP in the MIP-modified SPE was

demonstrated on SEM images obtained on a Supra 40VP Field Emission SEM from Carl Zeiss Ltd (Cambridge, United Kingdom).

2.2.1.6. HTM modifications

2.2.1.6.1. Thermal Wave Thermal Analysis (TWTA)

In addition to standard HTM measurements, thermal wave thermal analysis (TWTA) has been used for a number of experiments[28]. The advantages of TWTA over HTM include shorter measurement time, spatial information on the target-receptor dynamics, and the potential to improve the S/N ratio. For the TWTA a less stringent control of the heat sink temperature is required. For this technique a sinusoidal modulation of linear temperature ramps (amplitude (α) of 0.1 ± 0.02 °C), and varying frequency (0.01 and 0.05 Hz) is applied around the set point (Figure 2-3). Changes on the functional interface will affect the amplitude and cause a phase shift (ρ) of the measured output signal in the liquid.
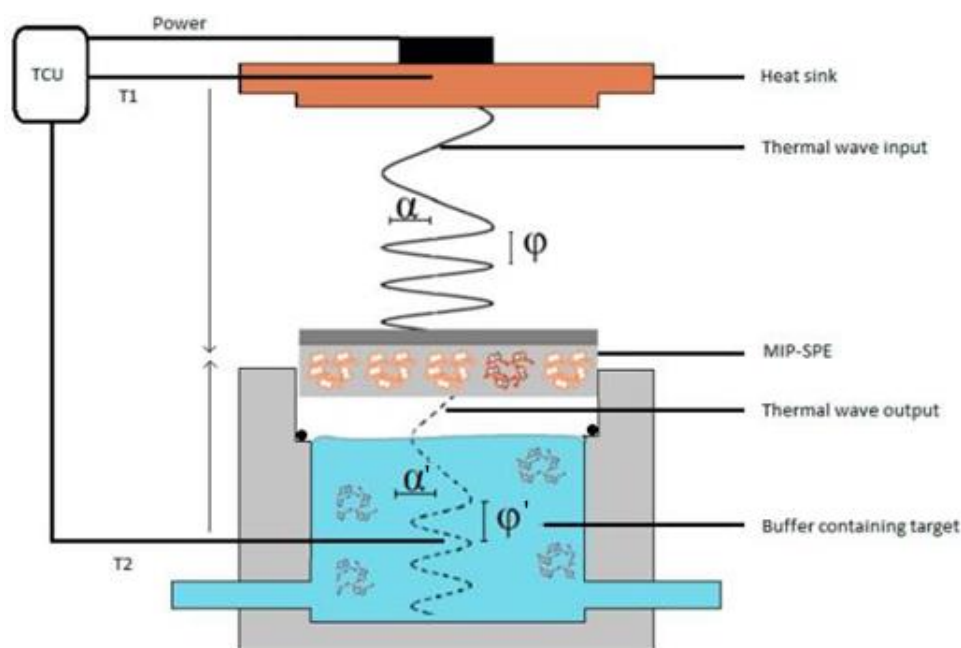
Figure 2-3. Schematic representation of the thermal wave analysis transport. The thermal control unit (TCU) generates and controls the imposed sinusoidal modulation of linear temperature ramps (with phase φ) and registers the output signal (φ') in the liquid opposite of the MIP-modified SPE. The image is obtained from Peeters _et al._ [28].

Any alteration on the surface will register as a delayed response time at T_2. The more pronounced the change, for example binding of higher target concentrations to a MIP interface, the larger the time delay will be. This delay is converted to a

phase shift using a vector representation (the time of one modulation is measured as the output at 360°). The normalized phase shift will be used to construct a dose response curve.

2.2.1.6.2. Functionalization of temperature sensor (T_2) surface

An alternative to functionalization of the electrodes that are attached to the heat sink would be to directly functionalize the thermocouple that measures the temperature in the liquid [42, 57]. A previous study used a polylactic acid coated thermocouple that was roll coated with MIP particles [57]. In this work, nano-sized MIP particles are directly applied onto the thermocouple. The layer is formed by dipping the tip of the thermocouple into a nano-MIP solution for 60 s and subsequently withdrawing the thermocouple at a rate of 5.1 cm min^{-1}. The functionalised thermocouples were subsequently air-dried at room temperature for a minimum of 2 h, and the presence of the MIP particles was confirmed by SEM [42].

2.2.2. Molecularly Imprinted Polymers (MIP)

In this work, a variety of molecularly imprinted polymers (MIP) were synthesized for a number of target molecules. Corresponding non-imprinted polymers (NIPs) were prepared to serve as a reference. The general principle to form these MIP and NIP particles will be described section 2.2.2.1, the precise formulation for each specific target MIP will discussed in subsequent chapters.

2.2.2.1. Synthesis of MIP micro particles

The target molecule and functional monomer are dissolved in a suitable porogen, allowing formation of the monomer-template complexation. After adding crosslinker monomers and an azoinitiator, the solution is sonicated and degassed with N_2 for 5 min. The polymerization is initiated by heating the sample to 65 ± 0.1 °C, this temperature was maintained for 12 h ensuring the polymerization reaches completion. The obtained block of polymer is ground to a powder and sieved to obtain particles with a size of 50 µm or less. The target is removed from these particles by continuous Soxhlet extraction using a mixture of methanol and water (50/50) or a mixture of acetic acid and methanol (50/50). When no trace of the target

could be detected in the extract using optical techniques the extraction was determined to be completed. Hereafter, the powder is washed with water and dried overnight under vacuum. The thermal stability of the particles was ensured by running a ThermoGravimetric Analysis (TGA) experiment on a TG4000 from Perkin Elmer (London, United Kingdom),

2.2.2.2. Batch rebinding experiments

For each experiment, 20 mg of MIP or NIP powder was added to a 5 mL PBS solution containing the target molecule in concentrations (C_i) of 0 to 0.5 mM. The resulting suspensions were placed on a rocking table (110 rpm) for 15 min to 15 h. After binding, each sample was filtered and the free concentration (C_f) (mol/L) of target was determined using a calibration curve on an Agilent 8453 spectrophotometer (Stockport, United Kingdom). The difference between C_i and C_f is the bound concentration (C_b) (mol/L), which can be used to calculate the amount of target that is bound in the respected matrix (S_b) (mol/g) by multiplying it by the volume (L) used for the rebinding and dividing they by the mass of powder (m_p) (g) added to the sample (Equation 2-4).

$$S_b = \frac{(C_i - C_f) \times V}{m_p}$$

Equation 2-4

The binding isotherms were constructed by plotting the S_b against C_f, and fitting a Freundlich isotherm function (Equation 2-5) [170] to the data. Were A and n are constants that adsorbate and adsorbent at a temperature. Here 1/n indicates the dependence on pressure, when 1/n = 1 the adsorption is independent of pressure, if 1/n = 0 adsorption is directly proportional to pressure.

$$S_b = A \times C_f^{\frac{1}{n}}$$

Equation 2-5

To determine the affinity of the produced MIP for its target the imprint factor (IF) is calculated by dividing the binding isotherms of the MIP over those of the NIP at a certain concentration (Equation 2-6).

$$IF = \frac{S_{b\ MIP}^{C_i}}{S_{b\ NIP}^{C_i}}$$

Equation 2-6

2.2.3. Microbial cultivation

2.2.3.1.   Growth media

Nutrient broth (NB), and yeast extract peptone dextrose (YEPD) were used as standard growth broths, where YEPD contains 1% yeast extract, 2% peptone bacteriological, 2% D(+)-glucose and 0.03% adenine sulfate. For solid medium plates, nutrient agar (NA) and YPED plates with 2% additional agar were used.

2.2.3.2.   Yeasts, Saccharomyces (S.) cerevisiae

2.2.3.2.1.   Source information

Baking or budding yeasts, *Saccharomyces (S.) cerevisiae*, were used as proof of concept for the majority of this work. Laboratory strain DLY640 was used as a standard wild type (WT) strain, and DLY1108 was used as a temperature sensitive mutant (mut). Both strains originate from the lab or Rodney Rothstein. The WT strain has an optimum growth temperature ~ 35 °C [92], whilst the DLY1108 strain (optimum growth temperature: 22-24 °C) has a *cdc13-1* mutation that will rapidly form excessive single-stranded DNA (ssDNA) at telomeres, leading to arrest and ultimately cell death when grown above 30 °C [94-97]. This mutation is of particular interest for this study as it will generate one restriction site for the EcoR1 enzyme in the *CDC13* gene.

2.2.3.2.2.   Storage and cultivation

A fresh colony of yeasts was obtained from a YEPD agar plate, suspended and grown at 23 ± 0.05 °C in 250 mL of YEPD broth for approximately 48 h. Hereafter, an optical density (OD) of at least 1.4 (corresponding to 3.82×10^7 CFU/ml) was registered at 660 nm using a Jenway 6305 UV/Visible Spectrophotometer (Bibby Scientific , UK) [171]. The culture obtained was washed three times and after the final wash suspended in YEPD broth containing an additional 20% glycerol serving as a cryo-protector before storage at -80 ± 0.1 °C [172].

2.2.3.3.   Waste water samples

2.2.3.3.1.   Source information

Municipal samples (digestate) were collected on 27/7/2018, 15/8/2018 and 09/41/2018 at 14.00. The digestates originated from a recycling centre (Greater Manchester, United Kingdom) after the anaerobic bioreactors, near completion of hydraulic retention time for organic waste treatment. An industrial sample originated from a brewery and distillery (Greater Manchester, United Kingdom) effluents was collected on the 12/11/2018 at 15.00.

2.2.3.3.2.   Cultivation of *S. aureus*

The strain of *Staphylococcus aureus* (ATCC 9144) was obtained from the microbiological laboratory of School of Healthcare Science at Manchester Metropolitan University. Twenty millilitres of nutrient broth was inoculated with a single colony of *S. aureus* and grown overnight at 37 ± 0.1 °C while shaking at 200 rpm. Cells were harvested by centrifugation (3000 rpm for 10 minutes) and the pellet was washed with 20 mL of sterilized water. Finally, the cells were re-suspended in sterilized water until an OD of 1.0 ± 0.1 ($\lambda = 600$ nM), corresponding to concentration of 0.1×10^8 colony forming units per mL (CFU/mL), was obtained. Samples were diluted to the density $1.0\ 10^2$ CFU/mL and plated out on NA.

3. Evaluating enzymatic reactions and bio catalysis with a new thermal principle: the heat-transfer method (HTM)

3.1. Abstract

The study of enzyme activity, or enzyme assays, is a sensitive process of which most are based on optical techniques, requiring for one of the reaction components to be detectable by UV-vis or fluorescence. The HTM should be able to study the activity of restriction enzyme, such as EcoR1, on DNA that is attached to a surface. To this end DNA was coupled to a gold electrode via a self-assembled monolayer (SAM). The short-comings in this attachment procedure are discussed and alternatives are suggested to promote DNA binding.

3.2. Introduction

The versatility of the HTM has been discussed in Section 1.1 and included MIP based detection (additional research presented in Chapter 6), SIP based detection, a newly introduced cell viability study (Chapter 4) and DNA based detection. To date no HTM studies have been reported on enzyme activity. Enzymes are macromolecular biological catalysts that allow chemical reactions in living beings to occur with great speed and under mild conditions [173]. They lower activation energy of the reaction without being consumed, just as an inorganic catalyst does. However, enzymes are more effective than their inorganic counterparts and have a high specificity towards their target. However, the application of enzymes in industry remains limited to: biofuel cells [174], pulp and paper industry[175], textile industry [176], food industry [177], organic synthesis [178] and the cosmetics industry[178].

Enzymes are classified into six different categories: oxidoreductase, transferase, hydrolase, lyases, ligases and isomerases. Each of these groups has its own effect as the category name implies i.e. they catalyse redox reactions, transfer reaction,

hydrolysis (-OH bonds), lysate (C-C bonds), isomer formation and ligation. An enzyme binds the substrate at the active site and forms the enzyme-substrate complex. This complex performs the catalysis on the substrate were-after the complex falls apart, forming the product and leaving the enzyme intact and ready for the next catalysis. Some enzymes require the presence of a coenzyme, or cofactor before they become active, as for example with the EcoR1 restriction enzyme. This enzyme is part of the lysate group and requires Mg^{2+} before it can cleave the DNA. The EcoR1 enzyme will digest a specific sequence and would make an ideal candidate for a first proof-of-application on the HTM. As mentioned in Section 1.2, the mutated yeast strain contains one restriction site for EcoR1 in the CDC13 gene and would be a target that could be studied by HTM (Figure 3-1) .
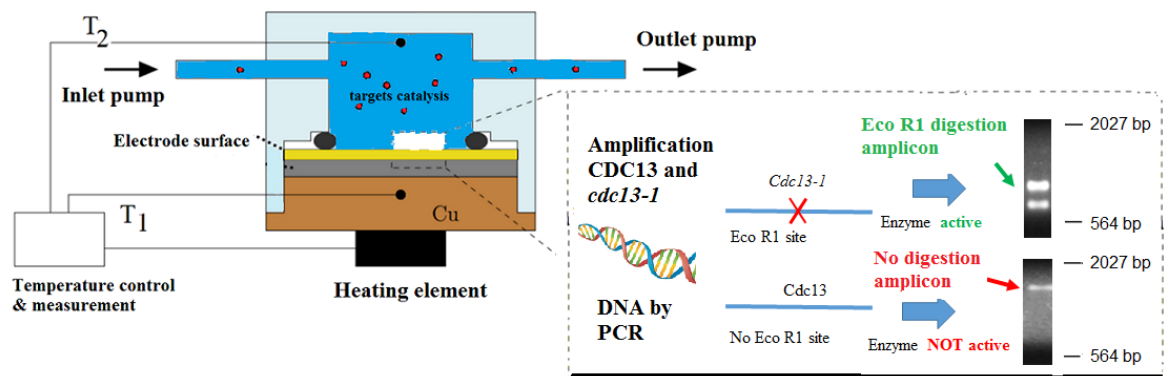
Figure 3-1. Schematic layout of thermal set-up. On HTM the activated enzyme is expected to cut the mutated *cdc13-1* and produce a different thermal response.

The restriction activity could be studies on DNA attached to the surface, thus providing a comparison with previous work by van Grinsven *et al.* [1]. Upon restriction of the DNA the thermal resistance is expected to decrease as a shorter dsDNA strand will have lower R_{th} value. This work will discuss the attachment procedure to link a 36 bp ssDNA probe to a gold electrode using a SAM layer of 11-mercaptoundecanoic acid (11-MUA), and the corresponding hybridisation with a 29 bp target sequence.

3.3. Materials and methods

3.3.1. Preparation of mixed alkanethiol monolayers on nanofiber gold surface and covalent binding of amine-modified dsDNA

In previous work by van Grinsven *et al.* [1] DNA was grafted onto synthetic diamond surfaces using 10-undecanoic acid as a spacer between the surface and DNA. DNA can be grafted to on a variety of surfaces such as glass [179], diamond and glassy carbon [180], silica electrodes [181], mercury electrode[182], carbon electrode [183], indium tin oxide (ITO) [184], gold electrode [185, 186], and chemically modified electrodes [187, 188]. For gold electrodes, the immobilization of DNA can be achieved in two ways; directly, by using a thiol modified DNA strand, or indirectly using a mercaptoundecanoic spacer that forms a self-assembled monolayer on the surface [189]. In this work, gold electrodes were used due to their high thermal stability and their compatibility with microorganisms, whilst mercaptoundecanoic acid (11-MUA) was used to mimic the spacer used on the synthetic diamond surface, 11-MUA has a thiol group on one end that interacts with the gold surface forming a monolayer.

3.3.2. DNA functionalization

Freshly cleaned gold electrodes were functionalized with probe ssDNA, see Table 3-1 for an overview of the oligonucleotide sequences used, according to the protocol described by Pecky *et al.* [189]. In short, the SAM was formed by treating the gold electrode overnight with 5 mM solution of 11-MUA in ethanol. After rinsing with ethanol and water the carboxylic group on the 11-MUA was activated by with a 15 min treatment in 2 mM EDC 5 mM sulfo-NHS in 0.1 M MES (0.5 M NaCl, pH=6.0). The probe ssDNA strand was dissolved in 0.1 M (TEA) (0.45 M KH_2PO_4 / 0.45 M K_2HPO_4, pH=7.0) to obtain a final concentration of 300 pmol in water. From this, 100 µL of solution was applied on top of the gold electrode and left overnight at room temperature while gently agitating at 50 rpm on a rocking table. Finally, the reactions were quenched by the addition of 100 mM hydroxylamine to each chip (final concentration 10 mM in water).

Table 3-1. The sequence of the oligonucleotides with the respective modifications.

Name	Sequence	T_m(°C)	Modification (side)
ss-DNA (probe)	3'-CCA AGC CCC CAT ATG TAC CCG ACG TCC CC - A AAA AAA C_6H_{12}-NH_2-5'		TARMA (3')
ss-DNA (target)	5'-GGT TCG GGG GTA TAC ATG GGC TGC AGG GG-3'	79.5	Alexa (5')

The immobilized probe was subsequently hybridized using ssDNA (target) according to the method described by van Grinsven *et al.* [1]. In short, 100 µL of a 600 pmol target solution in 10 x PCR buffer (10 mM Tris-HCl, 50 mM KCl, and 1.5 mM $MgCl_2$, pH 8.3) was added on the gold surfaces and incubated in a sealed environment at 30 ± 0.1 °C for 2 h. Non-reacted target DNA was removed by rinsing with 2× SSC buffer containing 0.5% SDS (30 min, room temperature), followed by two washing steps that were five min each. First, the sample was washed in 2x SSC buffer followed by a final wash in 0.2 x SSC buffer.

Each of the steps in the immobilization process was followed by obtaining the contact angle (CA), diffused reflectance IR spectra and HTM information. The samples were first investigated using a Thermo–Nicolet Nexus (Madison, USA) fitted with a Spectra-Tech DRIFTS cell (now available as the Thermo Collector™ II Diffuse Reflectance Accessory). The spectrometer and sample compartment were copiously purged with zero-air from a Balaston purge gas generator, the spectra were made up of 36 scans between 4000 and 400 cm^{-1} with a resolution of 4 cm^{-1}, the background was a blank gold electrode. Thereafter, the contact angle for each functionalization was determined using a Theta Lite optical tensiometer (Biolin Scientific, Manchester, UK) and the OneAttension software, the stationary state of the demineralized water droplet on the electrode was recorded at 15 frames per second for 10 seconds resulting in an average contact angle. The electrodes were subsequently placed into the HTM setup, were the signal was stabilized for 30 min at 37 ± 0.02 °C in PBS, subsequently a TWTA measurement was applied. The attachment of a TARMA fluorophore (Eurofins Genomics, Germany) to the probe DNA and/or the corresponding hybridisation with an Alexa 488 (Thermo Fisher Scientific, UK) modified target DNA were made visible on a Zeiss Axio Imager Z1 fluorescence microscope (Cambridge, United Kingdom). The images obtained were

36

analysed using ImageJ (version 1.6.0_24) to establish the uniformity of the samples. Finally, the electrode that showed full hybridisation on the fluorescence microscope were denatured in the HTM setup by heating and cooling the sample between 30 and 90 ± 0.02 °C using a heating rate of 1 °C/min.

3.3.3. Surface plasma pre-treatment

After the standard RCA cleaning, the gold electrodes were placed inside a dielectric-barrier discharge (DBD) plasma reactor. A flow of 5 sccm of air was used to generate a 17 kV oxygen plasma at a frequency of 17 Hz. The surface of the gold electrode was plasma cleaned and oxidised over the next minute. These activated gold electrodes were then used within 30 minutes for the attachment of probe DNA.

3.4. Results and discussion

3.4.1. Initial HTM analysis

Initially, a blank electrode was placed in the setup and heated and cooled three times between 37.00 and 90.00 ± 0.02 °C, corresponding to the protocol used by van Grinsven *et al.* [1]. By increasing the temperature, the thermal resistance decreases consistently over all three runs as can be seen in Figure 3-2A. Hereafter, a functionalized electrode (5 mM 11-MUA, 300 pM probe and 600 pM target) was placed in the flow cell and heated correspondingly. Figure 3-2B shows the corresponding measurement, however the expected denaturation around 63 °C did not occur.
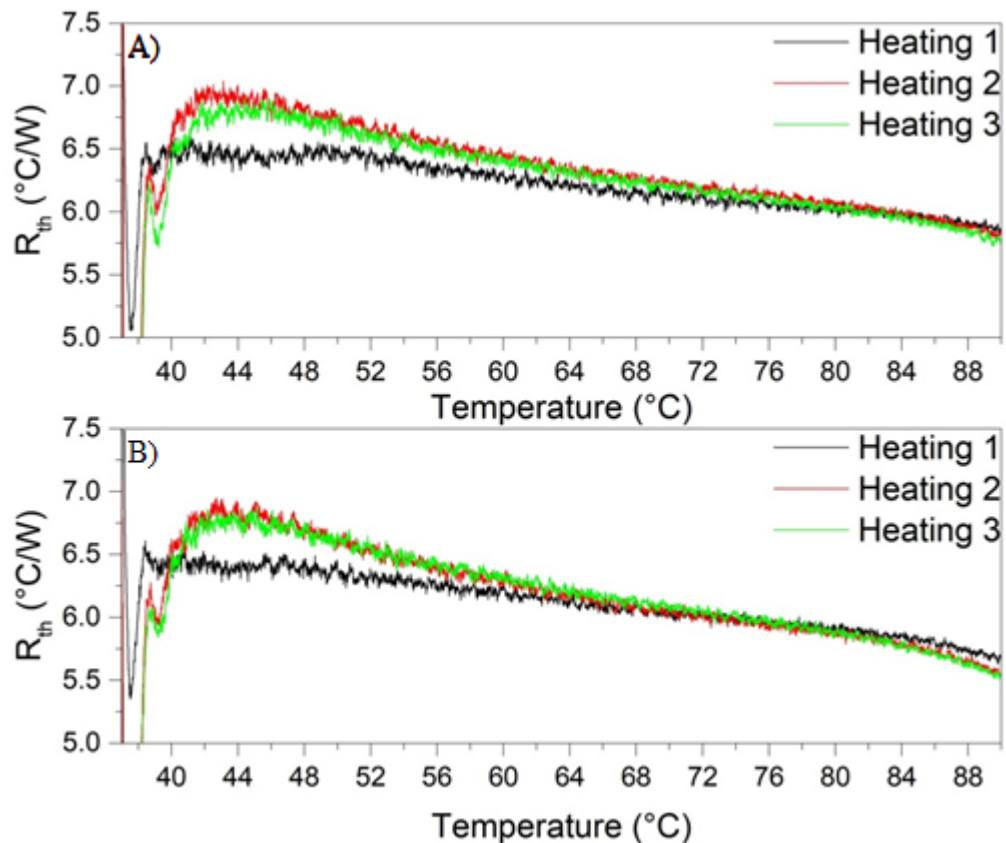
Figure 3-2. Denaturation measurement on a gold electrode. (A) Represents a blank gold electrode. (B) Shows a functionalised electrode, the absence of the actual denaturation around 47 °C indicated that no dsDNA is present on the surface.

The variations observed on the blank measurement were not significant and could be caused by some surface contamination. The difference observed on the functionalized electrode (Figure 3-2B) between the first heating and the subsequent runs closely resembled the blank, indicating that no dsDNA is present. To establish whether or not dsDNA is present on the surface, fluorescence target DNA was used for the hybridisations whilst altering the concentrations of 11-MUA (5, 10, 25 and 50 mM) in pure ethanol and the concentration of probe DNA (300, 450, 600 and 900 pM, and 1.5, 3, 6, 15, 25, 50 and 100 nM) but keeping the target sequence at two times the probe concentration. Additionally, the activation of EDC was prolonged to 2 h instead of 15 min whilst ensuring the pH remained in the range of 5.0-6.0. Fluorescence images were analysed with ImageJ using an inversed triangle threshold filter and the majority of the samples the surface coverage did not exceed 1 %. The surface coverage on gold electrode depends on the length of the oligonucleotide, and a surface coverage of up to 80 % is expected for sequences

below 48 bp [190]. The few samples that did show a surface coverage above 1 % were functionalized with either 10 or 25 mM of 11-MUA. It was observed that with higher concentrations of probe DNA used during functionalization more samples showed coverage above 1 %. However, the coverage did not exceed 2 % on average over all the spots measured on the electrode. For all electrodes that had a surface coverage of at least 1 %, HTM denaturation experiments were performed. However, none of these showed an increase in thermal resistance that could be attributed to the denaturation of DNA. It could be observed that there were some differences based on the composition of the functionalization mixture, but these results were not conclusive and therefore will not be discussed.

Thereafter, the fluorescence of the target DNA was compared to hybridized samples prior to the washing steps. It was found that the target solution was fluorescence and a surface coverage of about 5 % was found after hybridisation, but before the washing steps. After the washing steps the intensity could not be distinguished from blanks. An overview of the hybridisation and washing is shown in Figure 3-3.

A) 0.25 %   B) 6.62 %   C) 0.24 %

D) 1.51 %   E) 8.67 %   F) 1.15 %

F) 6.87 %
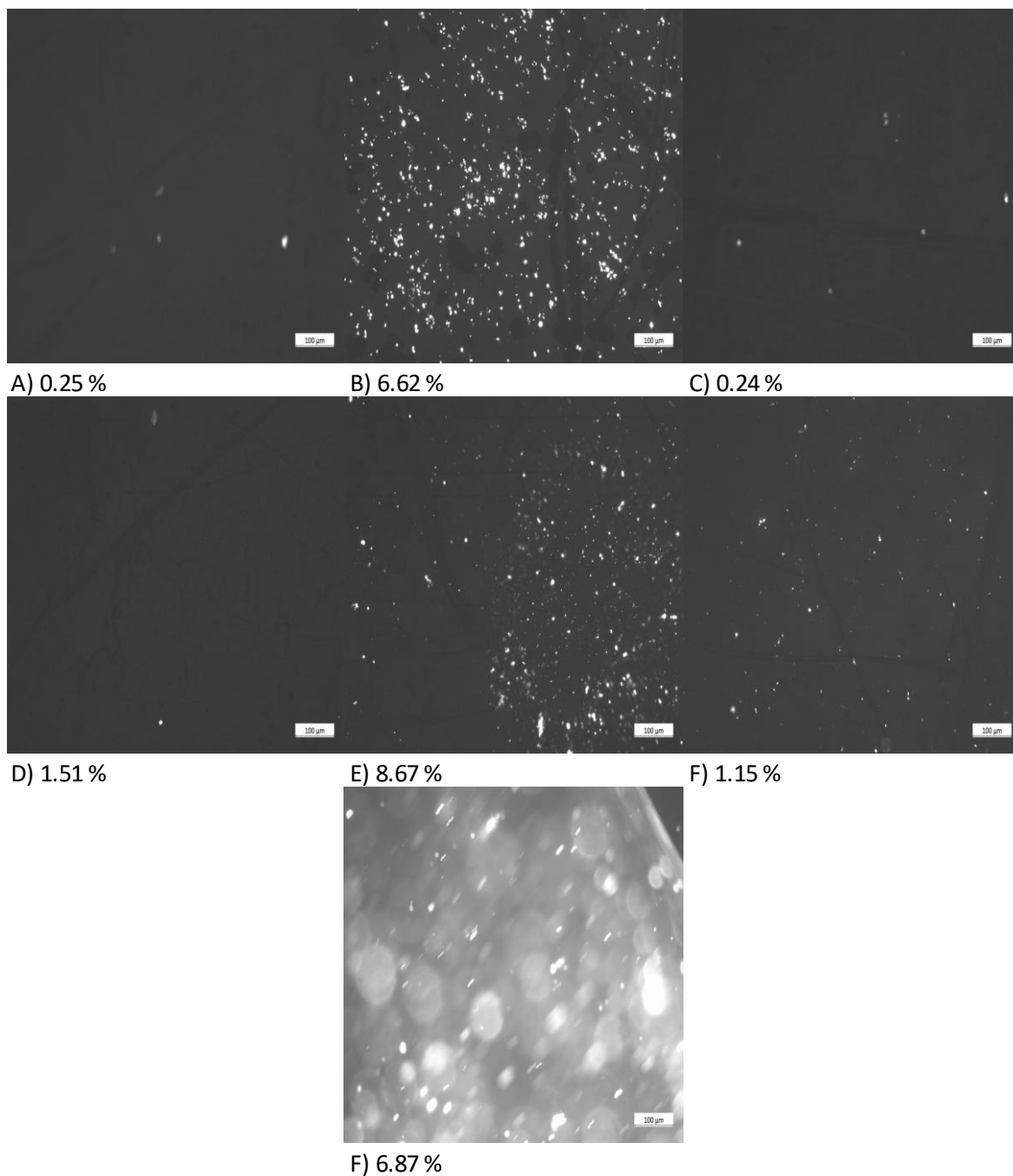
Figure 3-3: Fluorescence microscopy images of the hybridisation. Images A, B and C are made with 5 mM 11-MUA and 1.5 nM ssDNA, images D, E and F with 50 mM 11-MUA and 1.5nM ssDNA (A) no dsDNA solution. (B) 3 nM dsDNA not washed. (C) 3 nM dsDNA washed. (D) No dsDNA solution. (E) 3 nM dsDNA not washed. (F) 3 nM dsDNA washed. .(G) 1.5 nM ssDNA, 3 nM dsDNA solution. The scale bar in all images is 100 µm.

This indicated that the hybridisation, or one of the prior steps does not occur. To check if the probe DNA was attached the EDC coupling was extended to 2 h, but again no increase in the surface coverage was observed after hybridisation.

An attempt was made to use a TARMA fluorescence probe DNA and couple this to the surface; however, the reflectance of the gold surface interfered with the images that where obtained on the fluorescence microscope. An additional surface cleaning step and activation using oxygen plasma did not result in a surface coverage higher than 1 %. However, there was one hybridisation run that did not follow this trend and showed hybridisations above 5 % and one area on the 50 mM electrode showed a coverage just under 70 % (Figure 3-4).

A) 1.63%

B) 14.04 %

C) 17.70 %

D) 69.22 %
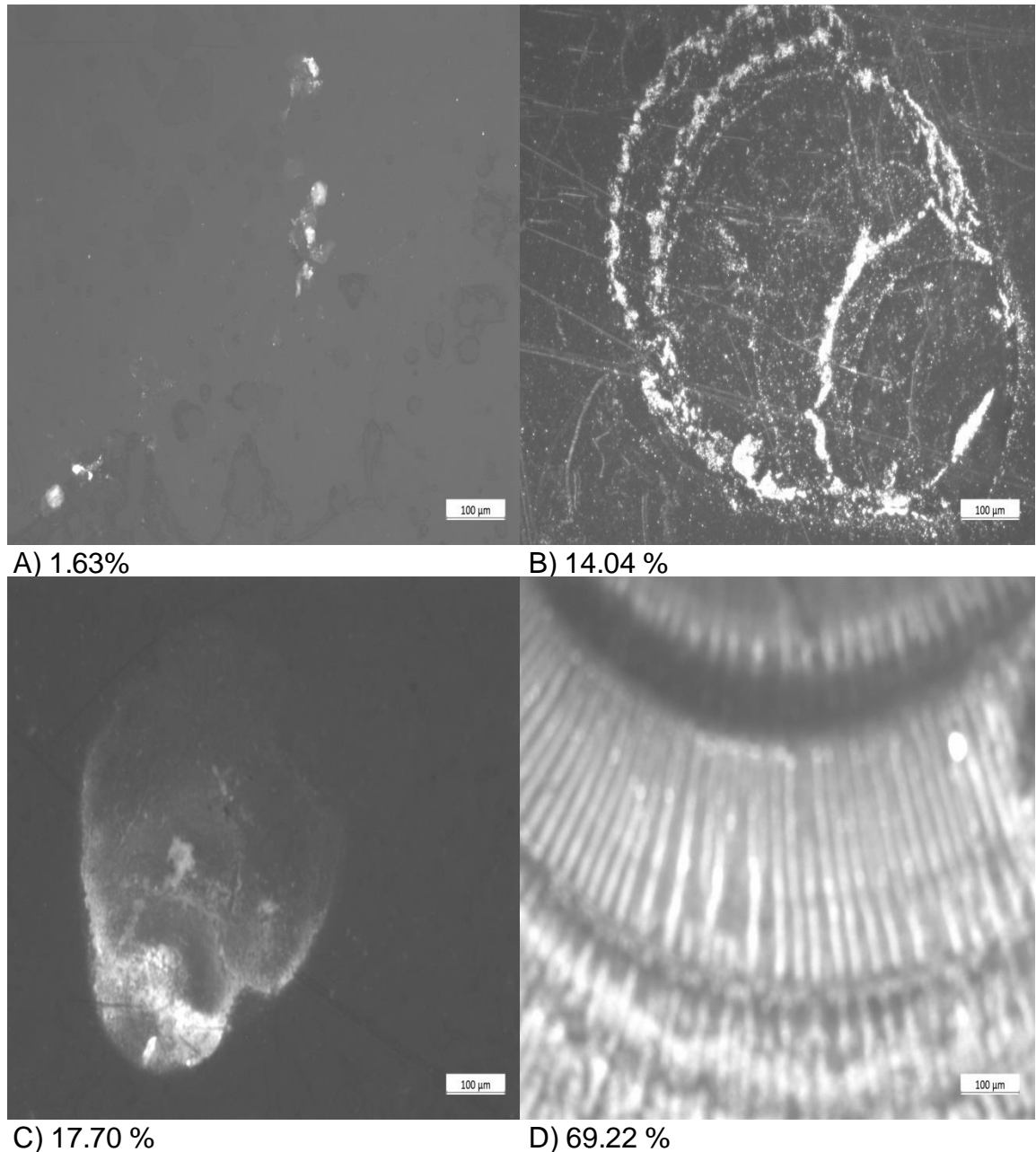
Figure 3-4: Fluorescence microscopy images using plasma treated electrodes and 300pM ssDNA and 600pM dsDNA, the 11-MUA concentration per sample is (A) 5mM, (B) 10mM, (C) 25mM and (D) 50mM The scale bar in all images is 100 µm..

It has to be noted that these samples where plasma cleaned prior to functionalization and that the areas were hybridisation took place resemble droplets that dried on the surface. These samples were then placed inside the HTM flow cell and a denaturation experiment was performed. The results of the 50 mM 11-MUA electrode are shown in Figure 3-2.
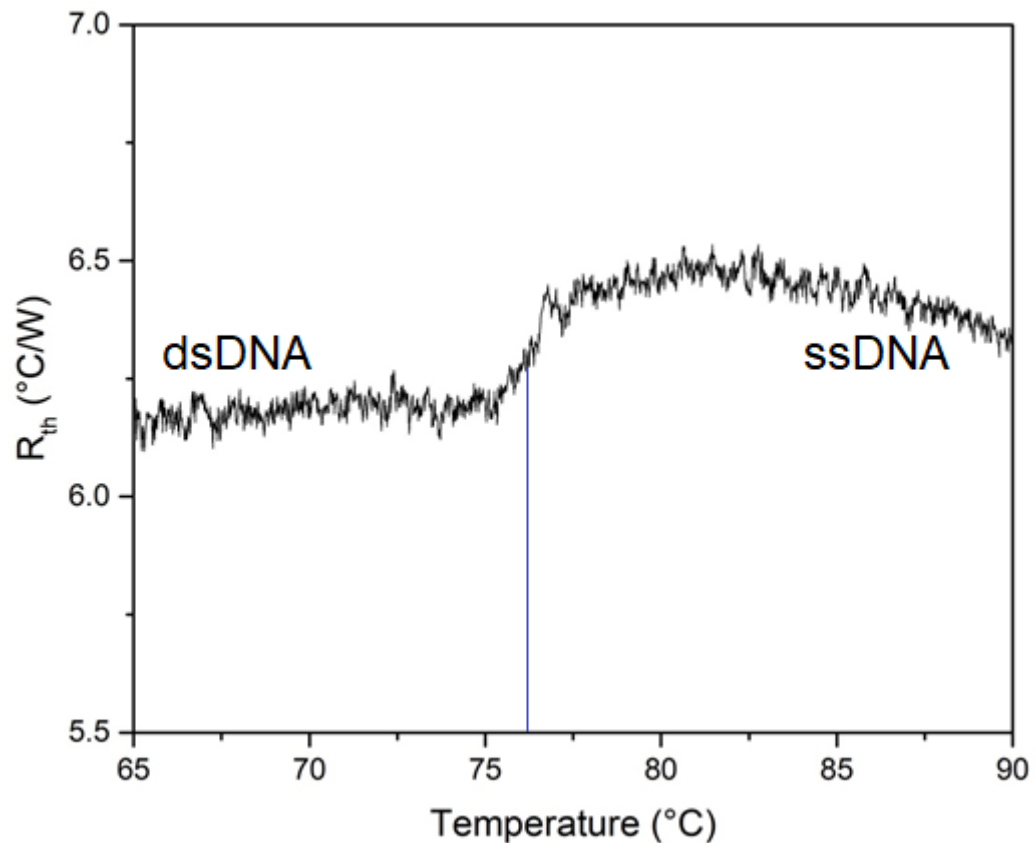
Figure 3-5. DNA denaturation measured on HTM. Before the melting at 76 °C (midpoint of the melting is indicated with a blue line), only dsDNA is present, while after only ssDNA is present.

The dsDNA state has an average R_{th} of 6.20 ± 0.03 °C/W, which upon melting increase to 6.50 ± 0.03 °C/W, corresponding to a 4.8 % increase. The midpoint of this denaturation (T_m) is at is approximated using a Boltzmann fit, resulting in a temperature of 76.41 ± 0.03 °C ($R^2 = 0.96$). A previous study by van Grinsven *et al.* [1] reported an increase of 16 %, and a T_m of 63.0 ± 0.1°C. The observed difference can be explained by the low surface coverage obtained, which is reported to have a smaller increase [191]. Attempts were made to reproduce these results and denaturation runs were performed on different samples and conditions. Some of the plasma pre-treated samples had a difference between the first heating runs and the

second indicating the presence of dsDNA; however, no melting temperature could be established. The RCA cleaned samples gave even smaller and in some cases zero differences between the first and second heating runs, corresponding with the fluorescence images. To understand why the surface coverage of the electrodes with ds-DNA was limited, the intermediate steps of the protocol were studied using HTM, TWTA, CA and FTIR. The HTM and TWTA analysis for the 5 and 50 mM 11-MUA are shown in Figure 3-6, where the 50 mM ds sample was not included due to a technical failure during the measurement.
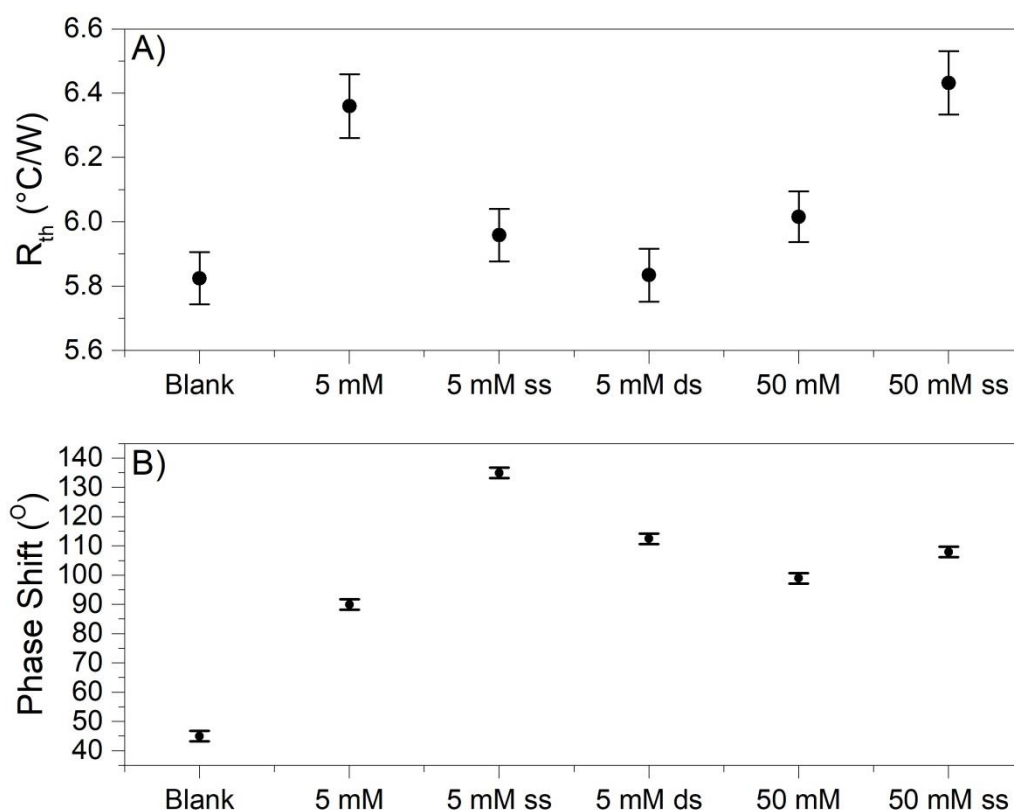
Figure 3-6. Thermal hybridisation analysis. A) shows the HTM analysis were the error bars represent the standard deviation on the signal B) TWTA analysis. The HTM data is averaged over 700 data points, were the error bars represent the corresponding standard deviation on the signal.

The HTM and TWTA data mostly corresponds with what was expected, the blank electrode has the lowest value, which increase for TWTA on the formation of the monolayer. The attachment of probe DNA increases both signals whilst the hybridisation showed a decrease that indicated the presence of dsDNA. The data obtained corresponds with CA measurements performed Table 3-2. The decrease in the contact angle on the addition of 11-MUA was expected since it is hydrophilic

in nature [192]. The higher contact angle for the higher concentration could indicate that the formation of double layers altering the contact angles in for these measurements.

Table 3-2. Average contact angles and the corresponding standard deviation over 150 data points of the different stages in DNA functionalization on a gold electrode. The concentration of 11-MUA is included in the sample name, as is type of DNA present.

Sample	Mean (°)	St. Dev. (°)
Blank	44.10	0.68
5 mM	25.72	0.11
5 mM ss	28.18	1.11
5 mM ds	29.37	0.19
50 mM	30.48	0.25
50 mM ss	35.90	0.09
50 mM ds	10.53	0.08

The observed increase of the CA on the addition of ssDNA was unexpected since DNA is a hydrophilic molecule; however, the increase is small and could be explained by the increased thickness of the surface structure. The hybridisation to dsDNA decreases the CA at the 50 mM 11-MUA sample indicating that more DNA is bound and hybridised compared to the 5 mM sample. In addition, the effect of plasma cleaning of the sample was clearly observed on CA, where it decreased from 74.00 ± 0.19 ° to 16.41 ± 0.010 ° after cleaning. This increase corresponds to the hydrophilic nature of clean gold and disappears within 90 minutes in an ambient environment due to the formation of an gold oxide layer on the surface [193], which will interfere with the ability to form a 11-MUA monolayer. Based on the HTM, TWTA and CA measurements it seems that the protocol is working but with a low efficiency. The most likely cause is in either the EDC coupling of the probe DNA or the formation of the monolayer. To resolve this FTIR measurements where perform on fully functionalized samples (Figure 3-7).
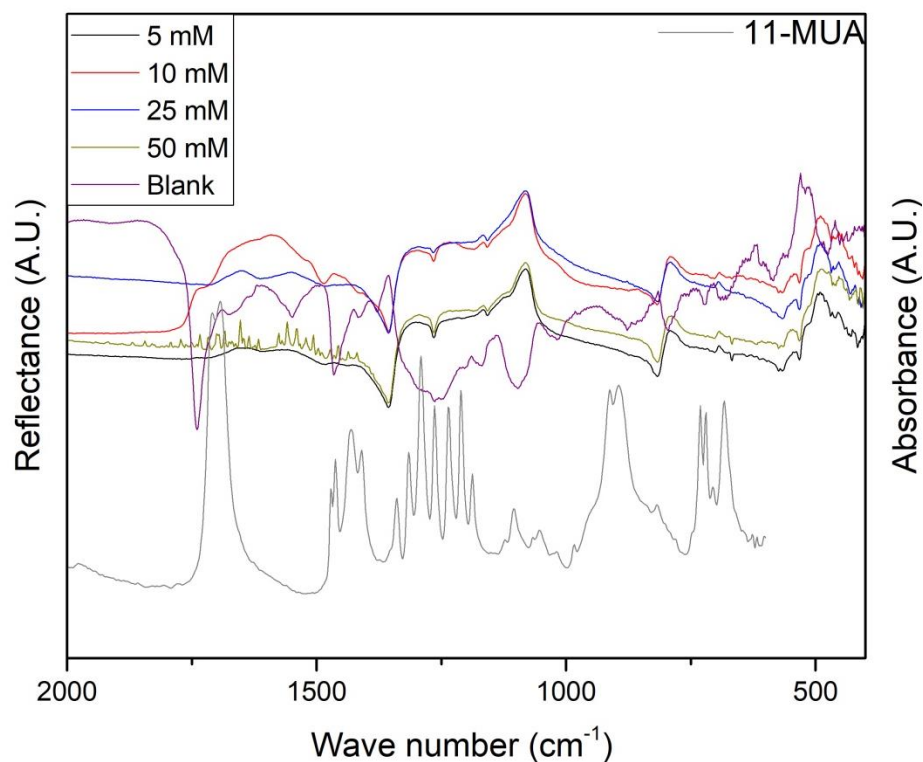
Figure 3-7. FTIR measurements on fully functionalized gold electrodes. the peaks around 1500 cm^{-1} are caused by DNA. The grey spectrum of 11-MUA (note this is in absorbance) was obtained by M. Khorshid *et al.* (unpublished data).

The peak values around 1500 cm^{-1} indicate the presence of dsDNA on the electrodes [194], with an increased amount on the 10 and 25 mM 11-MUA samples, corresponding with the fluorescence measurements. The amount of 11-MUA seems to contribute to the efficiency of the protocol, with an optimum between 10 and 25 mM. This is higher than the recommended concentration of 5 mM that was used in to original protocol by Pecky *et al.* [189]. The higher amount needed to form the monolayer corresponds with the results in Figure 3-8, where the influence of washing of the electrode was studied. The 11-MUA spectra itself is not found in the DNA spectra indicating full binding of the attached monomers with DNA.
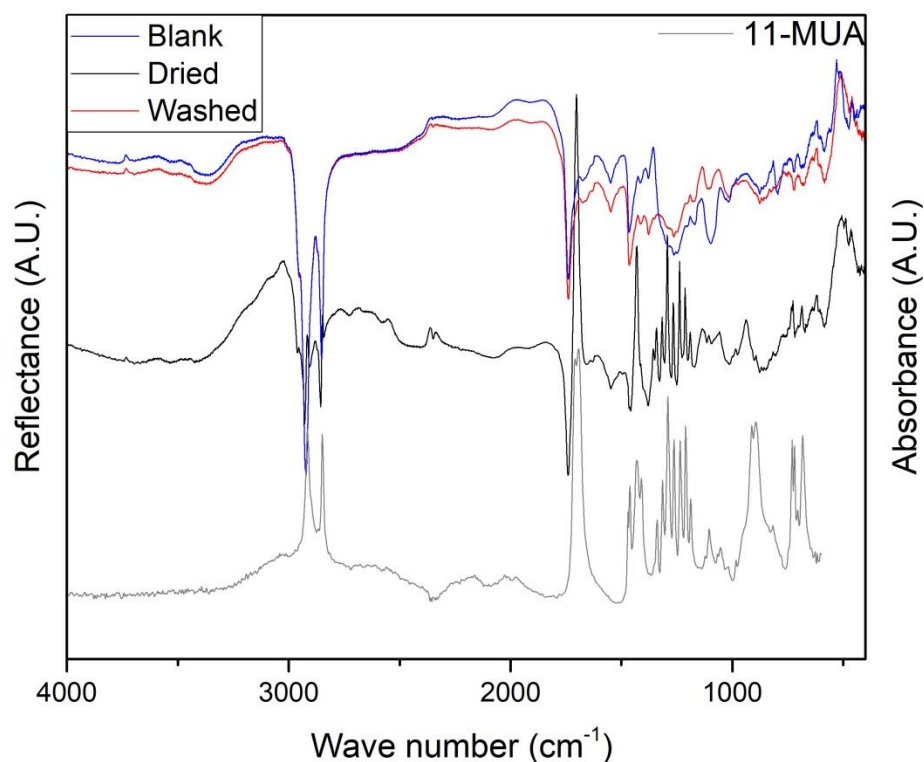
Figure 3-8 FTIR study of the 11-MUA functionalization. The grey spectrum of 11-MUA (note this is in absorbance) was obtained by M. Khorshid *et al.* (unpublished data). The inverse derivative shaped peak at around 1750 cm^{-1} in the spectrum of the dried sample (in black) is due to specular reflectance components.

The presence of 11-MUA is clearly visible and confirmed by the absorbance spectra shown in grey on the electrode after the overnight incubation and prior to the washing steps. After washing there were only minor differences between the blank electrode and the functionalized electrode, indicating that the 11-MUA functionalization decreases the overall efficiency. It needs to be noted that the angle of incidence of the IR beam, when the DRIFTS cell is used as a reflection sampler, is too high to detect the SAM layer after functionalization, causing a false negative.

The plasma cleaned electrodes were shown to be more effective in enabling formation of the monolayer, but due to limited availability of the DBD reactor, not all samples could be pre-treated. It is suggested that during plasma treatment OH radicals are generated on the gold surface increasing hydrophilicity of the electrode. The instability of these radicals leads to a rapid decrease of the hydrophilicity as natural gold oxide is recovered [193]. Therefore, a short time between the plasma cleaning and applying the 11-MUA is required [195]. This time could be extended by

placing the electrodes into an oxygen and water free environment such as a glovebox. This should additionally facilitate in the formation of the SAM layer. However, during the majority of the work there was no access to such an environment.

3.5. Conclusion

Before one can study the enzyme activity of EcoR1 with thermal analysis, the presence of dsDNA should be detectable by the HTM. This work showed one incidental situation where the functionalization of ds-DNA was successful. This was obtained on a plasma cleaned electrode, using 50 mM of 11-MUA, 300 pM probe DNA and 600 pM of target DNA. This resulted in a melting temperature of 76 °C and an R_{th} increase of 4.8 % which is in line with lower hybridisation values reported by Bers *et al.* [191]. The majority of the samples did not show a sharp increase in thermal resistance upon reaching the melting temperature of the ds-DNA, there were only small differences detected. This was caused by a low amount of dsDNA present on the surface of the electrode, with the majority of the electrodes having a surface coverage below 2 % as was determined by fluorescence microscopy. This coverage could not be increase with the use of higher amounts of either probe or target DNA during the functionalization process. Looking at the different stages of the protocol using HTM and TWTA, a low response was observed in the excepted directions. The surface properties corresponded to what could be expected using CA measurements. However, it was observed that a plasma pre-treatment of the surface resulted in very hydrophilic conditions that should benefit the attachment of ss-DNA.

The FTIR analysis performed showed only low amount of dsDNA functionalized to the surface and indicates a correlation with the amount of 11-MUA used. The high concentrated samples had a better response, it is further implied that 11-MUA is not forming the SAM layer on the gold surface and is washed away during the cleaning steps, however it needs to be noted that the FTIR method used might not be able to detect the SAM. This can be attributed to the low activation if at all of the gold surface, decreasing the interaction with 11-MUA.

Based on the findings in this chapter, it is suggested to repeat the attachment procedure using plasma cleaned samples that are transferred to a controlled environment free form carbon and oxygen for further processing. The use of alternative fluorescence labelled probe DNA will provide additional insight into the EDC coupling between the 11-MUA monolayer and the probe ssDNA. Lastly, the use of a thiolate probe sequence should provide direct linkage to the gold electrode, omitting the SAM formation, thereby increasing the success rate of the attachment procedure. These suggestions should result in the functionalization of the gold electrode with DNA, alternatively other electrodes could be investigated.

4. Real-time analysis of microbial growth by means of the Heat-Transfer Method (HTM) using Saccharomyces *cerevisiae* as model organism

4.1. Abstract

This work explores the use of the Heat-Transfer Method (HTM) for the *real-time* analysis of microbial growth using *Saccharomyces cerevisiae* as a model organism. The thermal response of gold electrodes was monitored and exposure to suspensions of *S. cerevisiae* (wild type strain DLY640) demonstrated an increase in thermal resistance at the solid-liquid interface with higher concentrations of the microorganism. Flow cells were manufactured using 3D-printing to facilitate longitudinal experiments.

A clear discrimination was made between the growth of *S. cerevisiae* under optimal conditions and under the influence of factors that inhibit the replication process. These factors included the use of nutrient depleted growth media, elevated temperature, and the presence of toxic compounds. In addition, it is possible to determine the kinetics of the growth process and quantify yeast replication which was demonstrated by measuring a mutant temperature sensitive strain. This is the first time HTM has been used for the *real-time* determination of factors that impact microbial growth.

4.2. Introduction

Without the ability to attach the DNA to the surface electrode it became difficult to study the enzyme activity. However, there was still a strong interest to study the growth of a microorganism using the HTM. Therefore, yeast was studied as a model organism with a simple gold electrode as yeast cells readily adhere to the surface.

S. cerevisiae is widespread in nature and can be found on plants, fruit and in the soil [196]. As indicated in Section 1.3, *S. cerevisiae* have been used by humanity for a long time and more recently it has been included in some diets or heath foods [197]. *Saccharomyces boulardii,* a subtype of *S. cerevisiae*, is used in probiotic preparation for the treatment and preventions of various diarrheal disorders [198]. However, S. *cerevisiae* can in rare cases cause infectious disease especially in immunocompromised or critically ill patients and the incidence has significantly increased since the 1990s [197]. However, the epidemiologic characteristic of S. cerevisiae infections is not fully understood. Of additional interest is that antibodies against *S. cerevisiae* are found in 60–70 % of patients with Crohn's disease and 10–15 % of patients with ulcerative colitis (and 8 % of healthy controls) [199]. As long as the organism remain viable they cause a risk of infection [200]. There are viability studies available, based on vital staining, cell replication, and metabolic activity. However, it remains difficult determine subtle differences in the proliferation activity of live cells [201].

S. cerevisiae has been widely and historically studied and much is known about its life cycle. The yeast cells follow the mitosis life cycle, which consists of five phases: Gap 0 (G_0), Gap 1 (G_1), Synthesis (S), Gap 2 (G_2) and the mitosis (M) phase [202]. Normally cells are in the resting G_0 phase, if a cell is going to divided it starts the G_1 phase were it increases in size. During the S phase that follows the DNA is replicated, followed by another cell growth phase G_2 ultimately leading to the mitosis of the cell M phase [203]. Yeast cells can grow in either haploid or diploid form, the difference between both forms is the amount of DNA present in the cell core. Haploid cells only have half the amount of chromosomes, while diploid cell contain a full genome. When growing the cells under stress conditions, such as nutrient depletion, the haploid cells will die [204]. The diploid cells 'however' will undergo the process of meiosis, a different form of cell division resulting in four haploid spores (two a types

and two α types) [83, 205]. These two types allow for mating of yeast cells which involves genetic recombination. The yeast cells can be grown both aerobically and anaerobically, different carbohydrates are consumed in each process. All yeasts require nitrogen and phosphorus to grow.

Yeast growth is inhibited in a reversible manner when there are insufficient nutrients present; the cells will remain in the G_0 phase until a new source of nutrients is present or if no new food source is found over time the cells will die. They are even able to survive elevated temperatures, but will die when exposed to higher temperatures for a short while. Yeasts are very sensitive to copper surfaces, or the addition of copper ions, which exhibit strong antimicrobial properties against a variety of microorganisms [206]. The exact mode of action for antimicrobial efficacy is very much an on-going topic of study; several reports suggest *S. cerevisiae* is inactivated within minutes of making contact with a copper surface in a process called contact-mediated killing [171, 207]. In this study, the HTM will be used to perform viability measurements on yeasts. It will be shown that the growth can be inhibited using a variety of parameters and that copper ions kill the yeast cells if present in sufficiently high concentrations. Standard plating techniques [55] and the determination of the concentrations of yeast cells by spectrophotometric methods [172] were used to confirm the results, where the spectrophotometric methods were unable to provide any additional information if the cells were dead or alive.

4.3. Materials and methods

4.3.1. Chemicals and equipment

Nutrient-deficient medium (ex-YEPD) was obtained after incubating WT yeast cells in fresh YEPD broth for at least 72 h at 30 ± 0.1 °C. After incubation, the culture was centrifuged, and the supernatant was autoclaved to obtain sterile and nutrient-deficient medium. The ex-YEPD that is formed on this way will contain additional waste products (such as toxins and acids) from the previous cell grown in the medium, these components could cause additional blockage of cell growth in this medium, besides the lack of nutrients.

4.3.2. HTM measurements

4.3.2.1.   Redesigned flow cell

Initially, measurements were performed in a standard Perspex flow cell that was previously described in literature by van Grinsven *et al.*[1]. However, due to the build-up of gasses in the flow cell, the design had to be revisited. Therefore, a novel design was constructed in Solid Works and 3D-printed as described in Section 2.2.1.1 (Figure 4-1) (for a full working drawing see Appendix 1).
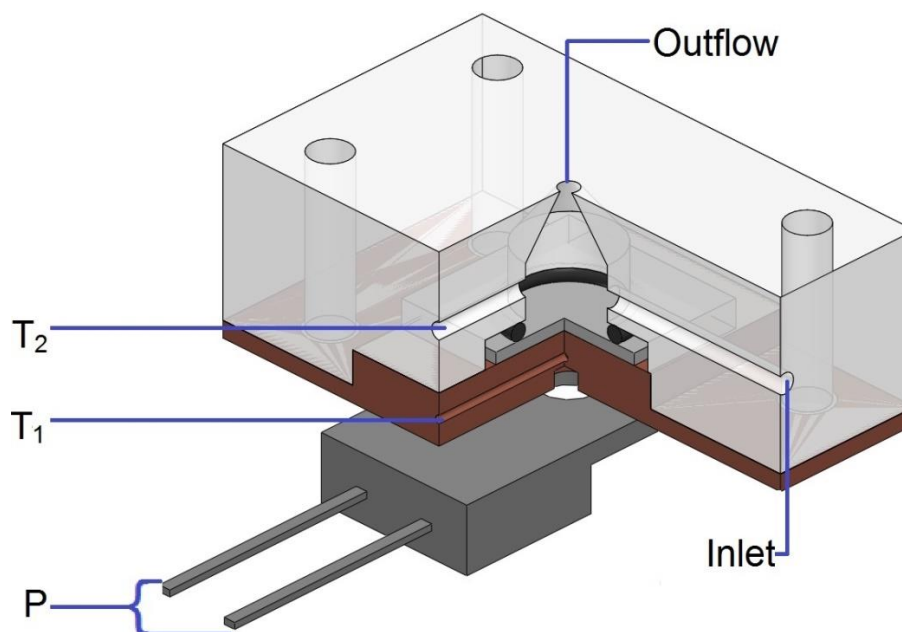
Figure 4-1. Schematic lay-out of redesigned flow cell. The outlet is moved to the top to facilitate gas removal.

These redesigned flow cells were used in all further HTM measurements that evaluated the growth of yeast cells, without the disturbance of gas building up in the flow chamber.

4.3.2.2.   Storage, medium and calibration

The influence of the storage medium and the addition of glycerol as a cryo-protector on the storage of yeast cells were studied. Therefore, a new batch of clean liquid medium (YEPD) culture was grown over two days. This culture was divided in to three aliquots and washed with either YEPD, 1X Phosphate Buffered Saline (PBS) or distilled water (H_2O). Each of these fractions was divided in to two parts, and glycerol was added to a final concentration of 20% to one of the aliquots before cryo-storing the samples at -80 ± 0.1 °C for a month.

The required volume of yeast solution was thawed and washed three times in YEPD (unless stated otherwise). For every sample the OD value at 660 nm was obtained and the corresponding colony forming unit (CFU) per mL determined [171]. A broad dilution range from 10^3 to 10^8 CFU/mL were prepared for the calibration measurements and all samples are stored on ice until the HTM measurement. For dilutions between 10^5 and 10^8 the CFU was approximated using the OD values at 600 nm. No OD values could be resolved above or below these values, thereby setting the upper limit, the lower limit was set to 10^3 using conventional plating techniques.

4.3.2.2.1. HTM profile

Initially, electrodes were stabilized for 1 h into a solution of YEPD, PBS or water corresponding to the measurement at hand. Thereafter, a stepwise injection of yeasts was performed at 1 h intervals at a flow rate of 200 µL/min.

4.3.2.3. Viability study

To ensure sufficient exchange of nutrients and metabolic waste products during the viability measurements of microorganism the flow rate needed to be optimized. Therefore, flow rates were varied between 200 µL/h and 1500 µL/h at intervals of 100 µL/h. After a 30 min initial stabilization of the electrode in YEPD 1 mL of WT yeasts (~10^4 CFU/mL) were injected and the flow was initiated. For every flow rate, the thermal resistance was monitored over 20 h at 37 ± 0.02 °C. A flow rate of 800 µL/h was the lowest rate which did not show a significant build-up of gasses and was used as standard.

Hereafter, the optimum growth temperature was evaluated by determining the growth rate for both WT and Mut strains. Therefore T_1 was increased every 5 h with 1 ± 0.02 °C (initial temperature 19 ± 0.02 °C). This temperature is well below 30 °C, ensuring the activity of the mutant strain.

4.3.3. Validation of thermal results with agar plating methods

The influence of temperature, the nutrient composition and the presence of copper on the growth of yeast cells was studied. In these investigations, the evolution of thermal resistance over a minimum of 6 h before the introduction of a thermals shock (95 ± 0.02 °C for 10 min), or the addition of copper sulfate (0.15 mM Cu_2SO_4 in YEPD) were compared to the evolution after exposure. The influence of nutrient composition of the medium was studied by growth in YEPD for 14 h, directly followed by 14 h in ex-YEPD and lastly 3 h in YEPD. These thermal measurements were validated on agar YEPD plates that were inoculated with 100 µL of cell suspensions after exposure. After 24 h incubation at 37 ± 0.1 °C, the plates were scored for viability. The toxicity of copper sulfate was evaluated over time by incubating a culture of ~10^5 CFU/mL in YEPD with 0.15 mM Cu_2SO_4 added for 0, 2, and 24 h before plating. Additionally, agar YEPD plates containing 0.15 mM Cu_2SO_4 were also inoculated and incubated.

4.4. Results and discussion

4.4.1. Experiments on budding yeast

Prior to HTM measurements, every batch of cells was inspected for contamination with other microbes. Any contamination of the sample would remain unobserved by HTM since there is no selection of the yeast cells during the measurement. Therefore, 10 µL of sample was investigated using a standard phase contrast microscope (Carl Zeiss, Germany) at 40 times magnification. The yeast cells should appear as round or oval cells (5-8 µm in size) as confirmed in Figure 4-2A, buds are also sometimes apparent (Figure 4-2B). Any other cells detected will most likely be human hosted bacteria introduced during handling of the samples, or from non-autoclaved materials used to treat the culture.
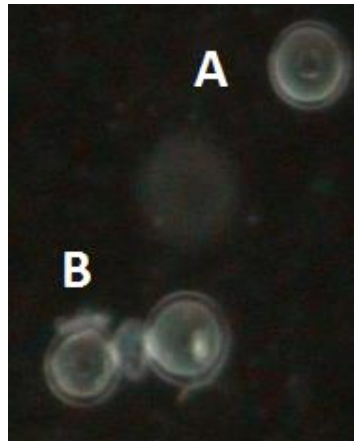
Figure 4-2. Light microscope image of yeast cells at 40x optical magnification. A single yeast cell is indicated with (A), and yeast cells that are dividing (budding) are indicated with (B).

Observations of conventional inoculated plates that were incubated for 24 to 48 h at 30 ± 0.1 °C provided additional information on the yeast cells and any contamination present in the sample. The viability of the sample was obtained by counting the round yeast colonies of a "creamy" colour (arrows in Figure 4-3), other morphologies indicate contamination of the sample (Figure 4-3A).
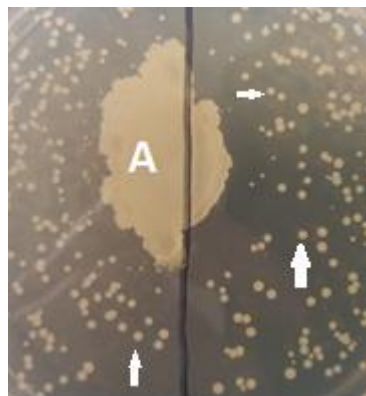
Figure 4-3. Solid medium culture of budding yeasts. Yeasts form spherical colonies on solid agar plates, some of which are indicated with an arrow, the agglomeration indicated with A is due to contamination with other microbes.

Samples found to be contaminated were discarded, and an additional random sample from the batch was studied. If more samples were found to be contaminated, the entire batch was discarded of and experiments were repeated with a new and clean batch.

4.4.2. The effect of different solutions on the cryopreservation of yeast cells

The influence of the -80 ± 0.1 °C storage conditions will be presented below with the results of the agar cultures shown in Figure 4-4 and the HTM measurements in Figure 4-7.

4.4.2.1. Cultures on agar medium

The benefit of glycerol as a cryo-preserver becomes visible with the uniform size of the colonies in Figure 4-4 D-F. The concentration (CFU/mL) is determined based on these plates.
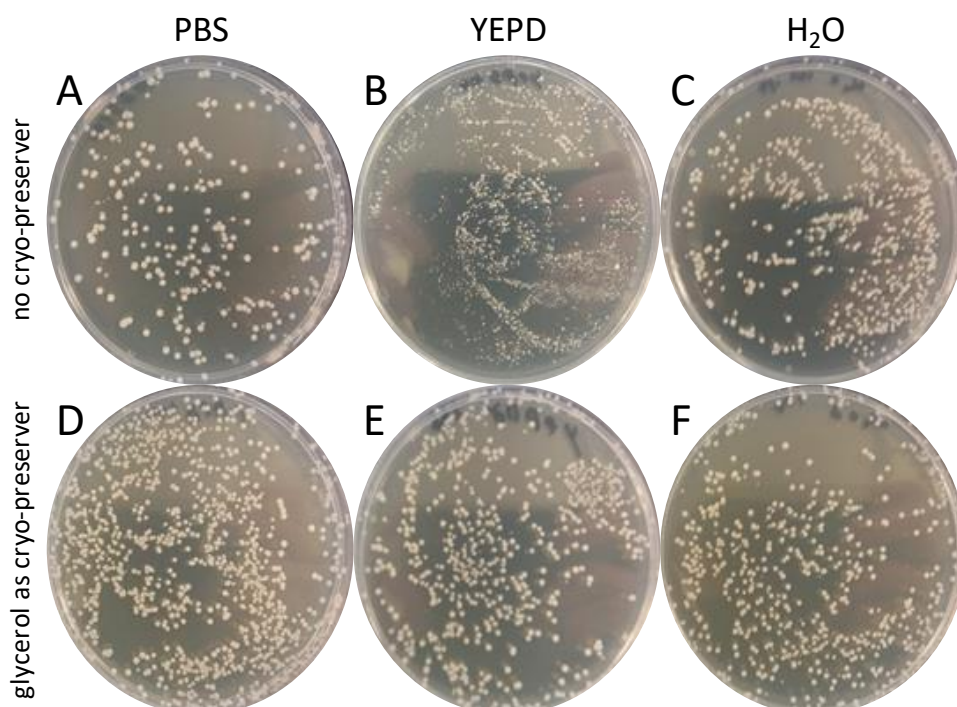
Figure 4-4. Viability of yeast cells after -80 ± 0.1 °C storage. After being stored 1 month at -80 ± 0.1 °C the samples where thawed and diluted 100 times, 50 µL of this dilution was used to create these plates. The different storage media used were PBS (A,D), YEPD (B,E) and H_2O (C,F) either in the presents of glycerol (D-F) or without (A-C).

The highest viability is observed in YEPD (Figure 4-4 B) and the lowest in PBS (Figure 4-4 A). Here it is notable that the glycerol conditions showed a lower viability with YEPD and H_2O, but did give a higher equality in morphology between the individual colonies. A possible explanation could be the exposure time to glycerol prior to cryo-storage, the PBS samples were prepared first, followed by YPED and H_2O. Whilst all samples were placed in the freezer together directly after finishing

the H_2O samples, it is the time of exposure of the cells to glycerol at room temperature that is considered critical. These interpretations maybe better resolved by repeating experiments and ensuring equal time between preparation and storage, and from investigating the storage time over a larger period.

4.4.3. HTM measurements

4.4.3.1. Calibration to yeasts

4.4.3.1.1. Electrode selection

An electrode should have a high thermal conductivity (as explained in section 2.2.1.3.1), and biocompatible with cell culture used during the measurement. Therefore, the thermal response of Au, Au/Pd and Si electrodes to increasing concentrations of yeast cells was evaluated in PBS buffer. As can be seen in Figure 4-5, all electrodes exhibited higher R_{th} values with increasing amount of cells.
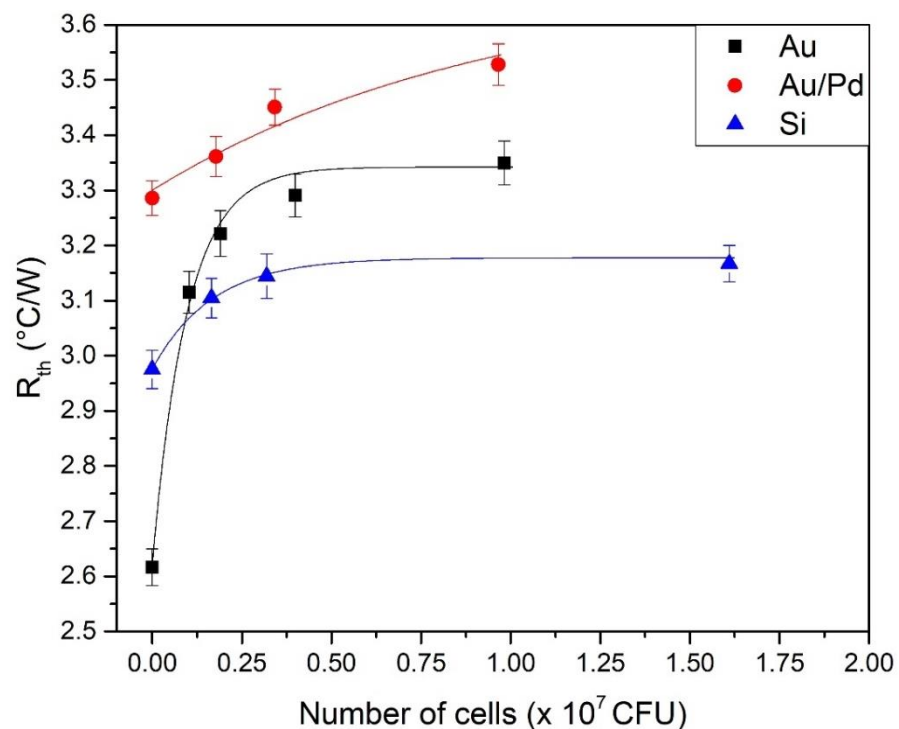
Figure 4-5. The calibration curve for yeast cells at various concentrations as determined by HTM. Electrode surfaces are represented as follows: Si (blue triangles), Au/Pd (black squares) and Au (red circles) electrodes. Error bars represent the standard deviation of the signal taken over at least 50 points. CFU/mL values were determined by means of UV-vis spectrometry. The trend line represents the dose response fit with R^2 values of 0.96, 0.95 and 0.98 for Si, Au/Pd and Au, respectively.

Figure 4-5 clearly indicates that the gold-coated electrodes had the widest dynamic range (10^4 to 10^7 CFU/mL) and proved to be the most sensitive. Therefore, gold electrodes were used for all subsequent studies. Hereafter, the system was calibrated using concentrations between 10^2 and 10^8 CFU/mL (Figure 4-6).
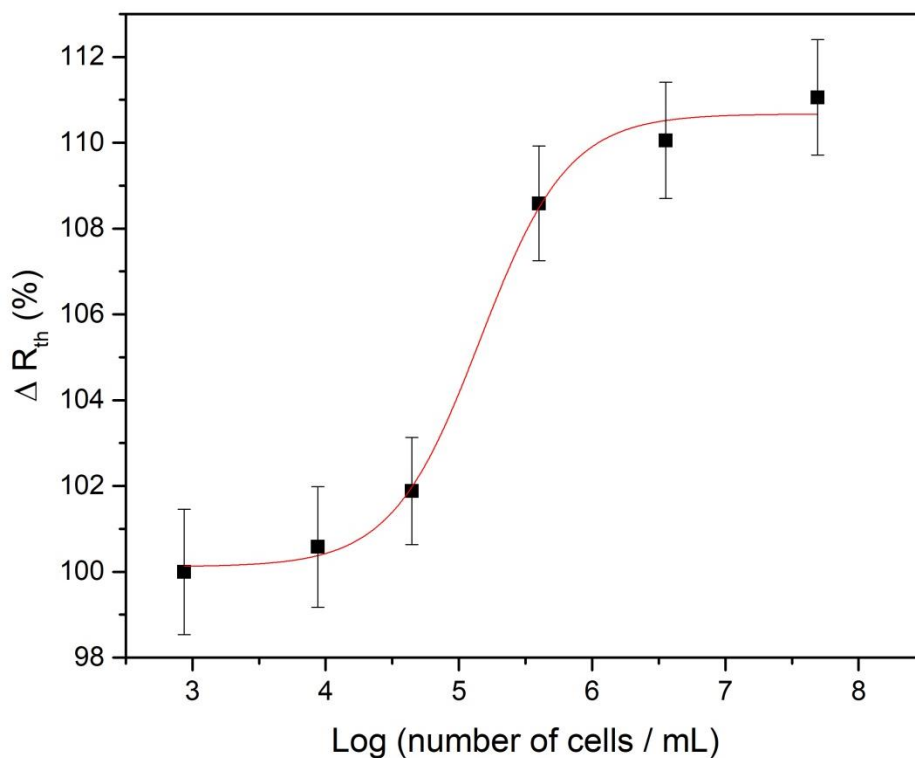
Figure 4-6. Dose-response curve for yeast cells on a gold electrode. The thermal resistance is averaged over at least 600 data points and shown as the % increase relative to the blank. The error bars represent the standard deviation. The curve was fitted with a standard dose-response fit ($R^2 = 0.99$).

Figure 4-6 shows the thermal response to increasing numbers of yeast cells, a standard dose response ($R^2 = 0.99$) was fitted to the data. The linear range for the system is between $10^4 – 10^7$ CFU/mL, after which saturation of the electrodes occurred. Vigorous rinsing (1699 mL/h for 3 min) was performed between the additions to minimize adhesion of cells to the surface. Additional CFU values between 10^5 and 10^6 CFU/mL were not obtained due to limitations of the conventional plating and spectrophotometric techniques.

4.4.3.1.2. Media selection

The influence of a cryo-preserver in different storage media using conventional plating was discussed in section 4.4.2.1. In addition to this experiment, HTM

measurements were performed (Figure 4-7 B) using the same samples. For each condition an average of at least 500 points was obtained and used to make the boxplot in Figure 4-7 A. The presence of yeast cells on the surface resulted in a higher heat transfer resistance in all fractions compared to the baseline (2.51 ± 0.04 °C/W). The variation on H_2O and PBS with glycerol seem to be artefacts of random drift Figure 4-7 A shows similarities in HTM signal between all fractions with yeast cells present compared to the baseline except for PBS with glycerol. Additionally, a one sided ANOVA test was performed on this data, and at a 95 % confidence level it indicated that all samples are significantly different. This indicates that the storage medium is of minor influence on the HTM signal.
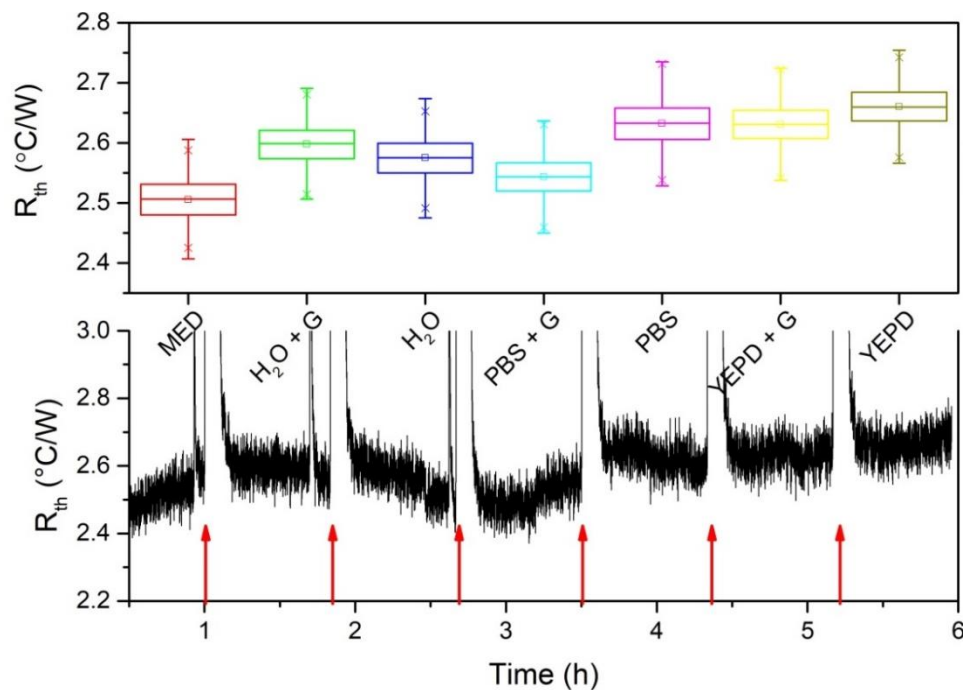
Figure 4-7. Bottom: Thermal resistance measurement of yeast cells after cryo-storage. Prior to the measurement all samples were washed with YEPD ensuring that the HTM signal was not affected by the storage medium itself. The Au electrode was stabilized in YEPD medium (MED) for 1 h before each sample injection (red arrows) and allowed to stabilise for 45 min. Top: Boxplot for the average and standard deviations the raw HTM data storage condition are indicated in the graph where +G indicates the presence of glycerol during storage.

Conventional plating experiments and HTM measurements showed the highest viability in YEPD (plate counts show in Figure 4-8). With the morphological data obtained from the plating experiments, the benefits of adding a cryo-preserver was clearly shown; therefore, YEPD with glycerol was used for all further cryo-storage of yeast cells. The calibration experiments for yeast were performed in PBS to ensure that there was no increase in the signal due to proliferation. This resulted in slightly lower values when comparing starting concentration (Figure 4-8). However, for any growth experiments YEPD will be used since PBS does not contain the nutrients required for the cells to proliferate.
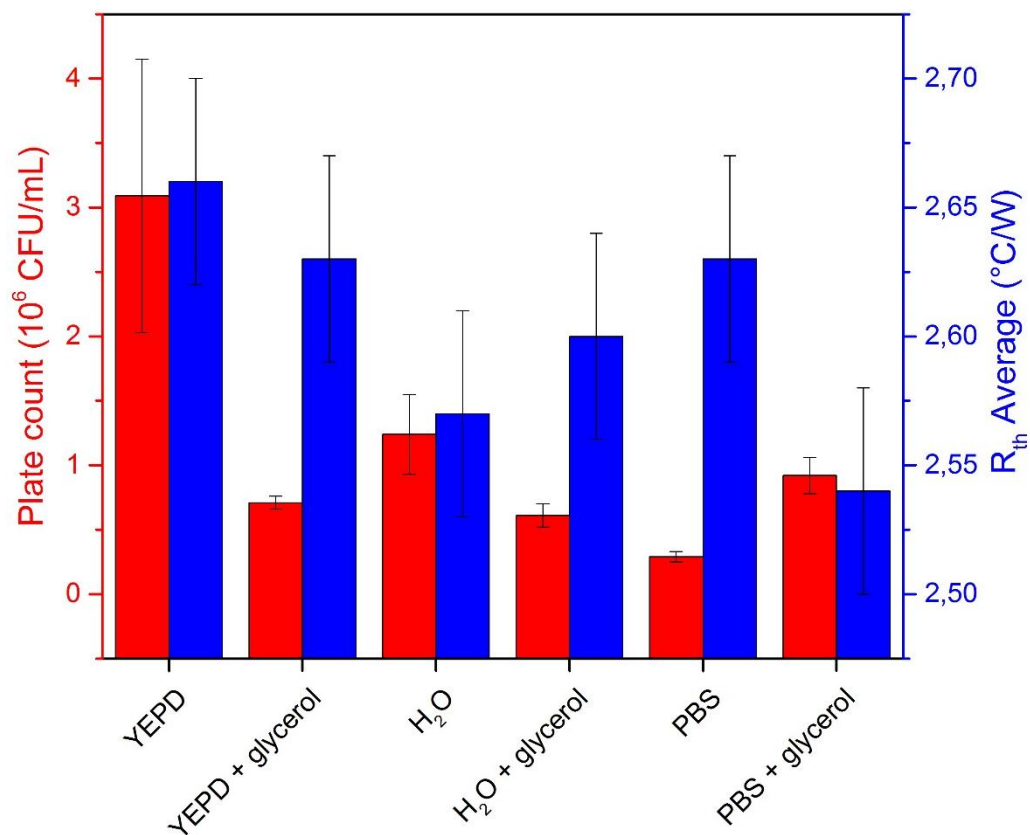
Figure 4-8 Viability of yeast cells after -80 ± 0.1 °C storage. The CFU values and errors were obtained by averaging six plates per condition (except for YEPD and YEPD with glycerol, for which only three plates each where used) from Figure 4-4 and their respective standard deviations.

Up to this point all measurements were performed with the flow cell design described by van Grinsven *et al.*[1, 208]. However, after growing the yeast suspensions for several hours the thermal resistance increased excessively due to the build-up of CO_2 gas that interferes with the thermal measurement (Figure 4-9).
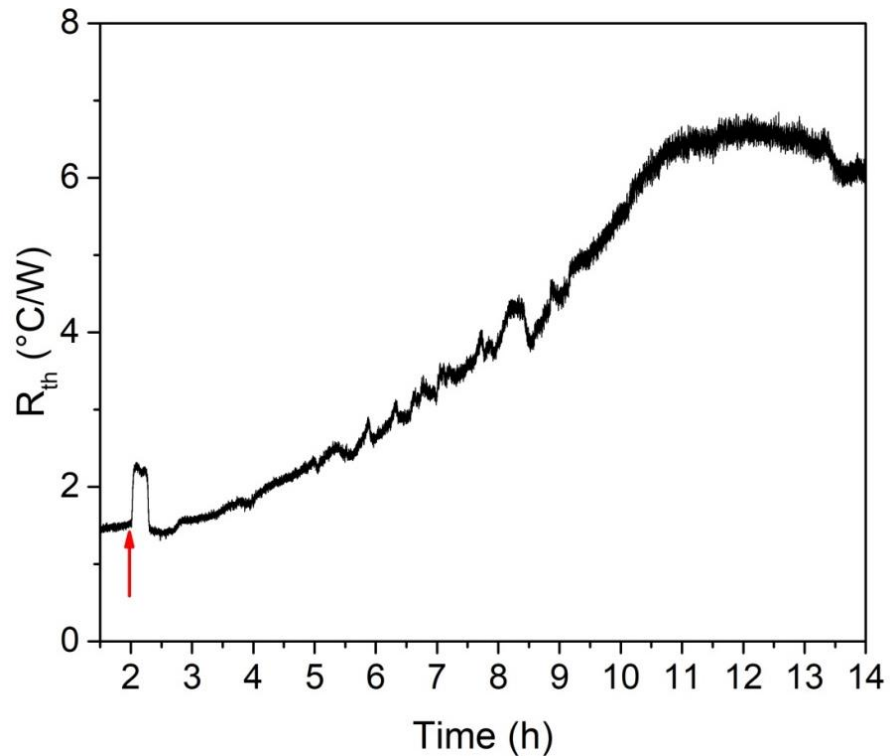
Figure 4-9. Yeast cell proliferation with continuous (800 µL/h) YEPD flow on an Au electrode. The red arrow points out the moment yeast cells are introduced. The observed increase in R_{th} indicates the growth of yeast cells. However, the formation of gas bubbles was observed in the flow cell, causing an additional increase in the signal.

In an attempt to flush out the gas before it starts to interfere with the measurement, the flow rate was adjusted by trial and error between 200 µL/h and 1500 µL/h and altered between continues and discontinuous flow. For the discontinuous flow, 200 µL was injected with a flow rate of 250 µL/min at intervals of 2 h, 1 h, 30 min and 15 min, respectively. However, this pattern led to excessive disturbance of the thermal resistance signal as observed at the 15 min interval measurement (Figure 4-10).
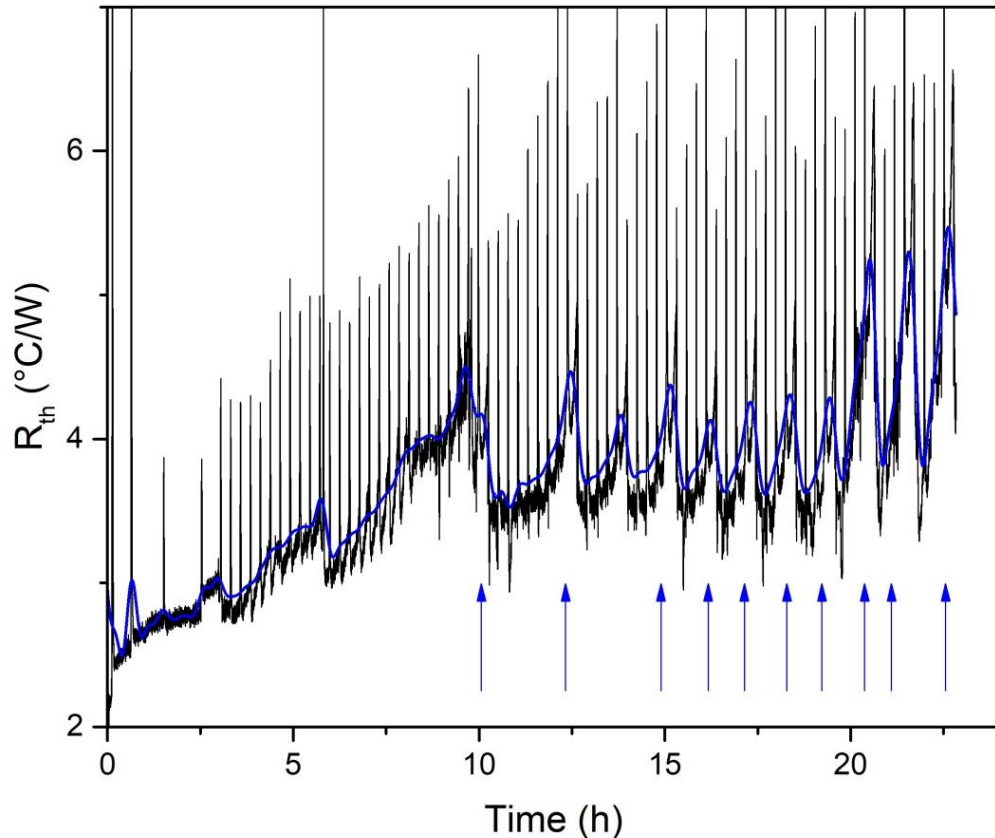
Figure 4-10. Growth of yeast in a discontinuous flow. During the first 2.5 h no flow was present, next an aliquot of 200 µL YEPD was injected at a rate of .25 mL/min and repeated every 15 min. The blue line represents a 600 point fast Fourier transformation, and the blue arrows indicate flushing out of gas bubbles.

Interestingly, it was observed that gas bubbles formed in the flow chamber were flushed out every 4 or 5 injections and corresponded to a slight decrease in the signal as is indicated with the blue arrow. The blue line averages the signal using a 600 point Fourier transformation, decreasing the interference caused the injections and the build-up of gasses and gives a first indication of yeast growth in the setup. These results indicated that a continuous flow rate of 800 µL/h was found to be the least disturbing on the signal, but was unable to remove all gas from the system (Figure 4-9). Other adjustments such as a gas permeable membrane were insufficient to further improve the signal stability, therefore all further measurements were performed using a revised flow cell design (Figure 4-6).

4.4.4. Evaluation of yeast growth under different conditions employing 3D printed flow cells

To ensure that the novel design was able to measure yeast growth rate, blank measurements on YEPD solutions were performed at 30 and 37 ± 0.02 °C, respectively, over a period of 14 h in the absence of yeast cells (Figure 4-11).
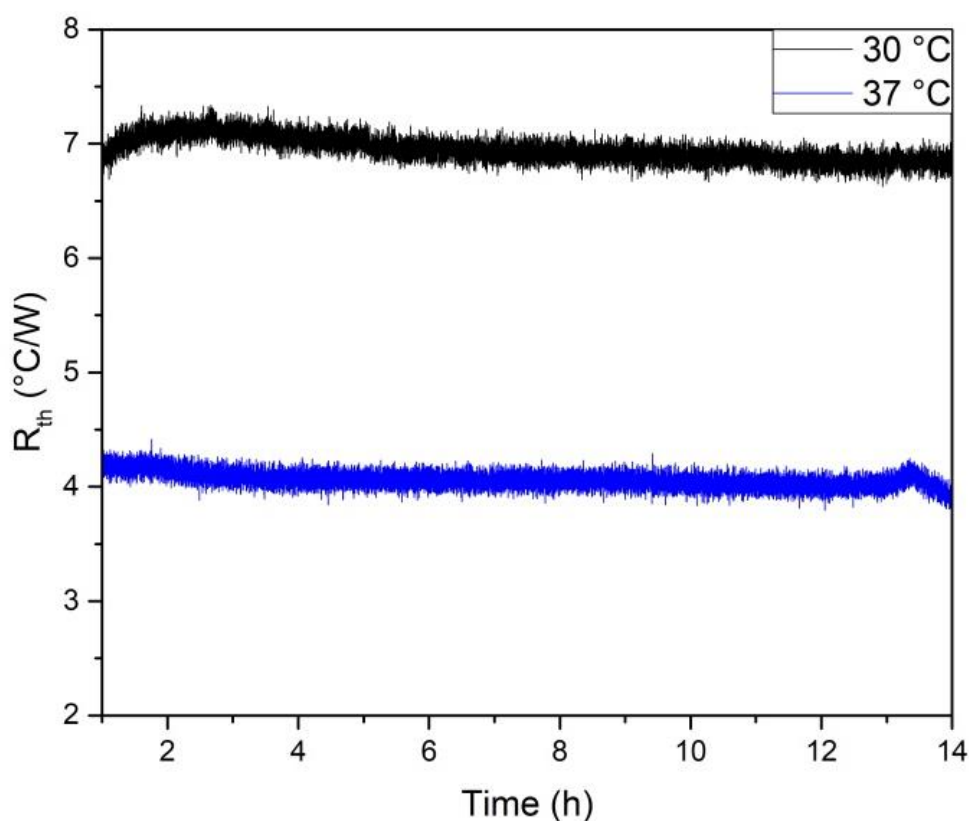
Figure 4-11. Blank measurements of the new flow cell. T_1 is set to either 30 or 37 ± 0.02 °C while YEPD is exchanged at a flow rate of 800 µL/h. The signal over the gold electrode is monitored and the resulting R_{th} is shown.

The signal stabilised to 6.95 ± 0.1 °C/W at 30 °C and 4.06 ± 0.06 °C/W at 37 °C, respectively. During the next 14 h no significant differences where observed, establishing a baseline, and confirming that the design will be suitable for yeast measurements. The difference in intensity between the two signals was due to a higher rate of heat dissipation to the environment at 37 °C, lowering the R_{th} value. The deviations of the thermal resistance for these measurements compared with the previous flow cell are due to differences in distribution of thermal flow across the flow cell. Measurements were performed in triplicate, with similar starting values (standard deviation 0.1 °C/W).

4.4.4.1.   Influence of the environment temperature

The rate of heat transfer is proportional to the temperature difference between the environment and flow cell (Equation 4-1)[209]. Here Q (W) is the heat transfer rate, A (m^2) the surface area over which the heat is transferred, $\hbar$ the average heat transfer coefficient (W/m^2K) (per surface area) and T_{body} and T_{envi} (°K) are the respective temperatures of the body and environment. For heat dissipation to the environment, this equation is also known as Newton's Law of Cooling. Therefore, more power needs to be supplied to the thermistor to keep the copper heat sink at a higher temperature, resulting in a lower R_{th} value. From Equation 4-1, it also becomes clear that any fluctuation in the environmental temperature will cause a disturbance in the signal.

$$\frac{Q}{A} = \bar{h}\left(T_{body} - T_{envi}\right)$$

Equation 4-1

Figure 4-12 represents such a fluctuation caused by the lack of active temperature control over night. The red arrow indicated the moment that the room air conditioning (AC) was switched off (decreasing the room temperature), whilst the blue arrow indicates the moment the AC was switched back on the following morning. To provide a better control of the environment the flow cell was placed inside an incubator, thereby decreasing the fluctuation in the environment to 0.1 °C. The influence of this can directly be observed when comparing the stability of the flow cell temperature (T_2) inside (red line) and outside (blue line) of the incubator (Figure 4-12).
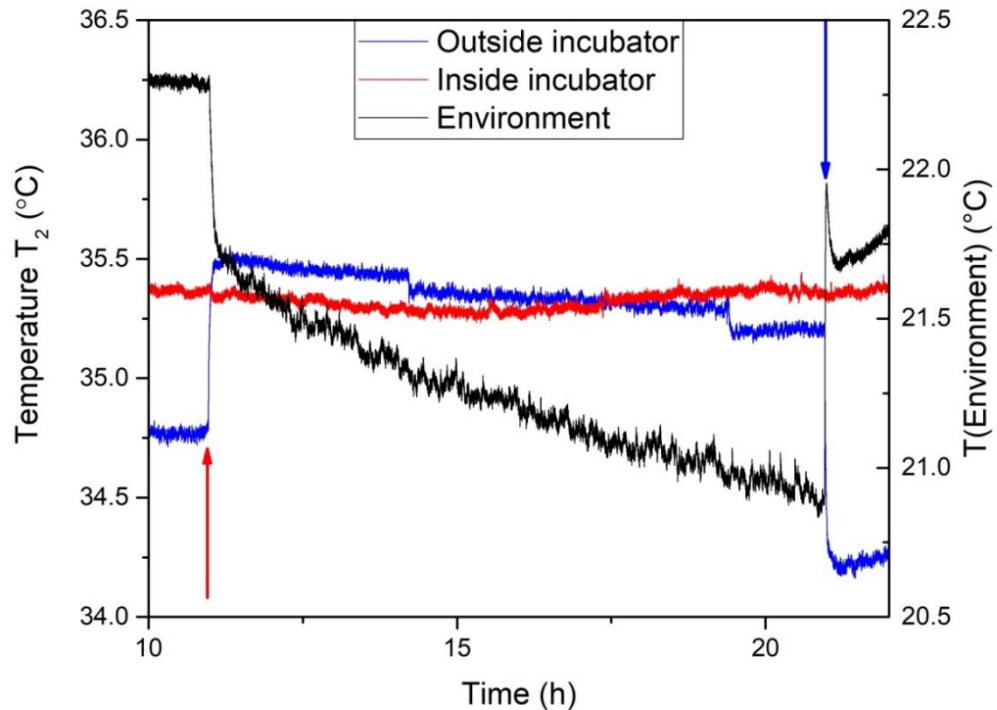
Figure 4-12.Effect of the environmental temperature on the core temperature. The black line it the temperature of the room in which the HTM setup is located, the red arrow indicates when the air conditioning (AC) unit for is turned off, while the blue arrow indicates when it is turned back on. The effect of the AC unit on T_2 (blue line) is no longer detected after placing the flow cell inside an incubator (red line).

It has to be noted that in previous articles on HTM, measurements were not performed in an incubator which is most likely due to the fact that these experiments were performed in rooms that were not controlled by means of AC. For the remainder of this work and for consistency, all further measurements will be performed inside an incubator.

4.4.4.2.   Optimization of growth temperature

To evaluate the kinetic effects of growing yeast at various temperatures, a study was performed with a WT (optimal growth ~ 37 °C) and a Mut strain (optimal growth temperature ~ 23 °C). The Mut strain will initially go to cell cycle arrest (G_0) when grown at temperatures above 30 °C were they remain viable. These experiments were performed to evaluate the influence of external parameters on the growth of yeasts and to quantify the yeast growth.

Yeast cells were injected with a starting value of ~ x 10^4 CFU/mL. The temperature of the heat sink was varied in steps of 1 ± 0.02 °C every 5 h from 17 °C to 31 °C and

30 °C to 51 °C for the mutant strain and the WT strain respectively. Figure 4-13 represents a section between 21 °C and 27 °C of such a study for the Mut strain.
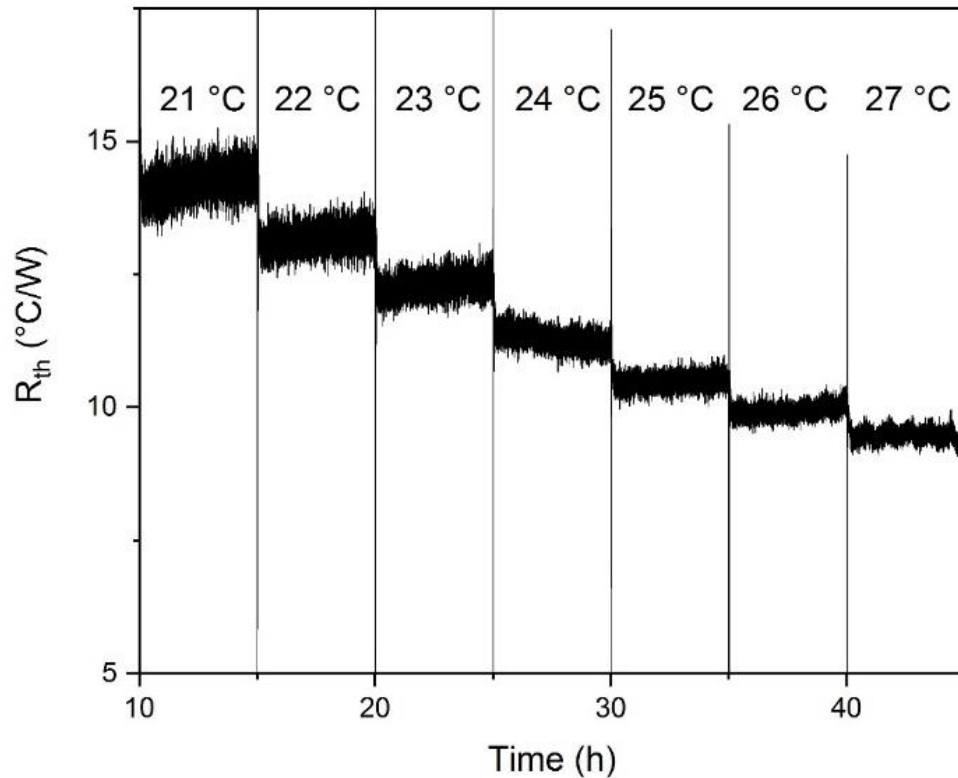
Figure 4-13. Temperature dependent growth the mutant strain (starting concentration ~10⁴ CFU/mL). Every 5 h the temperature of the copper heat sink was increased with 1 ± 0.02 °C. During the full measurement a fresh YEPD solution was applied at a flow rate of 800 µL/h.

The sharp decline in the thermal resistance observed on increasing the temperature (Figure 4-13) is due to the dependency of environment temperature and the temperature gradient ($T_1 - T_2$), see section 4.4.4.1. At lower temperatures this gradient is larger, resulting in a decreases in R_{th}. The growth kinetics for each strain were determined for every temperature according to Equation 4-2, here the growth rate ((°C/W)/h) is determined by dividing the difference in R_{th} (°C/W) over the measurement time were t_{stab} is the initial stabilisation time (30 min) and t_{meas} the full measurement time per (5 h).

$$Growth\ rate = \frac{\Delta R_{th}}{(t_{meas} - t_{stab})}$$
Equation 4-2

An overview of the growth kinetics observed is shown in Table 4-1. Here a minimum of 16200 points was used to determine the growth rate. It was found that the highest growth rates are at a temperature of 38 °C for WT (0.143 °C/W per h) and at 24 °C

for the mutant strain (0.051 °C/W per h). The growth rates at the remaining temperatures were normalized to these values, respectively.

Table 4-1. Growth kinetics of the WT (T ranging 30 – 50 °C) and the mutant strain (T ranging from 21 to 33 °C). Values were normalised relative to the highest growth rate, obtained from Betlem *et al.* [52].

T_1	T_2	Growth rate	St. Ddev	Normalised signal
°C	°C	°C/W per h	10^{-4} °C/W per h	%
WT strain				
30	29.30	0.016	9.40	11
31	29.99	0.033	6.37	23
32	30.96	0.030	5.16	21
33	31.75	0.041	4.28	29
34	32.88	0.010	3.68	7
35	33.60	0.035	3.72	24
38	35.56	0.143	4.24	100
39	36.27	0.060	3.99	42
40	37.78	0.050	2.97	35
42	40.33	0.045	5.00	31
45	42.94	0.013	1.53	9
50	42.98	0.065	3.68	45
51	43.96	0.054	3.67	38
Mutated strain				
21	19.27	0.049	1.31	96
22	20.94	0.020	4.96	39
23	21.01	0.026	8.14	50
24	22.14	0.051	5.92	100
25	23.45	0.027	4.33	52
26	23.97	0.051	1.80	99
27	24.84	0.016	4.56	31
28	25.74	0.028	3.74	55
29	26.68	0.029	3.56	58
30	27.62	0.022	3.40	43
31	28.63	0.017	3.14	34
32	29.48	0.016	3.14	31
33	30.32	0.023	2.27	46

For each 5 h (30 min initial stabilization) incubation period the slope of the signal was determined using a standard linear fit.

From Table 4-1 it is apparent that a higher heat sink temperature (T_1) results in a larger temperature difference relative to the flow chamber temperature (T_2). This observation is consistent with the explanation related to the environmental

temperature on the stability of the R_{th} value (section 4.4.4.1). The exact temperature of the electrode surface, and therefore the growth temperature of the yeast cells, will be close to, but lower than T_1. This is due the fact that the thermal conductivity of metals is in general higher than those of liquids.

It can also be observed in Table 4-1 that the WT strain replicates about 20 ± 5% faster than the mut strain, this corresponds with the data shown in Figure 4-13. The growth rates at a given temperature were plotted and a Gaussian distribution was found, see Figure 4-14 for the WT data. From this distribution, the highest rate of replication is at 37 °C for the WT and at 23 °C for the Mut strain, corresponding to literature[95].
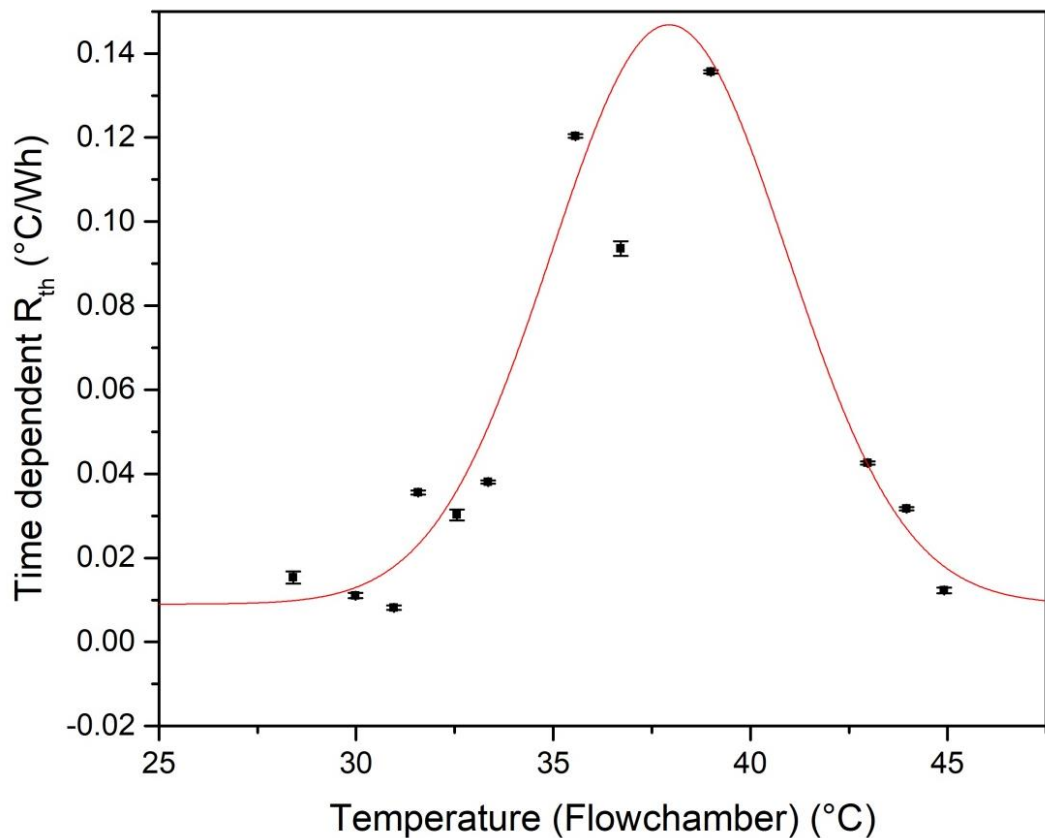
Figure 4-14. Growth rate (°C/W per h) for WT yeasts. The rates are plotted against T_2 between 27 °C and 45 °C and fitted with a Gaussian fit (R^2 = 0.99). the error bars represent the stander deviation on the growth rate.

Subsequently, these optimized conditions were used to evaluate the continuous growth of the WT and Mut strains. For both strains, a starting concentration of approximately 10^4 CFU/mL was used and the thermal resistance was monitored over at least 60 h. Figure 4-15 shows the hourly average in thermal resistance over time for both yeast strains.
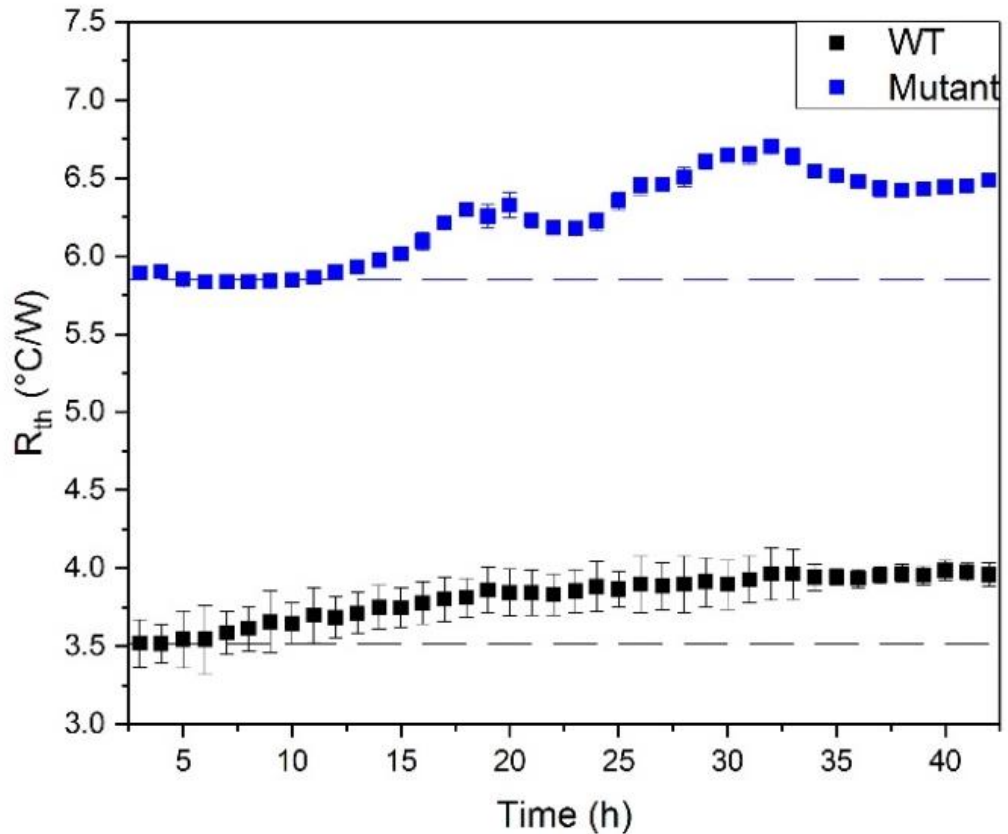
Figure 4-15. The hourly average R_{th} value of a standard growth curve for both the WT and mutant strain. The starting concentration for each measurement was ~ 10^4 CFU/mL. The WT strain (black) was grown at a temperature of 37 ± 0.02 °C and the DLY1108 mutant (blue) at 25 ± 0.02 °C. The initial lag phase (30 min) is not displayed. The error bars represent the standard deviation on these averages.

The difference observed in initial R_{th} value (3.5 ± 0.1 °C/W for WT and 5.9 ± 0.1 °C/W for the mutant strain) is due to the different growth temperatures (section 4.4.4.1). However, a clear increase of 15 % for WT and 9 % for the Mut. strain was observed over the next 42 h.

For the WT yeasts, the thermal resistance changes at a rate of ~ 0.06 °C/W per hour over the first 20 h, hereafter it decreased to approximately 0.02 °C/W per hour. This change in rate is the result of saturation of the electrode surface with a single layer of yeast cells. Further replication leads to an increase in overall thickness of the layer of cells, decreasing the effect on the change in thermal resistance. Such a change was not observed for the mut strain; hence, saturation of the surface is not occurring yet. This corresponds with a lower replication rate corresponding to an overall rate change in thermal resistance of 0.02 °C/W per hour. However, minor fluctuations were observed on the mutant strain (around 30 h) which is due to the lower growth temperature, at which the signal is more prone to perturbations in the external temperature. All measurements were performed in triplicate, with flow rates ranging from 0.04 to 0.06 °C/W per hour for the first 20 h on the WT strain.

4.4.5. Inhibition of yeast growth

With the functional parameters established, the limitations on the growth of WT yeasts by different factors (temperature, medium and toxic compounds) were investigated. All measurements were initiated using ~ 10^5 CFU/mL of WT yeast and grown under optimized conditions for the first hours. Hereafter, the conditions were altered and the response was analysed.

First, after 7 h the temperature was ramped to 99 ± 0.02 °C in 10 min and kept there for 10 min eliminating the yeast cells. The temperature was then gradually decreased to 37 ± 0.02 °C where no further increase of the signal was observed (Figure 4-16).
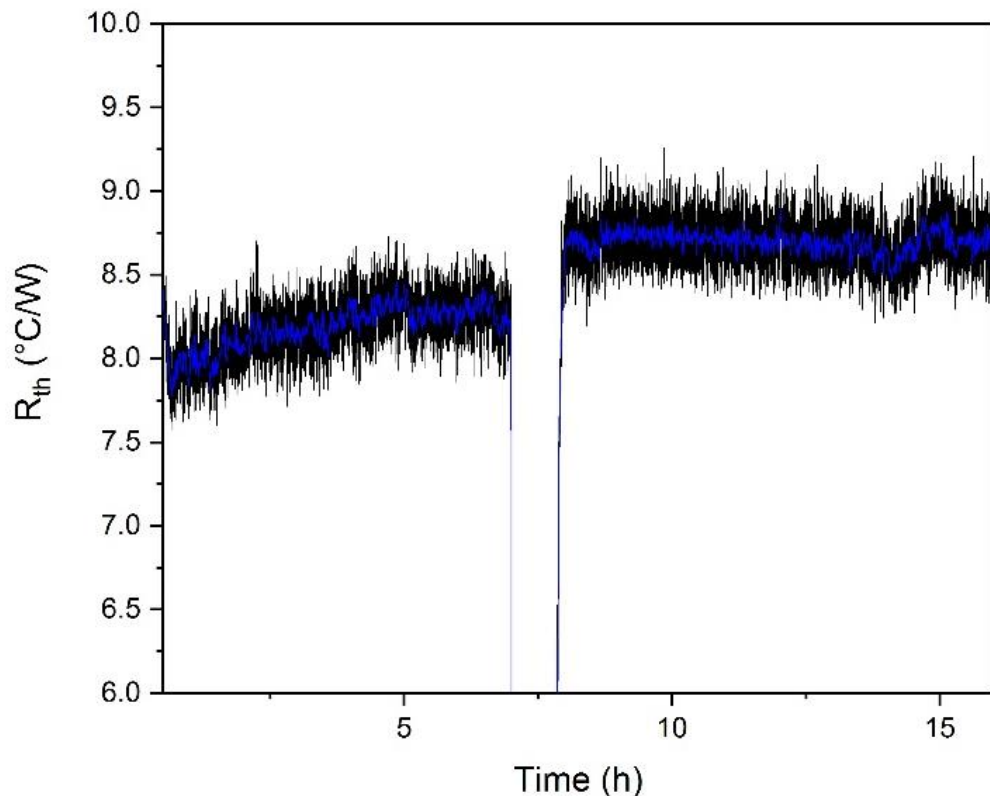
Figure 4-16. Thermal elimination at 99 ± 0.02 °C of WT yeast. A starting concentration of ~10^5 CFU/mL WT yeast was where grown at 37 ± 0.02 °C for 7 h. Hereafter, the temperature of T_1 was increased (in 10 min) to and kept at 99 ± 0.02 °C for 10 min before cooling back down to 37 ± 0.02 °C (in 20 min). The blue line represents a gentle 50 point median filter. The constant but elevated R_{th} value (due to disintegration of the cells) after the temperature ramp demonstrates that the yeast culture is thermally eliminated.

When yeasts were replicating at 37 °C, the R_{th} signal increased at 0.06 °C/W per h, which is in line with previous rates found and similar to that stated in Table 4-1. The signal remained stable after boiling the yeasts (hence, no replication), but was increased by 0.5 ± 0.1 °C/W in comparison to before the boiling. This increase can be attributed to the disintegration of dead yeast cells collecting at the bottom, thereby creating a dense layer on the electrode surface blocking the heat-flow. The continuous flow rate of 800 μL/h was not sufficient to remove the dead cells from the surface. A higher flow rate of 200 μL/min would be able to remove the dead cells from the surface (Figure 4-17), but would have been to disturbing for the measurement. Figure 4-17 shows a reversible signal increase upon the addition yeast cells that where boiled for 10 min in a Eppendorf tube in preparation for the HTM measurement.
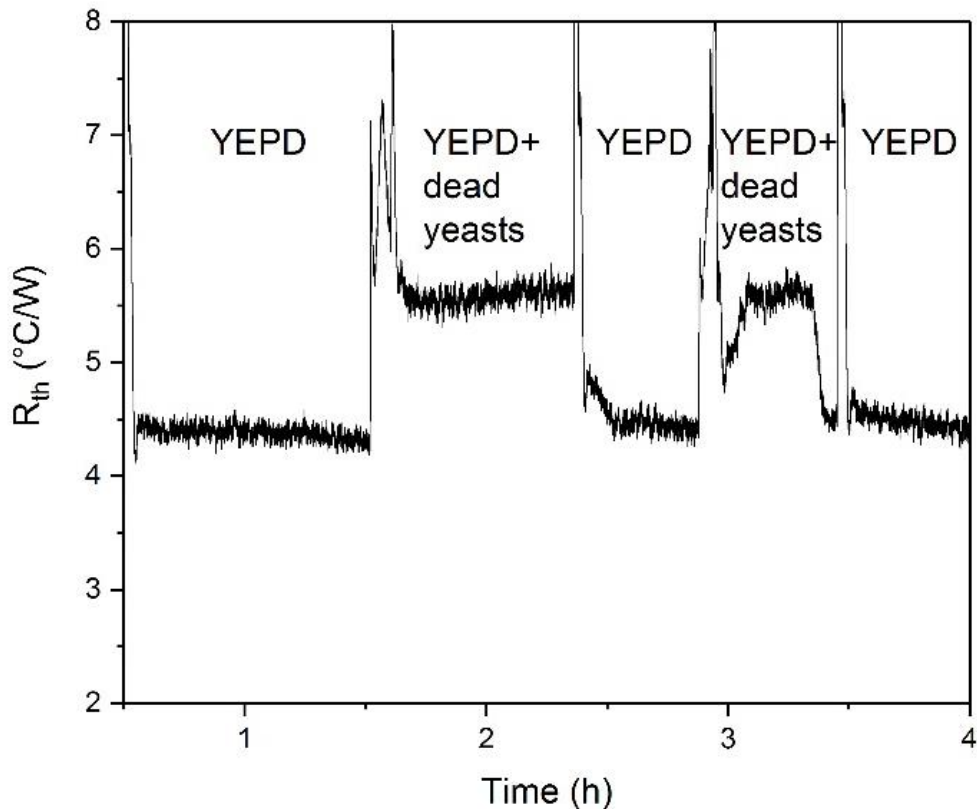
Figure 4-17. This graph is a measurement where first, a stabilization was performed with YEPD followed by addition of a known concentration of dead yeast cells. This led to a significant increase in thermal resistance. However, no increase in thermal resistance was seen over time indicating that no replication occurred (confirmed by plating experiments). After vigorous flushing with YEPD, the signal returned back to baseline and returned to approximately the same level after addition of YEPD again.

The electrode was stabilized in YEPD (4.38 ± 0.06 °C/W) for 1.5 h, and subsequently, two injections of yeast cells that were boiled at 100 °C were performed with a YEPD wash in between. The signal increased to 5.59 ± 0.08 °C/W and 5.60 ± 0.08 °C/W for the first and second injection respectively. Upon washing the signal stabilized at 4.45 ± 0.07 °C/W and 4.47 ± 0.06 °C/W respectively. An aliquot of the boiled sample was plated and incubated at 30 ± 0.1 °C for 2 days, confirming that no growth occurred.

Furthermore, the exposure of copper ions to growing yeast cells was evaluated. To this end, a solution of 15 mM Cu_2SO_4 in YEPD was injected (blue arrow) and left for 2 h with the yeast, the results are represented in Figure 4-18.
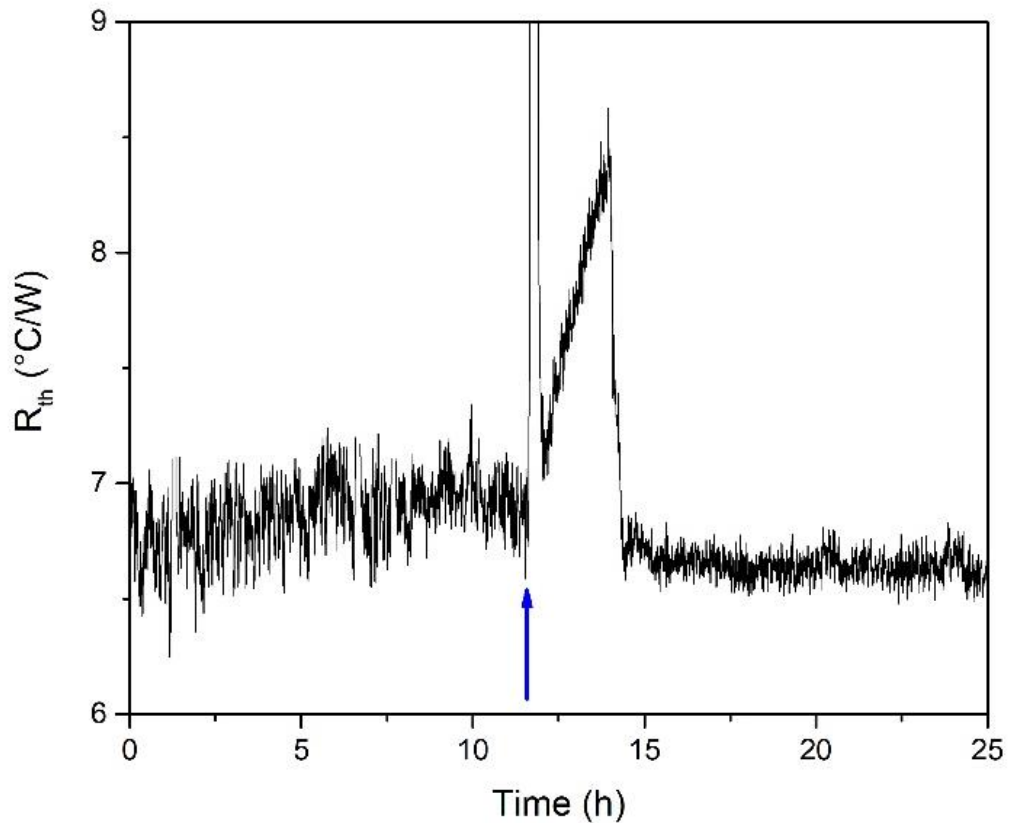
Figure 4-18. Toxicity of copper sulphate for WT yeast cells. Normal growth of WT yeast in YEPD at 37 ± 0.02 °C is observed as an increase in thermal resistance before the presence of 15 mM Cu_2SO_4 (indicated by the blue arrow) and is absent upon returning to normal conditions.

The blue arrow indicates the moment that the medium was exchanged to 15 mM Cu_2SO_4 and left to incubate for 2 h (no flow during the incubation). Hereafter, the flow of YEPD was reinstated at a flow/rate of 800 µL/h gradually exchanging the medium back to YEPD. A signal increase of 0.03 °C/W before the additions of copper sulphate was no longer present after the incubation, demonstrating that no yeast growth is observed after incubation with copper ions to the solution. These results were confirmed with plating experiments (Figure 4-19).
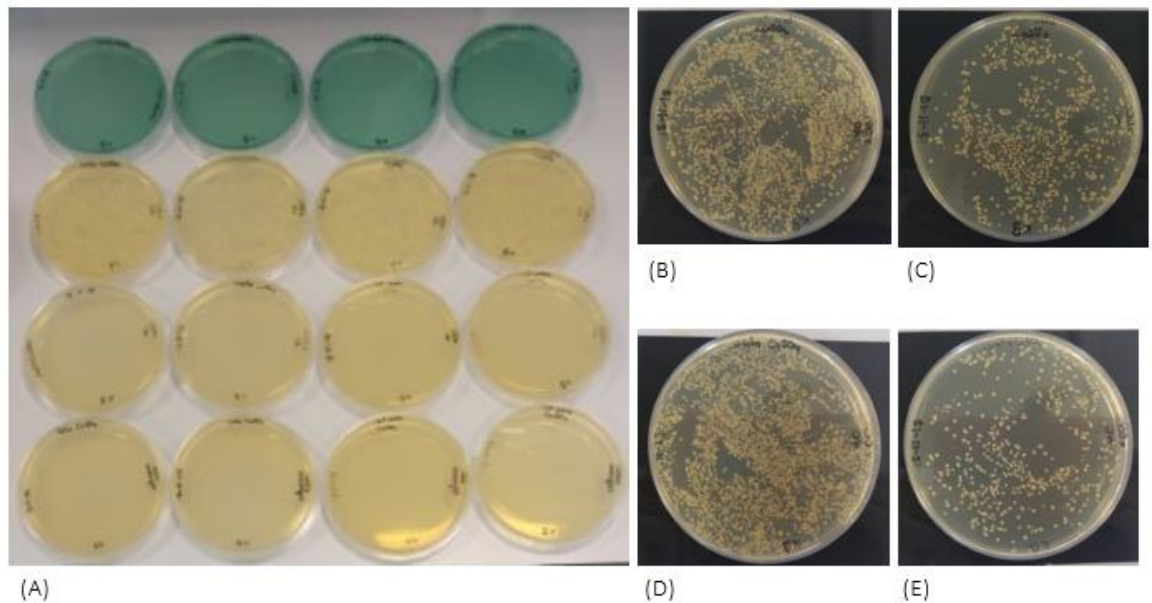
Figure 4-19. This figure shows the plating of the following experiments. A) WT yeast a 100 x and 1000 x diluted, autoclaved and not autoclaved, 100 μL added on 15 mM CuSO$_4$ YEPD plates. Grown for 3 days at 37 ± 0.1 °C. Also WT yeasts incubated for 0 h, 2 h and 12 h in 15 mM CuSO$_4$ before application on YEPD plates demonstrating no presence of yeast cells (B) WT yeast a 100 x diluted, not autoclaved 15 mM CuSO$_4$ for 0 h incubation. Concentration of $1.6 \cdot 10^6$ CFU/mL. (C) WT yeast a 1000 x diluted, not autoclaved 15 mM CuSO$_4$ for 0 h incubation. Concentration of $5.4 \cdot 10^5$ CFU/mL. (D) WT yeast a 100x diluted, autoclaved 15 mM CuSO$_4$ for 0 h incubation. Concentration of $1.9 \cdot 10^6$ CFU/mL (E) WT yeast a 1000 x diluted, autoclaved 15 mM CuSO$_4$ for 0 h incubation. Concentration of $6.0 \cdot 10^5$ CFU/mL.

Finally, the growth kinetics of WT yeasts in YEPD and ex-YEPD were compared. Initially, yeast growth of 0.06 °C/W per hour was observed (Figure 4-20 A), corresponding to Table 4-1. Hereafter, the medium syringe was exchanged to ex-YEPD and pumping continued at 800 μL/h exchanging the medium over the next 14 h. Upon exposure to ex-YEPD no significant increases in thermal resistance were observed (Figure 4-20 B).
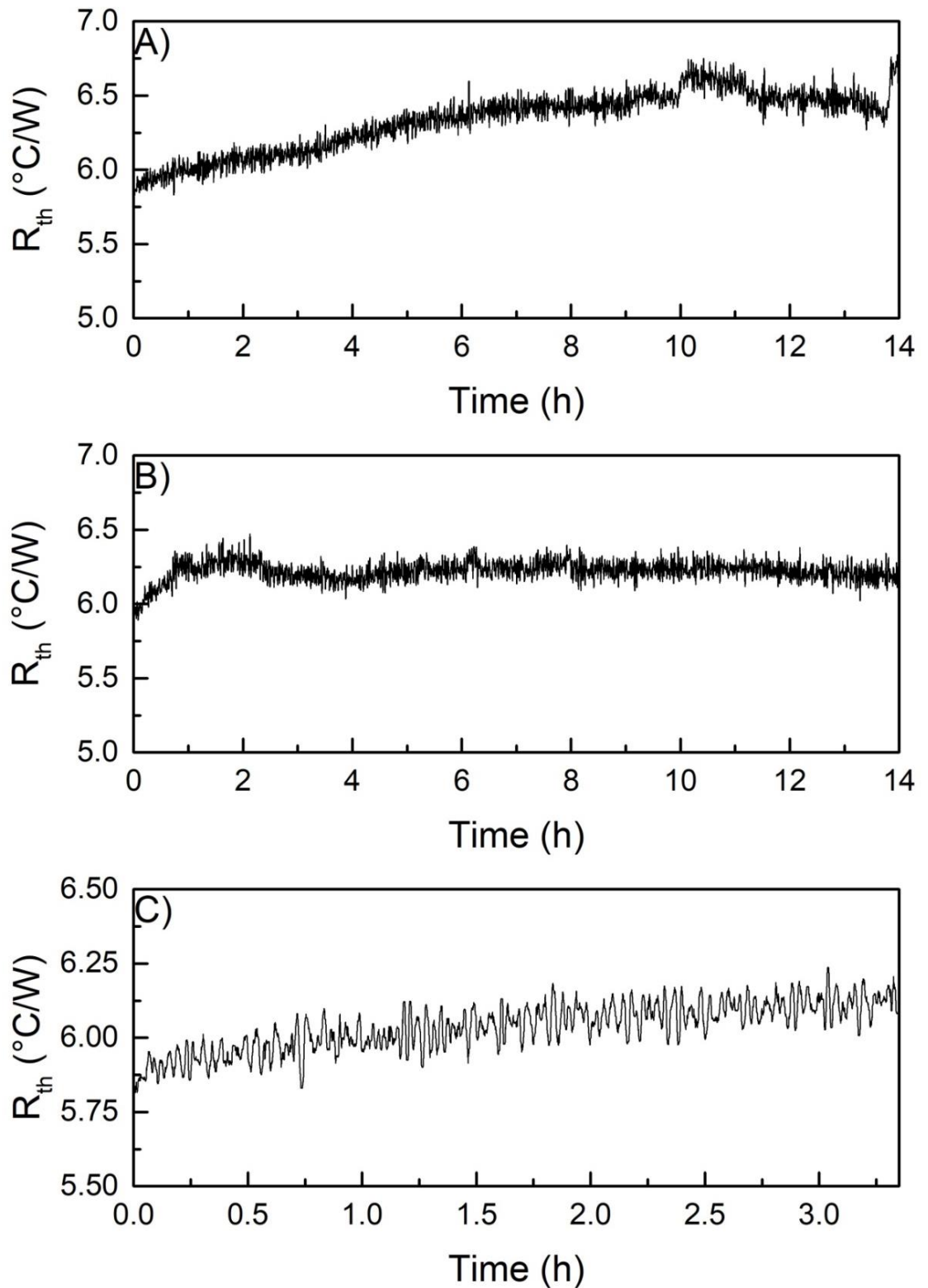
Figure 4-20. The influence of the medium on the growth of WT cells at 37 °C. A) The first 14 h of the measurement with 800 µl/h of fresh YEPD broth. B) second part of 14 h with 800 µl/h of ex-YEPD. C) The last 3.5 h with 800 µl/h of fresh YEPD broth

Figure 4-20 clearly demonstrates the influence of the nutrient composition of the medium on the yeast growth rate, the growth rate correlates with similar conditions prior to the inhibition of growth. However, in comparison to previous experiments yeast cells are able to remain viable when lacking nutrients, they first entered an arrested cell state and can survive for several hours. Figure 4-20C shows the reversibility of this process, here after 14 h of incubation in ex-YEPD, the medium was exchanged back to YEPD. The re-addition of nutrients to the cells restored the growth properties of the yeast. However, it has to be noted that there is a difference in increase of the thermal resistance before and after the ex-YEPD phase, this could indicate that the optimum conditions are not fully restored for all yeast cells in this short incubation time, or that the incubation period in ex-YEPD was too long resulting in sub-lethal damage to the cells.

4.5. Conclusions

In this work, *S. cerevisiae* was used as a model organism demonstrating that the HTM can analyse the growth behaviour of microorganisms. It was demonstrated that a higher thermal resistance at the electrode interface was caused by higher concentrations of *S. cerevisiae* (WT) cells in buffered solutions. From the different electrodes (Au, Au/Pd and Si) that were evaluated the gold electrodes had the highest performance and thermal response in buffed solutions and therefore were used in all further experiments. These electrodes had an excellent stability, minimal noise on the signal (0.83% at 37 °C) and wide dynamic range (10^3 - 10^7 CFU/mL), allowing for the accurate quantification of *S. cerevisiae* cultures.

Cryo-storage of the cells with 20 % glycerol in YEPD showed the highest viability of *S. cerevisiae* and ensured that all cells were in G_0 phase at the start of a measurement. In order to measure growth of *S. cerevisiae* one needs to ensure sufficient exchange of medium. Therefore, an optimized flow rate of 800 µL/h was used providing the required nutrients and removing the waste products. However, this was still inadequate to remove all metabolic waste gas, leading to a re-designed of the flow cell by incorporating a gas outlet. These flow cells where 3D-printed with FORM2 Clear Resin, enabling easy scale up of production thereby increasing the commercial potential of the method.

A more stringent control of the environmental temperature, by means of an incubator, was required to study the growth kinetics of both WT and Mut stains. Thermal analysis was performed on both strains, specified temperature ramps were applied and the increase in thermal resistance was monitored. This increase is converted to a growth rate and the highest rate found is in agreement with what has been reported in literature[168]. The corresponding temperatures for this growth rate can be used to quantify replication, thereby directly comparing the influence of external parameters on microbial growth.

No differences in the thermal resistance were observed with reference measurements on dead yeast caused by incubation at 100 ± 1 °C for 10 min prior to measurement or inhibiting the growth of yeasts in nutrient depleted media. However, with the restoration of the nutrient media a corresponding increase was observed. Additionally, the increase in the thermal resistance ceased upon exposing the yeast cells to either elevated temperatures or the addition of a copper sulfate solution.

All thermal analysis conditions were confirmed by standard plating methods and UV determination, however no information was obtained about any sub lethal damage to the cells, this could be a future objective.

5. A Novel Application of the Heat-Transfer Method (HTM): Real-Time Monitoring of *Staphylococcus aureus* Growth in Buffered Solutions and Digestate Samples

5.1. Abstract

The identification and quantification of microorganisms in water samples is a crucial component for the improvement of processes in organic waste treatment facilities. Most of the currently available tests are either labour-intensive or costly, and they do not allow determination of the dynamics within microbial communities in digestate samples. This study is the first report on the use of thermal analysis, specifically the HTM, to monitor microbial load in aqueous solutions and digestate samples. *Staphylococcus aureus (S. aureus)* was used as a model organism for bacteria and different concentrations in water were measured by HTM. It was demonstrated that there was a positive correlation between the thermal resistance and concentration of the bacterial cells. Subsequently, the influence of temperature on growth conditions was studied and confirmed by plating experiments and Scanning Electron Microscopy (SEM). These results showed the possibility to monitor the temperature dependent growth of *S. aureus* using HTM. To determine if this technique can be applied to the study of complex matrices, such as digestate, samples were collected from a communal wastewater treatment site and from an industrial source and cultivated on nutrient agar plates to determine the composition. The bacterial cultures derived from single colonies were characterised and identified by 16S genome sequencing. Subsequently, HTM measurements were performed in raw digestates that were diluted or centrifuged to remove large sedimentations that would interfere with the microfluidics. These samples were enriched with *S. aureus* and studied on HTM. The results indicated that it was possible to evaluate microbial load even in a complex system. The thermal analysis method provides a low-cost

monitoring option, which was simple to use and provided *real-time* analysis, which has the potential to improve existing procedures in organic waste treatment facilities.

5.2. Introduction

With successful quantification of yeast growth serving as proof-of-application for the HTM, the next logical step was to establish whether or not the growth of other bacteria could be studied in real-time. *Staphylococcus aureus* was selected for its immobile nature ensuring that the cells would sink to the electrode where their growth would cause change at the electrode interface.

Staphylococcus aureus is a gram-positive facultative aerobe and can grow by fermentation in the absence of oxygen [210]. *S. aureus* part of the microbiome of the upper respiratory tract [211] and skin [212]. It is continuously carried by about 30 % of the world population [213]. The persistence of *S. aureus* depends on age, sex and race [214]. The most common place for *S. aureus* to survive is the nasal cavity, a carrier has a higher risk of obtaining an infection, ranging from minor skin infections and chronic bone infections to devastating septicemia and endocarditis [215]. Most of the infections with *S. aureus* can be treated with antibiotics but there an increase in the prevalence of Methicillin-resistant Staphylococcus aureus (MRSA). This is mostly due to conjugation, a process were non-resistant bacteria obtains the resistance through direct contact with resistant type. Alternatively bacteria can obtain genetic information directly from the environment (transformation) or by bacteriophage transduction (due to a virus) [216]. *S. aureus* cells can survive for months on any type of surface and can easily transfer to hands when in contact [217].

S. aureus is a normal contaminant of municipal digestates and are present in approximately 80 % of the wastewater samples. When comparing influent and effluent of a wastewater treatment plant with each other a decrease of *S. aureus* was noted. Out of the 40 *S. aureus* found in the samples, only one of these was methicillin-resistant [218]. Another study reported a presence of a methicillin-resistant strains in 83 % in the raw sewage [219], indicating that wastewater treatment plants are a source of contamination for MRSA and cause a concern for the public health. However, conventional methods would not allow evaluation of the dynamics in bacterial communities and influence of stochastic factors [112]. Most studies available

on the microorganisms in wastewater only establish which bacteria are present and at what stage of the process they are most prevalent, but only few do look at the viability of bacteria during the possess [220]. In this study, the viability of *S. aureus* will be evaluated in samples of municipal digestates using the HTM. Demonstrating a proof-of-concept for the real-time monitoring of microbial growth in complex matrixes.

5.3. Experimental

5.3.1. Viability and attachment of *S. aureus* to the gold surface

To determine the attachment of *S. aureus* to the gold surface, SEM images were recorded using a Supra 40VP Field Emission instrument from Carl Zeiss Ltd (Cambridge, UK) after running growth experiments and after exposure to elevated temperatures. To enhance the contrast of these images, a thin layer of Au/Pd was sputtered onto the electrodes with a SCP7640 from Polaron (Hertfordshire, UK). SEM measurements were conducted before and after a growth experiment to determine the concentration of bacterial cells. For the temperature-dependent experiments, suspensions of *S. aureus* cells in water (1.0 x 10^6 CFU/mL) were incubated at 37 °C, 50 °C and 90 ± 0.1 °C for 30 min to determine the influence of temperature on morphology. Subsequently, these suspensions were drop cast onto the gold substrates and the morphology of the cells was determined using SEM. The average size of the cells was determined with ImageJ software and four different areas of the electrodes were studied, with at least 90 cells considered obtaining a representative standard deviation. This experiment was carried out as it has been demonstrated that mutations occur in *S. aureus* genes at induced pressure, including growth at temperatures >42 °C [221].

5.3.2. Analysis of the digestate samples and sequencing with 16S ribosomal RNA gene fragments

The efficiency of removing larger sedimentations from the wastewater samples whilst retaining the bacteria was investigated in two ways: i) using dilution series and ii) removing sediments by centrifugation. In the first approach, serial dilutions

from 10^{-1} up to 10^{-5} were prepared. In the second approach, 25 mL of the digestate suspension was centrifuged three times at 4200 rpm for 30 min. After removal of supernatant, the pellet was re-suspended in 25 mL of nutrient broth. From each of those samples, 100 μL was plated and incubated for one day at either ambient atmosphere or in a 5.0 ± 0.1 % CO_2 environment using a LEEC CO_2 incubator at 37 $\pm$ 0.1 °C. For digestate sample 3 (originating from a brewery), additional plating's were performed on YEPD plates due to the high presence of yeast in these samples as part of the beer brewing process. The incubation period was extended to two days due to slower microbial growth of the bacteria from this sample, which is line with samples analysed previously containing yeast [52].

Subsequently, the bacteria were isolated on colony morphologies using a 4 x magnification on a Stemi SR microscope (Zeiss, Germany).

The single colonies were subjected to Gram staining and identified using 16S rRNA sequencing. Gram staining was performed according to the protocol by Clause *et al.* [222] and the results were recorded with 100 times magnification using a Leica DM 500 with a ICC50HD camera.

Subsequently, 16S ribosomal RNA gene sequencing was performed. For this, single colonies were re-suspended in 300 μL of sterile water. The cells of each isolate were lysed by freezing at - 80 $\pm$ 0.1 °C for 15 min, followed by heating to 95 $\pm$ 0.1 °C for 15 min. The lysate obtained was mixed and centrifuged at low speed (300 rpm for 3 min) to precipitate cell debris. The supernatant was used as a DNA template source for PCR. The PCR mixture was prepared according to Table 5-1.

Table 5-1. Reagents used for PCR

Reagent	Volume (μL)
Biomix (Bioline)	7.5
16s 27F primer	0.5
16s 518R primer	0.5

DNA sample	1
PCR grade water	5.5
Total volume for the reaction	15

This mixture contained forward 27F-UNI primer (5'- AG AGT TTG ATC MTG GCT CAG-3') and reverse 518R primer (5'-CGT ATT ACC GCG GCT GCT GG-3') to amplify a hypervariable region of approximately 400 bp of the 16S rRNA gene. The PCR conditions included heating the mixture in a PCR thermocycler (QcyclerII, Quantabiotech, UK) to 94 °C for 2 min. This was followed by 5 cycles of 94 °C for 30 s and 40 °C for 1 min, and then 30 cycles of 94 °C for 30 s, 50 °C for 1 min and 72 °C for 3 min.

To visualise PCR products of the expected length, gel electrophoresis was performed in 1.5% agarose containing midori green (Geneflow, UK). From each PCR reaction, 5 µL of the PCR product was loaded on the gel, electrophoresed at 90 V for 20 min, and visualised on a geneflash bio-imager (Syngene, UK).

To clean the PCR samples for sequencing, 5 µL of the remaining PCR product was mixed with 2 µL of ExoSAPIT and incubated at 37 ± 0.1 °C for 15 min. The ExoSAPIT reagent was inactivated by incubating the sample at 85 ± 0.1 °C for 15 min. After that, 3 µL of the cleaned PCR product was added to a mixture containing 6 µL of PCR grade water and 1 µL of 27F-UNI primer. These samples were then sent for Sanger sequencing by University of Manchester. To identify bacterial species, the obtained sequences were matched to those available on the BLAST database.

5.3.3. HTM measurements

For these measurements, the optimal PID value with the lowest noise on the signal consisted of settings P = 1, I = 8, D = 0.1 or settings P = 1, I = 14, D = 0.3, depending on the dimensions of the heat sink used [36].

Gold-coated electrodes were mounted in the flow cell and stabilized in either water or in nutrient broth. Bacterial suspensions were manually injected in the flow cell to

ensure adherence to the gold substrate and prevent contamination of the tubing. Initially, experiments were conducted in water (pH = 7.4) to determine whether it was possible to discriminate between different concentrations of *S. aureus* in water. Five suspensions with *S. aureus* concentrations between 10^3 and 10^7 CFU/mL were used (concentrations determined by UV-vis). Water was used in this experiment as it did not contain nutrients and thereby slowed the growth of *S. aureus*, thus making it possible to accurately determine the bacterial load.

In the next stage of this work, growth experiments were conducted with the temperature of the copper, T_1, fixed at 37 ± 0.02 °C except for a temperature dependent growth measurement and one measurement in which bacteria were exposed to elevated temperatures (90 ± 0.02 °C).

Initially, growth experiments were conducted at a flow rate of 800 μL/h and with *S. aureus* suspended in nutrient broth at a concentration of 1.0 x 10^4 CFU/mL. In subsequent measurements, the flow rate was increased to 1 mL/ h and suspensions with *S. aureus* concentrations of 1.0 x 10^2 CFU/mL were used. Lower concentrations were used to increase the measurement time of the experiment and to prevent saturation of the electrode from occurring.

After incubation of the cells, a continuous flow of nutrient broth (at a flow rate of 1 mL/h) was provided enabling microbial growth. After 8h, the mixture was heated to 90 °C for 10 min. After the short exposure of the cells to 90 ± 0.02 °C for 10 min, the heat sink was cooled down to 37 ± 0.02 °C, this was all done under a continuous supply of broth solution using an automated syringe pump (flow rate = 1 mL/h). In this thermal experiment 90 ± 0.02 °C was used since at this temperature growth of *S. aureus* was fully inhibited and therefore, the measurement demonstrated that the change is thermal resistance was due to microbial growth. In further experiments, the temperature dependency of the growth was quantified. To this end, the temperature was varied between 35 and 55 °C, using 2 h intervals of 5 ± 0.02 °C. The slope of the graph at a given temperature was correlated to the growth rate of *S. aureus*.

Analysis of variance (ANOVA) [222] was used to investigate the effect on cell growth (°C/Wh) of Temperature T_1, using Excel and Design Expert (v.11). This was followed

by a Least Significance Difference (LSD)-test as Post Hoc comparison method to assess which temperature regime has a major influence on cell growth.

Next, to see whether it was possible to determine microorganism growth in the complex digestate samples were used. Municipal digestate samples or industrial digestate samples were centrifuged to remove all sediments and subsequently washed with NB three times. After manual injection of this suspension to the flow cell, the heat sink was kept at 37 ± 0.02 °C and the thermal resistance was monitored over 30 h. This experimental procedure was then conducted with fresh municipal sample, except this sample was 1000x diluted and filtered to remove all sediments and added to a *S. aureus* suspension of 10^2 CFU/mL in NB in a 1:1 ratio.

5.4. Results and Discussion

5.4.1. Evaluating the concentration of S. *aureus* cells in samples

The thermal response of glass and gold-coated electrodes to aqueous solutions (pH = 7.4, T = 37 ºC) increasing concentrations of *S. aureus* cells was studied. The gold-coated electrodes where stabilized in water for 15 min, resulting in a R_{th} value of 2.3 ± 0.1ºC/W. Under identical conditions, R_{th} values of 2.8 ± 0.1 ºC/W were obtained with the glass electrodes. This difference in thermal resistance can be explained by the lower thermal conductivity of glass compared with gold and the increased thickness of the glass substrates (1.2 mm for glass *vs* ~0.5 mm for gold electrodes). After exposure of the electrodes to increasing amount of cells, a significant increase was observed for both electrodes. The thermal resistance of a gold-coated electrode exposed to a *S. aureus* concentration of 1.0 x 10^7 CFU/mL in water increased with 7 ± 1 % compared to the baseline. For the glass electrodes, a maximum increase of 6 ± 1 % was recorded at the same bacterial concentration. The normalized R_{th} values, defined as the thermal resistance at a certain concentration divided that over the baseline level, are shown in Figure 5-1.
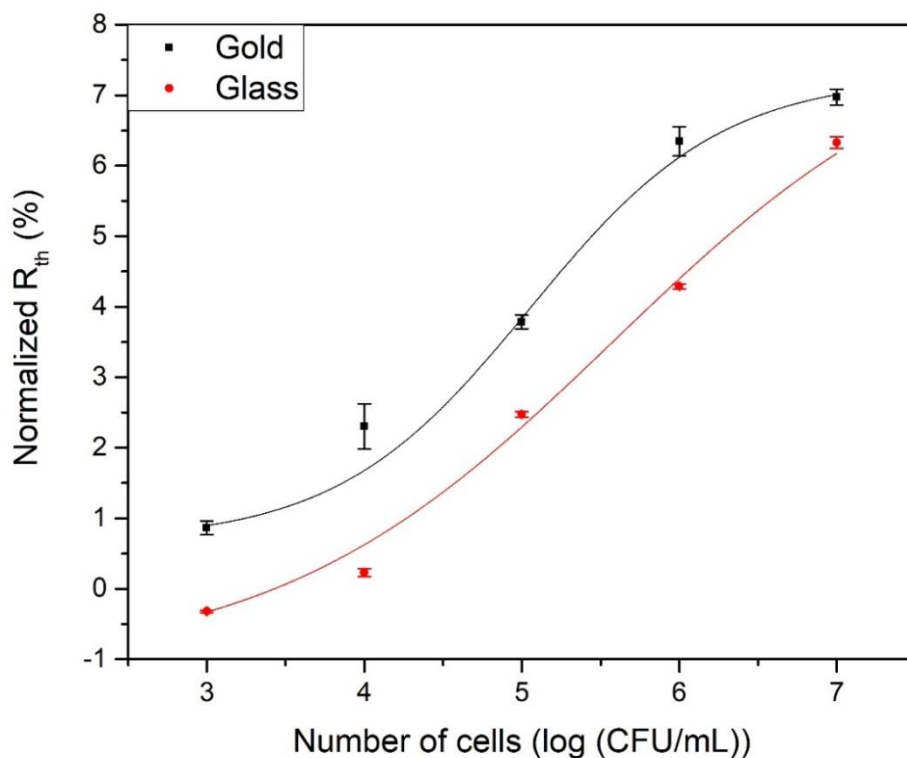
Figure 5-1. The normalized thermal resistance for gold-coated (black line) and glass (red line) electrodes upon exposure to different concentrations of *S. aureus* in water (T_1 = 37.00 ± 0.02 °C). The curve was fitted with a standard dose-response fit (R^2= 0.99). Standard deviations were determined by taking the average of at least 600 points.

The syringe pump with a flow rate of 250 μL/min was used to administer aqueous suspensions of *S. aureus* to the flow cell. Injection at a high flow rate was necessary to prevent adhesion of the cells to the gold-coated electrodes and ensure the there is no build-up of microorganism in the cell, which could lead to inaccuracy in the measurements. Prior to the measurement, the CFU/mL were determined by standard UV-vis methods.

The dynamic range of the gold-coated and glass electrodes was between 1.0×10^4 and 1.0×10^7 CFU/mL. Previous work by Betlem *et al.*, [52] reported similar values when monitoring suspensions of yeast in aqueous solutions ranging from 1.0×10^4 to 1.0×10^7 CFU/mL. To the author's knowledge, this, is the first report on the use of gold electrodes and HTM to monitor bacterial concentrations.

The limit of detection of the developed sensor platform was estimated by taking the concentration at which the signal is equal to three times the standard deviation on the baseline signal (according to conventional three sigma method). For gold-coated

electrodes this was equal to approximately 0.5×10^2 CFU/mL, whilst for glass electrodes 1.0×10^4 CFU/mL was attained. Due to the enhanced sensitivity of the gold-coated electrodes compared with glass, the former were used in further experiments on studying the growth of *S. aureus* under different conditions.

5.4.2. Evaluation of *S. aureus* growth in the nutrient broth

The effect of a continuous flow of nutrients (flow rate = 1 mL/h) on the thermal response of the gold-coated electrodes over a prolonged time was evaluated. This flow rate was based on results from previous work [52], and ensured minimal disturbance in the thermal resistance signal whilst still providing sufficient nutrients for the microorganisms to grow. There is no significant effect on the thermal resistance and a clear baseline was established.

The determination of the impact of microorganisms on the thermal resistance at the solid-liquid interface of the gold-coated electrodes was then established. *S. aureus* has a duplication time of approximately 30 min in aqueous media at its physiological temperature [114]. *Staphylococci* spp. are able to grow over at a wide temperature range but their optimal range is between 30-37 ºC [223, 224]. Therefore, experiments were performed by maintaining T_1 of the heat sink (copper block) at 37 ºC.

An experiment to determine bacterial growth was conducted with a starting concentration of *S. aureus* at 1.0×10^4 CFU/mL. The cells were maintained at 37 ºC and supplied with a continuous flow of fresh nutrients with a syringe pump that administered fresh nutrient broth solutions at a rate of 1 mL/h. After an initial lag phase (duration of ~1h) that was omitted from the graph, a continuous increase of 0.03 ºC/W per hour was observed (Figure 5-2). SEM images confirmed that *S. aureus* adhered to the gold electrode, and the concentration of bacteria retained on the surface was dependent on the concentration in the medium.
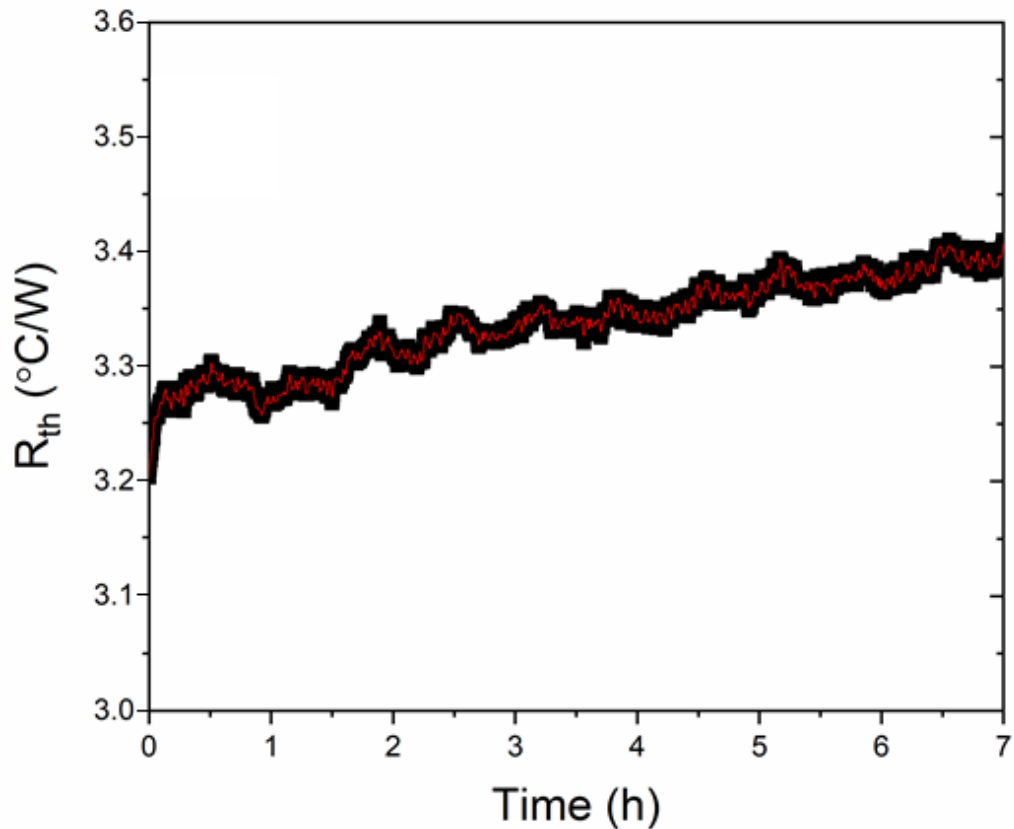
Figure 5-2. Growth of *S. aureus* inside the HTM. A flowrate of 1 mL/h was applied during the full measurement, the red line represents a 100 %-tile filter on 2 min interval

Using conventional plating methods, the impact of a 30 min exposure to elevated temperature on bacterial growth was evaluated. The exposure of the bacteria to 50 ± 0.1 °C slowed down their growth rate, which is to be expected as the viability of the cells is affected at this temperature. Full inhibition of growth was observed after incubating the bacteria at 90 ± 0.1°C, which means they are no longer viable. Previous reports indicate that disintegration of the bacterial cell wall can occur at this temperature [225, 226]. It should be noted that during this study, no attention was given to the influence of sub-lethal cell damage.

SEM images (Figure 5-3) also illustrated that the bacterial cell morphology was affected by exposure of the cells to elevated temperatures. An average size of 717 nm $\pm$ 71 nm at 37 ± 0.1 °C was found, which is under the optimal growth conditions of *S. aureus.* On the contrary, at 50 °C there was a mixture of bacteria present with an average of 195 nm $\pm$ 83 nm (some cells intact and some shrunk) and at 90 ± 0.1 °C all cells were significantly smaller or defragmented with an average size of 126 nm $\pm$ 38 nm.
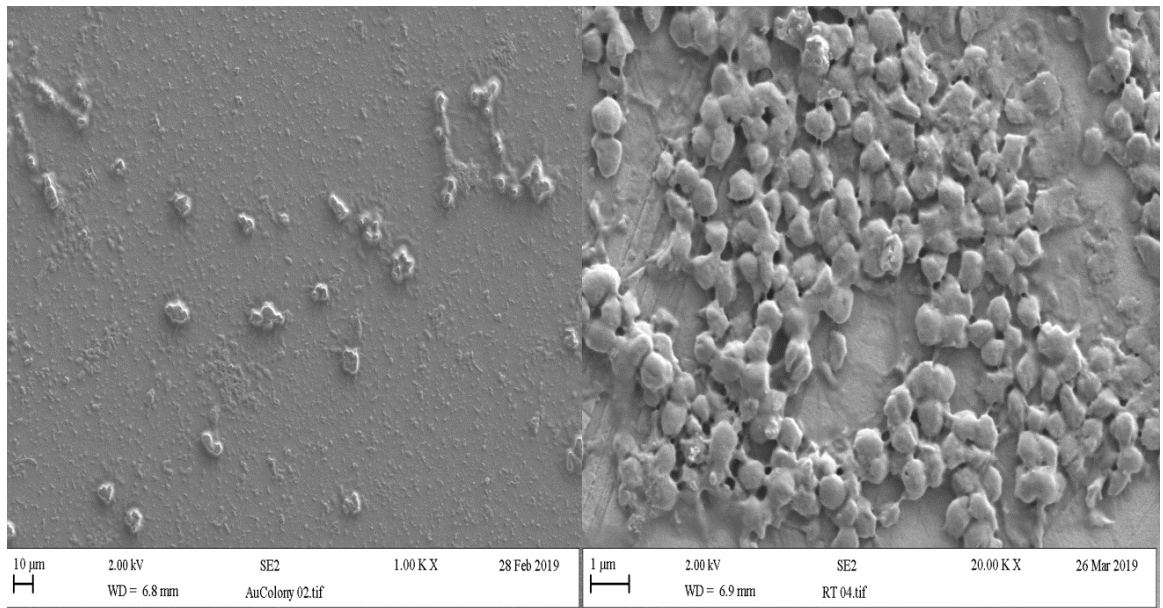
A) HTM   B) Room temperature
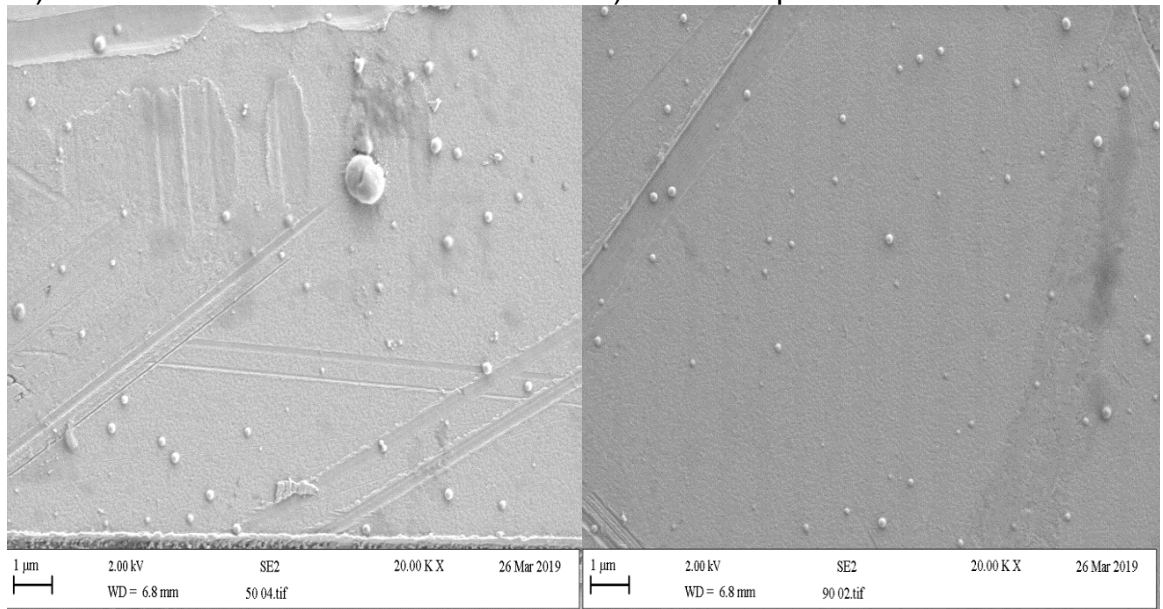
C) 50 °C   D) 90 °C

Figure 5-3. SEM image of *S. aureus* on gold after 30 min incubations. A) This electrode was used for a thermal elimination experiment of *S. aureus*. B) Incubation at room temperature. C) Incubated at 50 °C. D) Incubated at 90 °C. To be noted is that A) has a lower magnification as the other images due that this electrode was scanned prior and independently to the rest.

Figure 5-4 shows the thermal resistance in time after exposure of the cells to 90 ± 0.02 °C for 10 min, which is known to impact on their viability and cell morphology.
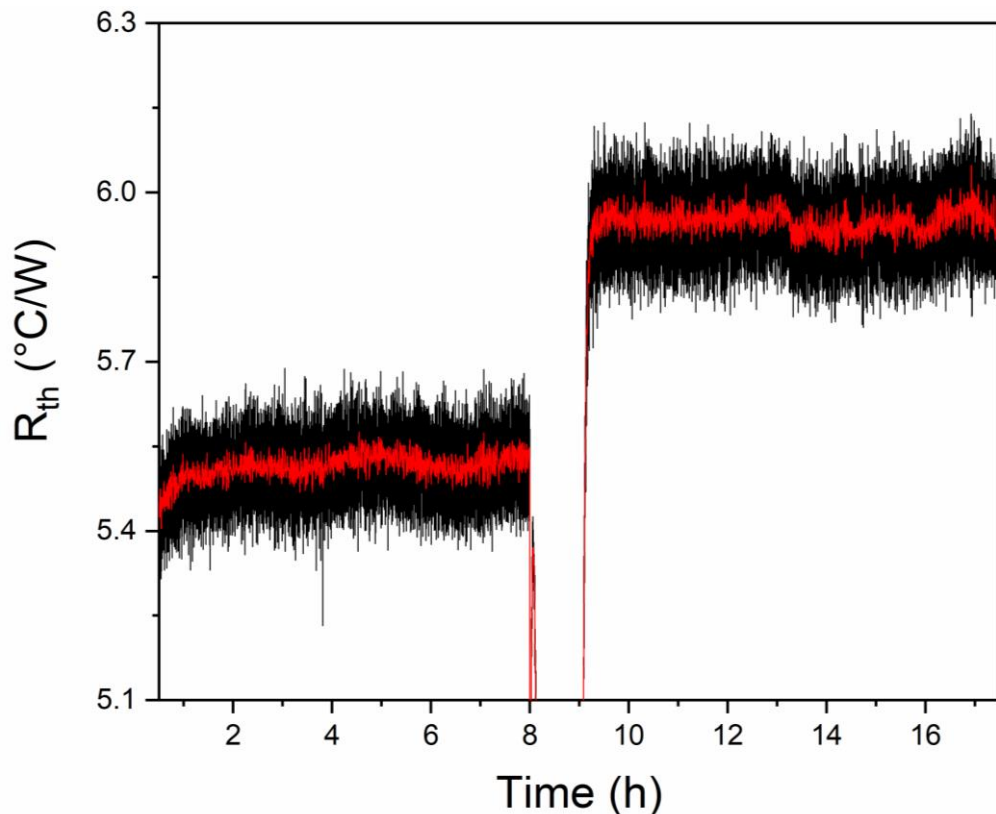
Figure 5-4. Thermal elimination of a suspension of S. aureus in water at 90.00 ± 0.02 °C. The measurement was started with ~10^2 CFU/mL of S. aureus cells that where grown at 37.00 ± 0.02 °C for 8 h. Hereafter, the temperature of T_1 was increased to 90.00 ± 0.02 °C over 10 min and maintained for 10 min before reducing to 37.00 ± 0.02 °C over 20 min. The red line corresponds to a gentle median filter (50 points) applied to the raw thermal resistance data (black line).

During replication of *S. aureus* at 37.0 ºC, an increase in the thermal resistance (~0.025 ºC/W per hour) was observed. After exposure of the bacteria to elevated temperatures, a step of only ~0.5 ºC/W was observed which remained stable over time. The increase in signal can potentially be attributed to the disintegration of the dead bacteria into small pieces that sink down closer to the electrode surface, thereby creating a densely packed layer that blocks heat-flow. This effect has previously been observed after boiling of yeast cells [52]. The fact that no further increase in the thermal resistance was observed indicated that there were no viable cells left. This confirms that the initial increase in thermal resistance was caused by bacterial growth.
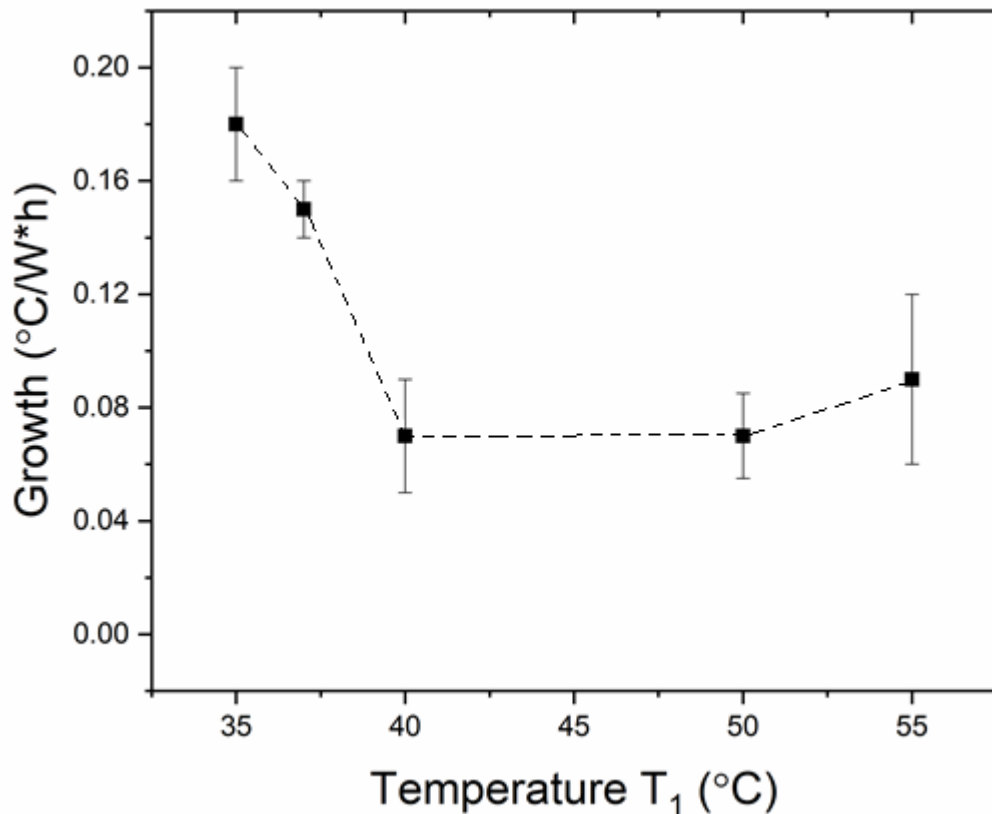
Figure 5-5. The relative change in thermal resistance per hour when S. aureus was grown in nutrient broth at temperatures of 35 ⁰C, 37 ⁰C, 40 ⁰C, and 50 ⁰C, 55⁰C. The growth at each temperature was monitored for 2h and the gradient was determined over an average of >600 data points.

Furthermore, the impact of temperature on the growth of *S. aureus* was determined. To this end, *S. aureus* as added to the flow cell, and a continuous flow of nutrient broth was applied with a flow rate of 800 µL/h (Figure 5-5). Results from the one-way ANOVA in Table 5-2 indicated that the variable 'temperature' (T_1) has a significant impact on cell growth. This result was also confirmed by the small p-values identified (p=0.0015). The LSD test was conducted with a t ($\frac{\alpha}{2}$, N-a) of 0.03. This test revealed statistically that cell growth was most influenced over the temperature range 35-37 °C (Figure 5-5) this is entirely consistent with the literature [227]. Fit statistics indicate the response has a good regression as Predicted R^2 is in agreement with the Adjusted R^2, while significance is confirmed by the values of adequate precision (>4).

Table 5-2. ANOVA table for Temperature T$_1$ impact on cell growth

Source of Variation	SS	df	MS	F	p-value	F$_{crit}$	F>F$_{crit}$
Between Groups	0.01435	4	0.0036	25.511	0.00156	5.19	*Significant*
Within Groups	0.0007	5	0.0001				
Total	0.01506	9					
R^2 = 0.9533; Adj. R^2 = 0.9159; Pred. R^2 = 0.8132; Adeq. Precision = 13.90.							

It was expected that growth rates of *S. aureus* would decrease after exceeding the optimum growth temperature of 37˚C. However, it has been reported that temperatures of 50˚C and higher can lead to disintegration of the bacterial cell walls [226]. The consequence of this is the dense packing of dead cells, or components thereof, on the electrode surface that can increase the thermal resistance, as previously has been reported for the thermal elimination of yeast cells [52].

5.4.3. Identification of bacteria present in wastewater samples

Biogas is a promising bioenergy technology offering a two-fold advantage for combining treatment of various organic wastes along with the generation of a versatile and storable energy carrier. To understand the biogas-producing capabilities of the digestate samples, it was necessary to characterise the microbial community. An overview of the bacteria encountered in the samples was determined (Table 5-3).

Source	No. of		Bacterial phyla (No. of OTUs in phylum)				
	Clone seq.	OTUs	Actino bacteria	Firmicutes	Proteo bacteria		Bacteroidetes
			Actino bacteria	Bacilli	B	γ	Flavobacteriia
Municipal	8	4	1		2		1
Industrial	22	15	6	1	4	4	

An interesting study [228] conducted to characterise the biogas-producing microbial community by short-read next generation DNA sequencing, revealed the composite microbial consortium developing in a biogas fermenter was characterised by members of the Clostridia (36%) and Bacilli (11%) classes, together with members of the Bacteroidia (3%), Mollicutes (3%), Gammaproteobacteria (3%) and Actinobacteria (3%) classes. Most species identified by Wirth *et al.* [229] were in agreement with those characterised in this study (Table 5-3). *Kocuria spp.* are isolated from marine sediments and have been successfully used for wastewater treatment as they are excellent for biogas formation at lower working temperatures giving energy savings and increase energy conversion efficiencies. *Bacillus thuringiensis* are the most well-known biological agents for selective control of pest insects and can be grown on post-biogas production residues, as they contain the necessary nutritional elements to sustain the growth of microbes. It has been found [230] that the optimum substrate for growth are actually brewer grains, with at least 50% of this biomaterial in the growing media. *Actinobacteria* (that act like fungi) are used for soil conditioning as the decomposing matter is transformed into nutrients that can be up taken by plant for growth. They are abundant in natural waters, and are a small minority of typical digester consortia [228] and their presence was therefore expected in these digestate samples.

These results confirm the complexity and heterogeneity of the digestate samples used. Within the wastewater community, there is a high demand for the

development of sensors that can monitor microbial load *in-situ* as the build-up of microorganisms has been linked to bioagumentation failure [231]. Furthermore, microbial load is an important parameter for the control of food hygiene and determination of drinking water quality. Current culturing techniques are time-consuming and cannot be implemented on-site, whereas thermal analysis could provide rapid screening. Therefore, further experiments were conducted with digestate samples and those spiked with *S. aureus*, to demonstrate proof-of-application of the sensor platform for complex samples.

5.4.4. Thermal analysis of diluted digestate samples spiked with S. aureus

A fresh municipal digestate sample was added to the flow cell. This sample with an unknown composition and bacterial concentration was used as a first test to determine whether bacterial growth can be monitored in a complex sample.

The results demonstrated with the digestate there was more noise (around 2.5 %) on the signal. This was somewhat higher than the normally expected ~ 0.5 - 1 %, and could be due to the complex nature of the digestate samples. After an initial period of 30 min, the signal increased for a period of ~ 5 h with a rate of 0.035 ºC/W per hour after which it remained stable. This could be due to complete coverage of the electrode with bacteria, as bacteria further away from the surface or in the planktonic state would not have a significant influence on the thermal resistance. The platform developed is not selective towards the bacteria present in the sample, but has the capability to monitor bacterial load in a simple and low-cost manner. SEM images confirmed the presence of a mixture of bacteria on the surface and indicated that the increase in thermal resistance was due to the presence of microorganisms and not caused by build-up of organic material on the electrodes.

Fresh municipal digestate samples with an added *S. aureus* suspension were analysed. After incubating a gold-coated electrode with this sample for 15 min at 37 °C, the R_{th} value stabilized at 3.0 ± 0.1 ºC/W (Figure 5-6).
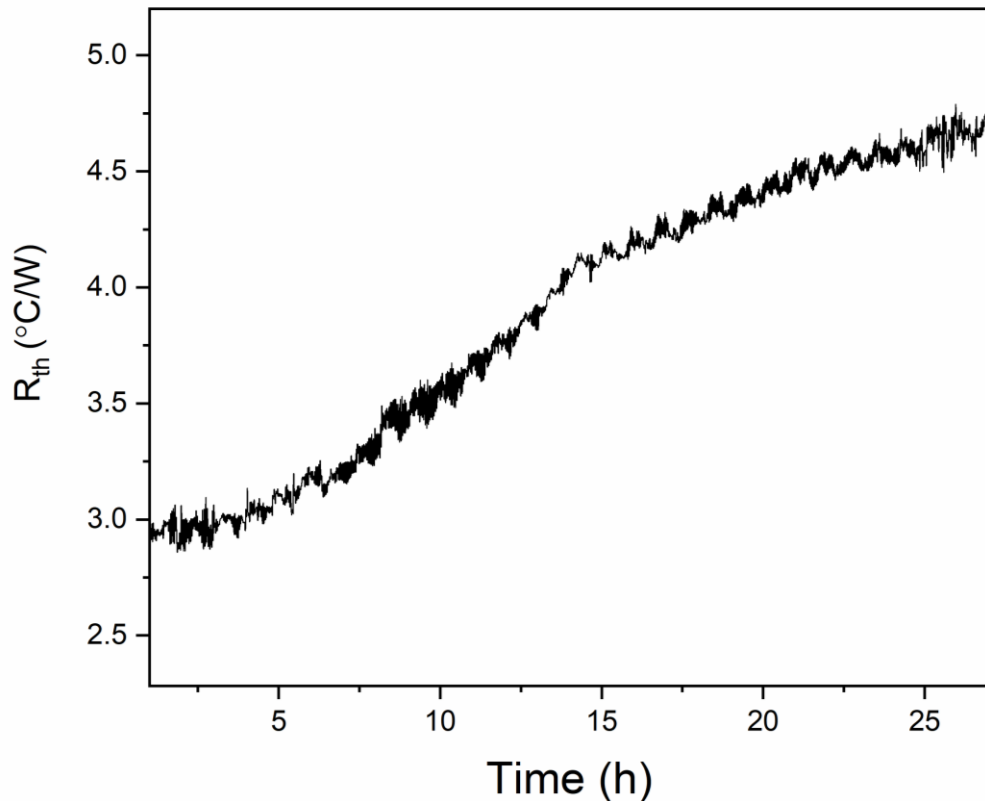
Figure 5-6. Thermal resistance over time of a 1000x diluted municipal digestate that was mixed in a 1:1 ratio with a suspension of S. *aureus* (1000 CFU/mL) in water. A gentle median filter (50 points, corresponding to 1 measurement point per minute) was applied to the data.

When *S. aureus* was measured as a suspension in water, growth started after an incubation time of 30 min. In this measurement however, the thermal resistance did not increase before approximately 4 h. The longer lag time could be due to the lower concentration of *S. aureus* used or due to the inoculation of other microorganisms that can interact with each other. There are limited reports on the impact of other microorganisms on *S. aureus* growth, but most predictive models state that growth is generally led by the most resistant strain, particularly under stressful conditions [232].

After 27 h, the thermal resistance increased to 4.5 °C/W, which corresponds to an increase of nearly 50%. The data was fitted ($R^2 =0.95$) with a double linear fit with an initial increase of 0.08 °C/W from 4 to 14h (average of time period of 10 h), after which the original growth slowed down to 0.03 °C/W. The latter was comparable to what was reported for the growth of *S. aureus* in buffered solutions whereas the initial growth was higher compared to buffered solutions. The higher growth rate at

the initial stages of the experiment could indicate that the sensor platform is capable of monitoring the overall microbial load and not *S. aureus* exclusively. This characteristic would be preferential for measurement of digestate samples, which are complex and contain many microorganisms, the overall load is an indication of the efficacy of the organic waste treatment.

Because the *S. aureus* concentration incubated at the start of the measurement was lower compared with other experiments, it could be that saturation takes longer to occur. Furthermore, due to presence of bacteria with different morphologies, it would be possible to form a denser packing on the surface that could overall lead to a higher thermal resistance.

This experiment provides proof-of-application for monitoring bacterial load in complex samples, which could have applications in the field of food safety, organic waste treatment and infection control.

5.5. Conclusions

In this work, the HTM was employed to monitor bacterial load on electrodes using *S. aureus* as a model organism. The reason for using *S.* aureus was i) because it is an opportunistic pathogen that is frequently encountered in skin infections and food poisoning ii) it has the capability to adhere to surfaces. Measurements of *S. aureus* suspension in water demonstrated that higher concentrations of the microorganism corresponded to a higher thermal resistance at the solid-liquid interface. Dose-response curves were constructed for both glass and gold-coated electrodes which exhibited a similar dynamic range, but the gold-coated electrodes had lower limit of detection compared with the glass electrodes.

Subsequently, the influence of bacterial growth was monitored in a nutrient broth solution. A steady increase of 0.03 °C/W per hour was encountered when *S. aureus* was kept at 37 °C. No significant response in the thermal resistance was found after thermal elimination of the cells and this confirmed that the increase in thermal resistance was due to the bacterial growth. Furthermore, a temperature dependent HTM experiment demonstrated that it was possible to determine the kinetics of *S. aureus* replication. SEM analysis validated that *S. aureus* adhered to the surface and its morphology was affected by temperature.

Next, the influence of a complex mixture (digestate sample) on *S. aureus* growth was determined. Digestate samples were collected from various sources and characterised by 16S ribosomal sequencing. The majority of the bacteria (~53%) belonged to class of Proteobacteria with also colonies of Actinobacteria (27%) and Bacilli (11%) found, highlighting the complexity of the sample. Thermal measurements confirmed that growth was encountered in pure digestate samples. When spiking those samples with *S. aureus,* a higher increase in the thermal resistance was found which indicated the sensor platform is capable of determining the overall microbial load of complex matrices. Considering the simplicity and low-cost of the sensor platform developed, in addition to the ability to implement thermal analysis *on-site,* this could be a useful diagnostic tool for determining microbial load in water and food samples.

6. Determination of small organic molecules by using Molecularly Imprinted Polymers coupled to heat-transfer based detection

6.1. Abstract

MIPs are synthesized for the selective detection of caffeine and noradrenaline. The polymerization process is optimized by changing the functional monomer and crosslinker composition and ratios thereof, batch rebinding experiments are performed and evaluated with optical detection. The selectivity is assessed by comparing the response of caffeine to chemical compounds with similar structures (theophylline and theobromine) and dopamine, a neurotransmitter, whilst for noradrenaline the selectivity was evaluated against adrenaline, dopamine, L-Dopa and tyramine. Subsequently, the MIP polymer particles are integrated into bulk MIP-modified SPEs with a paper, tracing paper or PVC substrate for noradrenaline and a polyester substrate for both caffeine and noradrenaline. The sensors are used to measure caffeine or noradrenaline content in various samples employing the HTM. At first, the noise is minimized by adjusting the settings of temperature feedback loop. Second, the response of the different substrates for the MIP-modified SPE is studied at 37 °C, whilst for caffeine the temperature ranged from 37 °C to 50 °C and 85 °C. The binding to MIP-modified SPEs has never been studied for different substrates or at elevated temperatures since most biomolecules are not stable at those temperatures. The paper based electrode showed the highest response and was used in further experiments. With caffeine as proof-of-concept, it is demonstrated that at 85 °C the detection limit is significantly enhanced due to higher signal to noise ratios and enhanced diffusion of the biomolecule. TWTA was applied to noradrenaline and resulted in detection limits in the micro-molar range. For

caffeine the TWTA is optimized at 85 °C producing a limit of detection of ~1 nM. The use of MIP-modified SPEs in combination with the HTM provides a sensors platform that is fast, low cost and can be used on-site. This holds great potential for determination of contamination in environmental samples. The platform is generic and be used on a range of relevant targets by adapting the MIP layer.

6.2. Introduction

Caffeine is present in a variety of food and beverages and is considered the most widely consumed drug in the world [233]. It is used in many pharmaceuticals due to certain analgesic effects in cough, cold and headache medicine [234]. The prolific use of caffeine results in an accumulation in waste water generally ranging from 200-300 µg/L [235]. In some countries such as Greece [236] and Taiwan [237] concentrations between 5,000-13,000 ng/L were reported. Traces of caffeine have ubiquitously been found in surface water; in Swiss lakes and rivers concentrations of ~2ng/L were reported [155] and a comprehensive Brazilian study found that 93% of all surface water samples contained caffeine [238]. The presence of micro-pollutants, such as caffeine, in surface water is a serious concern as this is used to produce drinking water in water treatment plants [239]. Additionally, it has a significant effect on aquatic life as caffeine has been suspected to decrease hemocyte adherence in mussels [240] . The European Parliament has set strict environmental quality standards for a number of these micro pollutants [241]. Therefore, sensitive detection of caffeine is required and performed by chromatographic techniques such as electrospray triple-quadrupole mass spectrometry [238], high-performance liquid chromatography-mass spectrometry [242, 243], micro-gravimetric methods [244], gas chromatograph mass spectrometry [245, 246] or the use of immunoassays [247, 248].

Caffeine further acts as a cardiac and cerebral stimulant of to the methylxanthine class [249, 250], where it activates the noradrenergic neurons [251]. The primary neurotransmitter for this neuron is norepinephrine, better known as noradrenaline. It belongs to the class of catechol neurotransmitters and has a crucial role in the function of the renal, hormonal, cardiovascular and central nervous system [249, 252]. High levels of noradrenaline indicate stress, thyroid hormone deficiency [253] and congestive heart failure[254], while low levels are associated with depression and postural hypotension [255]. There are a variety of drugs available that have

noradrenaline as an active component to counterbalance these low levels [256]. The presence of noradrenalin in urine and plasma samples has been associated with pheochromocytoma, an endocrine tumour of the adrenal glands that secretes high amount of catechol amines [257, 258]. These tumours have a high risk of mortality [259], hence the importance or noradrenaline as a tumour biomarker [260]. To detect noradrenaline various analytical techniques have been employed, of which the most common methods are chromatographic [144, 261] and electrochemical biosensor techniques [140-142].

All those techniques for the detection of caffeine or noradrenaline are either time-consuming, exhibit a low sensitivity [209, 210] or require the use of a lab environment, which does not allow on-site quality control [262]. A polymer based platform is a suitable alternative and has potential for the use in pharmaceutical applications because of it its simplicity, low-cost, and portability of the set up [263]. The ability to adapt the MIP layer offers a great versatility [120] and can be made specific and selective for either noradrenaline or caffeine. By mixing these MIPs into screen-printing ink, mass producible MIP-modified SPEs [28] can be made on a variety of substrates. These sensors are then used to measure their respective target in various samples employing the HTM and TWTA, offering a great opportunity as a point-of-care sensor for drug screening.

6.3. Experimental

6.3.1. MIP and NIP syntheses

6.3.1.1.   Caffeine

A total of five MIPs were synthesized for caffeine, the composition for each of these MIPs is listed in Table 6-1.

Table 6-1. The composition of the different caffeine MIPs, listing the amount of template, functional monomer, crosslinker monomers, initiator (4,4-azobis(4-cyanovaleric acid)), and porogen used [44].

	MIP-1	MIP-2	MIP-3	MIP-4	MIP-5
Caffeine (mmol)	0.35	0.35	0.35	0.35	0.35
MAA (mmol)	1.3	2.6	-	-	0.7
AM (mmol)	-	-	1.3	-	-
HEMA (mmol)	-	-	-	1.3	0.7
TRIM (mmol)	3.0	3.0	3.0	3.0	3.0
Initiator (mg)	50	50	50	50	30
DMSO (mL)	7.0	7.0	7.0	7.0	4.0

For each MIP, a reference NIP was synthesized accordingly but without the presence of the caffeine.

6.3.1.2.   (±)-Noradrenaline hydrochloride

For simplicity, in the remainder of this text we will refer to (±)-noradrenaline hydrochloride as noradrenaline. A total of five MIPs and their corresponding NIPs were prepared for noradrenaline. The composition for each of these MIPs is listed in Table 6-2.

Table 6-2. The composition of the different noradrenaline MIPs listing the amount of template, functional monomer, crosslinker monomers, initiator (4,4-azobis(4-cyanovaleric acid)), and porogen used. [91]

	MIP-23	MIP-24	MIP-31	MIP-32	MIP-33
Noradrenaline (mmol)	0.38	0.38	0.38	0.38	0.38
IA (mmol)	-	-	0.77	0.77	0.77
MAA (mmol)	0.77	-	-	-	-
AA (mmol)	-	0.77	-	-	-
EGDM (mmol)	7.7	7.7	7.7	7.7	7.7
Initiator (mg)	50	50	50	50	50
DMSO (mL)	4	4	3	4	5

The completion of the extraction was verified using single bounce diamond ATR-FTIR spectroscopy (Nicolet 380 fitted with Smart iTR™ accessory (Thermo Scientific (Loughborough, UK))

6.3.2. Batch rebinding experiments evaluated with optical detection

6.3.2.1. Caffeine

The concentration of free caffeine in solution (C_f) was determined by comparing the absorbance at a wavelength at $\lambda = 281$ nm to a calibration curve. After exposure of the MIP particles to the caffeine solutions for more than one hour, no significant changes in absorbance were observed, indicating that the system is at equilibrium. Therefore, in all further experiments the binding time was fixed at one hour. In order to determine the imprint factor (IF) values for each MIP, the substrate binding at C_f = 0.22 mM was determined. The selectivity for caffeine of MIP-1 and MIP-3 was examined by comparing the binding of caffeine with that of similar molecules; theophylline and theobromine that differ from caffeine by one methyl group.

6.3.2.2. Noradrenaline

For each experiment, the C_i of noradrenaline in water was varied between 0 and 0.3 mM. After 1 h the particles were saturated with noradrenaline and the C_f was

determined at λ=282 nm. Binding of target to MIP particles can depend on the pH of the solution and therefore the pH dependence of the molecular recognition was studied. Therefore, the pH was adjusted in the range of 3-6 by adding drops of HCl solution (0.1 mM). Hereafter, the IF was calculated for each MIP at a C_f = 0.05 mM. The selectivity was demonstrated using adrenaline, dopamine, L-Dopa and tyramine, all of which have chemically similar structures to noradrenaline.

6.3.3. HTM and TWTA measurements with MIP-modified SPEs

MIP-1 and NIP-1 were used to fabricate the MIP-modified SPEs that were printed on a standard polyester substrate. The noradrenaline modified-SPEs were printed using MIP-32 and NIP-32 on different substrates including tracing paper, paper, PVC and polyester.

As indicated in section 2.2.1.3.1, the PID settings depend on the electrode material and the temperature used in the experiment. Therefore, optimization for each substrate of the noradrenaline modified-SPEs was performed at 37 ± 0.02 °C (see Table 2-2) resulting in optimum settings of 1, 10, 0 for all electrodes. Whilst for caffeine modified-SPEs the PID settings were optimized for each measurement at various temperature (30, 50, 70 and 90 ± 0.02 °C, respectively). The PID setting giving in the lowest S/N ratio for all selected temperatures was found to be 1, 8, 0.1. These PID settings for the caffeine and noradrenalin electrodes were fixed for all further measurements.

6.3.3.1. Caffeine

The influence of temperature on the binding of the template to the polymer layer was investigated by measuring increasing concentrations of caffeine (2.5, 5, 10, 25, 50, 100, and 250 nM) in PBS with MIP-modified SPEs at 37, 50 and 85 ± 0.02 °C. The dose response curves at each temperature was constructed by determining the R_{th} value per concentration, enabling the calculation of the LOD and the dynamic measurement range of the sensor. The selectivity of the sensor platform was established, using identical measurements on an NIP-modified SPE. In order to evaluate the selectivity of the sensor platform, solutions with high (1 mM) concentrations of similar molecules, including theophylline, theobromine and dopamine were analysed. The selectivity was further evaluated in the presence of

an excess of theophylline (250 nM), proving that a trace amount of caffeine could selectively and qualitatively be detected in a sample containing a competitive component.

Next, the performance of the MIP-based sensors were evaluated using caffeine containing beverages. Both coffee (Aldi's Fairtrade Colombian Instant Coffee, UK ~ 2 % caffeine content) and black tea (Tesco original, Cheshunt, UK – 0.7 % tea content according to label) were measured in the HTM set up. The coffee sample was prepared by dissolving 2.6 mg of instant coffee in 10 mL of PBS heated to ~ 80 °C. It was estimated the maximum caffeine content is 2 %, from which dilutions were made containing approximately 1 and 37 µM of caffeine in PBS. For the tea samples a serial dilutions of 1/100 and 1/10 in PBS were used. Finally, the performance of the MIP-modified SPEs was evaluated by measuring digestate samples and tap water spiked with caffeine (0 – 100 nM).

6.3.3.2. Noradrenaline

Each noradrenaline modified-SPE substrate was stabilized in water for 1 h before adding aqueous solutions with a 1 mM concentration (pH=6) of noradrenaline. The signal was left to stabilize for 30 min before testing the reusability of the sensor by flushing the cell with aqueous solution and a second exposure to the 1 mM noradrenaline solution. The response of the system is determined for different concentrations and normalized according to Equation 6-1.

$$Response = \frac{R_{th}^{t=c}}{R_{th}^{t=0}} \times 100\%$$
<div align="right">**Equation 6-1**</div>

Here, the baseline is represented as R_{th} at t = 0, while R_{th} at t=c refers to the thermal resistance at a certain concentration.

Due to the high initial response to a 1 mM noradrenaline solution and advantageous material properties of the paper based electrode all further measurements were conducted using this electrode type. A dose response curve was constructed using the normalized response of the electrode to various increasing concentrations of noradrenaline solutions (0, 0.5, 1, 2.5, 5, 10, 25 mM in distilled water). After a 1 h stabilization the solutions were injected at interval of 30 minutes, with a flow rate of 200 µL/min.

6.3.3.3.   TWTA measurements

By comparing the delay in response time for the thermal wave on different target concentrations to a blank solution, a calibration curve can be obtained. For measurements on caffeine, the thermal wave was applied 17 minutes before every injection and at all temperatures. For measurements on noradrenaline, the thermal wave was applied alternately between directly after the injection or 17 minutes before an injection. Measurements with NIP modified-SPEs were performed to determine the specificity of the developed sensor platforms. The selectivity of the noradrenaline modified-SPE was determined using adrenaline or dopamine (1 mM) in aqueous solution.

6.3.4. Evaluation of monomer-template binding using NMR analysis

NMR analysis was performed according to Xu *et al.* [264], with some minor changes to accommodate the current study. A 18.4 mM soluiton of MAA was made by dissolving 1.6 mg in 1.0 mL of either DMSO-D_6 or $CDCl_3$. An. NMR spectra was obtained using a Jeol ECS-400 spectrometer (Welwyn Garden City, UK). Hereafter, the concentration of caffeine in the solution was increased by sequentially adding either 0.9, 1.8, 3.6, 7.2 or 14.4 mg of caffeine. After each addition of caffeine, the solution was homogenized and a new ^1H spectrum was recorded.

To determine if the obtained peak shifts are concentration dependent or caused by an interaction between monomer and template, a set of control experiments were performed with either pure caffeine or pure MAA dissolved in DMSO-D_6. Therefore, NMR tubes were prepared with caffeine concentrations of 4.6, 36.8 and 147.2 mM and for MAA, the concentrations were 0.2, 1.3 and 10.4 mM.

All recorded data were further processed using MestreNova (v6.0.2-5475).

6.4. Results

6.4.1. Batch rebinding results

The affinity of the MIP for a target depends on the electrostatic interaction, hydrogen bounds, hydrophobic interactions or a combinations of these interactions between

the target and the functional monomer [265]. Selecting the correct functional monomer is crucial; therefore, different functional monomers were used in caffeine MIPs 1, 3 and 4; and noradrenaline MIP's 23, 24 and 32, whilst the rest of the mixture remained constant. The IF was calculated for each of these MIP's at a C_f of 0.22 mM of caffeine and a C_f of 0.05 mM for noradrenaline

For noradrenaline MIP-32 with IA as functional monomer has the highest IF, with a value of 1.2, which is in correspondence with literature [136]. For caffeine MIP-3, with AM as functional monomer, has the highest IF with a value of 4.1. The amount of porogen and the pH have a strong influence on the shape of the cavities and target biding affinity of the MIPs. This is of particular interest for noradrenaline which is only soluble in water under acidic conditions. Depending on the pH of the solution, the carboxylate groups of IA will lose their charge resulting in blocking the binding sites in the MIP for noradrenaline. IA has two carboxylate groups resulting in pKa values of 3.85 and 5.44, respectively, each influencing the binding [266]. Table 6-3 allows a direct comparison for both of these factors, representing the IF values at a C_f of 0.05 mM for three polymers made with different amounts of porogen (3-5 mL), each determined at a pH range between 3 and 6.

pH	IF MIP31	IF MIP32	IF MIP33
3*	1.01	0.97	1.20
4	1.16	1.35	1.35
5	1.10	1.28	1.31
6	1.19	1.61	1.52

*at pH 3, binding was below 10 µmol/g and a linear fit was used to determine IF instead of the Freundlich isotherm.

Table 6-3 reveals that a moderate amount porogen (corresponding with MIP-32) and a pH value of 6 will give the highest IF. The functionality of the MIP can be further enhanced by adjusting the ratio between the target and the functional monomer (MIP-1 and MIP-2) or a mixture of the latter (MIP-5), as has been done for caffeine in Table 6-4.

Table 6-4. The amount of binding for each MIP and NIP at $C_f = 0.22$ mM [44].

Polymers	Functional monomer : Target	Impact factor $C_f = 0.22$ mM
MIP-1	4:1 (MAA)	3.5
MIP-2	8:1(MAA)	1.5
MIP-5	2:1 (MAA) 2:1 (HEMA)	2.9

Increasing the ratio of functional monomer to target had an adverse effect on the binding. The amount non-specific binding increased with a higher number of charges on the polymer surface. The addition of HEMA (MIP-5) changes the balance of charges leading to a higher affinity towards caffeine, though the IF value is lower compared with other polymers (MIP-1 and 3). To further study the shifting charges, NMR titration experiments were performed with caffeine and the MAA monomer. The protons present in caffeine and MAA that can be observed in the ^{1}H-NMR are labelled in Figure 6-1.
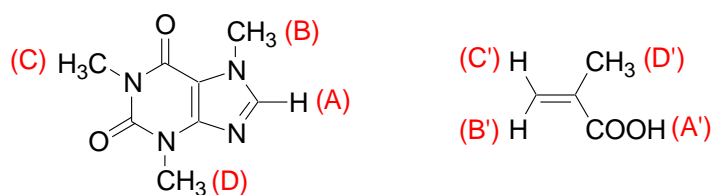
Figure 6-1. Labelled protons of caffeine (left) and methacrylic acid (right) that can be observed in the 1H-NMR spectra.

A reference ^{1}H-NMR measurement with increasing concentrations (0-100 mM) of either MAA or caffeine did not demonstrate any significant shifts in the proton signals. On the other hand, spectra of mixtures of MAA and caffeine in DMSO-d6 revealed a downfield shift (up to 0.04 ppm) of all the caffeine hydrogen atoms as the relative concentration of MAA increases (Figure 6-2).
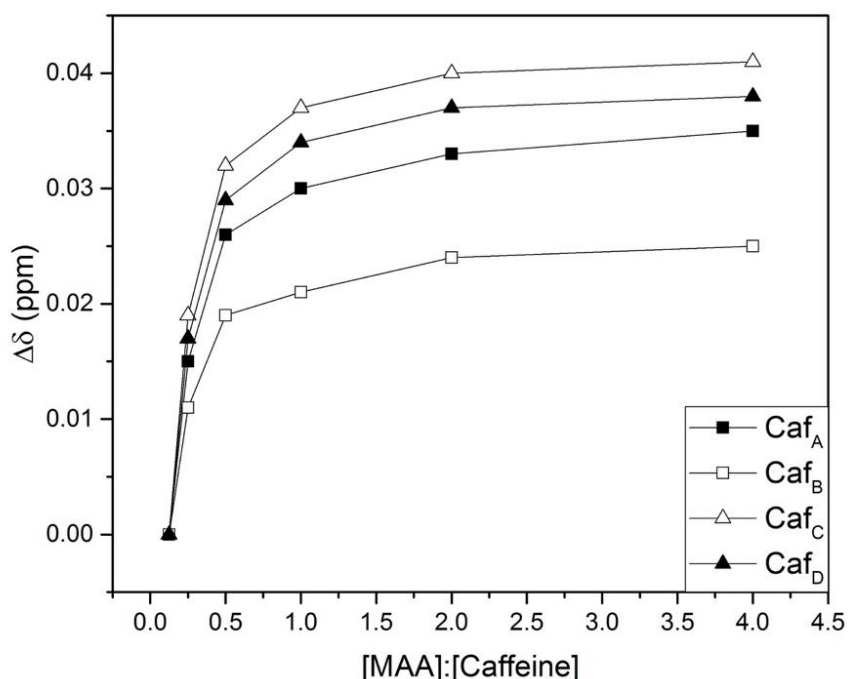
Figure 6-2. Differences in the chemical shifts of caffeine hydrogen atoms in function of the relative concentration of MAA. An internal reference, tetramethylsilane (TMS), was used in all experiments. The precision of the NMR experiments therefore corresponds to the precision of the instrument (±0.01 ppm).

These shifts are similar to those observed in literature by Xu *et al.* [264], and suggest an electronic-stacking interaction between both template and monomer. The observed deshielding effect is probably due to the electron-deficient double bond of MAA attached to the electron-withdrawing carboxylic group. Figure 6-3 shows the NMR spectra for each of the peaks shifts of the marked caffeine hydrogen atoms.

It is worth noting that the double bound in the MAA monomer will not be present in the MIP. The titration experiment was performed using the monomer. An alternative model compound such as 2-methylpropanoic acid could potentially circumvent this shortcoming. It should be noted that the interaction between the monomer and caffeine seems to mostly depend on proton A', demonstrating the importance of free access to this proton. In MAA the proton may be more exposed than in the polymer due to conjugation between the carbonyl group and the double bond. Further investigation is ideally needed to resolve this aspect.
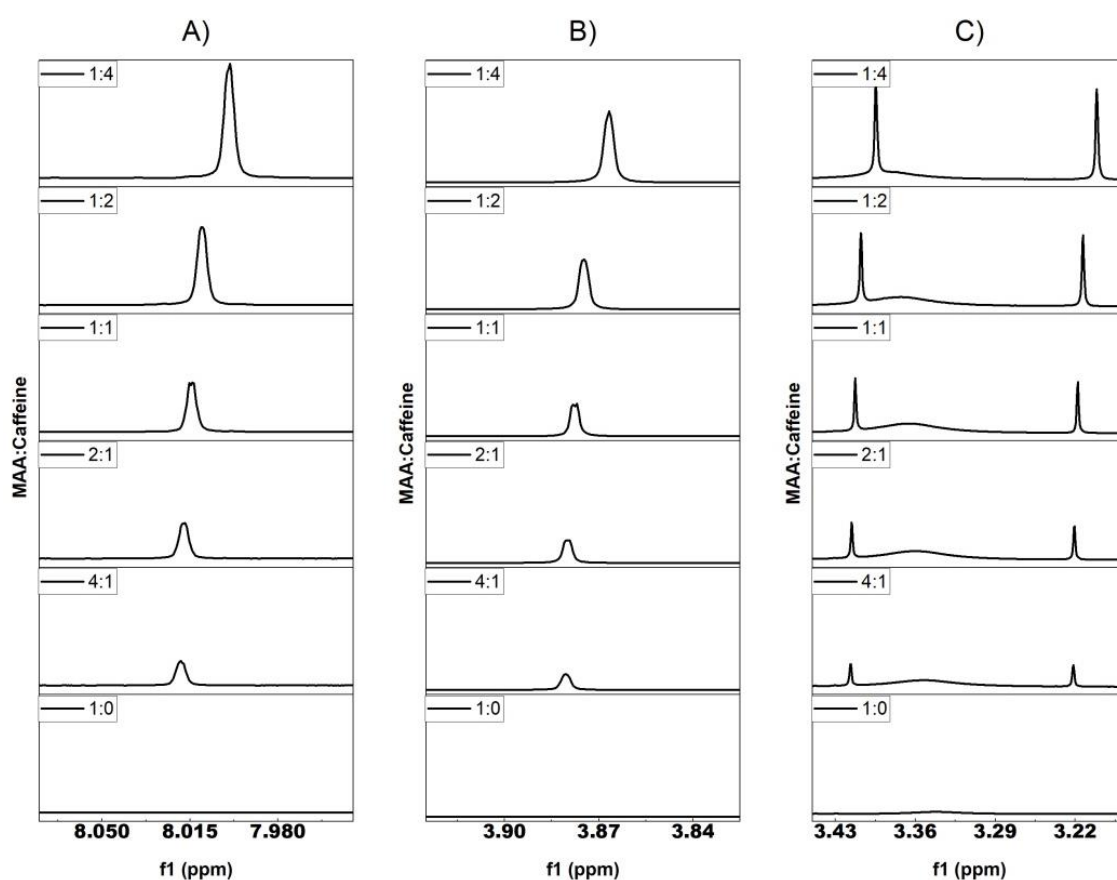
Figure 6-3. Peak shifts with increasing caffeine concentrations. The molar ratio of MAA: caffeine is from bottom to top 1:4, 1:2, 1:1, 2:1, 4:1 and 1:0. Plot A corresponds to CafA, plot B with CafB and plot C shows the shift of CafC (left) and CafD (right).

After optimizing the specific of the MIP to its target, one has to ensure that it also is selective for the designed target. Therefore MIP-32 was subjected to adrenaline, dopamine, L-Dopa and tyramine, which are structurally similar to noradrenaline (Figure 6-4), while MIP-3 was compared against theophylline and theobromine (Figure 6-5).
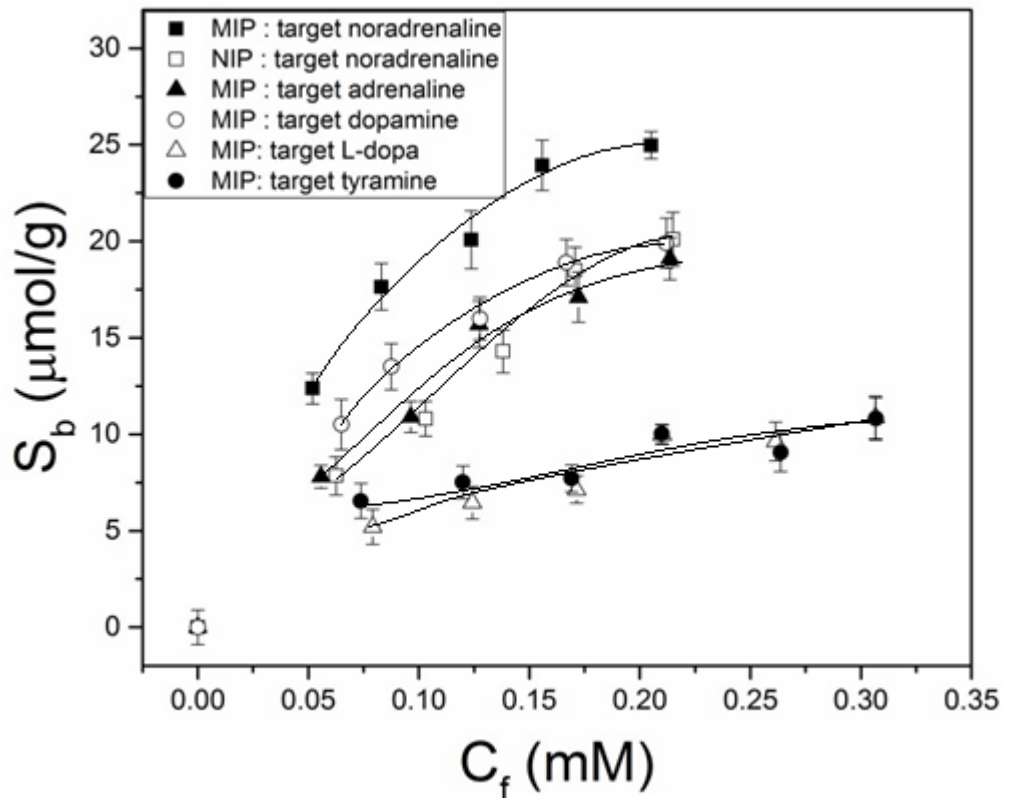
Figure 6-4. Binding isotherms obtained from batch rebinding of the MIP-32 over a 12 h period. The solid squares represent the MIP, while the open squares represent the corresponding NIP when exposed to a aqueous noradrenaline solutions (pH = 6). In addition the selectivity for adrenaline (solid triangles), dopamine (open circles), L-dopa (open triangles) and tyramine (solid circles) are shown. Error bars represent the standard deviation over three measurements.

Figure 6-4 shows the specificity and selectivity of MIP-32 toward noradrenaline. The difference in binding of noradrenaline to the MIP relative to the NIP is significant. On the other hand, the binding to the MIP by a variety of noradrenaline metabolites, including adrenaline, dopamine, tyramine and L-dopa, was significantly lower.
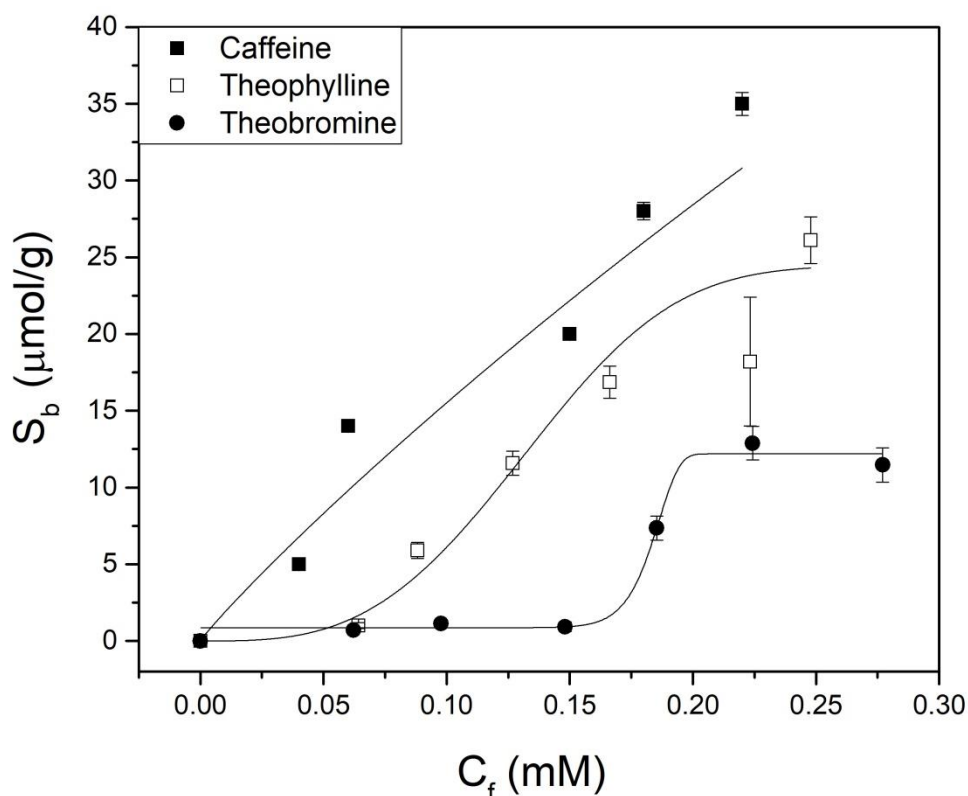
Figure 6-5. Binding isotherms of MIP3 in PBS solutions. The solid squares represent caffeine, the open squares are theophylline and the solid circles are for theobromine (as n=3). Error bars, represent the standard deviation.

Figure 6-5, shows that MIP3 absorbed ~34 μmol/g caffeine at C_f = 0.22 mM, whilst theobromine only absorbed ~12 μmol/g. Both these structures differ by one methyl group and show a significant difference in binding to the MIP. The binding of theophylline is lower than for caffeine, but considerably higher than theobromine. At a C_f of 0.05mM a threefold difference in s_b was recorded is found between caffeine (~10 μmol/g) and theophylline (~3 μmol/g). This difference became smaller at higher concentrations due to gradual occupation of the binding sites. In waste water samples the relevant concentration range for caffeine detection is in the lower nM range, The HTM is more sensitive than the batch rebinding experiments and was therefore used to evaluate the performance of the sensor to discriminate caffeine from its competitor molecule at nanomolar concentrations.

6.4.2. Thermal resistance measurements MIP-modified SPEs

The composition of the MIP influences the loading ratio of MIP particles in the ink formulation. For all MIP-modified SPEs the maximum permitted loading of MIP in the graphite ink was found to be 30 mass%. Increasing the MIP level beyond the later lad to impaired printability. To confirm the presence of MIPs in the SPEs the electrodes were SEM imaged (Figure 6-6).
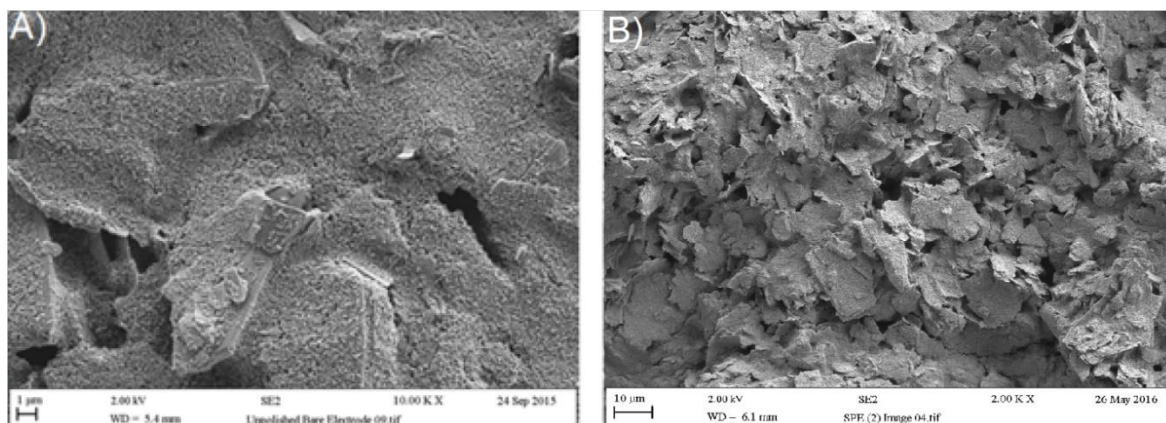
Figure 6-6. Scanning Electron Microscopy (SEM) image of the MIP-modified SPEs. Figure A represents a plain SPE, while figure B has a 30% mass percentage of MIP particles incorporated. Note the difference in magnification needed to get an effective global view of the particles.

The layered planar structure in Figure 6-6A is graphite, which makes up the bulk of the ink. When adding in the MIP particles the surface roughness changes clearly showing the particles present on the surface of the electrode (Figure 6-6B). There results were obtained using MIP-32 on a polyester substrate, and similar results were seen on tracing paper, paper and PVC. MIP-1 was integrated into the caffeine SPEs despite MIP-3 having a slightly higher IF value. The reason for this is that MIP 3 contained acrylamide derived structural units that may have, resulted in a less successful mixture with the graphite ink. MIP-5 was also incorporated into SPEs but resulted in a lower thermal resistance compared to MIP-1. A further optimization of the ratio of the different monomers in the MIPs could be beneficial and further increase the loading ratio of the ink.

Previous work by Geerets *et al.* showed the importance of optimizing the PID feedback loop in order to enhance the limit of detection of the sensor platform [36]. Therefore, optimization of the PID settings was performed for all substrates (with

noradrenaline MIP-modified SPEs) and all temperatures (for caffeine MIP-modified SPE). It was found that a PID of 1, 10, 0, had the lowest S/N ratio for all four substrates (at 37 ± 0.02 °C) used to fabricate the noradrenaline MIP-modified SPEs. For caffeine a PID setting of 1,8,0 was found to give the lowest S/N ratio over all investigated temperatures. These settings were fixed for all further measurements.

6.4.2.1.   HTM measurements on noradrenaline

The increase in thermal resistance upon exposure of MIP-modified SPEs to a 1 mM noradrenaline aqueous solution (pH=6) was determined for electrodes printed onto different substrates (Table 6-5). The average R_{th} value (50 point) of a stable baseline and that in the presence of noradrenaline were used to determine the effect size per electrode. The response was defined as the percentage increase from baseline to the thermal resistance when the signal had stabilized after injection of noradrenaline.

Table 6-5. The thermal response of the different substrate of noradrenaline MIP-modified SPEs [91].

SPE substrate	R_{th} value (°C/W)		Response (%)
	Stabilization	1 mM noradrenaline	
Polyester	3.83 ± 0.02	4.83 ± 0.03	26
Paper	3.61 ± 0.04	4.62 ± 0.03	28
Tracing paper	3.8 ± 0.1	4.3 ± 0.1	13
PVC	4.12 ± 0.03	4.93 ± 0.03	20

The difference in the R_{th} values upon stabilization between the different electrodes in Table 6-5 was due to substrate thickness (listed in Table 6-6) and thermal conductivity (Table 2-2). The paper-based electrodes tended to absorb water and this significantly increased mass (Table 6-6).

Table 6-6. Thickness and weight of SPE substrates before (dry) and after (wet) soaking into distilled water [91].

SPE substrate.	Thickness (µm) Dry	Weight (mg) dry	Thickness (µm) Wet	Weight (mg) Wet
Paper	280	19	310	43
Tracing paper	132	8	152	65
PVC	370	44	370	45
Polyester	406	31	406	35

After soaking the electrodes in distilled water for 30 min no significant water uptake was observed for the PVC and polyester electrodes, however the mass of the tracing paper electrode increased eight fold (Table 6-6). This led to deformation of the SPE, which in turn caused significant increase in the noise of the signal, making them unusable for further measurements. In contrast, electrodes printed on paper showed good stability, are water-compatible and had the highest effect size. The results of the full measurement, including stabilization, two additions of noradrenaline (1 mM in aqueous solution), with an intermediate PBS washing are shown in Figure 6-7.
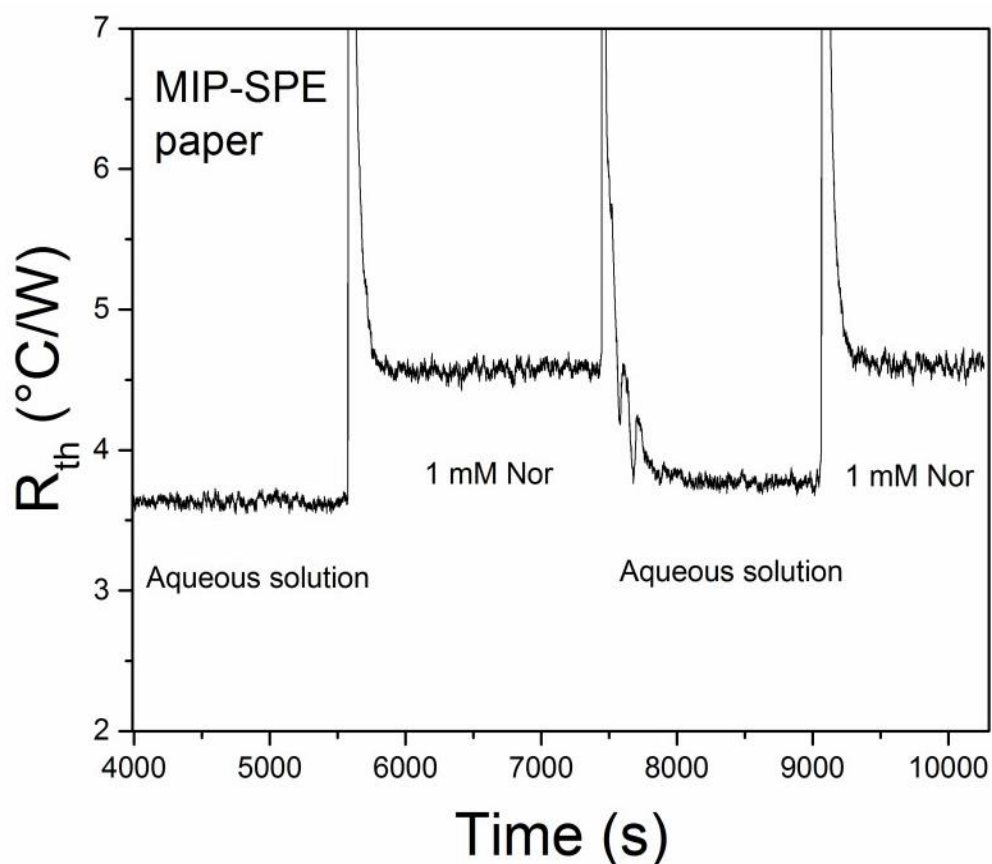
Figure 6-7. Thermal resistance of the paper MIP-modified SPE. A clear difference between stabilization and a 1 mM aqueous noradrenaline solutions is shown, as well as the intermediate washing step between the additions.

After 1 h stabilization in aqueous medium, the signal of MIP-modified SPE (printed on paper) stabilized to a R_{th} value of 3.61 ± 0.04 ˚C/W. Upon the addition of an aqueous noradrenaline solution, the signal increased to 4.62 ± 0.03 ˚C/W, corresponding to a 28 % increase. The signal decreased during the following water washing step to 3.83 ± 0.4 ˚C/W, which is above the original baseline indicating that there is residual noradrenaline bound in the MIP. In order to fully remove the strongly retrained noradrenaline, the washing period either needs to be extended or an organic solvent such as ethanol can be used to interfere with the interactions between target and polymer. After a second exposure of the MIP-modified SPE printed on paper to the 1 mM noradrenaline solution, the signal returned to 4.65 ± 0.03 ˚C/W. This indicated that these sensors are potentially re-usable. Due to their advantageous material properties and high thermal response, MIP-modified SPEs printed onto paper were used for al further experiments.

Measuring the noradrenaline on MIP-modified SPEs in distilled water will be a more accurate representation of pharmaceutical applications. As was done on HTM and TWTA, by fine tuning of the PID settings and reductions of environmental influences the stability was increased enough to compete with measurements performed in buffered solutions.

For each measurement, the electrodes were soaked for 30 min in distilled water, mounted in the set up and thereafter stabilized in distilled water for 1 h. Subsequently, a concentration range (0, 0.5, 1, 2.5, 5, 10, 25 mM) of noradrenaline solutions were added to the flow cell. Upon stabilization of the thermal signal after each addition, a sinusoidal modulation of linear temperature ramps (amplitude of 0.1 °C) was applied from the heat sink to the MIP-modified SPE (Figure 6-8). NIP-modified SPEs were used to determine the specificity of the system whilst performing identical experiments. The selectivity of the system was demonstrated by examining the response of the MIP-modified SPE to the competitor molecule adrenaline.

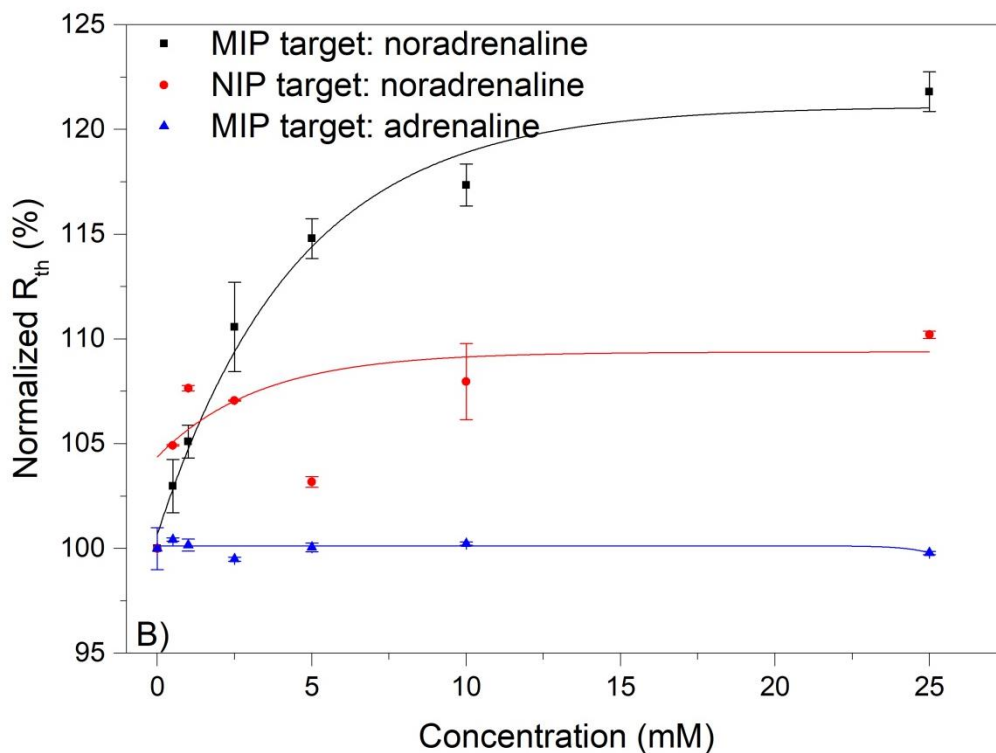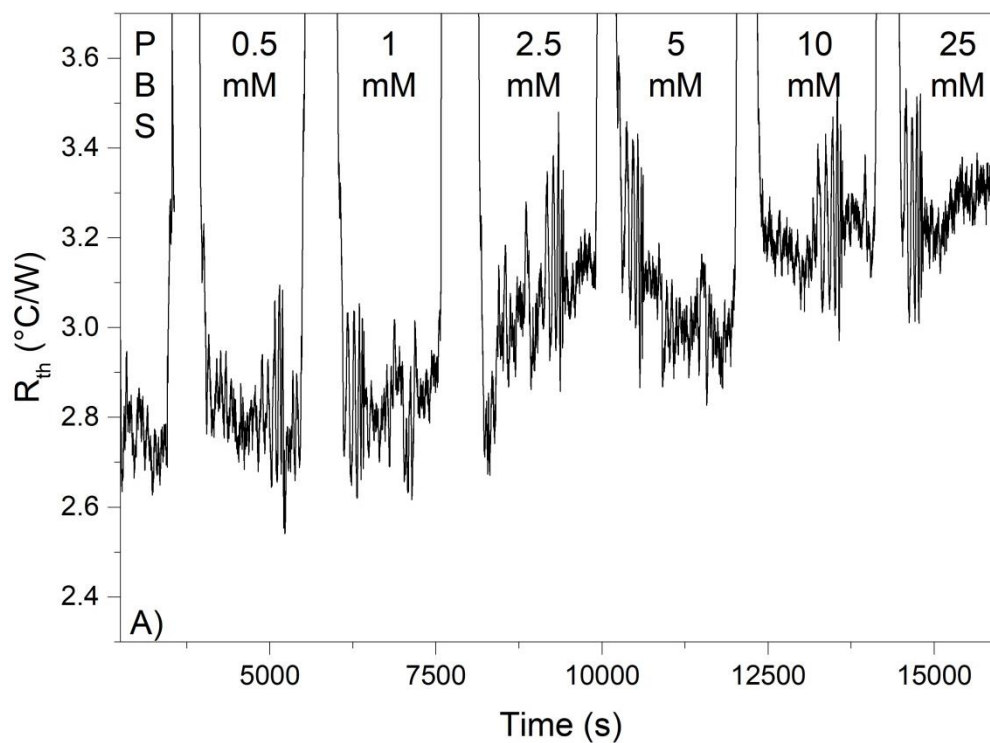Figure 6-8. a) Represents the thermal response of the paper based MIP-modified SPE upon the exposure to increasing concentrations (0, 0.5, 1,2.5, 10 and 25 mM) of aqueous noradrenaline solutions. b) Shows the HTM dose-response curves (R^2 = 0.98) for the MIP-modified SPE exposed to solutions of noradrenaline and adrenaline, (red circles represent the NIP-modified SPE upon the exposure to noradrenaline solutions).

116

A minimum of 50 points were used to calculate the average of the thermal signal for each concentration in Figure 6-8A, which were then used to construct a dose-response curve for the MIP-modified SPE. Similar experiments were performed with an NIP electrode and a competitor molecule (adrenaline) on the MIP-modified SPE. For the adrenaline experiment no response could be obtained while for the NIP exposed to noradrenaline some binding was detected, however no dose response curve could be fitted to the data (R^2 <0.5). The normalized dose response curves for each of these combinations are displayed in Figure 6-8B. The distinct patterns at 4800 s, 6000 s, 9000 s, 10200 s, 13200 s, and 14400 s originate from the thermal wave that was applied to the heat sink after each addition. The thermal wave on the base line was conducted at 1800 s and is therefore not shown on the graph in order to show the overall stability of the signal.

The MIP-modified SPE stabilized to a R_{th} value of 2.75 ± 0.04 ˚C/W in water, which was lower than the thermal resistance values obtained during the screening of the different substrates (3 - 4 ˚C/W). The reason for this is that these experiments were performed in PBS buffer, which has a different thermal conductivity to distilled water. The increase in thermal resistance with each addition corresponds with binding of the noradrenaline to the MIP layer. The selectivity of the system is proven by exposing the MIP-modified SPEs to adrenaline, and the specificity was verified using a NIP-modified SPE was exposed to noradrenaline.

The thermal resistance increased to a maximum of 3.22 ± 0.02 ˚C/W at the highest concentration (25 mM), corresponding to a percentage increase of 17 %. However, at this concentration the sensor was performing outside of the linear range that was observed up to 2.5 mM. Assuming that at a linear relationship exists at low concentrations the LOD was calculated to be approximately ~ 270 µM, which is a similar concentration when it is used as a drug (40 mg/L) for treatment of low blood pressure in emergency situations.

6.4.2.2.   TWTA on noradrenaline

During the application of a thermal wave, a time delay between T_1 and T_2 is recorded. This delay depends on the thermal conductivity of the electrode surface and can be seen in Figure 6-9. The thermal conductivity of the MIPs depends on the amount of target bound, and decreases when more target specific pores are blocked

due to binding of the target. This results in a decrease of the response time between the copper heat sink and T_2 in case of a temperature change, such as a thermal wave.
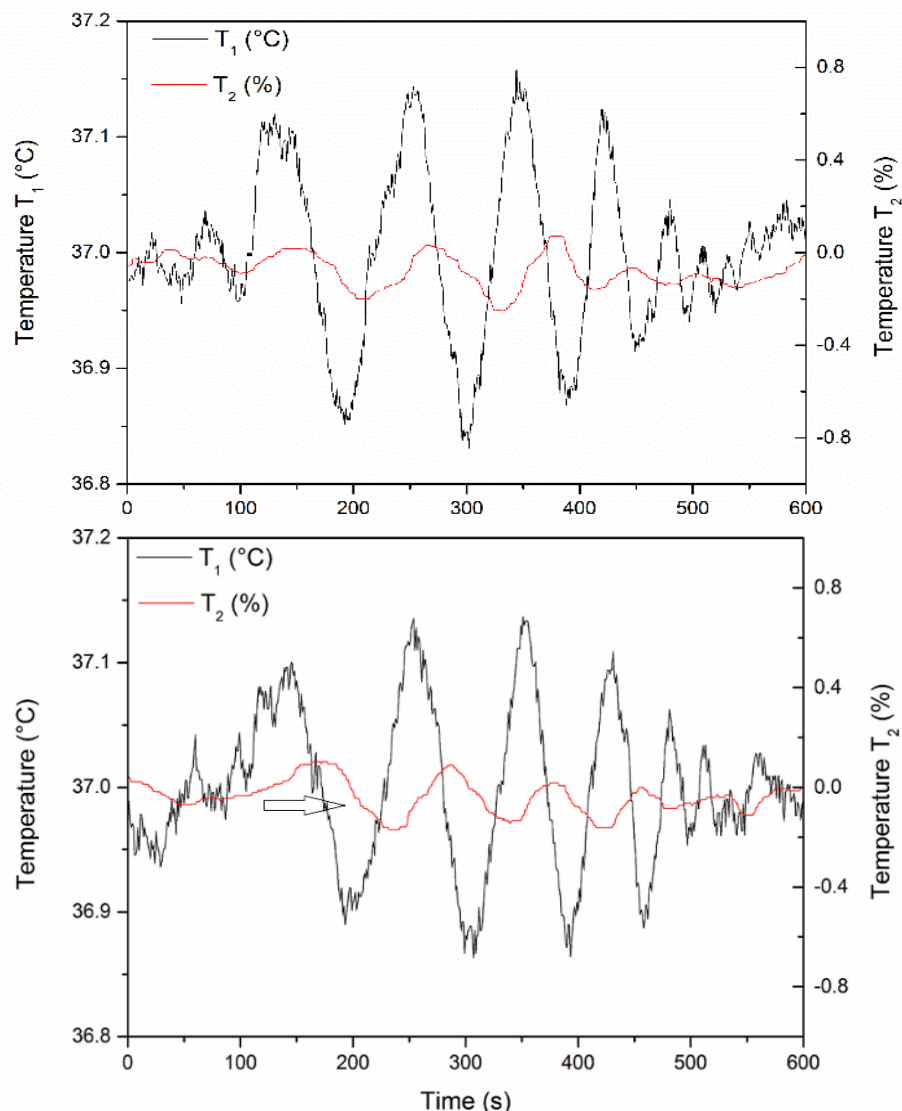
Figure 6-9. The length of one full thermal wave, which shows the different frequencies of the thermal wave. The top panel is the thermal wave at the baseline, whilst the bottom panel shows the output at a noradrenaline concentration of 10 mM.

The frequency range that can be applied to the system varies between 0.008 and 0.05 Hz and depends on the thermal mass of the copper block as has been reported by van Grinsven *et al.* [28]. Figure 6-9 shows the application of a full thermal wave over all frequencies. When comparing a thermal wave applied at base line (Figure 6-9 Top) to that with the MIP-modified SPE exposed to a 10 mM noradrenaline solution (Figure 6-9 Bottom), a phase shift was observed as indicated by the arrow.

118

The time delay at each frequency was recorded for each noradrenaline concentration, resulting in a dose response curve. Figure 6-10 shows dose response curves for the input frequencies of 0.03, 0.04 and 0.05 Hz.
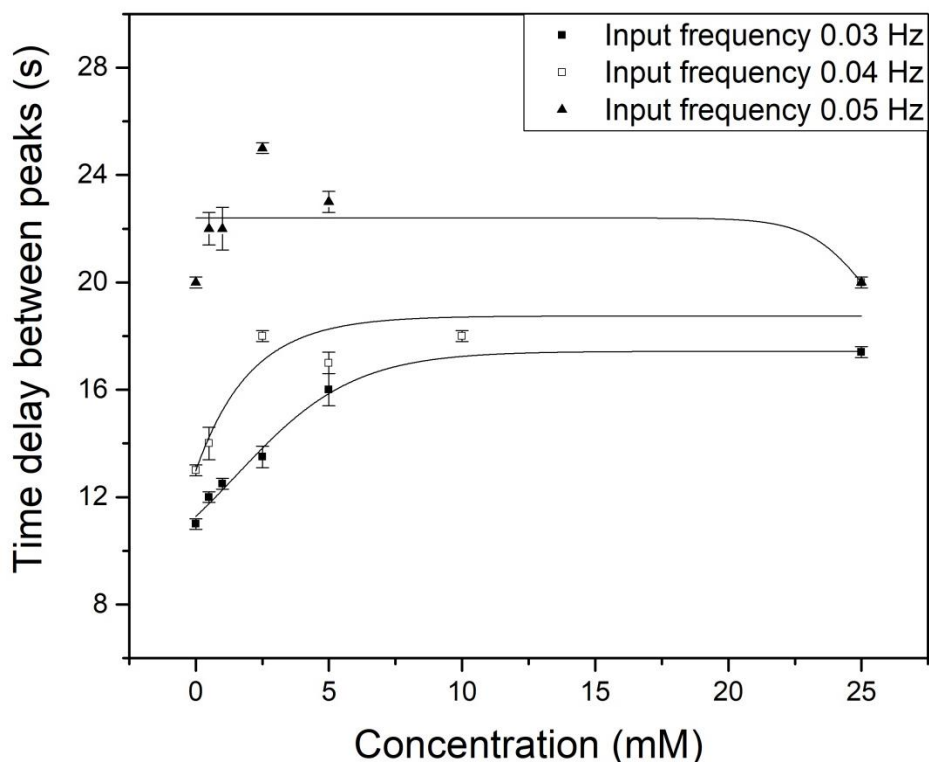
Figure 6-10. The time delayed response for the paper based MIP- modified SPE at input frequency 0.03, 0.04 and 0.05 Hz upon the exposure to aqueous noradrenaline solutions with increasing concentrations (0, 0.5, 1, 2.5, 10 and 25 mM). The trend lines show that only the 0.03 Hz follows the dose response fit (R^2 = 0.98)

An increase in the time delay was observed at each frequency when MIP-modified SPEs were exposed to solutions with noradrenaline concentrations of 0.5 mM and higher. A dose response curve was fitted to each input frequency and resulted in a high correlation (R^2 = 0.98) fit at 0.03 Hz. The delay in seconds was then converted into a phase shift by using the whole length of the signal as one wave. For example, a delay of 18 s was found when exposing the MIP-modified SPE to a 10 mM noradrenaline solution at an input frequency of 0.03 Hz, this corresponded to a phase shift of 72 ± 2˚. The baseline normalized results are represented as a dose-response curve (Figure 6-11). From these curves the linear regime of the sensor was determined to be in the range of 0-10 mM, before reaching saturation. The limit of detection slightly improved compared to HTM and was estimated to be ~230 µM.

The TWTA protocol showed a similar selectivity of the sensor towards noradrenaline as was found during standard thermal measurements, as no significant effects on the thermal response were observed when solutions of adrenaline and dopamine were injected into the set-up.
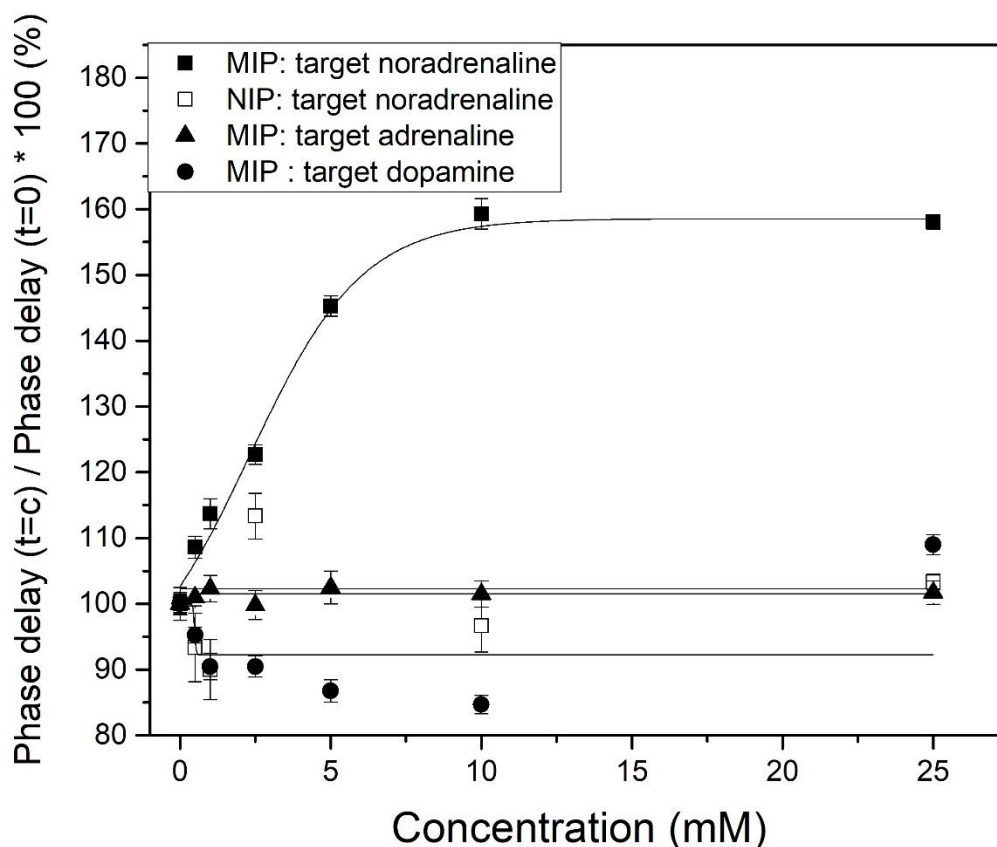
Figure 6-11. Shows the phase shift of the normalized TWTA dose-response curves (at input frequency 0.03 Hz) for MIP and NIP-modified SPEs exposed to increasingly concentrated solutions of noradrenaline, adrenaline and dopamine. The dose response curve for the MIP with noradrenaline has a high correlation (R^2 = 0.99) while for the other solutions no fit was obtained.

To demonstrate the potential of the sensor platform in a clinical setting it was deemed necessary to include measurements in neutral and buffered solutions. Therefore, ascorbic acid was added as an anti-oxidant ensuring the stability of catecholamines in solutions. Using these PBS buffered solutions the TWTA signal was obtained as is shown in Figure 6-12A for the time delayed response and the phase shifted dose-response curve (Figure 6-12B).
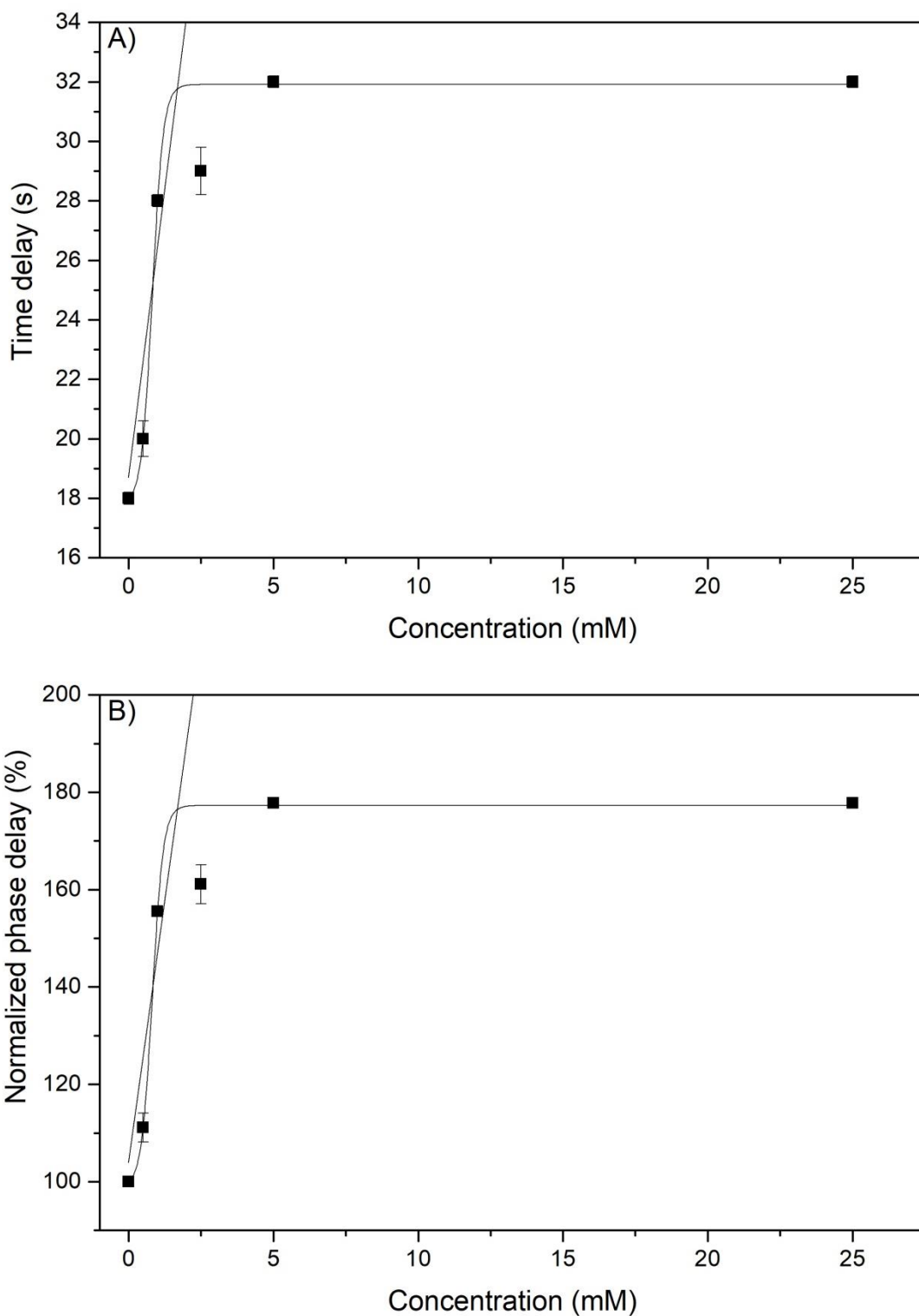
Figure 6-12. TWTA response for the paper based MIP-modified SPE at an input frequency of 0.02 Hz, using PBS buffered solutions with increasing concentrations of noradrenaline (0, 0.5, 1, 2.5, 10 and 25 mM) and ascorbic acid. A) Shows the time delayed response, B) shows the phase shifted response. the error bars represent the noise on the signal, and both a dose response curve (R^2 =0.99) and a linear fit (R^2 = 0.75) are preformed

The stability of noradrenaline in a buffered solution was guaranteed by the addition of ascorbic acid to the solution. Saturation of the sensor occurred when the MIP-modified SPE was exposed to a solution of 5 mM noradrenaline and the LOD was estimated to be around ~350 µM. This indicates that the sensor can be used for buffered and biological samples since the dynamic range is comparable to measurements performed in aqueous solutions.

6.4.2.3.   Thermal measurements on caffeine

During the analysis of noradrenaline with the HTM the temperature of the copper heat sink was kept constant at 37 ± 0.02 °C. This was done to mimic body temperature and to prevent thermal degradation, which occurs at higher temperatures for most biological components. Caffeine is stable up to about ~ 200 °C as can be seen in the Thermogravimetric analysis in Figure 6-13.
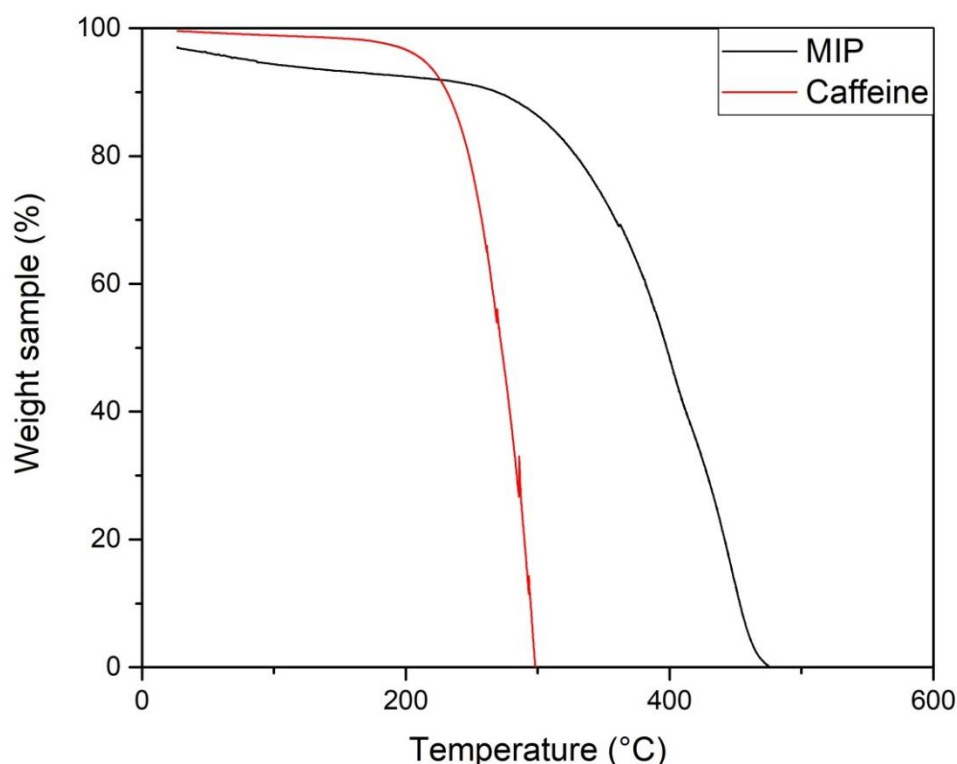
Figure 6-13. TGA for caffeine and the corresponding MIP. For both components weight loss is not observed before ~200˚C, indicating the thermal stability for the MIP and caffeine during a measurement at a temperature of 85 ± 0.02 °C.

One of the advantages of MIPs is their thermal stability at higher temperatures, as is the case for the MIPs developed for caffeine. There is no significant loss of mass when the particles are heated to about ~ 250 °C (Figure 6-13), well above that of caffeine and the applied temperatures during the current analysis.

The efficiency of the PID feedback loop depends on the temperature that needs to be maintained. Initial optimization of the system was performed at 30 ± 0.02 °C, resulting in PID settings of 1, (7, 8) and (0, 0.1), respectively. The percentage error for all configurations was determined to be ~2 %, which is a factor of two higher compared with the settings used for noradrenaline at 37 ± 0.02 °C. Therefore, the sensor platform was deemed not suitable for the detection of caffeine at lower temperature. By measuring the same PID settings at 50, 70 and 90 ± 0.02 °C, respectively the S/N ratio can be examined (Table 6-7).

Table 6-7. Shows the different PID settings and the corresponding noise levels for each temperature of interest. The R_{th} values and standard deviation (SD) were determined over at least 600 datapoints points [44]. The * indicates the settings with the lowest noise.

P	I	D	T	R_{th}	SD	%-error (noise)
			°C	°C/W	°C/W	%
1	8	0.0	30	6.97	0.14	2.00
			50	5.79	0.04	1.00
			70	5.47	0.02	0.40 *
			90	4.71	0.05	1.00
		0.1	30	7.31	0.13	2.00
			50	5.91	0.04	1.00
			70	5.40	0.02	0.40 *
			90	4.79	0.02	0.40 *
	7	0.0	30	6.91	0.14	2.09
			50	5.08	0.03	0.68
			70	4.58	0.02	0.45
			90	4.55	0.04	0.95
		0.1	30	6.93	0.15	2.15
			50	5.33	0.04	0.72
			70	4.81	0.02	0.47
			90	4.74	0.03	0.56

The noise on the signal decreased at higher temperatures (Table 6-7). The lowest value of 0.40 % was attained with PID settings of 1, 8, (0 and 0.1) at a temperature of 70 ± 0.02 °C. This decrease in the noise with increasing temperatures was expected for such a feedback loop as it is easier to control larger differences in temperature. A further increase from 70 to 90 ± 0.02 °C did not lead to a further reduction on the noise. This could be due to increased thermal flow of the PBS solution, causing fluctuations in the acquisition of the temperature. In an attempt to optimize the balance between the thermal flow and the noise one additional measurement at 85 ± 0.02 °C was performed using the MIP and NIP-modified SPEs resulting in a decrease of the noise level to ~ 0.3 % using PID settings of 1, 8, 0. The PID settings and maximum temperature were therefore fixed to these values for all further experiments.

First, a reference was established by exposing a NIP-modified SPEs (T = 85 °C) to PBS solutions with varying caffeine concentrations (0-250 nM). None of the additions led to a significant increase of the thermal resistance indicating that no specific binding of caffeine to the NIP layer occurred (Figure 6-14). Subsequently, the response in thermal resistance was obtained at 37, 50 and 85 ± 0.02 °C by exposing the MIP-modified SPEs to identical PBS solutions with increasing caffeine concentrations. After each addition of PBS solutions with caffeine to the flow cell, a clear increase in the thermal resistance was observed (Figure 6-14A). Upon stabilization after each addition, an average R_{th} value was calculated using 600 data points. This was normalized to the baseline signal and converted to the corresponding dose response curves (Figure 6-14B).
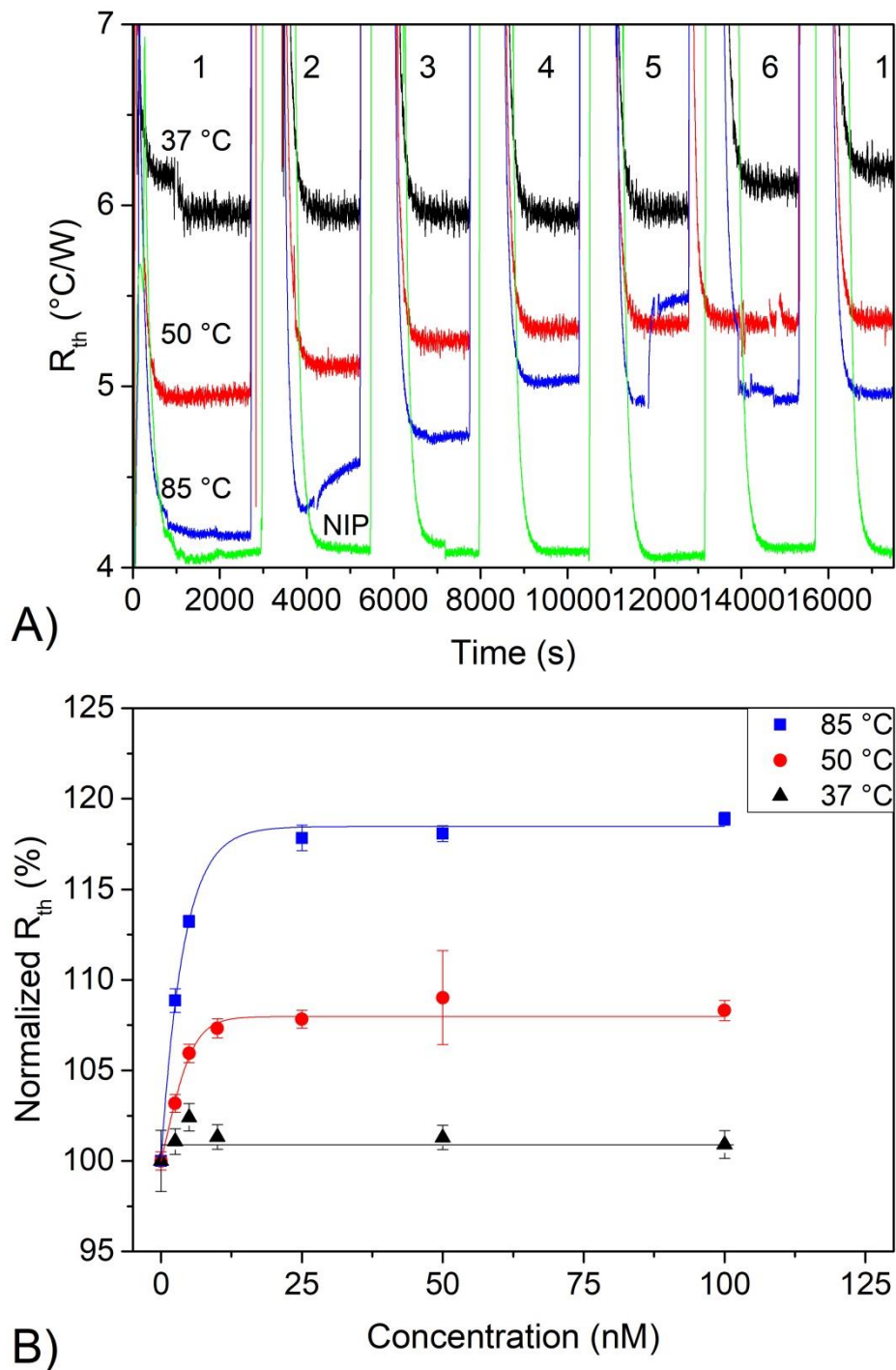
Figure 6-14. Calibrating the setup for Caffeine. A) demonstrates the thermal resistance over time at T = 37, 50 and 85 ± 0.02 °C for the MIP-modified SPEs at 85 ± 0.02 °C and for the NIP-Modiefied SPE. the initial stabilization is performed in PBS (1). The numbers (2-6) correspond with increasing concentration of caffeine (0, 2.5, 5, 10, 25, 50, 100 nM). B) shows the normalized HTM dose-response curves fitted for the MIP (R^2 of 0.99, 0.99 and 0.98 for 85, 50 and 37°C respectively), with the errorbars represent the standard deviation.

The decrease in thermal resistance at a higher measurement temperature was due to a lower temperature difference between T_1 and T_2. The baseline values clearly showed this reduction from 5.8 ± 0.05 °C/W at 37 °C, to 4.95 ± 0.03 °C/W at 50 °C, and a further reduction to 4.17 ± 0.02 °C/W at 85 °C. These results corresponded with the reduction of the noise levels observed during fine tuning of the PID. The sensitivity of the system is therefore also dependent on the measurement temperature; at 37 ± 0.02 °C minimal changes were observed below 50 nM, an increase was seen at 5 nM at 50 ± 0.02 °C, whilst for 85 ± 0.02 °C this was the case at 2.5 nM. When looking at the effect size at 100 nM, the sensitivity was even more pronounced; at 37 ± 0.02 °C the effect size is 1%, increasing to 8 % at 50 ± 0.02 °C and 19 % at 85 ± 0.02 °C. Limits of detection were estimated as three times the standard deviation on the signal and varied from ~40 nM (37 ± 0.02 °C) to ~10 nM (50 ± 0.02 °C) and <1 nM (85 ± 0.02 °C). Indicating that the LOD can be fine-tuned by changing the temperature. Trace amounts in drinking water could be detected at 85 ± 0.02 ºC, whilst at 37 ± 0.02 °C there is potential to determine caffeine levels in food. The results obtained in this study compare favourably to other methods reported in literature, a sample of which are shown in Table 6-8.

Table 6-8. An overview of various detection methods for caffeine in literature along with the corresponding detection limits [44].

Method	Recognition Element	Electrode Material	Sample	LOD x10^{-8}M	LOQ x10^{-8}M	Ref
DPV	Bismuth film	SPE	Beverages / Coffee	2.7	9.0	[267]
DPASV	Graphene/ nafion	SPE	Beverages /Coffee	2.1	6.6	[268]
DPV	MIP	Carbon paste	Beverages / Tea	1.5	-	[269]
SLM-PZ	MIP	Au	Coffee/ Tea	2.8	-	[270]
Thermal	MIP	SPE	Coffee/ Tea	0.1		This Work [156]

Abbreviations: DPV (Differential Pulse Voltammetry), DPASV (Differential Pulse Anodic Stripping Voltammetry) and SLM-PZ (supported liquid-membrane piezoelectric).

Next, the selectivity of the sensor platform was evaluated at 85 ± 0.02 °C. The MIP-modified SPEs was exposed to a 1 mM solutions of theophylline, dopamine and theobromine these components are similar in chemical structure or biological function (Figure 6-15).
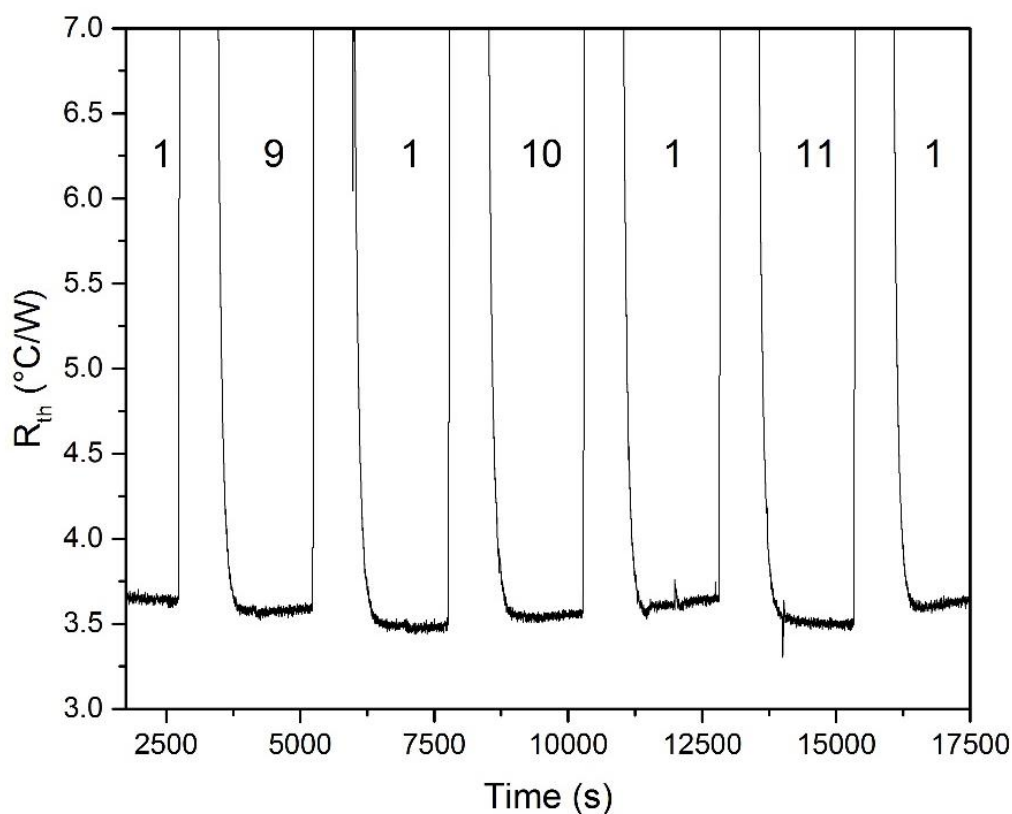
Figure 6-15. Demonstrates selectivity of the system at 85 ± 0.02 °C. The MIP-modified SPEs were stabilized in PBS (1), followed by addition of 1 mM in PBS solutions of either theophylline (9), dopamine (10) or theobromine (11). The loosely boud molecules were washed away with intermediat washing steps with PBS (1).

The baseline in PBS stabilized to a signal of 3.62 ± 0.03 °C/W, and on the addition of a 1mM theophylline PBS solution no significant differences in thermal resistance were observed. The electrodes were washed with PBS in between the steps, followed by the additions of high concentration solutions of either dopamine or theobromine. The addition of any of these compounds did not result in a significant change of the R_{th}. This demonstrates the high selectivity of the system, as was found with the batch rebinding experiments. When determining the concentration of caffeine in the presence of an excess of theophylline (250 nM) the detection was significantly influenced as can be seen in Figure 6-16.
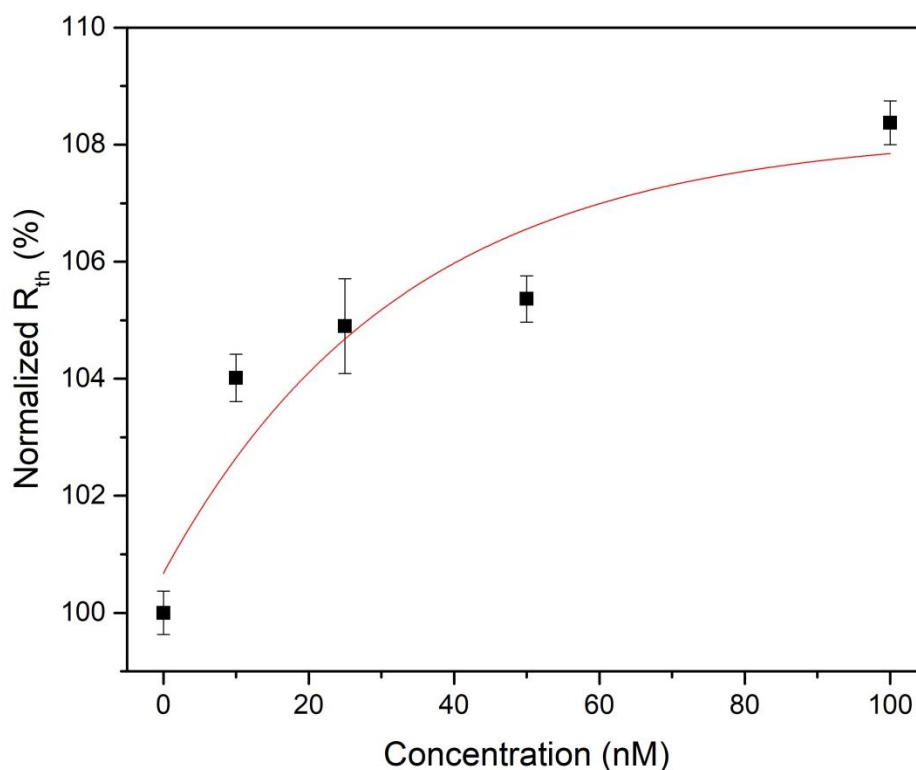
Figure 6-16. The normalized dose response curve on a MIP-modified SPE (T = 85 ± 0.02 °C) using a PBS solution containing an excess of theophylline (250 nM). The response is obtained for varius caffeine concentrations (0-100 nM), resutling in a maxium increase of 8.5 %. The error bars are represent te standard deviation on at least 225 datapoints.

The effect size at 100 nM reduced from 19 % to 8.5 %. When comparing to PBS this is a factor of two lower, however there was only a minimal impact on the LOD (3-5 nM). The selectivity of the system has been demonstrated with a molecular similar component (theophyline), this clearly demonstrats the ability to perform measurements in the presence of contaminants.

To evaluate the proof-of-application of this sensor platform, more complex sample mixtures, such as coffee and tea samples were investigated. Therefore, MIP-modified SPEs stabilized in PBS after which dilutions of instant coffee (containing 2 % caffeine according to the manufactures label) in PBS were added. Figure 6-17 shows the results of these experiments at 50 and 85 ± 0.02 °C. The response at 37 ± 0.02 °C was not significant and is therefore omitted from the graph.
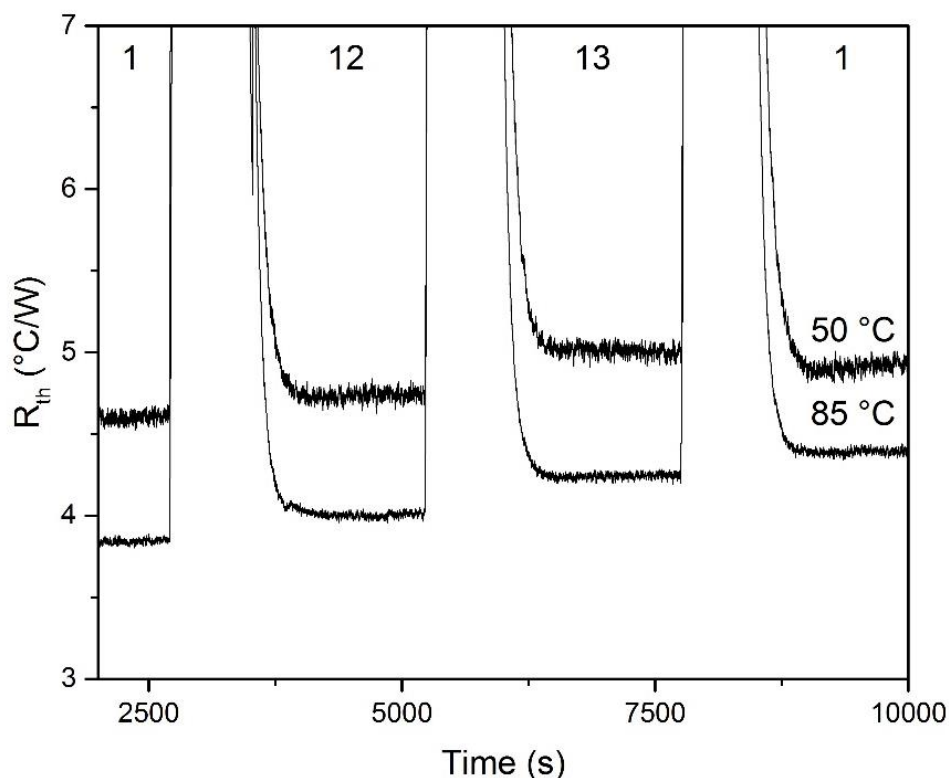
Figure 6-17. The thermal resistance at 50 ± 0.02 °C (top trace) and 85 ± 0.02 °C (bottom trace) on the MIP-modified SPE for coffee solutions. Initial stabilization in PBS (1) was followed by additions of diluted instant coffee samples in PBS with an estimated caffeine concentration of 1 μM (12) and of 37 μM (13).

The signal at 50 ± 0.02 °C stabilized at 4.6 ± 0.2 °C/W in PBS and increased to ~5.0 ± 0.2 °C/W (8.7 % increase) when exposed to a mixture of PBS and coffee containing approximately 37 μM of caffeine. The effect size at 85 ± 0.02 °C was ~21 %, which was similar to that measured at the highest measurable concentration (100 nM) before saturation in a buffered solution. Quantification of caffeine levels above the linear range are complicated, but this serves as proof-of-concept for measuring complicated samples such as beverages.

Diluted tea samples were examined next, here for a 1/100 and 1/10 dilutions in PBS were made. These experiments were performed in duplicates (with minimal variation 0.5 %) at both 37 and 85 ± 0.02 °C to highlight the effect of measurement temperature (Figure 6-18
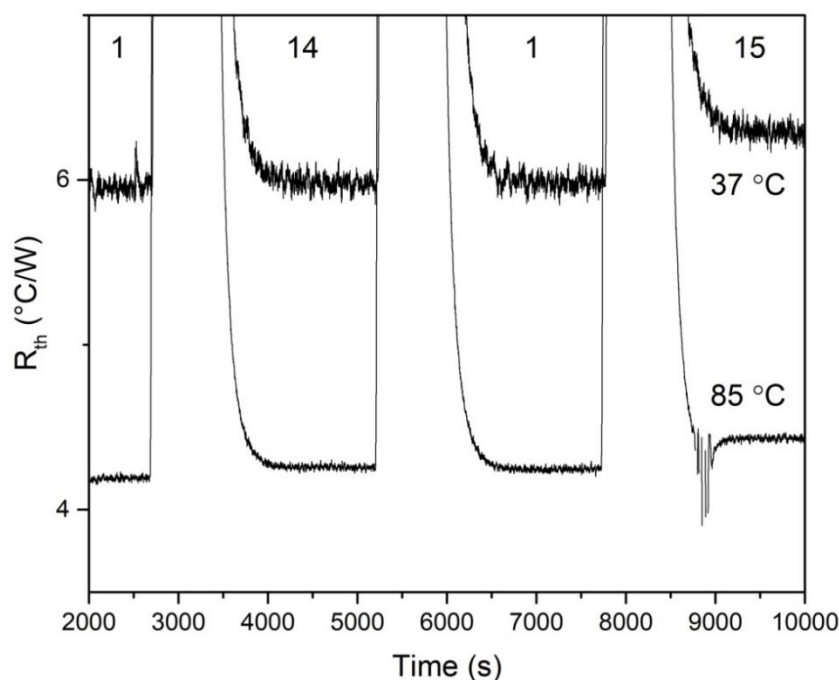
Figure 6-18. MIP-modified SPEs exposed to diluted tea samples measured at 37 (top) and 85 ± 0.02 °C (bottom). After stabilization in PBS (1) a 1/100 in PBS diluted tea sample (14) was added, followed by a washing with PBS (1) and subsequent addition of (15) a more concentrated tea (1/10 in PBS) solution.

Stabilization of the thermal resistance occurred at 6.0 ± 0.1 °C/W (37 °C), and showed a significant increase on the addition of the 1/100 tea vs. PBS sample. However, an increase in the thermal resistance of 4.2 % to 6.2 ± 0.1 °C/W was measured for the addition of the 1/10 tea *vs.* PBS. Repeating the experiment at 85 °C, led to a stabilization of the thermal resistance at 4.20 ± 0.02 °C/W, which was in line with previous results (Figure 6-14). A minor but significant increase of the signal to 4.25 ± 0.02 °C/W was detected on the addition of a 1/100 tea sample. According to the dose-response curve constructed at this temperature, this increase corresponds to a ~1 nM concentration of caffeine. The signal increased by 6.7 % (4.46 ± 0.02 °C/W) when measuring the 1/10 dilution of tea. However, caution is advised as these dose-curves were obtained using in buffered solutions, and competitor molecules will be present in the tea sample that could affect the binding thereby resulting in an over estimation of the actual concentration of caffeine.

The effect of the mixture on the detection of caffeine was examined further by spiking tap water and Digestate samples. The samples were spiked with caffeine in the range of 0 to 100 nM and measured at 85 ± 0.02 °C. The results for the spiked

waste water samples on the MIP and NIP sensors are shown Figure 6-19a. The dose-response curves obtained for all these mixtures are depicted Figure 6-19b.
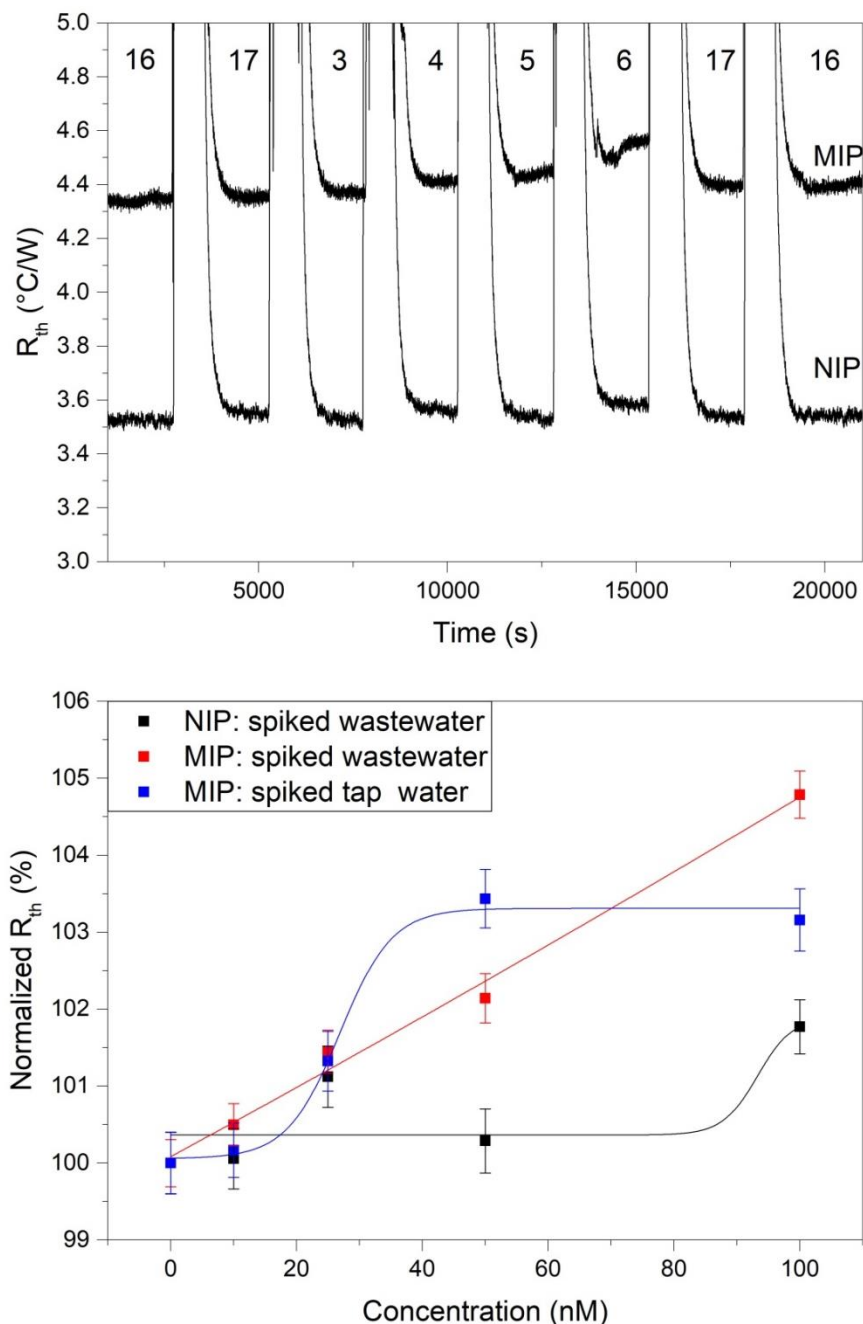
Figure 6-19. Thermal response of MIP and NIP-modified SPEs at 85 ± 0.02 °C using waste water. A) Raw thermal response data, after stabilization in Milli-Q water (16) wastewater was added (17), followed by spiked wastewater samples. B) The corresponding dose-response curves for MIP (red) and NIP (black) in spiked wastewater samples. The blue squares represent the dose response obtained from spiked tap water samples. The error bars represent the normalized standard deviation on at least 180 data points.

The thermal resistance stabilized at 3.5 ± 0.1 °C/W at 85 ± 0.02 °C for the NIP-modified SPE and at 4.3 ± 0.1 °C/W for the MIP-modified SPE. When comparing the noise on the signal for caffeine solutions in mixtures (0.03 °C/W) to those in PBS (0.1 °C/W) an increase with a factor of three was noticed. From this, it was shown that the matrix has an influence on the electrodes. Upon the addition of a 25 nM caffeine or higher, spikes sample the thermal resistance showed a significant increase. On the exposure of a 100 nM spiked solution, increases of ~ 5 % in wastewater and 3% in tap water were observed for the MIP electrodes, whilst the NIP electrode give an increase of only ~2 %. The response of the MIP is at least 1.5 times higher than the NIP in tap water and 2.5 times in wastewater samples, this is still sufficient for the detection of caffeine but greater sensitivity is possible in buffered conditions. The signal increase of the NIP in PBS was only 0.25 %, indicating fouling of the NIP-modified electrode surface by contaminants in the water. Microorganisms could adhere to the electrode surfaces and thus cause the observed increase in R_{th}. Therefore, it is recommended that for sensing purposes both MIP and NIP electrodes are measured simultaneously to establish an appropriate reference. Whilst the sensor performance was reduced relative to the buffered solutions, measurements resolution in the low nanomolar range is never the less possible, therefore, demonstrating a proof-of-application for these sensor platforms. The sample pre-treatment was minimal and additional filtration of the wastewater sample before the measurement can boost the level of detection.

Finally, the re-usability of the sensor set up was evaluated (Figure 6-20), demonstrating that washing with PBS was not sufficient to regenerate the sensor platform after the exposure to high concentration solutions of caffeine. This observation indicates that the MIP layer has a high affinity for caffeine.
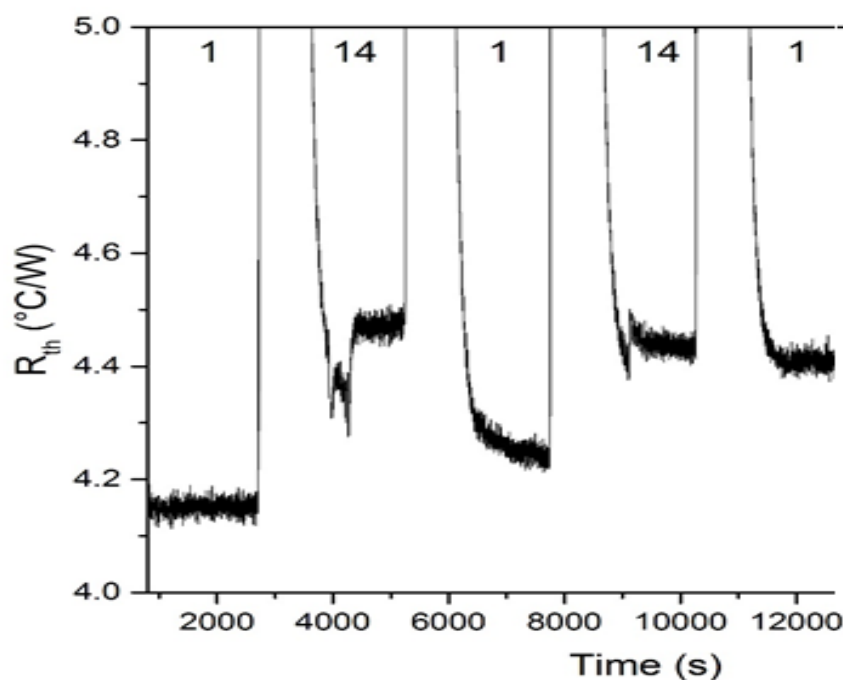
Figure 6-20. The MIP-modified SPE measured at a temperature of 85 ± 0.02 °C with alternating injections of PBS (1) and 2.5 µM caffeine in PBS (14). The binding of caffeine to the MIP was to strong to overcome with just washing.

Organic solvents such as ethanol, introduced at a low flowrate, could be a better alternative for regeneration of the SPEs, however previous experiments revealed cracks in the polymer-based flow cell. As the SPEs are low-cost (£0.10 or less for electrodes printed in-house) regeneration the sensor platform would be more expensive than use of a freshly prepared electrode. The low traces of caffeine present in most environmental samples would potentially require a high flow rate with PBS for regeneration to be effective.

6.4.3. TWTA results for caffeine

The TWTA protocol was only used at 37 ± 0.02 °C during the detection of noradrenaline and dopamine and resulted in comparable LODs as recorded for HTM [28, 39]. Here, it was demonstrated that a thermal wave with an amplitude of 0.1 ± 0.02 °C can be applied around the set point of 85 °C for MIP-based sensor platforms. However, the higher base-line temperature necessitated reassessment of the input frequencies. Therefore, the input frequency was altered between 0.0083 Hz and 0.05 Hz and was applied 17 minutes before the injection of different concentrations of caffeine. Figure 6-21A shows the time delay between input and registration in the liquid for every input frequency and concentration. An input frequency of 0.017 Hz

showed the most effective response when measuring at 85 ± 0.02 °C, and was subsequently converted to a phase shift. Figure 6-21B was constructed by normalizing the phase shift to the baseline, resulting in the corresponding dose-response curve.
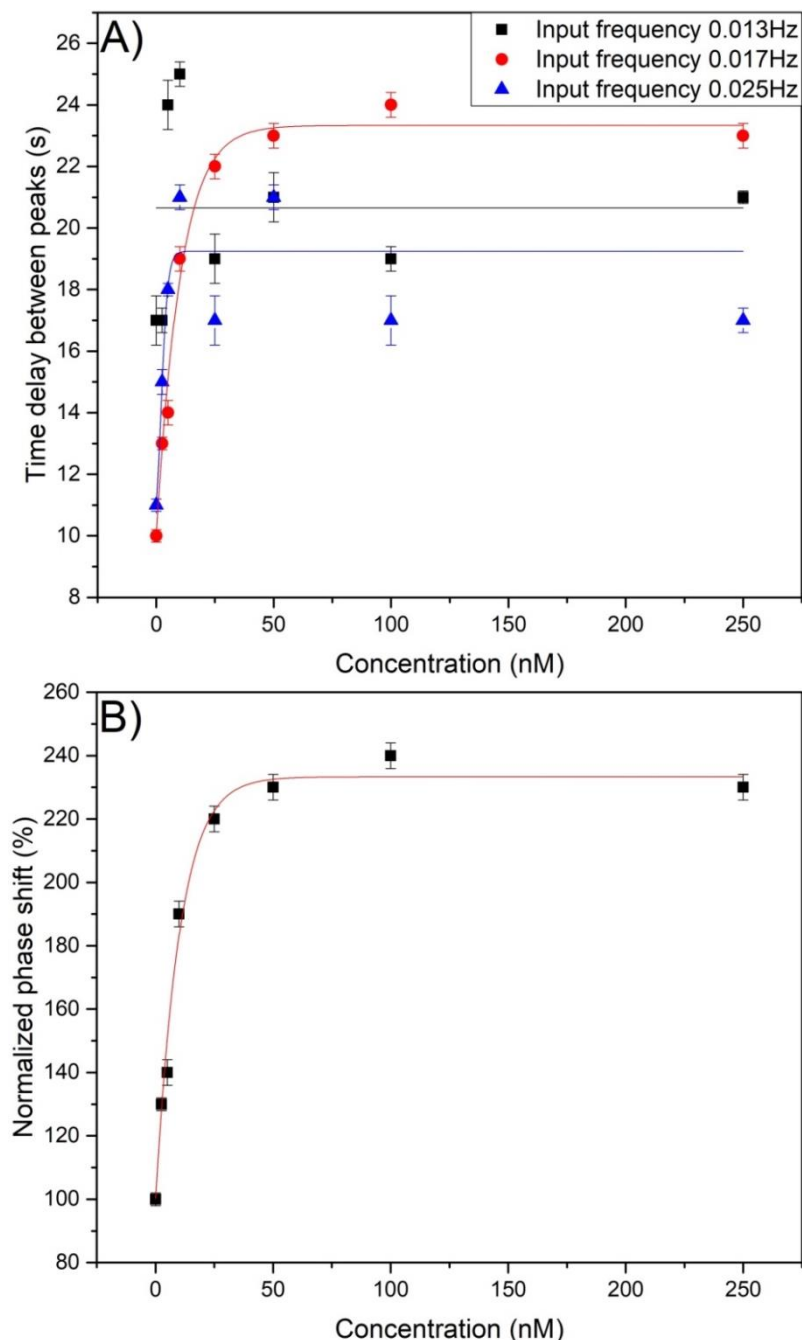
Figure 6-21. A) The time shifted dose response at input frequencies of 0.013 (black squares) not fitted, 0.017 (red circles) ($R^2 = 0.99$) and 0.025 Hz (blue triangles) ($R^2 = 0.95$), measured at T = 85 ± 0.02 °C for a range of caffeine concentrations (0, 2.5, 5, 10, 25, 50, 100 and 250 nM). B) The normalized TWTA dose-response curve ($R^2 = 0.99$) for caffeine at the optimum frequency of 0.017 Hz. Error bars represent the standard deviation from at least 100 data points.

On the input frequency of 0.017 Hz, a linear range for the dose-response curve was found between 0 and 15 nM. At higher concentrations saturation of the functionalized electrodes occurred, which was in line with results obtained from the HTM measurements. An LOD value of 40 nM was obtained on HTM at 37 °C, this decrease less than 1 nM at 85 °C, corresponding with TWTA results obtained at an input frequency of 0.017 Hz.

6.5. Conclusions

MIPs for the detection of either noradrenaline or caffeine were synthesized with different functional monomers. Each of these MIPs was evaluated using batch rebinding experiments and it was found that the MIP made with IA as a monomer has the highest recognition capability for noradrenaline (IF = 1.6). To increase the ability to recognize noradrenaline by the MIP, it was attempted to alter the porosity of the MIP by varying the amount of porogen. It was found that 4 mL of DMSO produced an MIP of sufficient porosity to allow access to the charged surface groups. The charge of these functional groups depends on the pH of the solution and it was found that a pH of 6 gave the highest binding (IF = 1.61) due to full protonation of the monomers leading to increased interaction with the positively charged nitrogen of noradrenaline.

For caffeine, the AA monomer was found to have the highest recognition capability (IF = 4.1). However, the incorporation of this monomer into the screen-printing ink was unsuccessful. Therefore, it was decided to continue with MAA as monomer to form the MIPs (IF = 3.5), increasing the mixture of particles vs. ink up to a 30 % ratio. The interaction of MAA with caffeine was further analysed using NMR, where peak shifts where observed with increasing ratios of caffeine to MAA, demonstrating the interaction between the monomer and template complex.

After fabrication and mounting the MIP-modified SPEs into the HTM setup, the PID setting were optimized for each of the electrodes. A PID setting of 1, 8, 0 was found to give the lowest noise on the signal for all noradrenaline MIP-modified SPEs, whilst for the caffeine MIP-modified SPEs, the optimum settings were found to be 1, 10, 0 at all temperatures. SPEs printed on paper resulted in the highest response (28 % signal increase) for the noradrenaline based MIP-modified SPEs. This increase can

be attributed to the wettability of the substrate promoting heat-flow from the electrode to the liquid. For the caffeine based MIP-modified SPEs the highest response (19% increase of signal) was found at a temperature of 85 ± 0.02 °C. The high measuring temperature for the caffeine based MIP-modified SPEs resulted in a lower noise on the signal (0.40%) and decreased the LOD down to 1 nM in buffered solutions. The LOD for the noradrenaline MIP-modified SPEs was 270 µM. The TWTA method gave no further improvement in the LOD; however, it decreased measurement time for both MIP-modified SPEs to less than 1 min. The input frequencies for the TWTA measurements are temperature dependent. Optimum input frequencies of 0.03 Hz at 37 ± 0.02 °C and 0.017 Hz at 85 ± 0.02 °C, were found.

Both MIP-modified SPEs were shown to be highly selective for their corresponding targets, making them suitable for medical applications. For the caffeine MIP-modified SPEs, the influence of the mixture was further investigated. Tap water and waste water led to a decrease in signal due to fouling of the electrode surface. The response obtained was still sufficient to implement the setup as a mobile monitoring station that can be used on site for the detection of caffeine, or other micro-pollutants.

7. Thermocouple approach: use of an alternative bio sensing platform

7.1. Abstract

MIPs are synthetic receptors that are able to specific and selectively bind their target molecule. In this work, solid-phase synthesis is used to produce MIP nanoparticles (nanoMIPs) for a range of templates with different sizes, including a small molecule (biotin), two peptides (one derived from the epithelial growth factor receptor and vancomycin) and a protein (trypsin). A thermocouple is dipcoated into the NanoMIPs solution and used to measure the temperature inside a liquid flow cell. The tip of the thermocouple (the sensitive area) is functionalized this way and will be blocked when the template binds to the MIP layer, thereby measuring a lower overall temperature. This is subsequently correlated to the concentration of the template, enabling measurement of target molecules in the low nanomolar regime. This is a magnitude of three orders better compared to previously used MIP micro-particles. This significant increase can be attributed to the high affinity of the nanoMIPs, which enhance the conductivity and increase the surface-to-volume ratio. This is the first use of the nanoMIPs in combination with thermal detection as well as the qualification of protein levels. This system has a fast response time, high selectivity and straightforward data analysis, thus making real-time monitoring of biomolecules entirely possible. The genericity of the system is demonstrated by the variety of biomolecules with varying sizes covered in this study. Additionally, the biocompatibility of the MIP receptor layer and the high commercial potential are an important step an in vivo diagnostic applications.

7.2. Introduction

Whilst the field of molecular imprinting is rapidly developing, commercialization remains a challenge. The use of MIP micro-particles as described in Chapter 6, has some significant disadvantages, including their low affinity, heterogeneous distribution, slow binding kinetics, and template leaching [271-274]. The use of MIP-modified SPEs simplifies the integration of these micron-sized MIPs into a sensor platform. The sensitivity of the sensor platform was sufficient to determine trace amount of micro-pollutants dispite fouling of electrodes with bacteria in complex media such as digestate samples. A few solid-phase approaches have been developed to overcome the advantages of the traditional bulk polymerization method to develop MIPs. In this chapter we will focus on the method pioneered by Piletsky [126], which involves the covalent attachment of target compounds to functionalised glass beads. Polymerization occurs around the target and the developed nanoMIPs are collected by exposing the beads to various temperature. Monomers and low affinity nanoMIPs are eluted at low temperatures, whereas the high affinity nanoMIPs are obtained at high temperature due to the strong complexation between polymer and template. This process is schematically shown in Figure 7-1.

Glass beads with immobilized melamine

+

Polymerization mixture

Polymerization

0 °C: elution of unreacted monomers and low-affinity NPs

60 °C: elution of high-affinity nanoMIPs

Initiation
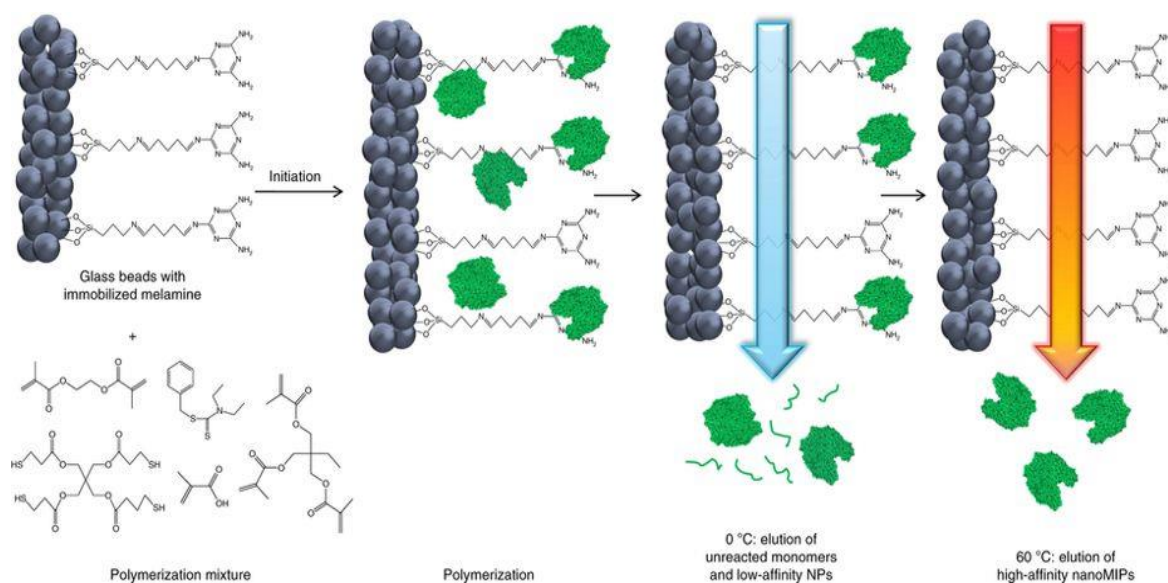
Figure 7-1. a schematic representation of the Solid-phase synthesis and separation of nanoMIPs [157].

This approach allows recycling of the template, which significantly reduces costs and has considerable advantages when working with expensive macromolecules such as proteins and biomarkers. The nanoparticles obtained are homogenous in size, have superior affinity compared with micro-particles [157], are water-soluble and are biocompatible [158, 159]. Due to the water-solubility, nanoMIP functionalisation is straightforward and they can be directly dip coated onto surfaces. This is in direct contrast to micro-particles, which require an adhesive layer of polylactic acid in order to be attached to the thermocouple surface. Previous work by Dilien *et al* [57]., described the impregnation of MIP micro-particles onto a thermocouple that was coated with polylactic acid as adhesive layer. Whilst it was possible to monitor dopamine levels in the micro-molar range, this sensor platform cannot compete with traditional ELISA assays [275] or electrochemical sensors [276] that can determine dopamine levels in the nM or pM range. These sensors cannot be used in a clinical setting due to their low affinity and use of micro-particles that are cytotoxic to cells. With the later in mind the two key aims of this work are as follows:

i. Improve sensitivity of a MIP-based thermocouple sensing platform via use of nanoMIPs that have high affinity and are homogeneous in size.
ii. Simplify preparation a MIP-based thermocouple via use of dip coating instead of an adhesive layer.

Such a sensor platform could easily be integrated into biomedical devices such as catheters, implants and stents. Therefore, it could be an excellent fit for the current niche in the market of therapeutics and diagnostics as it is often not possible to determine biomarker concentration *in-vivo.* Examples of application could include the determination of infection markers in catheters and implants, or monitoring of histamine and serotonin in the bowels as there is evidence that this has been linked to irritable bowel syndrome.

7.3. Methods

The nanoMIPs were obtained from MIPDiagnostics and used as received [157].

After inserting the nanoMIP functionalized thermocouples into the flow chamber, the system was stabilized in PBS for 45 min. Subsequently, PBS solutions with increasing concentrations of the respective target (0, 5, 10, 100, 500, 1000 nM) were

added. The recorded temperature data from T_2 was normalized and used to construct a dose-response curve for each of the nanoMIPs. These measurements were repeated with structural analogues or molecules which can act as interferents in the given matrix to prove the specificity of the system. In particular, pepsin was used in the case of trypsin nanoMIPs, teicoplanin for vancomycin nanoMIPs, ascorbic acid for biotin nanoMIPs and a related peptide sequence Beta-2-Microglobulin (hereafter referred to as B2MG) for EGFR nanoMIPs. As a proof-of-application that complex mixtures can be analyzed, measurements were conducted with EGFR spiked saliva samples. The saliva was diluted 1:1 with PBS to reduce viscosity and spiked with 5, 10, 100, 1000 and 10 000 nM EGFR.

7.4. Discussion

7.4.1. Production and characterization of nanoMIPs

By covalently immobilizing the target molecules to a solid support (*e.g.* glass beads, average diameter 75–90 µm) it is possible to create nano-sized high affinity MIPs. These nanoMIPs have a homogeneous distribution of the binding sites and are virtually free from their respective templates. These nanoMIPs can be made for a variety of targets including large peptides and proteins. The imprinting of these compounds is notoriously difficult due to the limit choice of monomers suitable for use in aqueous environments and the sensitive structural nature of proteins [277]. The size of these nanoMIPs depends on the mass of its respective target (Table 7-1)

Table 7-1. Hydrodynamic size of the four different nanoMIPs determined by dynamic light scattering (DLS) in distilled water [42]. The polydispersity (PDI) indicates a uniform size distribution.

Target	Size nanoMIPs (nm)	PDI	Functionalized target mass (kDa)
Biotin	161 ± 11	0.24	0.24
EGFR	239 ± 9	0.19	1.95
Vancomycin	275 ± 8	0.26	1.45
Trypsin	320 ± 7	0.22	23.9

The hydrodynamic size of the particles in water was obtained from MIPDiagnostics and was determined by dynamic light scattering (DLS) (Table 7-1) [42]. It should be noted that the hydrodynamic size as measured by DLS could be influenced by agglomeration/aggregation in solution and swelling. Therefor it is likely that DLS measurements may tend to overestimate the size of the nanoMIPs, Transmission Electron Microscopy may provide a more accurate result.

7.4.2. Thermal experiments with thermocouples functionalized with nanoMIPs

A bare (non-coated) thermocouple was used as a reference and exposed to PBS solutions with increasing concentrations (5, 10, 100, 500, 1000, 10 000 nM) of the EGFR peptide. After each injection the signal returned to its baseline level, indicating no significant difference was observed in the registered temperature for thermocouple T_2, (Figure 7-2).

Figure 7-2. Temperature (T_2) against time, with the initial stabilization in PBS and the subsequent addition of solutions with increasing concentrations of EGFR peptide (0-10000 nM). The red line indicates a bare (non-coated) thermocouple, which shows no significant change upon addition of the template. This is in contrast to when the thermocouple is coated with nanoMIPs for EGFR (black line), where temperature drops are recorded due to blocking of the heat-flow to the thermocouple.

Subsequently, thermocouples functionalised with nanoMIPs for EGFR were inserted into the setup and the temperature was monitored upon the addition of increasing concentrations of EGFR in PBS. The temperature of the heat sink (T_1) was strictly controlled at 37.00 ± 0.02 °C, resulting in a steady state of the flow chamber upon stabilization of the system after an injection. Any changes recorded at T_2 are the result of EGFR binding to the corresponding nanoMIPs, blocking the heat flow into the thermocouple. Figure 7-3A shows the decrease in temperature registered by T_2 after each injection of EGFR.

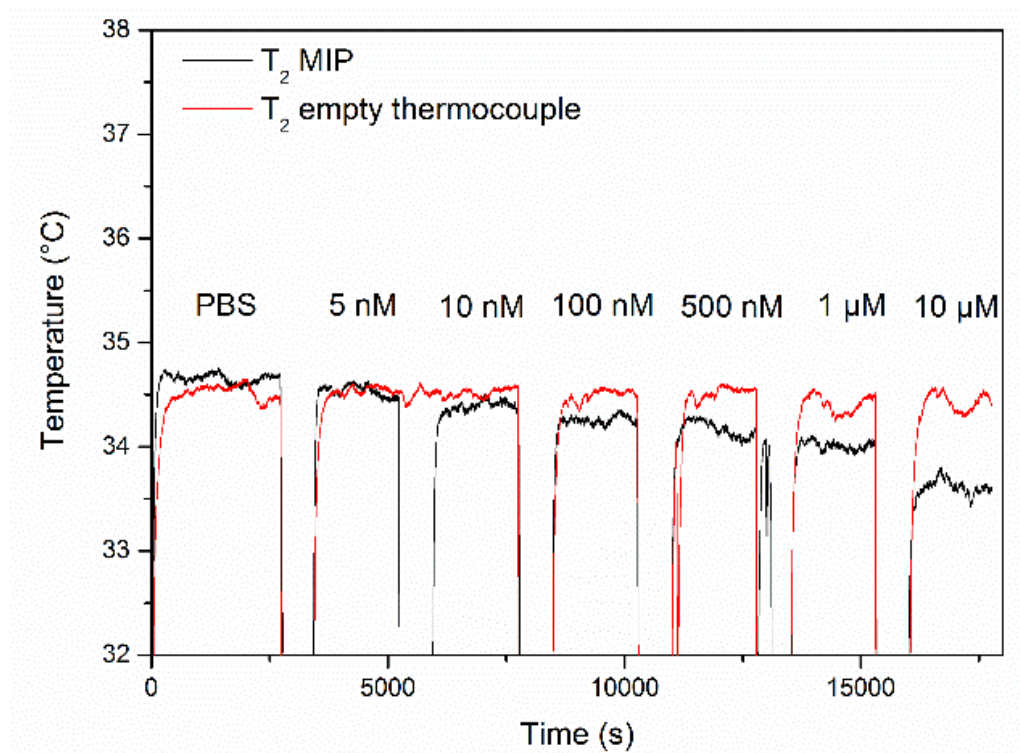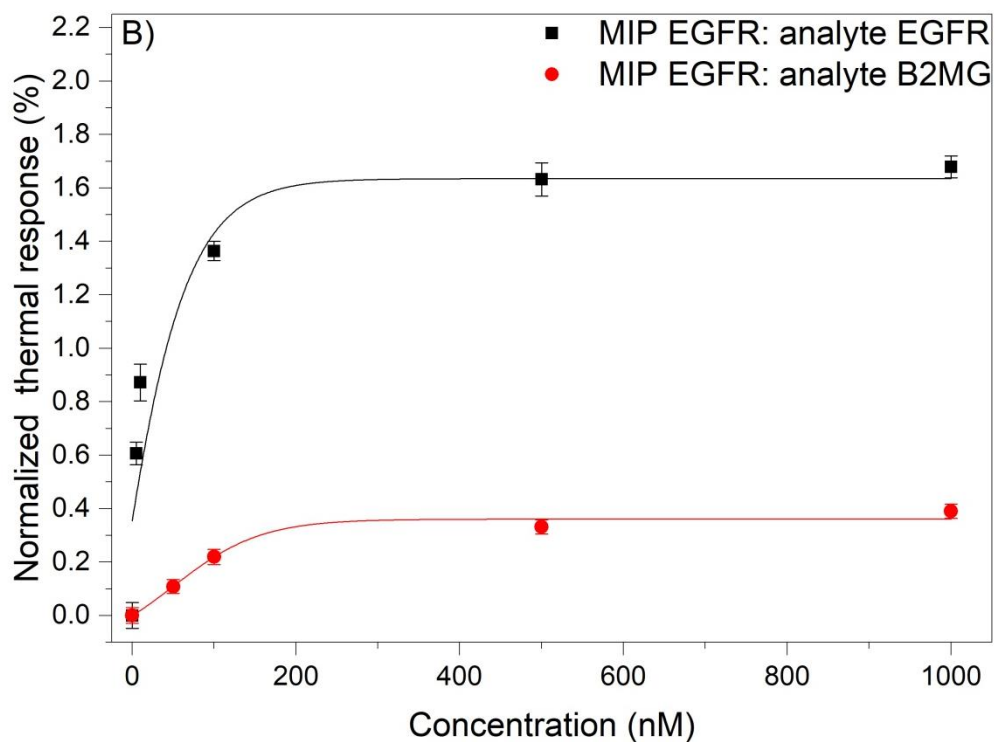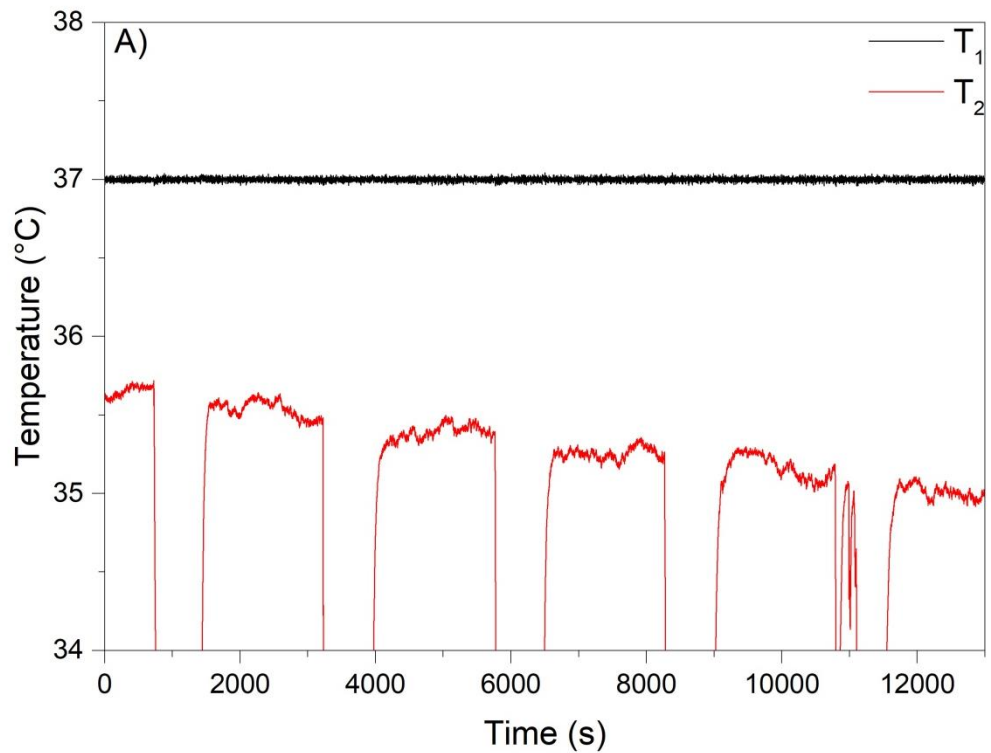**Figure 7-3. (A) The temperatures T_1 and T_2 are represented in time, after initial stabilization in PBS and the subsequent addition of solutions with increasing concentrations of EGFR peptide (0–1000 nM). (B) The normalized dose–response curves fitted with an dose response curve (R^2 = 0.90). The error bars represent the standard deviation on 200 datapoints.**

143

Addition of EGFR concentrations greater than 5 nM led to a significant change in the signal it is evident from Figure 7-3 that the dynamic range of the sensors is between 5-500 nM. Saturation of the signal was reached at a concentration of 1000 nM, corresponding to a decrease from 35.60 to 35.00 ± 0.05 °C, whilst the noise on the thermal signal was 0.05 °C (~0.15 %). The effect size is then calculated to be 1.90 ± 0.05 % at 1000 nM relative to the baseline (Figure 7-3B). Injecting similar concentrations of a non-related peptide sequence (B2MG), resulted in a small signal increase of 0.5 ± 0.04 % at 1000 nM (Figure 7-3B). It was expected that there would be some cross-selectivity issues due to the similarity of B2MG to the EGFR peptide. However, the response of the EGFR peptide was nearly a factor of four higher relative to the related peptide and this demonstrated the excellent selectivity of the sensor platform developed.

As proof-of-application for measurements in complex matrixes, an experiment was performed with spiked saliva samples. The electrodes were initially stabilized in PBS and a decrease in temperature of 10 % was registered when changing to a 1:1 mixture of saliva and PBS. Subsequently, spiked saliva samples were administered and the response was used to construct a dose-response curve to the PBS-saliva mixture (Figure 7-4).
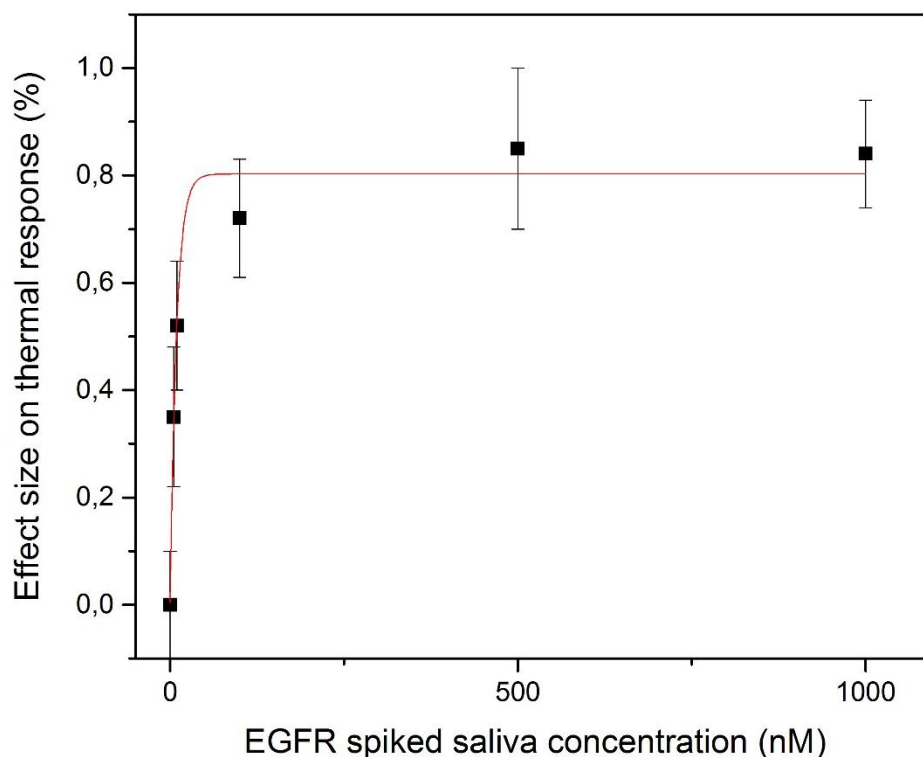
Figure 7-4. The dose–response curve ($R^2 = 0.95$) for nanoMIPs designed for EGFR while measuring saliva samples (diluted 1 : 1 with PBS) spiked with EGFR (0–1000 nM). Error bars represent the standard deviation on the average of at least 100 data points.

The error bars (± 0.1 %) in the saliva samples are significantly higher due to the matrix, which was more viscous and contains other proteins. However, there are significant differences in the thermal response to the EGFR spiked saliva samples (linear range 0–500 nM). This clearly demonstrates that the method holds promise for the detection of its target in a complex matrix.

Thermocouples were than coated with nanoMIPs targeting, biotin, trypsin and vancomycin and evaluated in PBS. In all cases a progressive decrease in temperature T_2 was observed on addition of increasing concentrations of their respective target molecules in PBS. The corresponding dose-response curves are represented in Figure 7-5.
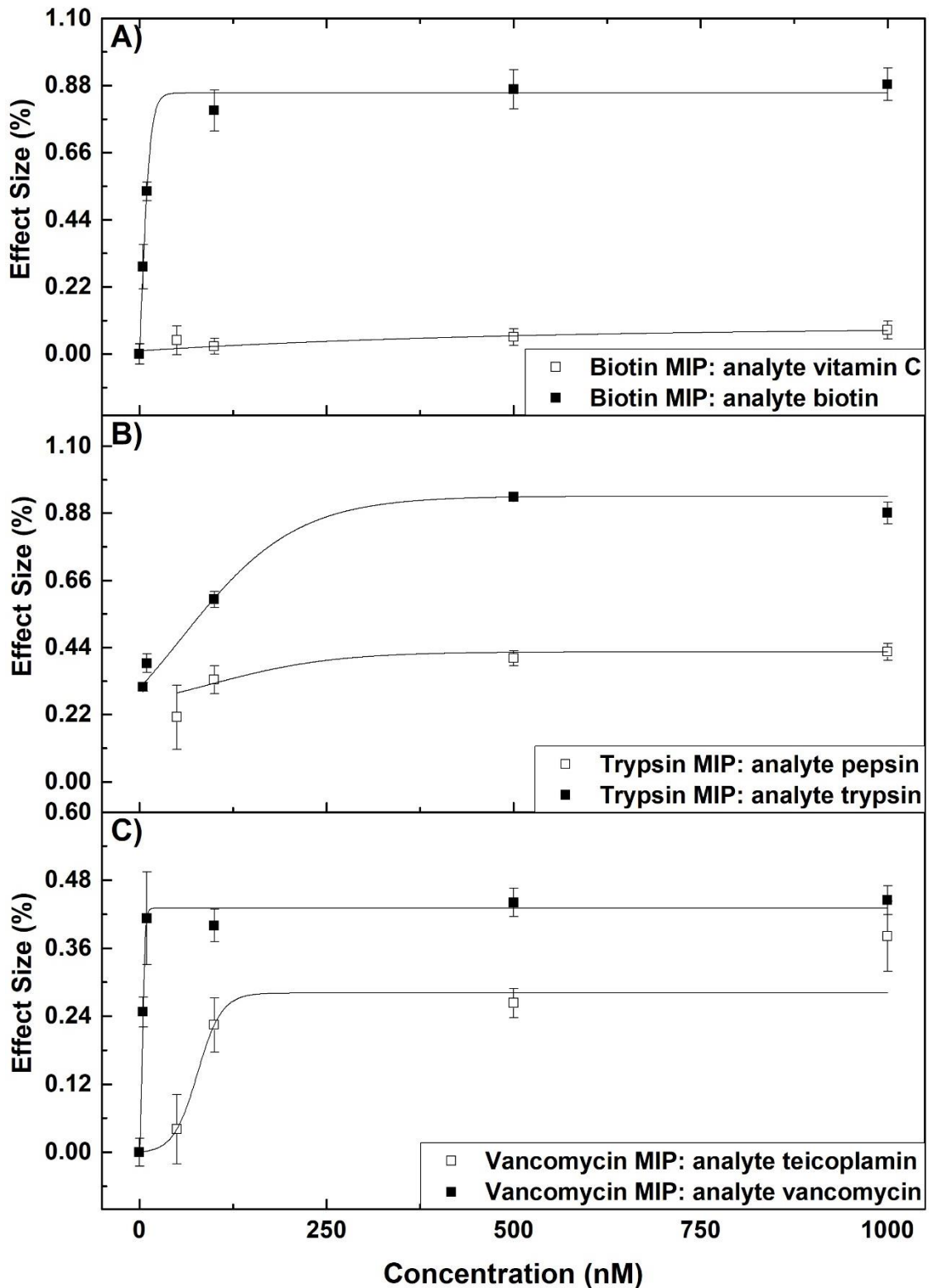
Figure 7-5. Dose-response curves for target and competitor molecules. (A) MIP for biotin and vitamin C as competitor. (B) MIP for trypsin and pepsin as competitor (C) MIP for vancomycin and teicoplanin as competitor. Data is fitted with a standard dose response fit ($R^2 > 0.99$ for all target molecules) showing saturation at the higher concentrations.

The dose-response curves in Figure 7-5 provide the response of the thermocouples to the actual target molecules compared with the response to similar biomolecules, which respectively are, vitamin C, pepsin and teicoplanin for biotin, trypsin and vancomycin. When comparing the response for each target and a competitor molecule at 100 nM, the selectivity factors (SF) can be determined (Table 7-2). Variations in the SF will be present at different concentrations, this is due to saturation of the binding sites. The SF values will be higher for smaller molecules as the MIPs can be made more specific. The SF values for EGFR and biotin are above 4, while for vancomycin a SF of 1.7 was determined. This lower SF value will be due to the very high structural similarity between vancomycin and its competitor teicoplanin.

Table 7-2. Overview of the sensor characteristics for the four different nanoMIPs [42].

Target	LOD (nM)	Response at 1000 nM (%)	Selectivity factor (c = 100 nM)	Linear range (nM)
			Target/competitor	
EGFR	3 ± 1	1.9 ± 0.1	4.5	0–200
Biotin	5 ± 2	0.8 ± 0.05	4.3	0–150
Trypsin	5 ± 2	0.98 ± 0.05	2.3	0–250
Vancomycin	4 ± 1	0.65 ± 0.03	1.7	0–100

Table 7-2 also provides an overview of the linear range, maximum response at 1000 nM and the LODs for each of the targets. The differences observed at the maximum response depend on multiple factors including the binding affinity of the nanoMIPs for their target, available surface area and the dimensions of the template. For example, in previous work with cells and Surface Imprinted Polymers changes in the thermal resistance of > 1°C/W were observed which can be attributed to the large area of the cells. In comparison, the addition of a single small vancomycin molecule would have a lower impact in terms of decreasing the heat-flow through the thermocouple relative to the effect of a large protein molecule such as EGFR.

The size of the nanoMIPs only differs a factor of two in relation to small and larger targets; therefore, the increase in surface coverage by these smaller nanoMIPs is not proportional to the actual pore blocking due to target recognition.

The LODs, as calculated to be the concentration at which the signal equals three times the standard deviation of the noise on baseline signal, are similar for all of the nanoMIPs (~3 – 5 nM). This is a significant improvement with LODs that are almost three orders of magnitude higher than those reported by Diliën et al.[57] in similar studies. The explanation behind this is threefold; first, the nanoMIPs have a higher affinity, secondly, the surface-to-volume ratio is higher for the nanoMIP and, third, Diliën et al. [57] used a polylactic acid (PLLA) coated thermocouple that was impregnated with MIP particles. This PLLA-sheet forms a thermally isolating layer of ~2 µM thickness over the entire thermocouple in the flow cell. When target binds to the MIP particles in this layer the thermal resistance of the sheet increases, leading to a decrease in heat loss over the thermocouple and overall increase in the temperature measured. In this study the nanoMIPs are only applied to the sensitive area at the tip of the thermocouple. This results in a ten-fold decrease in layer thickness, whilst only blocking heat flow to the sensitive part of the thermocouple upon binding of the target to the nanoMIPs. This results in a far stronger response and significantly reduced LOD.

Direct coating of the thermocouple with nanoMIPs is a substantial improvement relative to to the MIP-modified SPEs described in Section 6.3.3. The drawbacks of the MIP-modified SPEs are the lower affinity of the MIPs compared to the nanoMIPs and the relatively low surface coverage as the bulk ink only contains 30 mass% of MIPs. When measuring at higher temperatures, the LOD of the MIP-modified SPEs is increased, and similar results are expected for the nanoMIPs. However, the targets used in this work rapidly degrade at higher temperatures. The reported LODs and linear ranges obtained with the nanoMIPs are clinically relevant [278-280]. However, the system could be further improved by the use of TWTA, which would decrease the measurement time and potentially further increase the LOD.

7.5. Conclusions

High affinity nanoMIP particles were synthesised using a solid-phase approach and targeted for biotin, vancomycin, an EGFR peptide and trypsin. The particles had a hydrodynamic radius in the range of 161–320 nm in water, as measured by DLS. Subsequently, thermocouples were functionalized by dip coating them in aqueous solutions of nanoMIP, before being inserted into the flow cell. A baseline was

established by keeping the copper heat sink of the flow cell at a constant temperature of 37.00 ± 0.02 °C. Upon the addition of buffered solutions with increasing template concentrations (5–500 nM), significant decreases in temperature (~0.50 ± 0.02 °C) were measured by the MIP-functionalised thermocouples. The observed difference in temperature was due to the attachment of the template to the MIP layer blocking the heat flow at the interface of the thermocouple, resulting in a lower overall temperature of the liquid in the flow cell. Dose–response curves were constructed for each of the nanoMIPs to determine the LOD of the sensor platform developed. Additionally, the selectivity of the sensors was evaluated by exposing them to solutions containing biomolecules that are similar in terms of chemical functionality, or size and shape to the original target molecule.

The nanoMIPs have demonstrated their application as recognition elements in thermal sensing. With the LOD values in the low nanomolar range, this system is three orders of magnitude more sensitive compared with equivalent published studies where MIP micro-particles were embedded into a relative thick adhesive layer around the thermocouple[57]. Greater sensitivity was achieved by virtue of the higher affinity and smaller layer thickness of the nanoMIPs, thus promoting heat-flow through the surface. An additional improvement to this system may well be found by applying the TWTA protocol, which is faster and shows a ten-fold increase in detection limits when used on MIP-modified SPEs. Furthermore, another possibility would to covalently attach the nanoMIPs to the thermocouple surface by use of standard EDC coupling methods as the particles contain carboxylic moieties that can be linked to an amine terminated surface. This would allow control over the surface architecture and could promote the formation of a highly structured monolayer which is expected to further improve sensitivity.

8. General conclusions and outlook

In this chapter, a brief summary of the results obtained in this thesis toward the general aim of further expanding the scope of the HTM to other applications will be provided. This will be done according to the three objectives, concluding with suggestions for future continuation of the project:

1. Functionalisation of DNA on electrodes to study enzyme catalysis
2. Monitor growth of microorganism *in-real* time with bare electrodes
3. Use of MIPs as recognition elements in order to improve upon the specificity and selectivity of the sensors

The findings of this work were made possible due to international collaborations (Table 8-1) and have led to conference contributions (Table 8-2) and the contribution to scientific journals according:

Publications:

In preparation:

K. Betlem, A. Kaur, A. Hudson, G. Hurst, P. Singla, M. Zubko, S. Tedesco, K. Whitehead, and M. Peeters, A Novel Application of the Heat-Transfer Method (HTM): Real-Time Monitoring of Staphylococcus aureus Growth in Buffered Solutions and Wastewater Samples, ACS Applied Bio Materials

P. Singla, O. Singh, S. Sharma, **K. Betlem**, V K. Aswal, M. Peeters, Temperature Induced Solubilization of the Hydrophobic Active Pharmaceutical Ingredient Lamoterigine in Different Pluronics- a Spectroscopic, SANS, DLS, HTM and in vitro Release Study, ACS Omega, 4,(2019), 6, 11251-11262 [281].

Published:

K. Betlem, S. Hoksbergen, N. Mansouri, M. Down, P. Losada-Pérez, K. Eersels, B. van Grinsven, T.J. Cleij, P. Kelly, D. Sawtell, M. Zubko, C. Banks, M. Peeters, Real-time analysis of microbial growth by means of the Heat-Transfer Method (HTM)

using Saccharomyces cerevisiae as model organism, Physics in Medicine 6 (2018) 1-8 [52].

K. Betlem, I. Mahmood, R.D. Seixas, I. Sadiki, R.L.D. Raimbault, C.W. Foster, R.D. Crapnell, S. Tedesco, C.E. Banks, J. Gruber, M. Peeters, Evaluating the temperature dependence of heat-transfer based detection: A case study with caffeine and Molecularly Imprinted Polymers as synthetic receptors, Chemical Engineering Journal 359 (2019) 505-517 [44].

F. Canfarotta, J. Czulak, **K. Betlem**, A. Sachdeva, K. Eersels, B. van Grinsven, T.J. Cleij, M. Peeters, A novel thermal detection method based on molecularly imprinted nanoparticles as recognition elements, Nanoscale 10 (2018) 2081-2089 [42].

K. Betlem, M.P. Down, C.W. Foster, S. Akthar, K. Eersels, B. van Grinsven, T.J. Cleij, C.E. Banks, M. Peeters, Development of a Flexible MIP-Based Biosensor Platform for the Thermal Detection of Neurotransmitters, MRS Advances 3 (2018) 1569-1574 [91].

S. Casadio, J.W. Lowdon, **K. Betlem**, J.T. Ueta, C.W. Foster, T.J. Cleij, B. van Grinsven, O.B. Sutcliffe, C.E. Banks, M. Peeters, Development of a novel flexible polymer-based biosensor platform for the thermal detection of noradrenaline in aqueous solutions, Chemical Engineering Journal 315 (2017) 459-468 [39].

B. van Grinsven, **K. Betlem**, T.J. Cleij, C.E. Banks, M. Peeters, Evaluating the potential of thermal read-out techniques combined with molecularly imprinted polymers for the sensing of low-weight organic molecules, Journal of Molecular Recognition 30 (2017) e2563 [282].

Table 8-1. Research exchanges

Period	University	Location	Description
1-4-2017 / 28-4-2017	Maastricht University	The Netherlands	Nano-molar ranged thermal detection of small molecules, peptides and a protein using nanoMIP. Resulting in publication nr. 3
4-4-2018 / 26-4-2018	University of São Paulo	Brazil	Thermal detection of caffeine and a NMR study of the interaction between caffeine and methacrylic acid. Resulting in publication nr. 1
17-9-2018 / 21-9-2018	Université Libre de Bruxelles	Belgium	Installation thermal setup and thermal detection of phase changes in the formation of lipid layers

Table 8-2. Conference contributions

Year	Name	Location	Activity
2016-2018	Annual Science & Engineering Research Symposium	Manchester Metropolitan University	Poster / Flash presentation / **2018 1st poster prize**
2016-2018	Bioinspired materials	Manchester Metropolitan University	Poster
2016-2018	Chemistry research seminars	Manchester Metropolitan University	Oral presentations
2016	3rd Hans Suschitzky Organic Chemistry Symposium	University of Salford	Attendee
2017	Research & Innovation Showcase	Manchester Metropolitan University	Oral presentation
2017	Annual PGR Conference	Manchester Metropolitan University	Oral presentation
2017	Chemistry and Industrial Biotechnology Showcase	University of York	Oral presentation
2017	GSS MIP	ISEP, University of Porto	Oral presentation
2018	MRS fall meeting	Boston, MA	Oral presentation

8.1. Enzyme catalysis (Obj. 1)

The formation of SAMs on gold surfaces is widely used due to gold/thiol interaction being one of the strongest existing non-covalent bonds. Thereafter, DNA with an amine end group should be easily functionalised onto SAMs with a carboxylic end group via EDC coupling. However, for the majority of the samples in this work this functionalisation process was not straightforward and surface coverage of only ~ 2 % was achieved. It was attempted to improve the extent of functionalization of the surface by varying the parameters involved, including: the concentrations of 11-MUA, the probe DNA and the target DNA; incubation time of the SAM, EDC coupling and hybridisation time; plasma pre-treatment and the intermediate washing steps. Neither of these single conditions or in combination resulted in an adequate amount DNA being bound to the surface, the only samples showing some potential were plasma-treated samples, where a surface coverage of ~ 70 % was obtained. Upon thermal denaturation of the sample inside the HTM setup a small increase of 4.8 % in the thermal resistance was recorded at the melting temperature of 76 °C. Further studies to determine the underlying problem in the protocol were conducted and it is considered that the formation of the SAM was inhibited due to low surface activation. For future work, experiments should be carried out in a glovebox to prevent oxidation of the thiols. Plasma treatment should be performed on each sample to activate the gold surface and increase the likelihood of SAM formation.

8.2. Real time microbial growth (Obj. 2)

Next, the growth of microorganism was studied using *S. cerevisiae* as a model organism. It was shown that higher amounts of yeasts present in the flow chamber corresponded with an increase in the R_{th} value. To measure the growth of yeasts the flow cell was redesigned and 3D printed to prevent metabolic gasses from building up and interfering with the system. By performing progressive measurement on a WT and mutant strain the growth kinetics were evaluated resulting in optimum growth temperatures of 37 and 23 °C, respectively. With this setup, it was possible to study the influence of external factors that inhibit the growth, such as nutrient depletion, thermal shock and toxicity. The yeast cells remained viable after 14 h without nutrients, but were killed by heat and contact with copper(II) ions. This

method is also valid for the study of immobile bacteria, such as *S. aureus* for which a progressive increase in thermal resistance was detected upon the addition of increasing concentrated suspensions. The growth kinetics showed that a temperature range of 35 to 37 °C is favourable for growth, resulting in a steady increase of 0.03 °C/W per hour. No increase in thermal resistance was observed when *S. aureus* was exposed to 90°C, which demonstrates that growth was fully inhibited. SEM also elucidated that disintegration of the bacterial cell walls occurred at this temperature, confirming that the bacteria are not resistant to these elevated temperatures. In more complex matrixes, such as digestate samples, overall microbial load can be determined which was confirmed by analysing digestate samples spiked with *S. aureus*. However, this also demonstrates that the gold electrodes themselves are not selective towards bacterial strains and recognition elements (such as a SIP layer) need to be introduced in order to increase the selectivity of the sensor platform. This SIP layer will also allow for the setup to distinguish between live and dead cells.

8.3. MIPs to improve specificity and selectivity (Obj. 3)

With the use of MIP-modified SPEs, the HTM was able to detect caffeine in spiked digestate samples down to 25 nM (T=85 °C). However, this temperature is not suitable for biological components such as noradrenaline were measurement temperatures are limited to 37°C. The sensitivity can also be improved by varying the pH of the solution as binding depends on the charge density of the functional monomer used. A pH of 6 resulted in a LOD of ~350 µM of noradrenaline. However, this demonstrated that the sensitivity of the MIP-modified SPEs was not sufficient for accurate measurements of biomolecule concentrations in complex samples. Potential explanations for this are the low surface coverage and limited sensitivity of bulk microparticles that suffer from slow binding kinetics and template leaching. The application of TWTA did not change the LOD for either caffeine or noradrenaline relative to that obtained using HTM. However, the measurement time of the TWTA is shorter than that of the HTM and therefore could bring some benefits for industrial applications.

A further improvement in the HTM methodology was made by functionalizing nanoMIPs onto thermocouples. With this sensor platform, it was possible to reach a

154

limit of detection of 3 ± 1 nM (T = 37°C), which is similar to the LOD obtained for caffeine measurements performed at 85 °C. The fabrication and functionalization of the thermocouples with nanoMIPs is much more straightforward compared with the MIP-modified SPEs. Furthermore, nanoMIPs are regular in size and therefore demonstrate higher reproducibility, and have been reported to be biocompatible which could open new research avenues for *in-vivo* sensing. Whilst this functionalisation procedure is straightforward, it has to be noted that the production procedure of the nanoparticles is cumbersome without the use of an expensive automated reactor.

8.4.   Concluding remarks and future perspectives

Whilst the results presented show several novel applications of the HTM, it was not possible to complete objective 1 (study of enzyme catalysis). The continuation of the project would therefore be multi-directional. Additional improvements in sensitivity are expected when measuring with the functionalized thermocouples at a higher temperature, however one needs to keep in mind the thermal stability of the analyte in question. A combination this sensor platform with MIP-modified SPEs and a second blank thermocouple could enable simultaneous detection of microbes and pollutants. This will provide an accurate measurement of the concentration dependent toxicity to microbes, or could provide useful insight in how bacteria develop antimicrobial resistance upon exposure to pharmaceuticals. Furthermore, assay formats can be developed by for instance by redesigning 3D-printed flow cells to contain multiple thermocouples or directing flow through several flow cells with each of them containing different MIP-functionalised thermocouples (similar to laminar flow assay format).

The problems encountered with the surface attachment of DNA to gold need to be resolved. Suggestions for remediating this include repeating the attachment procedure using plasma cleaned samples that are transferred directly after treatment to a controlled environment free form carbon and oxygen for further processing (such as a glovebox). The use of alternative fluorescence labelled probe DNA will provide additional insight into the EDC coupling between the 11-MUA monolayer and the ssDNA probe. Lastly, the use of a thiolate probe sequence should provide direct linkage to the gold electrode, omission of the SAM formation

155

step, will increase the success rate of the attachment procedure. These suggestions should result in the functionalization of the gold electrode with DNA, alternatively other electrodes such as silica or artificial diamond could be investigated.

Finally, further optimization of the setup remains important and development of a true portable point of care system the following suggestions are made:

i.   Miniaturization of the HTM device, the smaller a device is the more accessible it will be to a wide public.

ii.   The system will need further automation a plug and play disposable flow cell will automatically detect what will be measured and run the appropriate profile to obtain the data. This data will be automatically analysed providing the user with a direct response.

iii. The analysis can be perform on the device itself or in a "cloud" environment so that any professional could access the data and provide a second opinion form anywhere.

9. References

1. B. van Grinsven, N. Vanden Bon, H. Strauven, L. Grieten, M. Murib, K. L. Jiménez Monroy, S. D. Janssens, K. Haenen, M. J. Schöning, V. Vermeeren, M. Ameloot, L. Michiels, R. Thoelen, W. De Ceuninck and P. Wagner, *ACS Nano*, 2012, **6**, 2712-2721.

2. I. E. Tothill and A. P. F. Turner, in *Encyclopedia of Food Sciences and Nutrition (Second Edition)*, ed. B. Caballero, Academic Press, Oxford, 2003, DOI: https://doi.org/10.1016/B0-12-227055-X/01374-2, pp. 489-499.

3. D. R. Thévenot, K. Toth, R. A. Durst and G. S. Wilson, 2001, **16**, 121-131.

4. P. D'Orazio, *Clinica Chimica Acta*, 2003, **334**, 41-69.

5. N. Bhalla, P. Jolly, N. Formisano and P. Estrela, *Essays in biochemistry*, 2016, **60**, 1-8.

6. M. K. Habib, *Biosensors and Bioelectronics*, 2007, **23**, 1-18.

7. A. Kaushik and M. A. Mujawar, *Sensors*, 2018, **18**.

8. J. Wang, *Biosensors and Bioelectronics*, 2006, **21**, 1887-1892.

9. A. K. Kaushik and C. K. Dixit, *Nanobiotechnology for Sensing Applications: From Lab to Field*, Apple Academic Press, 2016.

10. C. K. Dixit and A. Kaushik, *Microfluidics for Biologists: Fundamentals and Applications*, Springer International Publishing, 2016.

11. J. d. D. Habimana, J. Ji and X. Sun, *Analytical Letters*, 2018, **51**, 2933-2966.

12. S. L. R. Ellison, *Metrologia*, 2014, **51**, S199-S205.

13. A. Escarpa, M. C. Gonz3/4lez and M. A. L?pez, *Agricultural and Food Electroanalysis*, Wiley, 2015.

14. N. Bhardwaj, S. K. Bhardwaj, M. K. Nayak, J. Mehta, K.-H. Kim and A. Deep, *TrAC Trends in Analytical Chemistry*, 2017, **97**, 120-135.

15. A. K. Bhunia, *Future Microbiology*, 2014, **9**, 935-946.

16. E. Barbau-Piednoir, N. Botteldoorn, J. Mahillon, K. Dierick and N. H. Roosens, *International Journal of Food Microbiology*, 2015, **192**, 103-110.

17. W. H. Andrews, *Food Control*, 1996, **7**, 19-29.

18. B. R. Eggins, *Biosensors: an Introduction*, Vieweg+Teubner Verlag, 2013.

19. T. A. McMeekin, *Detecting Pathogens in Food*, Elsevier Science, 2003.

20. P. Leonard, S. Hearty, J. Brennan, L. Dunne, J. Quinn, T. Chakraborty and R. O'Kennedy, *Enzyme and Microbial Technology*, 2003, **32**, 3-13.

21. M. I. G. S. Almeida, B. M. Jayawardane, S. D. Kolev and I. D. McKelvie, *Talanta*, 2018, **177**, 176-190.

22. D. T. Jamison and D. C. P. Project, *Priorities in Health*, World Bank, 2006.

23. Y. Onuki, U. Bhardwaj, F. Papadimitrakopoulos and D. J. Burgess, *Journal of Diabetes Science and Technology*, 2008, **2**, 1003-1015.

24. M. Montagnana, M. Caputo, D. Giavarina and G. Lippi, *Clinica chimica acta; international journal of clinical chemistry*, 2009, **402**, 7-13.

25. E.-H. Yoo and S.-Y. Lee, *Sensors (Basel, Switzerland)*, 2010, **10**, 4558-4576.

26. J. D. Newman and A. P. Turner, *Biosensors & bioelectronics*, 2005, **20**, 2435-2453.

27. B. Solnica, J. W. Naskalski and J. Sieradzki, *Clinica Chimica Acta*, 2003, **331**, 29-35.

28. M. M. Peeters, B. van Grinsven, C. W. Foster, T. J. Cleij and C. E. Banks, *Molecules*, 2016, **21**.

29. B. van Grinsven, K. Betlem, T. J. Cleij, C. E. Banks and M. C. e. C. J. M. R. R. Peeters, 2017, **30**, e2563-n/a.

30. K. Bers, K. Eersels, B. van Grinsven, M. Daemen, J. F. Bogie, J. J. Hendriks, E. E. Bouwmans, C. Puttmann, C. Stein, S. Barth, G. M. Bos, W. T. Germeraad, W. De Ceuninck and P. Wagner, *Langmuir : the ACS journal of surfaces and colloids*, 2014, **30**, 3631-3639.

31. P. Cornelis, T. Vandenryt, G. Wackers, E. Kellens, P. Losada-Pérez, R. Thoelen, W. De Ceuninck, K. Eersels, S. Drijkoningen, K. Haenen, M. Peeters, B. van Grinsven and P. Wagner, *Diamond and Related Materials*, 2014, **48**, 32-36.

32. E. Perez-Ruiz, T. Vandenryt, D. Witters, D. Decrop, B. Van Grinsven, D. Spasic, P. Wagner and J. Lammertyn, 2014.

33. N. Vanden Bon, B. van Grinsven, M. S. Murib, W. S. Yeap, K. Haenen, W. De Ceuninck, P. Wagner, M. Ameloot, V. Vermeeren and L. Michiels, *International journal of nanomedicine*, 2014, **9**, 1629-1640.

34. M. S. Murib, W. S. Yeap, Y. Eurlings, B. van Grinsven, H. G. Boyen, B. Conings, L. Michiels, M. Ameloot, R. Carleer, J. Warmer, P. Kaul, K. Haenen, M. J. Schöning, W. De Ceuninck and P. Wagner, *Sensors and Actuators B: Chemical*, 2016, **230**, 260-271.

35. M. Peeters, P. Csipai, B. Geerets, A. Weustenraed, B. van Grinsven, R. Thoelen, J. Gruber, W. De Ceuninck, T. J. Cleij, F. J. Troost and P. Wagner, *Analytical and bioanalytical chemistry*, 2013, **405**, 6453-6460.

36. B. Geerets, M. Peeters, B. van Grinsven, K. Bers, W. de Ceuninck and P. Wagner, *Sensors*, 2013, **13**, 9148-9159.

37. M. Peeters, S. Kobben, K. L. Jiménez-Monroy, L. Modesto, M. Kraus, T. Vandenryt, A. Gaulke, B. van Grinsven, S. Ingebrandt, T. Junkers and P. Wagner, *Sensors and Actuators B: Chemical*, 2014, **203**, 527-535.

38. G. Wackers, T. Vandenryt, P. Cornelis, E. Kellens, R. Thoelen, W. De Ceuninck, P. Losada-Perez, B. van Grinsven, M. Peeters and P. Wagner, *Sensors*, 2014, **14**, 11016-11030.

39. S. Casadio, J. W. Lowdon, K. Betlem, J. T. Ueta, C. W. Foster, T. J. Cleij, B. van Grinsven, O. B. Sutcliffe, C. E. Banks and M. Peeters, *Chemical Engineering Journal*, 2017, **315**, 459-468.

40. T. Vandenryt, B. Van Grinsven, K. Eersels, P. Cornelis, S. Kholwadia, T. J. Cleij, R. Thoelen, W. De Ceuninck, M. Peeters and P. Wagner, *Sensors*, 2017, **17**, 2701.

41. C. J. Pawley, A. Perez-Gavilan, K. S. Foley, S. Lentink, H. N. Welsh, G. Tuijthof, E. Steen Redeker, H. Diliën, K. Eersels, B. Van Grinsven and T. J. Cleij, *Polymers*, 2017, **9**, 560.

42. F. Canfarotta, J. Czulak, K. Betlem, A. Sachdeva, K. Eersels, B. van Grinsven, T. J. Cleij and M. Peeters, *Nanoscale*, 2018, **10**, 2081-2089.

43. K. Eersels, H. Diliën, J. W. Lowdon, E. Steen Redeker, R. Rogosic, B. Heidt, M. Peeters, P. Cornelis, P. Lux, C. P. Reutelingsperger, L. J. Schurgers, T. J. Cleij and B. Van Grinsven, *Nutrients*, 2018, **10**, 751.

44. K. Betlem, I. Mahmood, R. D. Seixas, I. Sadiki, R. L. D. Raimbault, C. W. Foster, R. D. Crapnell, S. Tedesco, C. E. Banks, J. Gruber and M. Peeters, *Chemical Engineering Journal*, 2019, **359**, 505-517.

45. K. Eersels, B. van Grinsven, A. Ethirajan, S. Timmermans, K. L. Jimenez Monroy, J. F. Bogie, S. Punniyakoti, T. Vandenryt, J. J. Hendriks, T. J. Cleij, M. J. Daemen, V. Somers, W. De Ceuninck and P. Wagner, *ACS applied materials & interfaces*, 2013, **5**, 7258-7267.

46. K. Bers, K. Eersels, B. van Grinsven, M. Daemen, J. F. J. Bogie, J. J. A. Hendriks, E. E. Bouwmans, C. Püttmann, C. Stein, S. Barth, G. M. J. Bos, W. T. V. Germeraad, W. De Ceuninck and P. Wagner, *Langmuir : the ACS journal of surfaces and colloids*, 2014, **30**, 3631-3639.

47. K. Eersels, B. van Grinsven, M. Khorshid, V. Somers, C. Puttmann, C. Stein, S. Barth, H. Dilien, G. M. Bos, W. T. Germeraad, T. J. Cleij, R. Thoelen, W. De Ceuninck and P. Wagner, *Langmuir : the ACS journal of surfaces and colloids*, 2015, **31**, 2043-2050.

48. K. Eersels, B. van Grinsven, T. Vandenryt, K. L. Jiménez-Monroy, M. Peeters, V. Somers, C. Püttmann, C. Stein, S. Barth, G. M. J. Bos, W. T. V. Germeraad, H. Diliën, T. J. Cleij, R. Thoelen, W. D. Ceuninck and P. Wagner, *physica status solidi (a)*, 2015, **212**, 1320-1326.

49. B. van Grinsven, K. Eersels, O. Akkermans, S. Ellermann, A. Kordek, M. Peeters, O. Deschaume, C. Bartic, H. Diliën, E. Steen Redeker, P. Wagner and T. J. Cleij, *ACS Sens.*, 2016, **1**, 1140-1147.

50. W. Stilman, S. Jooken, G. Wackers, P. Cornelis, M. Khorshid, D. Yongabi, O. Akkermans, S. Dyson, B. van Grinsven, T. Cleij, L. van Ijzendoorn, P. Wagner and K. Eersels, *physica status solidi (a)*, 2017, n/a-n/a.

51. D. Yongabi, M. Khorshid, P. Losada-Pérez, K. Eersels, O. Deschaume, J. D'Haen, C. Bartic, J. Hooyberghs, R. Thoelen, M. Wübbenhorst and P. Wagner, *Sensors and Actuators B: Chemical*, 2018, **255**, 907-917.

52. K. Betlem, S. Hoksbergen, N. Mansouri, M. Down, P. Losada-Pérez, K. Eersels, B. van Grinsven, T. J. Cleij, P. Kelly, D. Sawtell, M. Zubko, C. Banks and M. Peeters, *Physics in Medicine*, 2018, **6**, 1-8.

53. B. van Grinsven, K. Eersels, S. Erkens-Hulshof, H. Diliën, K. Nurekeyeva, P. Cornelis, D. Klein, F. Crijns, G. Tuijthof, P. Wagner, E. Steen Redeker and T. J. Cleij, *physica status solidi (a)*, 2018, **215**, 1700777.

54. B. Heidt, R. Rogosic, J. W. Lowdon, M. Desmond-Kennedy, K. Jurgaityte, J. Ferrer Orri, Y. Kronshorst, S. Mendez, E. Polyakova, H. T. Rice, F. Crijns, H. Diliën, E. Steen Redeker, K. Eersels, B. van Grinsven and T. J. Cleij, *physica status solidi (a)*, **0**, 1800688.

55. M. Peeters, B. van Grinsven, T. J. Cleij, K. L. Jimenez-Monroy, P. Cornelis, E. Perez-Ruiz, G. Wackers, R. Thoelen, W. De Ceuninck, J. Lammertyn and P. Wagner, *ACS applied materials & interfaces*, 2015, **7**, 10316-10323.

56. P. Losada-Pérez, K. L. Jiménez-Monroy, B. van Grinsven, J. Leys, S. D. Janssens, M. Peeters, C. Glorieux, J. Thoen, K. Haenen, W. De Ceuninck and P. Wagner, *physica status solidi (a)*, 2014, **211**, 1377-1388.

57. H. Diliën, M. Peeters, J. Royakkers, J. Harings, P. Cornelis, P. Wagner, E. Steen Redeker, C. E. Banks, K. Eersels, B. van Grinsven and T. J. Cleij, *ACS Sens.*, 2017, **2**, 583-589.

58. W. Stilman, S. Jooken, G. Wackers, P. Cornelis, M. Khorshid, D. Yongabi, O. Akkermans, S. Dyson, B. van Grinsven, T. Cleij, L. van Ijzendoorn, P. Wagner and K. Eersels, *physica status solidi (a)*, 2017, **214**, 1600758.

59. H. Bisswanger, *Perspectives in Science*, 2014, **1**, 41-55.

60. S. C. Cheng, R. Kim, K. King, S. H. Kim and P. Modrich, *Journal of Biological Chemistry*, 1984, **259**, 11571-11575.

61. Y. Liu and I. Kobayashi, *Journal of Bacteriology*, 2007, **189**, 6928-6935.

62. D. H. Krüger and T. A. Bickle, *Microbiological Reviews*, 1983, **47**, 345-360.

63. a. W Arber and S. Linn, *Annual Review of Biochemistry*, 1969, **38**, 467-500.

64. J. Hedgpeth, H. M. Goodman and H. W. Boyer, *Proceedings of the National Academy of Sciences of the United States of America*, 1972, **69**, 3448-3452.

65. S. S. Morse, J. A. K. Mazet, M. Woolhouse, C. R. Parrish, D. Carroll, W. B. Karesh, C. Zambrana-Torrelio, W. I. Lipkin and P. Daszak, *Lancet (London, England)*, 2012, **380**, 1956-1965.

66. E. H. Chan, T. F. Brewer, L. C. Madoff, M. P. Pollack, A. L. Sonricker, M. Keller, C. C. Freifeld, M. Blench, A. Mawudeku and J. S. Brownstein, *Proceedings of the National Academy of Sciences of the United States of America*, 2010, **107**, 21701-21706.

67. T. W. Grein, K. B. Kamara, G. Rodier, A. J. Plant, P. Bovier, M. J. Ryan, T. Ohyama and D. L. Heymann, *Emerging infectious diseases*, 2000, **6**, 97-102.

68. K. F. Smith, M. Goldberg, S. Rosenthal, L. Carlson, J. Chen, C. Chen and S. Ramachandran, *Journal of the Royal Society, Interface*, 2014, **11**, 20140950-20140950.

69. F. Abbasian, E. Ghafar-Zadeh and S. Magierowski, *Bioengineering (Basel, Switzerland)*, 2018, **5**, 20.

70. L. Powers, *Real-time In-situ Detection of Microbes*, 2012.

71. N. S. Hobson, I. Tothill and A. P. F. Turner, *Biosensors and Bioelectronics*, 1996, **11**, 455-477.

72. E. A. Henchal, J. D. Teska, G. V. Ludwig, D. R. Shoemaker and J. W. Ezzell, *Clinics in Laboratory Medicine*, 2001, **21**, 661-678.

73. K. Eersels, B. van Grinsven, A. Ethirajan, S. Timmermans, K. L. Jiménez Monroy, J. F. J. Bogie, S. Punniyakoti, T. Vandenryt, J. J. A. Hendriks, T. J. Cleij, M. J. A. P. Daemen, V. Somers, W. De Ceuninck and P. Wagner, *ACS applied materials & interfaces*, 2013, **5**, 7258-7267.

74. K. Eersels, B. van Grinsven, M. Khorshid, V. Somers, C. Püttmann, C. Stein, S. Barth, H. Diliën, G. M. J. Bos, W. T. V. Germeraad, T. J. Cleij, R. Thoelen, W. De Ceuninck and P. Wagner, *Langmuir : the ACS journal of surfaces and colloids*, 2015, **31**, 2043-2050.

75. G. A. Cangelosi and J. S. Meschke, *Applied and Environmental Microbiology*, 2014, **80**, 5884-5891.

76. J. B. Emerson, R. I. Adams, C. M. B. Román, B. Brooks, D. A. Coil, K. Dahlhausen, H. H. Ganz, E. M. Hartmann, T. Hsu, N. B. Justice, I. G. Paulino-Lima, J. C. Luongo, D. S. Lymperopoulou, C. Gomez-Silvan, B. Rothschild-Mancinelli, M. Balk, C. Huttenhower, A. Nocker, P. Vaishampayan and L. J. Rothschild, *Microbiome*, 2017, **5**, 86.

77. R. Narang, S. Mohammadi, M. M. Ashani, H. Sadabadi, H. Hejazi, M. H. Zarifi and A. Sanati-Nezhad, *Scientific reports*, 2018, **8**, 15807.

78. D. Botstein, S. A. Chervitz and J. M. Cherry, *Science (New York, N.Y.)*, 1997, **277**, 1259-1260.

79. H. Karathia, E. Vilaprinyo, A. Sorribas and R. Alves, *PloS one*, 2011, **6**, e16015.

80. R. Li and A. W. Murray, *Cell*, 1991, **66**, 519-531.

81. W. K. Huh, J. V. Falvo, L. C. Gerke, A. S. Carroll, R. W. Howson, J. S. Weissman and E. K. O'Shea, *Nature*, 2003, **425**, 686-691.

82. J.-L. Legras, D. Merdinoglu, J.-M. Cornuet and F. Karst, 2007, **16**, 2091-2102.

83. I. Herskowitz, *Microbiological reviews*, 1988, **52**, 536-553.

84. K. Otterstedt, C. Larsson, R. M. Bill, A. Ståhlberg, E. Boles, S. Hohmann and L. Gustafsson, *EMBO Reports*, 2004, **5**, 532-537.

85. L. Alba-Lois and C. Segal-Kischinevzky, *Journal*, 2010, **3**, 17.

86. J. R. Dickinson and M. Schweizer, *Metabolism and Molecular Physiology of Saccharomyces Cerevisiae, 2nd Edition*, CRC Press, 2004.

87. T. Münch, B. Sonnleitner and A. Fiechter, *Journal of Biotechnology*, 1992, **24**, 299-314.

88. C. Beck and H. K. von Meyenburg, *Journal of bacteriology*, 1968, **96**, 479-486.

89. C. A. Rosa and G. Peter, *Biodiversity and Ecophysiology of Yeasts*, Springer Berlin Heidelberg, 2006.

90. W. Woodside and J. H. Messmer, *Journal of Applied Physics*, 1961, **32**, 1688-1699.

91. K. Betlem, M. P. Down, C. W. Foster, S. Akthar, K. Eersels, B. van Grinsven, T. J. Cleij, C. E. Banks and M. Peeters, *MRS Advances*, 2018, **3**, 1569-1574.

92. Z. Salvado, F. N. Arroyo-Lopez, J. M. Guillamon, G. Salazar, A. Querol and E. Barrio, *Applied and environmental microbiology*, 2011, **77**, 2292-2302.

93. J. S. Wood and L. H. Hartwell, *The Journal of cell biology*, 1982, **94**, 718-726.

94. M. K. Zubko and D. Lydall, *Nature cell biology*, 2006, **8**, 734-740.

95. M. K. Zubko, S. Guillard and D. Lydall, *Genetics*, 2004, **168**, 103-115.

96. D. Lydall and T. Weinert, *Science*, 1995, **270**, 1488-1491.

97. S.-C. Teng and V. A. Zakian, *Molecular and Cellular Biology*, 1999, **19**, 8083-8093.

98. R. A. Festa and D. J. Thiele, *PLOS Pathogens*, 2012, **8**, e1002887.

99. M. A. Lever and A. P. Teske, *Appl. Environ. Microbiol.*, 2015, **81**, 1426-1441.

100. S. Lim, S. Kim, K.-M. Yeon, B.-I. Sang, J. Chun and C.-H. Lee, *Desalination*, 2012, **287**, 209-215.

101. D. Y. Lyon and T. M. Vogel, in *Bioaugmentation for Groundwater Remediation*, eds. H. F. Stroo, A. Leeson and C. H. Ward, Springer New York, New York, NY, 2013, DOI: 10.1007/978-1-4614-4115-1_1, pp. 1-37.

102. M.-A. Yun, K.-M. Yeon, J.-S. Park, C.-H. Lee, J. Chun and D. J. Lim, *Water research*, 2006, **40**, 45-52.

103. F. Baquero, J.-L. Martínez and R. Cantón, *Current opinion in biotechnology*, 2008, **19**, 260-265.

104. A. Novo, S. André, P. Viana, O. C. Nunes and C. M. Manaia, *Water research*, 2013, **47**, 1875-1887.

105. S. Kim and D. S. Aga, *Journal of Toxicology and Environmental Health, Part B*, 2007, **10**, 559-573.

106. T. Zhang, X.-X. Zhang and L. Ye, *PloS one*, 2011, **6**, e26041.

107. R. I. Amann, B. J. Binder, R. J. Olson, S. W. Chisholm, R. Devereux and D. A. Stahl, *Applied and environmental microbiology*, 1990, **56**, 1919-1925.

108. K. E. Shannon, D. Y. Lee, J. T. Trevors and L. A. Beaudette, *Science of The Total Environment*, 2007, **382**, 121-129.

109. K. Lemarchand, F. Berthiaume, C. Maynard, J. Harel, P. Payment, P. Bayardelle, L. Masson and R. Brousseau, *Journal of microbiological methods*, 2005, **63**, 115-126.

110. M. Varma, R. Field, M. Stinson, B. Rukovets, L. Wymer and R. Haugland, *Water Res*, 2009, **43**, 4790-4801.

111. M. Fittipaldi, A. Nocker and F. Codony, *Journal of microbiological methods*, 2012, **91**, 276-289.

112. I. D. Ofiteru, M. Lunn, T. P. Curtis, G. F. Wells, C. S. Criddle, C. A. Francis and W. T. Sloan, *Proc Natl Acad Sci U S A*, 2010, **107**, 15345-15350.

113. M. T. Butler, Q. Wang and R. M. Harshey, *Proc Natl Acad Sci U S A*, 2010, **107**, 3776-3781.

114. S. R. Gill, D. E. Fouts, G. L. Archer, E. F. Mongodin, R. T. Deboy, J. Ravel, I. T. Paulsen, J. F. Kolonay, L. Brinkac, M. Beanan, R. J. Dodson, S. C. Daugherty, R. Madupu, S. V. Angiuoli, A. S. Durkin, D. H. Haft, J. Vamathevan, H. Khouri, T. Utterback, C. Lee, G. Dimitrov, L. Jiang, H. Qin, J. Weidman, K. Tran, K. Kang, I. R. Hance, K. E. Nelson and C. M. Fraser, *J Bacteriol*, 2005, **187**, 2426-2438.

115. M. C. Enright, D. A. Robinson, G. Randle, E. J. Feil, H. Grundmann and B. G. Spratt, *Proc Natl Acad Sci U S A*, 2002, **99**, 7687-7692.

116. M. Egholm, O. Buchardt, L. Christensen, C. Behrens, S. M. Freier, D. A. Driver, R. H. Berg, S. K. Kim, B. Norden and P. E. Nielsen, *Nature*, 1993, **365**, 566-568.

117. O. Brandt and J. D. Hoheisel, *Trends in biotechnology*, 2004, **22**, 617-622.

118. D. A. Spivak, *Adv Drug Deliv Rev*, 2005, **57**, 1779-1794.

119. K. Haupt and K. Mosbach, *Chemical Reviews*, 2000, **100**, 2495-2504.

120. G. Wulff, *Chemical reviews*, 2002, **102**, 1-28.

121. J. Svenson and I. A. Nicholls, *Analytica Chimica Acta*, 2001, **435**, 19-24.

122. R. Thoelen, R. Vansweevelt, J. Duchateau, F. Horemans, J. D'Haen, L. Lutsen, D. Vanderzande, M. Ameloot, M. vandeVen, T. J. Cleij and P. Wagner, *Biosensors and Bioelectronics*, 2008, **23**, 913-918.

123. L. Ye and K. Haupt, *Analytical and bioanalytical chemistry*, 2004, **378**, 1887-1897.

124. J. O. Mahony, K. Nolan, M. R. Smyth and B. Mizaikoff, *Analytica Chimica Acta*, 2005, **534**, 31-39.

125. S.-P. Tang, F. Canfarotta, K. Smolinska-Kempisty, E. Piletska, A. Guerreiro and S. Piletsky, *Analytical Methods*, 2017, **9**, 2853-2858.

126. F. Canfarotta, A. Waters, R. Sadler, P. McGill, A. Guerreiro, D. Papkovsky, K. Haupt and S. Piletsky, *Nano Research*, 2016, **9**, 3463-3477.

127. B. Sellergren and C. J. Allender, *Adv Drug Deliv Rev*, 2005, **57**, 1733-1741.

128. I. Chianella, A. Guerreiro, E. Moczko, J. S. Caygill, E. V. Piletska, I. M. De Vargas Sansalvador, M. J. Whitcombe and S. A. Piletsky, *Anal Chem*, 2013, **85**, 8462-8468.

129. V. Ratautaite, M. Nesladek, A. Ramanaviciene, I. Baleviciute and A. Ramanavicius, *Electroanalysis*, 2014, **26**, 2458-2464.

130. M. J. Whitcombe, N. Kirsch and I. A. Nicholls, *Journal of molecular recognition : JMR*, 2014, **27**, 297-401.

131. M. Menger, A. Yarman, J. Erdőssy, H. B. Yildiz, R. E. Gyurcsányi and F. W. Scheller, *Biosensors*, 2016, **6**, 35.

132. S. Nestora, F. Merlier, S. Beyazit, E. Prost, L. Duma, B. Baril, A. Greaves, K. Haupt and B. Tse Sum Bui, *Angewandte Chemie (International ed. in English)*, 2016, **55**, 6252-6256.

133. B. Claude, R. Nehmé and P. Morin, *Analytica Chimica Acta*, 2011, **699**, 242-248.

134. X. Zhang, S. Xu, J.-M. Lim and Y.-I. Lee, *Talanta*, 2012, **99**, 270-276.

135. J.-B. Ma, H.-W. Qiu, Q.-H. Rui, Y.-F. Liao, Y.-M. Chen, J. Xu, P.-P. Zhan and Y.-G. Zhao, *Journal of Chromatography A*, 2016, **1429**, 86-96.

136. B.-Y. Huang, Y.-C. Chen, G.-R. Wang and C.-Y. Liu, *Journal of Chromatography A*, 2011, **1218**, 849-855.

137. W. d. J. R. Santos, M. Santhiago, I. V. P. Yoshida and L. T. Kubota, 2012, **166-167**, 739-745.

138. I.-C. Chung, C.-C. Chang, H.-S. Chiu, S.-F. Jiang, M.-H. Lee, C.-L. Chung, B.-D. Liu, C.-Y. Huang and H.-Y. Lin, 2011, DOI: info:doi/10.1166/jnn.2011.3938.

139. A. Ramanaviciene, A. Ramanavicius and A. Finkelsteinas, *Journal of Chemical Education*, 2006, **83**, 1212.

140. J. Wagner, P. Vitali, M. G. Palfreyman, M. Zraika and S. Huot, *Journal of Neurochemistry*, 1982, **38**, 1241-1254.

141. B. H. C. Westerink and T. B. A. Mulder, *Journal of Neurochemistry*, 1981, **36**, 1449-1462.

142. A. L. Ghindilis, A. Makower, C. G. Bauer, F. F. Bier and F. W. Scheller, *Analytica Chimica Acta*, 1995, **304**, 25-31.

143. V. Ratautaite, D. Plausinaitis, I. Baleviciute, L. Mikoliunaite, A. Ramanaviciene and A. Ramanavicius, *Sensors and Actuators B: Chemical*, 2015, **212**, 63-71.

144. H. Hallman, L.-O. Farnebo, B. Hamberger and G. Jonsson, *Life Sciences*, 1978, **23**, 1049-1052.

145. M. A Fotopoulou and P. Ioannou, *Post-column terbium complexation and sensitized fluorescence detection for the determination of norepinephrine, epinephrine and dopamine using high-performance liquid chromatography*, 2002.

146. A. P. F. Turner, *Science*, 2000, **290**, 1315.

147. C.-Y. Huang, M.-J. Syu, Y.-S. Chang, C.-H. Chang, T.-C. Chou and B.-D. Liu, *Biosensors and Bioelectronics*, 2007, **22**, 1694-1699.

148. J. P. Metters, R. O. Kadara and C. E. Banks, *Analyst*, 2011, **136**, 1067-1076.

149. P. Leuenberger, S. Ganscha, A. Kahraman, V. Cappelletti, P. J. Boersema, C. von Mering, M. Claassen and P. Picotti, *Science*, 2017, **355**, eaai7825.

150. J.-X. Dong, Q. Li, Z.-C. Tan, Z.-H. Zhang and Y. Liu, *The Journal of Chemical Thermodynamics*, 2007, **39**, 108-114.

151. I. Baleviciute, V. Ratautaite, A. Ramanaviciene, Z. Balevicius, J. Broeders, D. Croux, M. McDonald, F. Vahidpour, R. Thoelen, W. D. Ceuninck, K. Haenen, M. Nesladek, A. Reza and A. Ramanavicius, *Synthetic Metals*, 2015, **209**, 206-211.

152. V. Ratautaite, S. D. Janssens, K. Haenen, M. Nesládek, A. Ramanaviciene, I. Baleviciute and A. Ramanavicius, *Electrochimica Acta*, 2014, **130**, 361-367.

153. Q. Zhu, C. Ma, H. Chen, Y. Wu and J. Huang, *Microchimica Acta*, 2014, **181**, 303-311.

154. X. Liu, N. Sun, Q. Zhu, M. Wu, Y. Ye and H. Chen, 2013, **1304**, 10-17.

155. Ignaz J. Buerge, Thomas Poiger, Markus D. Müller and H.-R. Buser, 2003, DOI: S0013-936X(02)00125-6.

156. K. Betlem, I. Mahmood, R. D. Seixas, I. Sadiki, R. L. D. Raimbault, C. Foster, R. Crapnell, S. Tedesco, C. Banks, J. Gruber and M. Peeters, *Evaluating the Temperature Dependence of Heat-Transfer Based Detection: A Case Study with Caffeine and Molecularly Imprinted Polymers as Synthetic Receptors*, 2018.

157. F. Canfarotta, A. Poma, A. Guerreiro and S. Piletsky, *Nature Protocols*, 2016, **11**, 443.

158. A. Poma, A. Guerreiro, M. J. Whitcombe, E. V. Piletska, A. P. F. Turner and S. A. Piletsky, *Advanced Functional Materials*, 2013, **23**, 2821-2827.

159. I. Basozabal, A. Guerreiro, A. Gomez-Caballero, M. Aranzazu Goicolea and R. J. Barrio, *Biosensors and Bioelectronics*, 2014, **58**, 138-144.

160. S. Korposh, I. Chianella, A. Guerreiro, S. Caygill, S. Piletsky, S. W. James and R. P. Tatam, *Analyst*, 2014, **139**, 2229-2236.

161. I. Chianella, A. Guerreiro, E. Moczko, J. S. Caygill, E. V. Piletska, I. M. P. De Vargas Sansalvador, M. J. Whitcombe and S. A. Piletsky, *Analytical Chemistry*, 2013, **85**, 8462-8468.

162. C. Cáceres, F. Canfarotta, I. Chianella, E. Pereira, E. Moczko, C. Esen, A. Guerreiro, E. Piletska, M. J. Whitcombe and S. A. Piletsky, *Analyst*, 2016, **141**, 1405-1412.

163. K. Smolinska-Kempisty, A. Guerreiro, F. Canfarotta, C. Cáceres, M. J. Whitcombe and S. Piletsky, *Scientific reports*, 2016, **6**, 37638.

164. F. Canfarotta, K. Smolinska-Kempisty and S. Piletsky, *Methods in molecular biology (Clifton, N.J.)*, 2017, **1575**, 389-398.

165. B. Van Grinsven, UHasselt, 2012.

166. J. A. Dean and N. A. Lange, *Lange's Handbook of Chemistry*, McGraw-Hill, 1999.

167. J. Ermer and J. H. M. B. Miller, *Method Validation in Pharmaceutical Analysis: A Guide to Best Practice*, Wiley, 1st edn., 2005.

168. S. Wolf and R. N. Tauber, *Silicon Processing for the VLSI Era: Process technology*, Lattice Press, 1986.

169. C. W. Foster, J. P. Metters and C. E. Banks, *Electroanalysis*, 2013, **25**, 2275-2282.

170. R. J. Umpleby, S. C. Baxter, A. M. Rampey, G. T. Rushton, Y. Chen and K. D. Shimizu, *Journal of Chromatography B*, 2004, **804**, 141-149.

171. D. Burke, D. Dawson, T. Stearns and C. S. H. Laboratory, *Methods in Yeast Genetics: A Cold Spring Harbor Laboratory Course Manual*, Cold Spring Harbor Laboratory Press, 2000.

172. C. Kurtzman, J. W. Fell and T. Boekhout, *The Yeasts: A Taxonomic Study*, Elsevier Science, 2011.

173. A. Blanco and G. Blanco, in *Medical Biochemistry*, eds. A. Blanco and G. Blanco, Academic Press, 2017, DOI: https://doi.org/10.1016/B978-0-12-803550-4.00008-2, pp. 153-175.

174. M. E. Himmel, S. Y. Ding, D. K. Johnson, W. S. Adney, M. R. Nimlos, J. W. Brady and T. D. Foust, *Science*, 2007, **315**, 804-807.

175. P. Bajpai, *Biotechnology progress*, 1999, **15**, 147-157.

176. R. Araujo, M. Casal and A. Cavaco-Paulo, *Biocatalysis and Biotransformation*, 2008, **26**, 332-349.

177. P. Fernandes, *Enzyme research*, 2010, **2010**, 862537-862537.

178. S. Sanchez and A. L. Demain, *Organic Process Research & Development*, 2010, **15**, 224-230.

179. S. Singh-Gasson, R. D. Green, Y. Yue, C. Nelson, F. Blattner, M. R. Sussman and F. Cerrina, *Nature Biotechnology*, 1999, **17**, 974.

180. W. Yang, O. Auciello, J. E. Butler, W. Cai, J. A. Carlisle, J. E. Gerbi, D. M. Gruen, T. Knickerbocker, T. L. Lasseter, J. N. Russell, L. M. Smith and R. J. Hamers, *Nature Materials*, 2003, **2**, 63-63.

181. Z. Lin, T. Strother, W. Cai, X. Cao, L. M. Smith and R. J. Hamers, *Langmuir : the ACS journal of surfaces and colloids*, 2002, **18**, 788-796.

182. K. Kerman, D. ÖZKAN, P. KARA, H. Karadeniz, Z. Özkan, A. Erdem, F. Jelen and M. Özsöz, *Turkish Journal of Chemistry*, 2004, **28**, 523-534.

183. F. Lucarelli, G. Marrazza, A. P. Turner and M. Mascini, *Biosensors and Bioelectronics*, 2004, **19**, 515-530.

184. J. Xu, J.-J. Zhu, Q. Huang and H.-Y. Chen, *Electrochemistry communications*, 2001, **3**, 665-669.

185. Y. S. Kim, H. S. Jung, T. Matsuura, H. Y. Lee, T. Kawai and M. B. Gu, *Biosensors and Bioelectronics*, 2007, **22**, 2525-2531.

186. J. I. A. Rashid and N. A. Yusof, *Sensing and Bio-Sensing Research*, 2017, **16**, 19-31.

187. H.-z. Pan, H.-w. Yu, N. Wang, Z. Zhang, G.-c. Wan, H. Liu, X. Guan and D. Chang, *Journal of biotechnology*, 2015, **214**, 133-138.

188. C. Zhang, S. Xu, X. Zhang, D. Huang, R. Li, S. Zhao and B. Wang, *Journal of Electroanalytical Chemistry*, 2014, **735**, 115-122.

189. D. B. Peckys, N. de Jonge, M. L. Simpson and T. E. McKnight, *Nanotechnology*, 2008, **19**, 435301.

190. A. B. Steel, R. L. Levicky, T. M. Herne and M. J. Tarlov, *Biophysical Journal*, 2000, **79**, 975-981.

191. K. Bers, B. van Grinsven, T. Vandenryt, M. Murib, W. Janssen, B. Geerets, M. Ameloot, K. Haenen, L. Michiels, W. De Ceuninck and P. Wagner, *Diamond and Related Materials*, 2013, **38**, 45-51.

192. W. Tsui-Hsun, L. Shu-Chuan, W. Yi-Shiuan, T. Shu-Ju, H. Yi-You, W. Hsin-Ming and C. Ko-Shao, *Current Nanoscience*, 2011, **7**, 950-954.

193. J.-W. Kim, K.-Y. Yang, S.-H. Hong and H. Lee, *Applied Surface Science*, 2008, **254**, 5607-5611.

194. M. Patel, P. Solanki, S. Khandelwal, V. Agrawal, S. G. Ansari and B. Malhotra, *Self-assembled monolayer based electrochemical nucleic acid sensor for Vibrio cholerae detection*, 2012.

195. J. Wu, H.-J. Bai, X.-B. Zhang, J.-J. Xu and H.-Y. Chen, *Langmuir : the ACS journal of surfaces and colloids*, 2010, **26**, 1191-1198.

196. K. J. Kwon-Chung and J. E. Bennett, *Medical Mycology*, Lea & Febiger, 1992.

197. A. Enache-Angoulvant and C. Hennequin, *Clinical Infectious Diseases*, 2005, **41**, 1559-1568.

198. P. R. Marteau, M. de Vrese, C. J. Cellier and J. Schrezenmeir, *The American journal of clinical nutrition*, 2001, **73**, 430s-436s.

199. L. J. WALKER, M. C. ALDHOUS, H. E. DRUMMOND, B. R. K. SMITH, E. R. NIMMO, I. D. R. ARNOTT and J. SATSANGI, *Clinical & Experimental Immunology*, 2004, **135**, 490-496.

200. D. P. Jensen and D. L. Smith, *Archives of Internal Medicine*, 1976, **136**, 332-333.

201. T. Imai and T. Ohno, *Applied and environmental microbiology*, 1995, **61**, 3604-3608.

202. S. L. Forsburg and P. Nurse, *Annual Review of Cell Biology*, 1991, **7**, 227-256.

203. B. Alberts, *Molecular Biology of the Cell: Hauptbd*, Garland Science Taylor & Francis, 2008.

204. B. C. Kilkenny and C. N. Hinshelwood, *Proceedings of the Royal Society of London. Series B - Biological Sciences*, 1952, **140**, 352-361.

205. M. Kaeberlein, *Nature*, 2010, **464**, 513-519.

206. C. Molteni, H. K. Abicht and M. Solioz, *Applied and environmental microbiology*, 2010, **76**, 4099-4101.

207. D. Yasokawa, S. Murata, E. Kitagawa, Y. Iwahashi, R. Nakagawa, T. Hashido and H. Iwahashi, *Environmental toxicology*, 2008, **23**, 599-606.

208. B. van Grinsven, K. Eersels, M. Peeters, P. Losada-Perez, T. Vandenryt, T. J. Cleij and P. Wagner, *ACS applied materials & interfaces*, 2014, **6**, 13309-13318.

209. J. H. Lienhard, *A Heat Transfer Textbook: Fourth Edition*, Dover Publications, 2013.

210. M. Masalha, I. Borovok, R. Schreiber, Y. Aharonowitz and G. Cohen, *Journal of Bacteriology*, 2001, **183**, 7260-7272.

211. L. P. Schenck, M. G. Surette and D. M. E. Bowdish, *FEBS Letters*, 2016, **590**, 3705-3720.

212. U. Wollina, *Clinical, cosmetic and investigational dermatology*, 2017, **10**, 51-56.

213. S. Y. C. Tong, J. S. Davis, E. Eichenberger, T. L. Holland and V. G. Fowler, *Clinical Microbiology Reviews*, 2015, **28**, 603-661.

214. H. F. L. Wertheim, D. C. Melles, M. C. Vos, W. van Leeuwen, A. van Belkum, H. A. Verbrugh and J. L. Nouwen, *The Lancet Infectious Diseases*, 2005, **5**, 751-762.

215. B. P. Howden, J. K. Davies, P. D. R. Johnson, T. P. Stinear and M. L. Grayson, *Clinical Microbiology Reviews*, 2010, **23**, 99-139.

216. N. Malachowa and F. R. DeLeo, *Cellular and Molecular Life Sciences*, 2010, **67**, 3057-3071.

217. G. L. Archer and K. B. Crossley, *The staphylococci in human disease*, New York (N.Y.) : Churchill Livingstone, 1997.

218. P. Gomez, C. Lozano, D. Benito, V. Estepa, C. Tenorio, M. Zarazaga and C. Torres, *Environmental pollution (Barking, Essex : 1987)*, 2016, **212**, 71-76.

219. *Nurse Educator*, 2013, **38**, 70.

220. J. Li, X. Zhao, X. Tian, J. Li, J. Sjollema and A. Wang, *Applied and environmental microbiology*, 2015, **81**, 2199-2205.

221. M. I. Goncheva, R. S. Flannagan, B. E. Sterling, H. A. Laakso, N. C. Friedrich, J. C. Kaiser, D. W. Watson, C. H. Wilson, J. R. Sheldon, M. J. McGavin, P. K. Kiser and D. E. Heinrichs, *Nature Communications*, 2019, **10**, 775.

222. D. Claus, *World Journal of Microbiology and Biotechnology*, 1992, **8**, 451-452.

223. A. Valero, F. Perez-Rodriguez, E. Carrasco, J. M. Fuentes-Alventosa, R. M. Garcia-Gimeno and G. Zurera, *Int J Food Microbiol*, 2009, **133**, 186-194.

224. D. Fatta, A. Achilleos, A. Nikolaou and S. Meric, *Analytical methods for tracing pharmaceutical residues in water and wastewater*, 2007.

225. J. Kennedy, I. S. Blair, D. A. McDowell and D. J. Bolton, *Journal of Applied Microbiology*, 2005, **99**, 1229-1235.

226. A. Ebrahimi, L. N. Csonka and M. A. Alam, *Biophysical Journal*, 2018, **114**, 609-618.

227. J. P. Sutherland, A. J. Bayliss and T. A. Roberts, *Int J Food Microbiol*, 1994, **21**, 217-236.

228. R. Wirth, E. Kovacs, G. Maroti, Z. Bagi, G. Rakhely and K. L. Kovacs, *Biotechnology for biofuels*, 2012, **5**, 41.

229. S. B. Kim, O. I. Nedashkovskaya, V. V. Mikhailov, S. K. Han, K. O. Kim, M. S. Rhee and K. S. Bae, *International journal of systematic and evolutionary microbiology*, 2004, **54**, 1617-1620.

230. W. Zhang, A. Gong, L. Qiu and R. Yao, *Transactions of the Chinese Society of Agricultural Engineering*, 2013, **29**, 212-217.

231. M. Berrettoni, D. Tonelli, P. Conti, R. Marassi and M. Trevisani, *Sensors and Actuators B: Chemical*, 2004, **102**, 331-335.

232. A. Vermeulen, K. P. Gysemans, K. Bernaerts, A. H. Geeraerd, J. F. Van Impe, J. Debevere and F. Devlieghere, *Int J Food Microbiol*, 2007, **114**, 332-341.

233. S. Ferré, *Journal of Caffeine Research*, 2013, **3**, 57-58.

234. A. S. Jansen, X. V. Nguyen, V. Karpitskiy, T. C. Mettenleiter and A. D. Loewy, *Science (New York, N.Y.)*, 1995, **270**, 644-646.

235. W. Stumm, *Chemical Processes in Lakes*, Wiley, 1985.

236. C. I. Kosma, D. A. Lambropoulou and T. A. Albanis, *J Hazard Mater*, 2010, **179**, 804-817.

237. A. Y. Lin and Y. T. Tsai, *The Science of the total environment*, 2009, **407**, 3793-3802.

238. K. C. Machado, M. T. Grassi, C. Vidal, I. C. Pescara, W. F. Jardim, A. N. Fernandes, F. F. Sodre, F. V. Almeida, J. S. Santana, M. C. Canela, C. R. O. Nunes, K. M. Bichinho and F. J. R. Severo, *The Science of the total environment*, 2016, **572**, 138-146.

239. R. Tröger, P. Klöckner, L. Ahrens and K. Wiberg, *Science of The Total Environment*, 2018, **627**, 1404-1432.

240. F. Gagne, C. Blaise, M. Fournier and P. D. Hansen, *Comparative biochemistry and physiology. Toxicology & pharmacology : CBP*, 2006, **143**, 179-186.

241. B. L. M. H.-G. PÖTTERING, *Journal*, 2008, 13.

242. Y. Zuo, H. Chen and Y. Deng, *Talanta*, 2002, **57**, 307-316.

243. P. R. Gardinali and X. Zhao, *Environment International*, 2002, **28**, 521-528.

244. T. Kobayashi, Y. Murawaki, P. S. Reddy, M. Abe and N. Fujii, *Analytica Chimica Acta*, 2001, **435**, 141-149.

245. J. Zou and N. Li, *Journal of Chromatography A*, 2006, **1136**, 106-110.

246. S. B. Hawthorne, D. J. Miller, J. Pawliszyn and C. L. Arthur, *Journal of Chromatography A*, 1992, **603**, 185-191.

247. J. J. Carvalho, M. G. Weller, U. Panne and R. J. Schneider, *Analytical and Bioanalytical Chemistry*, 2010, **396**, 2617-2628.

248. J. Grandke, L. Oberleitner, U. Resch-Genger, L.-A. Garbe and R. J. Schneider, *Analytical and Bioanalytical Chemistry*, 2013, **405**, 1601-1611.

249. K. Starke, *Reviews of physiology, biochemistry and pharmacology*, 1977, **77**, 1-124.

250. M. W. Schwartz, S. C. Woods, D. Porte, Jr., R. J. Seeley and D. G. Baskin, *Nature*, 2000, **404**, 661-671.

251. A. L. Benabid, B. Wallace, J. Mitrofanis, C. Xia, B. Piallat, V. Fraix, A. Batir, P. Krack, P. Pollak and F. Berger, *Comptes rendus biologies*, 2005, **328**, 177-186.

252. M. W. Schwartz, S. C. Woods, D. Porte Jr, R. J. Seeley and D. G. Baskin, *Nature*, 2000, **404**, 661.

253. P. C. Whybrow and A. J. Prange, *Archives of General Psychiatry*, 1981, **38**, 106-113.

254. J. A. Thomas and B. H. Marks, *The American journal of cardiology*, 1978, **41**, 233-243.

255. B. E. Leonard, *Journal of Psychopharmacology*, 1997.

256. D. S. Charney, G. R. Heninger and A. Breier, *Archives of General Psychiatry*, 1984, **41**, 751-763.

257. S. L. Aronoff, E. Passamani, B. A. Borowsky, A. N. Weiss, R. Roberts and P. E. Cryer, *The American journal of medicine*, 1980, **69**, 321-324.

258. E. L. Bravo and R. Tagle, *Endocrine reviews*, 2003, **24**, 539-553.

259. C.-Y. Lo, K.-Y. Lam, M.-S. Wat and K. S. Lam, *The American Journal of Surgery*, 2000, **179**, 212-215.

260. G. Eisenhofer, K. Pacak, T.-T. Huynh, N. Qin, G. Bratslavsky, W. M. Linehan, M. Mannelli, P. Friberg, H. J. Timmers and S. R. Bornstein, *Endocrine-related cancer*, 2011, **18**, 97.

261. M. A. Fotopoulou and P. C. Ioannou, *Analytica Chimica Acta*, 2002, **462**, 179-185.

262. W. S. R., *Angewandte Chemie International Edition*, 2003, **42**, 604-605.

263. B. van Grinsven, K. Eersels, M. Peeters, P. Losada-Pérez, T. Vandenryt, T. J. Cleij and P. Wagner, *ACS applied materials & interfaces*, 2014, **6**, 13309-13318.

264. W. Xu, T. H. Kim, D. Zhai, J. C. Er, L. Zhang, A. A. Kale, B. K. Agrawalla, Y. K. Cho and Y. T. Chang, *Scientific reports*, 2013, **3**, 2255.

265. S. Li, S. Cao, S. A. Piletsky and A. P. F. Turner, *Molecularly Imprinted Catalysts: Principles, Syntheses, and Applications*, Elsevier Science, 2015.

266. B. Taşdelen, N. Kayaman-Apohan, O. Güven and B. M. Baysal, *International Journal of Pharmaceutics*, 2004, **278**, 343-351.

267. K. Tyszczuk-Rotko and A. Szwagierek, *Journal of The Electrochemical Society*, 2017, **164**, B342-B348.

268. N. Lezi, S. Economopoulos, M. Prodromidis, A. Economou and N. Tagmatarchis, *International Journal of Electrochemical Science*, 2017, **12**, 6054-6067.

269. T. Alizadeh, M. R. Ganjali, M. Zare and P. Norouzi, *Electrochimica Acta*, 2010, **55**, 1568-1574.

270. M. Zougagh, A. Ríos and M. Valcárcel, *Analytica Chimica Acta*, 2005, **539**, 117-124.

271. Y. Wang, J. Zhou, C. Wu, L. Tian, B. Zhang and Q. Zhang, *Journal of Materials Chemistry B*, 2018, **6**, 5860-5866.

272. B. Sellergren, *Molecularly Imprinted Polymers: Man-made Mimics of Antibodies and Their Applications in Analytical Chemistry*, Elsevier, 2001.

273. X. Ding and P. A. Heiden, *Macromolecular Materials and Engineering*, 2014, **299**, 268-282.

274. G. Vasapollo, R. D. Sole, L. Mergola, M. R. Lazzoi, A. Scardino, S. Scorrano and G. Mele, *International journal of molecular sciences*, 2011, **12**, 5908-5945.

275. A. Vázquez-Guardado, S. Barkam, M. Peppler, A. Biswas, W. Dennis, S. Das, S. Seal and D. Chanda, *Nano Letters*, 2019, **19**, 449-454.

276. B. Si and E. Song, *Chemosensors*, 2018, **6**, 1.

277. E. Verheyen, J. P. Schillemans, M. van Wijk, M.-A. Demeniex, W. E. Hennink and C. F. van Nostrum, *Biomaterials*, 2011, **32**, 3008-3020.

278. J. H. Martin, R. Norris, M. Barras, J. Roberts, R. Morris, M. Doogue and G. R. Jones, *The Clinical biochemist. Reviews*, 2010, **31**, 21-24.

279. R. M. Trueb, *International journal of trichology*, 2016, **8**, 73-77.

280. J. Richard, C. Sainsbury, G. Needham, J. Farndon, A. Malcolm and A. Harris, *The Lancet*, 1987, **329**, 1398-1402.

281. P. Singla, O. Singh, S. Sharma, K. Betlem, V. K. Aswal, M. Peeters and R. K. Mahajan, *ACS Omega*, 2019, **4**, 11251-11262.

282. B. van Grinsven, K. Betlem, T. J. Cleij, C. E. Banks and M. Peeters, *Journal of Molecular Recognition*, 2017, **30**, e2563.
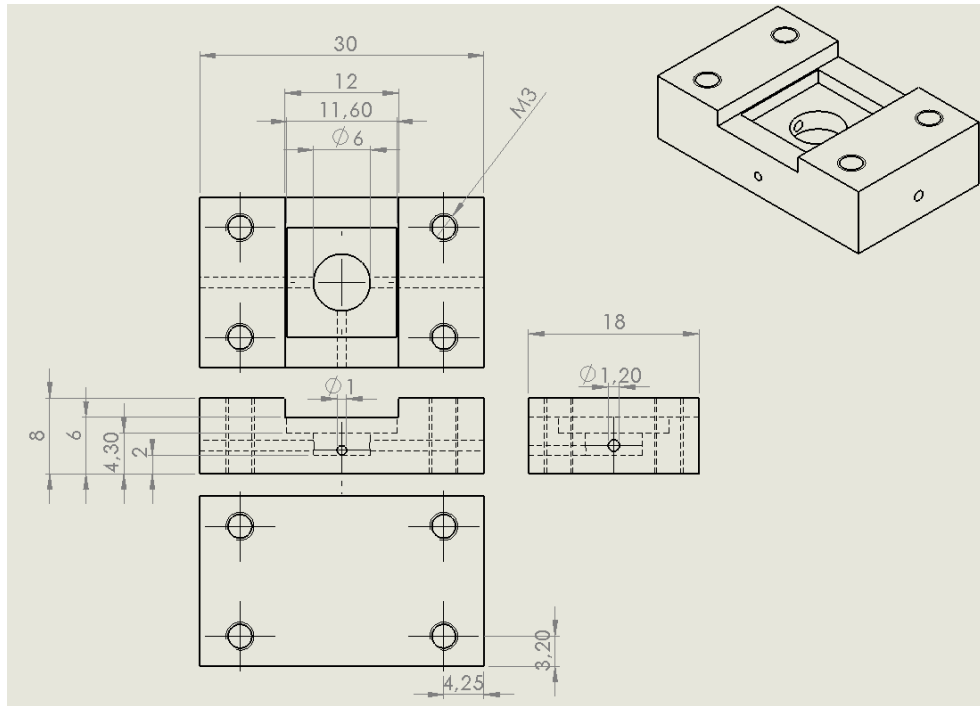
1. Appendix 1; working drawings of the flow cells

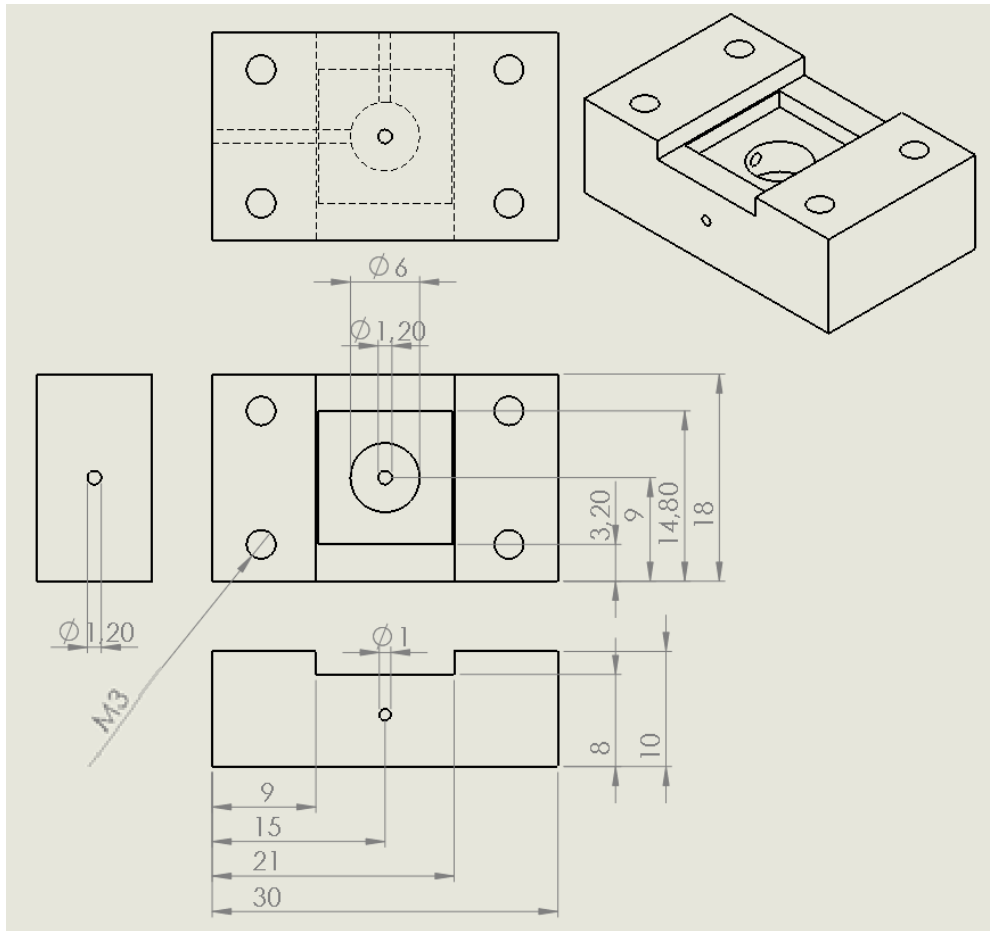**Figure S 1 Work drawings of the conventional flow cell.**
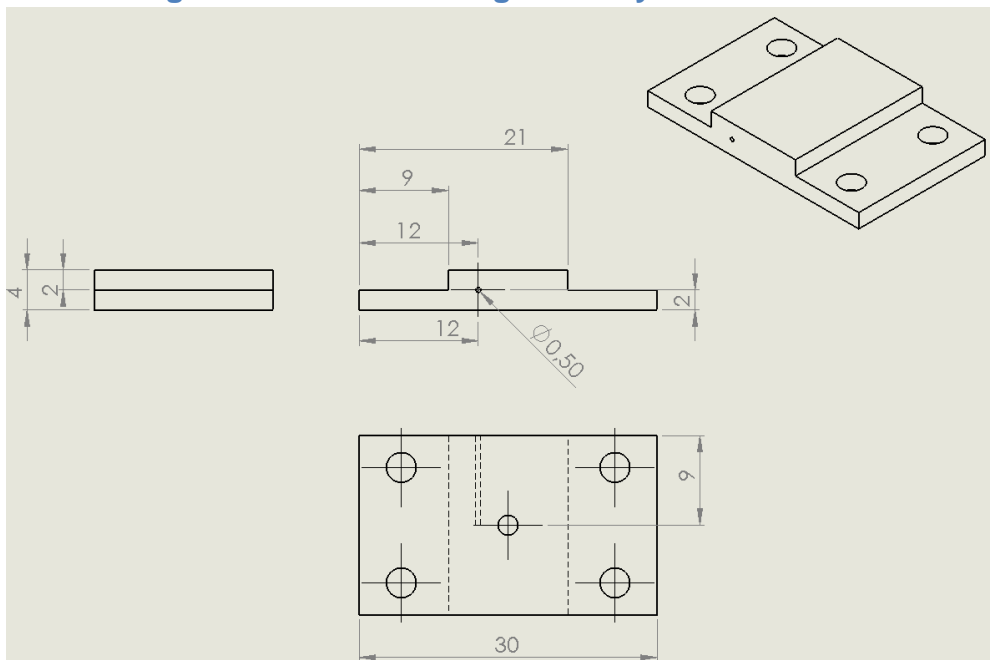
Figure S 2 Work drawings of the yeast flow cell.

Figure S 3 Work drawings of the copper heat sink